

Die approbierte Originalversion dieser Dissertation ist an der Hauptbibliothek der Technischen Universität Wien aufgestellt (<http://www.ub.tuwien.ac.at>).

The approved original version of this thesis is available at the main library of the Vienna University of Technology (<http://www.ub.tuwien.ac.at/englweb/>).

DISSERTATION

MICROMAGNETIC SIMULATIONS OF ANTIFERRO - AND FERROMAGNETIC STRUCTURES FOR MAGNETIC RECORDING

ausgeführt zum Zwecke der Erlangung des akademischen Grades
eines Doktors der technischen Wissenschaften

unter der Leitung von
Univ. Doz. Dr. Thomas Schrefl
Institut für Festkörperphysik E138

eingereicht an der Technischen Universität Wien
Fakultät für Naturwissenschaften und Informatik

durch

Dieter Süss
Rathausplatz 18, 3130 Herzogenburg
Matr. Nr. 9426424

Wien, am 3. Juni 2002



One must still have chaos in oneself to give birth to a dancing star.

- Friedrich Nietzsche -

Abstract

Finite element micromagnetic simulations are performed. The time evolution of the magnetization is obtained from the numerical time integration of the Landau-Lifshitz-Gilbert equation. It is shown that the efficiency of the time integration scheme can be drastically increased by the additional information of the energy curvature (preconditioning). The method is applied to study the magnetic properties of different applications of magnetic storage systems.

The switching time and switching field of perpendicular recording media is investigated. Numerical simulations show that with ultra fast field pulses (picosecond regime) fast switching modes exists for small external field strengths. Particularly interesting is the fact that in that regime the switching time decreases with smaller external field strengths. The damping parameter α , that describes in the Landau-Lifshitz-Gilbert equation the relaxation towards equilibrium, is found to change both the switching time and the switching mode.

The magnetic properties of chemically synthesized FePt was investigated in order to explain the experimentally observed remanence enhancement and the small coercive field compared to the anisotropy field. Both the coercivity and the remanence are found to agree well with experiments when multiple c-axes within every FePt nanoparticles are assumed.

Experiments on diluted $\text{Nd}_2\text{Fe}_{14}\text{B}$ nanoparticles in a non magnetic phase show that in the thermally demagnetized state a proportion of grains contains domain walls although the minimum energy state is single domain. Micromagnetic calculations confirmed the formation of domain walls in the thermally demagnetized state because the lowest energy state is separated by a large energy barrier.

A continuum approach is developed that allows to explore the magnetic domain structures in granular antiferromagnetic/ferromagnetic bilayers. The micromagnetic equation for both the ferromagnet and antiferromagnet are solved using the finite element method. The formation of lateral domain walls in the antiferromagnet is found to play an important role in order to explain the exchange bias effect. Although used in applications the origin of exchange bias at compensated interfaces cannot be explained by current theories. The presented model that relies on the granularity of the antiferromagnet results in exchange bias at compensated interfaces. The experimentally observed change of the bias field and the coercivity with the number of hysteresis cycles (training effect) is explained by the change of the domain structure in the antiferromagnet.

Kurzfassung

Mikromagnetische Simulationen mit Hilfe der Methode der finiten Elemente wurden durchgeführt. Die Zeitentwicklung der Magnetisierung folgt aus der Zeitintegration der Landau-Lifshitz-Gilbert Gleichung. Es wurde gezeigt, daß die Effizienz der Zeitintegration stark verbessert werden kann, wenn der Zeitintegration zusätzliche Information über die Krümmung der Energielandschaft bereitgestellt wird (Vorkonditionierung). Die Methode wurde für die Berechnung der magnetischen Eigenschaften von verschiedenen magnetischen Speichersystemen angewandt.

Die Ummagnetisierungszeit und das Koerzitivfeld von vertikalen Festplattenmedien wurde untersucht. Die numerischen Simulationen zeigen, daß bei ultra kurzen Feldpulsen (Picosekunden Bereich) schnelle Ummagnetisierungsmoden auftreten. Speziell bemerkenswert ist die Tatsache, daß in diesem Feldbereich die Ummagnetisierungszeit mit sinkender Feldstärke abnimmt. Die Dämpfungskonstante α , die in der Landau-Lifshitz-Gilbert Gleichung die Relaxation in das Gleichgewicht beschreibt, ändert sowohl die Ummagnetisierungszeit als auch die Ummagnetisierungsmode.

Die experimentell gefundene Erhöhung der Remanenz und die verglichen mit dem Anisotropiefeld relativ kleinen Koerzitivfelder wurden für chemisch synthetisierten FePt Teilchen untersucht. Sowohl das Koerzitivfeld als auch die erhöhte Remanenz stimmen sehr gut mit Experimenten überein, wenn mehrere leichte Richtungen in den FePt Nanoteilchen angenommen werden.

Experimente an $\text{Nd}_2\text{Fe}_{14}\text{B}$ Nanoteilchen, verdünnt in einer nichtmagnetischen Phase, zeigen, daß im thermisch entmagnetisierten Zustand Domänen in den Nanoteilchen auftreten, obwohl der Zustand mit minimaler Energie der Eindomänenzustand ist. Mikromagnetische Simulationen konnten zeigen, daß der Eindomänenzustand tatsächlich minimale Energie hat, dieser aber auf Grund einer Energiebarriere nicht erreichbar ist.

Ein Kontinuummodell wurde entwickelt, das die Untersuchung der Domänenstruktur von Ferromagnet/Antiferromagnet Schichtsystemen erlaubt. Die mikromagnetischen Gleichungen für den Ferromagnet und den Antiferromagnet werden mit Hilfe der Methode der finiten Elemente gelöst. Es wurde gezeigt, daß die Bildung von lateralen Domänenwänden im Antiferromagnet bei der Erklärung des "Exchange Bias" Effektes eine wichtige Rolle spielen. Obwohl der Effekt vielfach angewendet wird, gibt es keine Theorie, die das Auftreten des "Exchange Bias" Effektes an kompensierten Oberflächen befriedigend zu erklären vermag. Das vorgestellte Modell zeigt, daß für granulare Antiferromagneten der "Exchange Bias" Effekt auch an kompensierten Oberflächen auftreten kann. Die Änderung der Stärke des "Exchange Bias" Effektes und der Koerzitivität (Trainingseffekt) bei wiederholtem Durchlaufen der Hysteresekurve kann durch die Änderung der Domänenstruktur im Antiferromagneten erklärt werden.

Acknowledgment

It is a pleasure to say thank you to the whole magnetism working group around Josef Fidler and Thomas Schrefl. Thank you Thomas and Josef for your enthusiasm to provide a wonderful workplace at university for your students. Yes, sometimes we become aware of your effort. Your effort to apply for projects in order to be able to give students the possibility to follow their ideas and your effort to organize and manage the group.

More than five years ago Thomas Schrefl convinced me to start a student project work at the institute by saying: “My micromagnetic simulations are just like arranging compass needles. A compass needle just arranges in such a way that it lowers its energy in the external field”. Since it seemed to be a solvable problem to arrange compass needles I decided to start working in the group. After some time I had learned that modeling compass needles is not such a trivial problem as it was claimed to be. But to realize that was nice as well and I am really happy for the possibility to do work (sometimes a bit beyond compass needles) I was really enthusiastic with.

Since the arranging of compass needles turned out to be a bit of computational work more computers were required. Almost all the work to maintain the computers is done by Werner. So, if something did not work we just had to say: “Werner, there is a problem.....”, and the problem vanished. So, thank you Werner for all your help.

Of course I also want to thank the members who joined the group a bit later. Thanks Hermann that together it was possible to make a poster for a wonderful Greece conference within 1 hour. What a pity would it have been if we had not done it (Of course we have to forget your motorcycle accident). For example Rok would not have had the possibility to learn surfing, that was unfortunately a bit painful for his leg. Thomas and I would not have had the chance to improve our fitness and to enjoy sunrises by riding up the bike to the conference hotel. Also thanks to Vassilios who equipped our institute with such a huge amount of Ouzo that there is still something left.

But not only Greece was a wonderful place I was allowed to see during my time working on my Ph.D. I also had the possibility to go to Western Australia. Special thanks to Prof. Bob Stamps, Dr. Hong Sun and Dr. Rob Woodward for the invitation to work at the University of Western Australia. It was really a pleasure to discuss for hours with Bob Stamps. I will never forget his phrase: “I am just wondering.....” After that you knew that a new idea was born.

Thanks Joo-Von, who told me what exchange bias is, I could compare my computer program with his well tested one during some night sessions. I also want to thank Prof. Robert Street for taking time to discuss with a 60 year younger physicist about physical details. Of course special thanks to Stuard, Nada, Peter and Nicole for introducing me to the habits of Western Australia (jug, football aussi rules, cricket, subs, fullmoon surfing, that white pointers (white sharks) are our friends..) and to advise me which beer is best to buy for friday's beer symposium on the roof of the physics department.

Meinen Eltern möchte ich für die mitgegebenen Werte danken, die es mir ermöglichten ein Hochschulstudium abzuschließen und aktiv und glücklich zu leben.

Finally, I want to acknowledge the financial support of the Austrian Science Fund, Y-132 PHY, from the EC-5FPR Growth Project GRD1-1999-11125 and from the Australian Research Council.

Contents

1	Introduction	10
1.1	Outline of the thesis.....	14
2	Numerical Methods for Solving the Micromagnetic Equations.....	17
2.1	Introduction	17
2.2	Finite element micromagnetics	19
2.2.1	Calculation of the stray field	25
2.2.2	Boundary condition for the exchange field.....	26
2.3	Time integration	30
2.3.1	Preconditioning	32
2.3.2	Error control.....	33
2.3.3	Storage requirements	34
2.4	Performance of time integration scheme	35
2.4.1	μ MAG Problem # 4.....	35
2.4.2	Granular media	40
2.5	Conclusions.....	45
3	Micromagnetism for Perpendicular Recording Media	48
3.1	Introduction	48
3.2	Reversal modes	49
3.2.1	High damping reversal ($\alpha = 1$).....	49
3.2.2	Low damping reversal ($\alpha = 0.02$)	51
3.3	Energy barriers and thermally activated reversal modes.....	53
3.4	Switching times of small magnetic particles.....	59
3.4.1	Columnar grain.....	59
3.4.2	Single magnetic moment.....	62
3.4.3	Switching times at finite temperature.....	66
3.5	Conclusions.....	72
4	Magnetic Reversal Processes in Fe-Pt Nanoparticle Arrays.....	75
4.1	Introduction	75
4.2	Experimental data	76
4.3	Micromagnetic simulations of the hysteresis loop	77
4.3.1	Single c-axis.....	77
4.3.2	Multiple c-axis.....	80
4.3.3	Reduction in exchange stiffness	82
4.4	Conclusions.....	86

5 High Coercive Particles	88
5.1 Introduction	88
5.2 Calculation of the initial curve and coercivity.....	91
5.3 Conclusions.....	95
6 Magnetic Nanodots	97
6.1 Introduction	97
6.2 Reversal modes for a single dot	98
6.3 Logic gates.....	102
6.4 Conclusion.....	104
7 Exchange Bias	108
7.1 Introduction	108
7.2 Mechanisms.....	111
7.2.1 Uncompensated interfaces.....	111
7.2.2 Compensated interfaces - Spin flop coupling.....	116
7.2.2.1 Spin flop coupling strength	118
7.2.2.2 Interface energy term for spin flop coupling.....	119
7.2.2.3 Partial domain walls in the antiferromagnet.....	120
7.2.3 Interface defects	128
7.2.3.4 "Random field" Model.....	129
7.2.3.5 Transition from spin flop coupling to collinear coupling.....	130
7.3 Continuum theory for antiferromagnets	132
7.3.1 Coupling to a ferromagnet.....	141
7.3.2 Effective fields	143
7.3.3 Comparison with an atomistic model	145
7.4 Exchange bias at compensated interfaces	151
7.4.1 Finite element model.....	153
7.4.2 Granular model.....	158
7.5 Conclusions.....	171
A Appendix	175
A.1 Exchange coupling at mixed AF/F interfaces.....	175
A.2 Bias field for mixed interfaces.....	180
8 Selected Publications	188

1

INTRODUCTION

Every year the number of bits that are crammed onto each square centimeter of a commercial hard disk almost doubles. In some areas the exponential increase breaks down because of limited resources on earth (e.g. world energy consumption...). Fortunately there are also areas where it stops because of physical limits. The limit in the case of hard disc drives is given by an effect called superparamagnetism. It denotes the phenomenon that the magnetic regions on the disk cannot retain their magnetic orientation (=the data) over the lifetime of the product when they become too small. These small regions can switch from one equilibrium state (Bit 1) to the opposite state (Bit 0) because of thermal agitations. Considering the effect of superparamagnetism Charap [2] predicted in 1997 an areal density of 40 Gbits/in² as the upper bound.

A new technology overcame this limit. In May 2001 IBM first shipped in the Travelstar laptop hard disk drives with antiferromagnetically-coupled (AFC) media. The current world record of 130 Gbits/in² was achieved by Read-Rite at the end of April 2002. (130 Gbits/in² = 20.15 Gbits/cm² = 2.52 GBytes/cm²). This new level of storage density translates to 82 hours of DVD-quality video on a single disc.

Besides the areal density, another key factor of hard disc drives is the data rate. At today's data rates of 400 Mbit/s, the response time of the media is already in the nanosecond regime. At such writing speeds the magnetization reversal is determined by gyromagnetic precession. The switching becomes a highly nonlinear effect associated with large excursions of the magnetization from its equilibrium state. As a consequence new and unexpected features during magnetization reversal occur.

In common hard disk drives the information is stored in the magnetization state of a ferromagnetic granular film. A granular film is a composition of grains, that are regions with the same crystal structure favoring the magnetization to align parallel to one axis, called easy axis direction. Usually neighboring grains have the same crystal structure but the easy axis direction is different. In longitudinal recording the easy axes are randomly oriented in the plane of the film. In modern hard disk drives the grain size diameter is less than 10 nm. One bit is represented by the magnetization state of about 50 neighboring grains. Because of the inplane anisotropy in longitudinal recording the magnetization is parallel to the film plane. Small

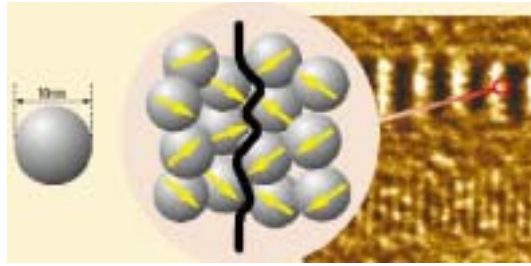


Figure 1.1: Transition between two magnetic bits on a granular longitudinal recording media. Smaller grain sizes support sharp transitions [3].

grains are required because the minimum bit length, below which neighboring transitions become indistinguishable, is determined by the transition width which in turn depends on the grain size of the film. Figure 1.1 shows that sharp transitions require small grains. Usually the grains are weakly exchange coupled to each other. For too strong exchange coupled grains the magnetization in neighboring grains aligns parallel, effectively larger grains are formed. Thus magnetic interaction increases the effective grain size. As a consequence larger bit lengths would be required. On the other hand completely decoupled grains are thermally unstable because the thermal stability decreases with decreasing grain volume. Thus an important task in longitudinal recording is to find the optimal exchange coupling strength between grains.

In addition, the thermal stability is decreased by the strong demagnetizing field that opposes the magnetization. At low recording density, when the bit length is much larger than the film thickness the demagnetizing field is small. However, at high densities where the bit length becomes smaller than the film thickness the magnetic charges inherent to longitudinal recording are pushed together and high demagnetizing fields occur.

The idea of perpendicular recording is to represent bits with magnetization directions perpendicular to the film plane. As argued above a perpendicular orientation of the magnetization reduces the demagnetizing field in the high density limit. Thus opposite bits act as domains that reduce the stray field. To achieve a perpendicularly magnetized configurations textured films with easy axes perpendicular to the film plane are used.

Another advantage of the aligned grains in perpendicular recording is a narrow switching field distribution. In conventional longitudinal media the grains are oriented randomly. Since the switching field depends on the angle between the easy axis and the external field, some grains may not switch, leading to a broadening of the transition between the bits.



Figure 1.2: In traditional longitudinal magnetic recording media ferromagnetic grains represent one bit as shown in the left image. The demagnetizing field that occurs at the transition between bits can be reduced by antiferromagnetically -coupled (AFC) media as shown in the right image [5]. The opposing magnetic orientations make the entire multilayer structure appear much thinner than it actually is.

A breakthrough to decrease the demagnetizing field in longitudinal recording was achieved by antiferromagnetically coupled media (AFC). Figure 1.2 shows the basic idea of (AFC) media. In contrast to common media where one ferromagnetic film stores the information as shown in the left image in figure 1.2, AFC media consist of two ferromagnetic films which are antiferromagnetically coupled. The opposite direction of the two films is achieved by an ultra-thin ruthenium layer which may be better known as “pixie dust”. The opposite orientation of the films decreases the demagnetizing field which makes the entire multilayer structure appear much thinner than it actually is. However the thermal stability is proportional to the sum of the two layer thicknesses. Thus, concerning thermal stability the system appears to be thick.

Another possibility to increase the thermal stability is using high anisotropy materials. Thermal stability is proportional to the grain volume times the anisotropy. However, the strength of the field produced by the write head is limited which in turn imposes a limit on the media coercivity. One possibility to overcome the writing problem is to employ temperature assisted methods. A laser beam heats up the region where the bit is intended to be written. The anisotropy decreases with temperature which makes it possible to write it with fields of common write heads. Promising candidates for high anisotropy media are rare earth materials such as NdFeB, Co_5Sm , or FePt. For example the anisotropy of Co_5Sm is about 20 times larger than that of pure Co that is a typical hard disk material. Co_5Sm offers thermally stable grain diameters down to 2.8 nm.

Another technology that is a possible candidate for high density recording up to the Tbit/in² regime relies on patterned media. Patterned media consist of a periodic array of discrete magnetic elements. Each element is exchange isolated from other elements but the grains within one element are strongly exchange coupled. The elements are sufficient small so that the magnetization state is a single domain state. The two possible directions imposed by the crystalline anisotropy are interpreted as the binary 1 or 0. Since the superparamagnetic limit applies to the whole single bit, not to each of the many grains as in a conventional continuous multigrain bit, the volume and switching energy for the single-element bit in the patterned media are much larger than that of a single grain in conventional continuous media. Another advantage of patterned media is that transition noise between bits is eliminated because the bits are well separated by a non magnetic phase. The problem with patterned media is that, until now, there are no cheap and mass-production-compatible manufacturing methods. Conventional lithographic methods are too time-consuming or do not have the desired resolution to handle the required small structure sizes.

A fascinating new approach for fabricating separated magnetic nanoparticles that arrange on a periodic lattice was discovered by S. Sun et al [8]. Chemical synthesis routes were applied to prepare FePt monodisperse particles. These monodisperse magnetic nanoparticles self assemble into a three dimensional array. The particle size that can be varied from 3-10 nm and the high crystalline anisotropy make self assembled FePt nanoparticles attractive for storage in the Tb/in² regime.

Another hot topic in the information science technology are magnetic random access memories (MRAMs). One MRAM element usually consists of two magnetic layers with different coercivity that are separated by a non-magnetic or insulating interlayer. Depending on the angle of the magnetization between the two ferromagnetic layers the resistivity of the trilayer changes. That effect called giant magnetoresistance (GMR) was discovered in 1988 [1]. It did not solely drastically improve the performance of MRAM's but it is also used to increase the sensitivity in read heads of hard disc drives. In MRAM elements the magnetization of the hard magnetic layer represents the data bit. The data is written by a magnetic field that is applied by a current through a conductor line adjacent to the element. The field is strong enough that the hard magnetic element can be magnetized in the field direction. An opposite current changes the magnetization of the element. The magnetization direction of the soft magnetic film can be changed by a smaller current, that does not change the magneti-

zation state of the hard magnetic film. The soft magnetic element is used to probe the state of the hard magnetic element. Depending on the state of the hard magnetic film and the imposed direction of the soft magnetic film the resistivity changes. MRAM elements are arranged in a rectangular array and are connected with conductor lines, allowing individual elements to be selected. The advantage of MRAM elements over common semiconductor-based dynamic random access memories (DRAMs) are low energy consumption and high storage densities. Furthermore MRAM elements are non-volatile storage devices so they retain information when the computer is switched off. To optimize the switching speed of MRAM elements a profound knowledge of the reversal process is important. Micromagnetic simulations are a suitable tool to resolve inhomogeneities during reversal that significantly influence the switching time. Further applications of magnetic nano-elements are sensors, magneto-electronics devices and logic magnetic gates [4,7].

The introduction of recording heads that are based on the giant magnetoresistance (GMR) in the late 1990s doubled the rate of areal density improvements for hard disc drives. Recording heads on the basis of the GMR effect consist of two ferromagnetic layers (reference layer and pinned layer) separated from each other by a thin spacer layer. The reference layer rotates in response to the signal field. To fix the pinned layer along one direction one makes use of the so called exchange bias effect that was discovered 1956 by Meiklejohn and Bean [6]. The exchange bias effect can be observed in systems, where an antiferromagnet is coupled to a ferromagnet. The presence of the antiferromagnet imposes a preferred direction of the magnetization in the ferromagnet. Commonly used antiferromagnetic materials are FeMn and IrMn. Although the exchange bias effect is successfully applied in GMR sensors there is still no theory available that can explain the exchange bias effect in detail. However, the optimization of GMR sensors requires a detailed understanding of the coupling between the ferromagnetic and antiferromagnetic layer.

1.1 Outline of the thesis

Section 2 introduces the basics of micromagnetic simulations and gives a short introduction to the finite element method. Furthermore a method to improve the time integration of the Landau-Lifshitz-Gilbert equation is explained in detail.

Section 3 deals with perpendicular recording. The switching time and the thermal stability of perpendicular recording media are investigated.

Computer simulations of the reversal process of self assembled FePt nanoparticles are performed in section 4. Especially the influence of the microstructure of the self assembled particles on the remanence and coercivity is simulated.

In section 5 micromagnetic simulations were performed to explain experimental data for NdFeB nanoparticles that are embedded in a non-magnetic phase.

The influence of the size and the damping parameter on the switching of circular magnetic nano elements is investigated in section 6.

In section 7 a continuum theory for antiferromagnets is introduced. The solution of the micromagnetic equations with the finite element method is explained in detail. The new approach is applied to investigate the exchange bias effect in granular ferromagnetic/antiferromagnetic structures. An explanation for the exchange bias effect for granular bilayers with completely compensated interfaces is given.

References

- [1] M. N. Baibich, J. M. Broto, A. Fert, F. Nguyen Van Dau, and F. Petroff, "Giant Magnetoresistance of (001)Fe/(001)Cr Magnetic Superlattices," *Phys. Rev. Lett.*, vol. 61, pp. 2472, 1988.
- [2] S. H. Charap, P. L. Lu and Y. He, "Thermal stability of recorded information at high densities," *IEEE Trans. Magn.*, vol.33, pp. 978, 1997.
- [3] R. Comerford, "Magnetic storage: The medium that wouldn't die ," *IEEE Spectrum*, pp. 36, December 2000,
- [4] R. P. Cowburn, M. E. Welland, "Room temperature magnetic quantum cellular automata," *Science*, vol. 287, pp. 1466, 2000.
- [5] http://www.research.ibm.com/resources/news/20010518_pixie_dust.shtml
- [6] W. H. Meiklejohn, C. P. Bean "New magnetic anisotropy," *Phys. Rev.* , vol. 102, pp. 1413, 1956.
- [7] G. A. Prinz, "Magnetoelectronics applications," *J. Magn. Magn. Mater.*, vol. 200, pp. 57, 1999.
- [8] S. Sun, C. B. Murray, D. Weller, L. Folks, A. Moser, "Monodisperse FePt Nanoparticles and Ferromagnetic FePt Nanocrystal Superlattices", *Science*, vol. 287, pp. 1989, 2000.

2

NUMERICAL METHODS FOR SOLVING THE MICROMAGNETIC EQUATIONS

A detailed description for the solution of the Landau-Lifshitz-Gilbert equation with the finite element method is given. The use of implicit time integration schemes with proper preconditioning is reported. Simulations of a single phase magnetic nanoelements without surface roughness and a magnetic nanoelement with a granular structure are performed to investigate the influence of the microstructure on the numerical behavior. Nanoelements with a granular structure cause an inhomogeneous computational grid. In granular systems preconditioning for time integration speeds up the simulations by three orders of magnitude as compared to conventional time integration schemes like the Adams method.

2.1 Introduction

Numerical micromagnetics is an essential tool to optimize magnets in magnetic storage devices and sensors. The application of these devices requires a profound knowledge of the reversal mechanism. Using the Landau-Lifshitz-Gilbert (LLG) equation the time evolution of the magnetization can be calculated. The treatment of systems with realistic size leads to a system of ordinary differential equations with up to one million unknowns. State of the art time integration schemes provide an efficient numerical solution of the equations.

Traditionally explicit time integration methods are used in numerical micromagnetics. These methods are easy to apply since only the right hand side of the Landau-Lifshitz-Gilbert equation has to be evaluated. Victoria applied a Runge-Kutta [23] method to solve the Landau-Lifshitz-Gilbert in an array of columnar CoNi particles. Different types of Adams formulas are commonly used in micromagnetics. Mansuripur applied an Adams method [16] to calculate the time evolution of thin film recording media. The Adams method that Zhu and Bertram used [26] is a varying order and varying step-size method and is well described by Gear [15]. Jones and Miles [15] used the LLG equation to simulate the magnetic behavior of a metal evaporated tape. They performed the integration by using a variable-order variable-step Adams method. More specifically, they used the NAG D02CHF routine. Tako et al [19] used the Adams 4th-order predictor-corrector method with error control and step size adjustment

described in [5]. McMichael and Donahue use a second order predictor-corrector technique of the Adams type to calculate the dynamic response of magnetic nanoelements [17].

However, for highly exchange coupled systems or complex microstructures the Adams methods and explicit time integration schemes require an intolerably small time step to maintain numerical stability. These problems are supposed to be stiff and can be more suitably solved with backward differentiation formula methods. Originally, Hayashi and Nakatani [13] applied the backward Euler method which is a backward differentiation method (BDF) of order 1, to solve the Landau-Lifshitz equation for magnetic bubble domain wall motion. Albuquerque and Miltat [1] treat the exchange term implicitly applying the Crank Nicolson method. This scheme applies a feedback mechanism from monitoring the damping coefficient, maximum torque and total energy to obtain high accuracy. E and Wang [8] developed a projection method. The key point of this method is that they relax the condition that the magnitude of the magnetization vector remains constant. After each time step the magnetization vector is projected back to the unit sphere. The proposed method is unconditionally stable.

The above methods are used together with a finite difference method for space discretization. The finite element method allows irregular grids suitable for complex microstructures and adaptive refinement. Toussaint and co-workers [22] showed that the time step required to obtain a stable solution of the Landau-Lifshitz Gilbert (LLG) equation with an explicit time integration scheme has to be proportional to h_g^2 , where h_g is the size of the spatial grid. Thus a fine mesh which is required to resolve magnetization inhomogeneities near edges or grain boundaries, limits the time step of explicit methods. BDF methods are more suitable. However, the linear system which has to be solved at every time step as part of the Newton method is ill conditioned. Proper preconditioning decreases the number of iterations when the system is solved iteratively and thus speeds up the computation considerably.

Yang and Fredkin [25] developed a numerical procedure to study the dynamic behavior in micromagnetic systems using the finite element method. They solved the damped Gilbert equation for a continuous magnetic medium, including all the interactions in standard micromagnetic theory in 3D regions of arbitrary geometry and physical properties. The magnetization is linearly interpolated in each tetrahedral element in a finite element mesh from its value on the nodes, and they use the Galerkin method to discretize the dynamic equation. The demagnetizing field is computed by solving Poisson's equation and they treat the external region by means of an asymptotic boundary condition. They apply the CVODE code [6-7] to

solve the stiff system of ordinary differential equations. CVODE provides the option to solve the equations either with the Adams or a backward differentiation formula (BDF) method. In order to apply a preconditioner for the linear system, CVODE requires an approximate Jacobian, which is the first derivative of the right hand side of the Landau-Lifshitz-Gilbert equation. Yang and co-workers cannot supply the Jacobian explicitly because they use the Galerkin method for space discretization. However, they are able to give a suitable approximation. A more detailed description of the numerical methods for ODEs in micromagnetics is given in [20].

In this paper we use the finite element method to compute the dynamic response of thin film elements of different shape and structure. Starting from the finite element discretization of the total energy, the effective field can be evaluated using the box method. Each node has its magnetic moment and its effective field. Thus the right hand side of the LLG equation and the Jacobian can be calculated explicitly. For the preconditioning only an approximation of the Jacobian is needed. Thus it is possible to keep the approximated Jacobian sparse, omitting the stray field part. In section 2 we introduce the finite element techniques used for space discretization, the calculation of the effective fields, and the approximate Jacobian. The demagnetizing field is calculated using a hybrid finite element boundary method as discussed in section 3. Section 4 treats the time integration of the discretized LLG equation. Section 5 gives numerical examples. The Adams method, the BDF method and the preconditioned BDF method are compared for μMAG Problem # 4 and a thin film element with granular microstructure. The results show a considerable decrease of the CPU time for the preconditioned BDF method for all investigated samples.

2.2 Finite element micromagnetics

Using micromagnetics the theoretical treatment of magnetization dynamics at zero temperature starts from the Gilbert equation [2],

$$\frac{\partial \mathbf{J}}{\partial t} = -|\gamma| \mathbf{J} \times \mathbf{H}_{\text{eff}} + \frac{\alpha}{J_s} \mathbf{J} \times \frac{\partial \mathbf{J}}{\partial t}, \quad (2.1)$$

where \mathbf{J} is the magnetic polarization vector, \mathbf{H}_{eff} is the effective field, and J_s is the spontaneous polarization. \mathbf{J} is assumed to be a continuous function of space. To obtain the general

form $\frac{dy}{dt} = f(t, y)$ for an ordinary-differential equation (ODE), we transform equation (2.1) into the mathematically equivalent Landau-Lifshitz-Gilbert (LLG) equation

$$\frac{\partial \mathbf{J}}{\partial t} = -\frac{|\gamma|}{1 + \alpha^2} \mathbf{J} \times \mathbf{H}_{eff} - \frac{\alpha}{1 + \alpha^2} \frac{|\gamma|}{J_s} \mathbf{J} \times (\mathbf{J} \times \mathbf{H}_{eff}), \quad (2.2)$$

with the gyromagnetic ratio

$$|\gamma| = 2, 210175 \times 10^5 \frac{\text{m}}{\text{As}}, \quad (2.3)$$

and the Gilbert damping constant α .

The finite element method is used to discretize equation (2.2). The magnetic polarization $\mathbf{J}(\mathbf{x})$ is expanded with linear basis functions $\varphi_i(\mathbf{x})$. For one component of \mathbf{J} we can write

$$J^k(\mathbf{x}) \approx J_{app}^k(\mathbf{x}) = J_s(\mathbf{x}) \sum_{i=1}^n u_i^k \varphi_i(\mathbf{x}). \quad (2.4)$$

$J_{app}^k(\mathbf{x})$ is the finite element approximation of the k -th component of the magnetic polarization. The coefficient u_i^k denotes the k -th component of the normalized spontaneous polarization ($|u_i^k| \leq 1$) on the node point i . The number of unknowns (u_i^k) is three times the number of node points of the finite element mesh. The basis functions obey

$$\varphi_i(\mathbf{x})\varphi_j(\mathbf{x}) = \delta_{ij}. \quad (2.5)$$

For practical reasons, the expansion of the unknown function is usually done on an element by element fashion in finite element packages. For the magnetic polarization follows

$$J_{app}^k(\mathbf{x}) = \sum_{e=1}^{N_e} J_{s,e} \sum_{i=1}^{N_b} u_{e,i}^k \varphi_{e,i}(\mathbf{x}). \quad (2.6)$$

N_e and N_b denote the number of finite elements and number of nodal points of each element, respectively. $J_{s,e}$ is the spontaneous polarization of element e . If we use linear polynomials for the shape functions $\varphi_{e,i}(\mathbf{x})$ the vertices of the finite elements are equal to the nodal points. At a nodal point i the values of the reduced magnetic polarization $u^k(\mathbf{x})$ are given by

the coefficients $u_{e,i}^k$. If tetrahedrons form the finite element mesh and linear shape functions are used $N_b = 4$. For quadratic shape functions $N_b = 10$. The shape functions obey

$$\sum_{i=1}^{N_b} \varphi_{e,i}(\mathbf{x}) = 1, \quad (2.7)$$

$$\varphi_{e,i}(\mathbf{x}_j) = \delta(\mathbf{x}_j - \mathbf{x}_i), \quad (2.8)$$

where \mathbf{x}_i and \mathbf{x}_j denote the positions of the local node points i and j of the element e respectively. To perform the time integration, we have to calculate the effective field on every node point of the finite element mesh. However we cannot directly use the analytic formula for the effective field, which follows from the negative functional derivative of the total Gibbs energy (equation 2.10) as,

$$\mathbf{H}_{eff} = -\frac{\delta E_t}{\delta \mathbf{J}} = \frac{2A}{J_s^2} \Delta \mathbf{J} + \frac{2}{J_s^2} K_1 (\mathbf{J} \mathbf{a}) \mathbf{a} + \mathbf{H}_s + \mathbf{H}_{ext}. \quad (2.9)$$

Here A is the exchange constant, K_1 is the magnetocrystalline anisotropy constant, \mathbf{a} is the unit vector parallel to the anisotropy axis, \mathbf{H}_s is the magnetostatic stray field, and \mathbf{H}_{ext} is the external applied field. The first term on the right side of equation (2.9) is the exchange field. Its calculation needs the second derivative of the magnetic polarization. Numerically the second derivatives cannot be calculated directly using linear basis functions. In addition, the calculation of the stray field which follows from the gradient of a scalar potential is crucial. With linear basis functions the gradient of the potential, which is proportional to the stray field, is only defined within an element but not on the node points. To overcome this problem we start from the total Gibbs energy for a ferromagnetic particle [3]

$$E_t = \int_{\Omega} e_t(\mathbf{J}) dV = \int_{\Omega} \left(A \left[\sum_k^{x,y,z} (\nabla u_k)^2 \right] + K_1 [1 - (\mathbf{u} \mathbf{a})^2] - \frac{1}{2} J_s \mathbf{u} \mathbf{H}_s - J_s \mathbf{u} \mathbf{H}_{ext} \right) dV \quad (2.10)$$

The exchange energy, the anisotropy energy, the demagnetization energy and the Zeeman energy contribute to the total energy [3]. The second term is simple uniaxial anisotropy energy. It would be no problem to replace it with any other form of anisotropy energy. No

surface anisotropy is assumed. We neglect the contributions to the total energy which arise from the conversion of the true microscopic exchange and dipole interactions to the continuum form as well as intrinsic surface anisotropy [3].

The total energy is an integral over the particle volume Ω . In the following we consider a discretization of the problem domain Ω into N_e finite elements Ω_e .

$$\Omega = \bigcup_{e=1}^{N_e} \Omega_e. \tag{2.11}$$

Thus the integral in equation (2.10) decomposes into a sum of integrals over finite elements

$$E_t = \int_{\Omega} e_t(\mathbf{J}) dV \cong \sum_{e=1}^{N_e} \int_{\Omega_e} e_t \left(J_{s,e} \sum_{i=1}^{N_b} u_{e,i}^k \Phi_{e,i}(\mathbf{x}) \right) dV. \tag{2.12}$$

For the magnetic polarization \mathbf{J} the expansion according to equation (2.6) is used. The k -th component of the effective field on node i is approximated using the box scheme [11],

$$H_{i\text{ eff}}^k \approx -\frac{1}{m_i} \frac{\partial E_t}{\partial u_i^k}, \tag{2.13}$$

where m_i denotes the magnetic moment on the node point i . It follows from the integral

$$m_i = \int_{V_i} J_s(\mathbf{x}) dV, \tag{2.14}$$

where V_i , as shown in figure 2.1, is the surrounding the volume of the node i , such that

$$\sum_j V_j = V \text{ and } V_i \cap V_j = 0 \text{ for } i \neq j. \tag{2.15}$$

Usually, in a single phase magnetic material the spontaneous polarization, J_s , is a constant in space. However the spontaneous polarization is a function of space and is discontinuous at grain boundaries if a magnet with different magnetic phases is modeled. In our model the

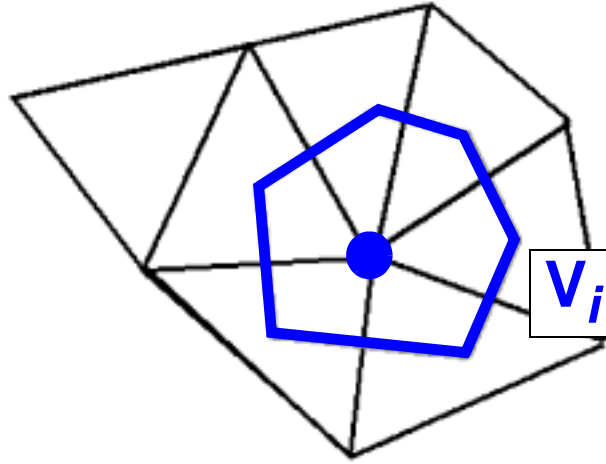


Figure 2.1: The volume V_i surrounding the node i shown in a 2 dimensional example.

nodes of the finite elements are located at grain boundaries. Regions with different values of the spontaneous polarization surround these points. Thus we assume an average magnetic moment for these nodes as given by equation (2.14).

The derivative of the total energy is calculated in an element-by-element fashion. First we have to calculate $\partial E_t / \partial u_{e,j}^k$ for all local coefficients $u_{e,j}^k$. Then the element level derivatives are assembled to obtain $\partial E_t / \partial u_i^k$, the derivative of the total energy with respect to the global expansion coefficients. The assembling process can be formally written using the connectivity matrix C_{ij}^e which is defined as,

$$C_{ij}^e = \begin{cases} 1 & \text{if global node } i \text{ corresponds to the local node } j \text{ in} \\ & \text{element } e \\ 0 & \text{else} \end{cases} . \quad (2.16)$$

Using C_{ij}^e the derivative of the total energy with respect to the global coefficients u_i^k follows from

$$\frac{\partial E_t}{\partial u_i^k} = \sum_{e=1}^{N_e} \sum_{j=1}^{N_b} C_{ij}^e \frac{\partial E_t}{\partial u_{e,j}^k} . \quad (2.17)$$

Let us first consider only the contribution of the exchange energy to the total energy, in order to give an example for the calculations of the derivative of the total energy with respect

to the local coefficients $u_{e,j}^k$. We start from the discrete form of the total energy (2.12). The derivative follows as

$$\frac{\partial E_{ex}}{\partial u_{e,j}^k} = \sum_{\tilde{e}=1}^{N_e} \int_{\Omega_e} A \sum_l^{x,y,z} \frac{\partial}{\partial u_{e,j}^k} \left(\nabla \sum_{i=1}^{N_b} u_{\tilde{e},i}^l \varphi_{\tilde{e},i}(\mathbf{x}) \right)^2 dV. \quad (2.18)$$

Applying the chain rule gives

$$\frac{\partial E_{ex}}{\partial u_{e,j}^k} = \sum_{\tilde{e}=1}^{N_e} \int_{\Omega_e} \left\{ A \sum_l^{x,y,z} 2 \left(\nabla \sum_{i=1}^{N_b} u_{\tilde{e},i}^l \varphi_{\tilde{e},i}(\mathbf{x}) \right) \cdot \frac{\partial}{\partial u_{e,j}^k} \left(\nabla \sum_{i=1}^{N_b} u_{\tilde{e},i}^l \varphi_{\tilde{e},i}(\mathbf{x}) \right) \right\} dV. \quad (2.19)$$

The derivative with respect to the local coefficient $u_{e,j}^k$ in the second factor gives

$$\frac{\partial E_{ex}}{\partial u_{e,j}^k} = \sum_{\tilde{e}=1}^{N_e} \int_{\Omega_e} \left\{ A \sum_l^{x,y,z} 2 \left(\nabla \sum_{i=1}^{N_b} u_{\tilde{e},i}^l \varphi_{\tilde{e},i}(\mathbf{x}) \right) \cdot \nabla \varphi_{e,j}(\mathbf{x}) \delta_{kl} \delta_{\tilde{e}e} \right\} dV \quad (2.20)$$

which finally leads to

$$\frac{\partial E_{ex}}{\partial u_{e,j}^k} = \int_{\Omega_e} A \left[2 \left(\sum_{i=1}^4 u_{e,i}^k \nabla \varphi_{e,i}(\mathbf{x}) \right) \nabla \varphi_{e,j}(\mathbf{x}) \right] dV. \quad (2.21)$$

Introducing the element matrix M_{lj}^e ,

$$M_{lj}^e = \int_{\Omega_e} \nabla \varphi_{e,l}(\mathbf{x}) \nabla \varphi_{e,j}(\mathbf{x}) dV, \quad (2.22)$$

the derivative of the exchange energy can be written as,

$$\frac{\partial E_{ex}}{\partial u_{e,j}^k} = 2A \left[\sum_{l=1}^{N_b} u_{e,l}^k M_{lj}^e \right]. \quad (2.23)$$

In a similar way one can calculate the Zeeman energy E_H , stray field energy E_s and anisotropy energy E_K . The derivatives are

$$\frac{\partial E_H}{\partial u_{e,j}^k} = -J_s \int_{\Omega_e} H_{ext}^k(\mathbf{x}) \varphi_{e,j}(\mathbf{x}) dV, \quad (2.24)$$

$$\frac{\partial E_s}{\partial u_{e,j}^k} = -J_s \int_{\Omega_e} H_d^k(\mathbf{x}) \varphi_{e,j}(\mathbf{x}) dV, \text{ and} \quad (2.25)$$

$$\frac{\partial E_K}{\partial u_{e,j}^k} = -2K_1 a^k \int_{\Omega_e} \sum_{c=1}^3 J^c(\mathbf{x}) a^c \varphi_{e,j}(\mathbf{x}) dV. \quad (2.26)$$

The space discretization of equation (2.2) leads to a system of ordinary differential equations. Its numerical solution can be very efficient if one can provide the Jacobian matrix of the system. The calculation of the Jacobian needs the second derivative of the total energy. Again the calculation is done element by element. Using equation (2.23)-(2.26) we build the second derivative of the total energy with respect to the local coefficients $u_{e,j}^k$. For the exchange energy and anisotropy energy follows

$$\frac{\partial^2 E_{ex}}{\partial u_{e1,m}^k \partial u_{e2,n}^l} = 2AM_{mn} \delta_{kl} \delta_{e1,e2}. \quad (2.27)$$

$$\frac{\partial^2 E_K}{\partial u_{e1,m}^k \partial u_{e2,n}^l} = -2K_1 \delta_{e1,e2} \int_{\Omega_e} a^k a^l \varphi_{e,m}(\mathbf{x}) \varphi_{e,n}(\mathbf{x}) dV. \quad (2.28)$$

Here a^k are the cartesian components of the unit vector parallel to the anisotropy axis. The uniform external field does not contribute to the second derivative. The stray field is omitted, in order to keep the Jacobian sparse. The assembling process from the local second derivatives to the global derivatives of the total energy can be formally written as

$$\frac{\partial^2 E_t}{\partial u_m^k \partial u_n^l} = \sum_{e=1}^{N_e} \sum_{i=1}^{N_b} C_{mi}^e \frac{\partial^2 E_t}{\partial u_{e,i}^k \partial u_{e,j}^l} C_{nj}^e \quad (2.29)$$

2.2.1 Calculation of the stray field

The stray field H_S is obtained from a boundary value problem,

$$\Delta u = \frac{\nabla \mathbf{J}_s}{\mu_0} \text{ and } H_S = -\nabla u \quad (2.30)$$

To apply the boundary condition $u = 0$ at infinity, a hybrid finite element boundary element method [9] is used. No finite elements are needed outside the magnetic particle to solve the boundary value problem (2.30). This is the advantage of the hybrid FE/BE method. For the solution of equation (2.30) with the hybrid FE/BE method one Poisson equation with Neumann boundary conditions and one Laplace equation with Dirichlet boundary conditions have to be solved. To obtain the boundary conditions a matrix vector product has to be performed. We split the total magnetic potential u into two parts, $u = u_1 + u_2$. The potential u_1 solves the Poisson equation (2.30) inside the magnetic particles with Neumann boundary conditions at the surface of the magnets and it is zero outside the magnets. The potential u_2 solves the Laplace equation everywhere in space and shows a jump at the surfaces of the magnets. Thus u_2 is the potential from a dipole sheet at the surfaces of the magnet. After discretization the integral operator may be expressed as a matrix vector product

$$\mathbf{u}_2 = B\mathbf{u}_1 \quad (2.31)$$

The storage requirement for the matrix B is the bottleneck of the method since B is a fully populated $N_S \times N_S$ matrix. N_S is the number of boundary nodes. Especially for thin films the method loses efficiency since most of the nodes are located at the boundary.

2.2.2 Boundary condition for the exchange field

The exchange field can be calculated using the formula,

$$H_{eff} = \frac{2A}{J_s} \Delta \mathbf{u}, \quad (2.32)$$

which follows from the variation of the total energy. \mathbf{u} denotes the unit vector of the magnetization. The variation of the total energy leads to the boundary condition that the normal derivative of the magnetization vanishes at the surface of the magnet,

$$\frac{\partial \mathbf{J}}{\partial \mathbf{n}} = 0. \quad (2.33)$$

In the following we will show that the discretization of equation (2.32) using the finite element method with an finite element size equal to the lattice constant leads to a classical Heisenberg model. In the classical Heisenberg model the spin operators are approximated as classical vectors. In the classical Heisenberg model the exchange energy can be written in the form

$$E_{ex} = - \sum_{i=1}^N \sum_{j \neq i}^N J_{ij} \mathbf{S}_i \cdot \mathbf{S}_j, \quad (2.34)$$

where J_{ij} is the exchange integral. Building the derivative of equation (2.34) with respect to the spin vector \mathbf{S}_i the exchange field on atom i follows. By considering the anisotropy energy, Zeeman energy, stray field energy the total effective field can be calculated in a very similar manner. Time integration of the Gilbert equation leads to equilibrium states in the Heisenberg model for the spin vectors. The calculated spin vectors can be used to interpolate a continuous function of space that describes the magnetization $\mathbf{u}(\mathbf{x})$. The question arises if the magnetization $\mathbf{u}(\mathbf{x})$, which follows from the Heisenberg model, fulfills the boundary condition given by equation (2.33). This question will be investigated in the following.

Let us consider a cubic crystal with exchange coupled spins under the action of an external field in z-direction. The spins are restricted to rotate within the y,z plane. $\theta(\mathbf{x})$ is the angle between the z-axis and the magnetic polarization. $\theta(\mathbf{x})$ is assumed to be only a function of \mathbf{x} . Since $\nabla \mathbf{J} = 0$ for this special magnetization configuration the stray field contribution to the total energy vanishes.

In the continuum limit the total energy density can be written as,

$$w_{tot} = \int A \left(\frac{\partial \theta}{\partial x} \right)^2 - J_s H \cos(\theta) dx \quad (2.35)$$

For a simple cubic crystal, such as iron the exchange constant

$$A = \frac{JS^2}{a}, \quad (2.36)$$

where a is the distance between nearest neighbors which is equal to the lattice constant.

We use the finite element method with a homogeneous element size d and linear shape function to discretize equation (2.35). The number of node points is N and the number of finite elements is $N-1$. We assume that the crystal is infinite in y and z direction.

For the total energy of one chain of spins, $E_{tot,per\ chain}$ ($E_{tot,per\ chain}$ is the total energy divided by the number of atoms in y and z direction) follows,

$$E_{tot,per\ chain} = a^2 d \left(- \sum_{i=1}^{N-1} \frac{A}{d^2} (2 \cos(\theta_{i+1} - \theta_i) - 2) - \sum_{i=1}^{N-1} J_s H \cos\left(\frac{\theta_{i+1} + \theta_i}{2}\right) \right) \quad (2.37)$$

For equation (2.37) we have used that for small differences of $\theta_{i+1} - \theta_i$ one can expand the cosine by writing,

$$\cos(\theta_{i+1} - \theta_i) \approx 1 - \frac{(\theta_{i+1} - \theta_i)^2}{2}. \quad (2.38)$$

If the element size d is equal to the lattice constant a and the zero level of the energy is redefined, equation (2.37) can be written in the form,

$$E_{tot,per\ chain} = a^3 \left(- \sum_{i=1}^{N-1} \frac{JS^2}{a^3} (2 \cos(\theta_{i+1} - \theta_i)) - \sum_{i=1}^{N-1} J_s H \cos\left(\frac{\theta_{i+1} + \theta_i}{2}\right) \right). \quad (2.39)$$

Equation (2.39) leads to the classical Heisenberg model under the following assumption:

First one has to assume that the change in direction of neighboring spins is small. Thus it is justified to assume,

$$(\theta_{i+1} - \theta_i) \approx \frac{(\theta_{i+2} - \theta_i)}{2}. \quad (2.40)$$

Secondly, we have to change the point where the magnetization is evaluated. In equation (2.39) the magnetization is evaluated on the node points of the finite elements. In the following we will evaluate the magnetization in the middle of one finite element. Thus we introduce the directions ϕ_i that describe the average magnetization direction in the finite element i .

$$\phi_i \approx \frac{(\theta_{i+1} + \theta_i)}{2}, \quad (2.41)$$

Using equation (2.40) and equation (2.41), equation (2.39) can be written as

$$E_{tot, per chain} = a^3 \left(- \sum_{i=1}^{N-1} \frac{JS^2}{a^3} (2 \cos(\phi_{i+1} - \phi_i)) - \sum_{i=1}^{N-1} J_s H \cos(\phi_i) \right), \quad (2.42)$$

For large N it is justified to assume that

$$\sum_{i=1}^{N-1} JS^2 (2 \cos(\phi_{i+1} - \phi_i)) \approx \sum_{i=1}^{N-2} JS^2 (2 \cos(\phi_{i+1} - \phi_i)). \quad (2.43)$$

If condition (2.43) is assumed the energy of a classical Heisenberg model follows,

$$E_{tot, per chain} = a^3 \left(- \sum_{i=1}^{N-2} \frac{JS^2}{a^3} (2 \cos(\phi_{i+1} - \phi_i)) - \sum_{i=1}^{N-1} J_s \cos(\phi_i) \right). \quad (2.44)$$

Using $J_s = \mu_0 g n \mu_B S$, where n is the number of spins per volume (for a simple cubic lattice $n=1/a^3$), S the total spin quantum number of one atom, g the Landé factor and μ_B the Bohr magneton, equation (2.44) can be rewritten as

$$E_{tot, per chain} = - \sum_{i=1}^{N-1} \sum_j J_{ij} S_i S_j - \mu_0 g \mu_B \sum_{i=1}^{N-1} S_i H, \quad (2.45)$$

where the second sum in equation (2.45) is the sum over the nearest neighbors.

For the first spin θ_1 the equilibrium condition

$$\frac{\partial E_{tot}}{\partial \theta_1} = 0, \quad (2.46)$$

applied to equation (2.37) using the approximations (2.38),(2.40), (2.41) and (2.43) yields

$$-\frac{J_s H \sin \theta_1}{A} d^2 = \sin(\theta_2 - \theta_1) \approx \frac{\partial \theta}{\partial x} d. \quad (2.47)$$

• **Continuum limit** $d \rightarrow 0$: In the limit of an infinitely small discretization length d , for the normal derivative follows from equation (2.47),

$$\frac{\partial \theta}{\partial x} = -\frac{J_s H \sin \theta_1}{A} d = 0. \quad (2.48)$$

Thus the boundary condition of vanishing normal derivative is fulfilled in that limit.

• **Atomic discretization** ($d=a$): If the finite element size d is equal to the distance a between nearest neighbors equation (2.47) yields,

$$\frac{\partial \theta}{\partial x} \Delta x \approx -\frac{J_s H \sin \theta_N}{A} a \Delta x. \quad (2.49)$$

The right hand side of equation (2.47) corresponds to the change of the angle θ on a distance Δx . Even for large fields of some Tesla the change of angle of neighboring atomic spins at the surface is very small,

$$\frac{J_s H \sin \theta_N}{A} a < 10^{-4}. \quad (2.50)$$

Therefore the change of the angle θ is

$$\frac{\partial \theta}{\partial x} a \approx 10^{-4}. \quad (2.51)$$

Thus in discrete spin calculations the boundary condition that the normal derivative of the magnetization vanish (2.48) is approximately fulfilled.

2.3 Time integration

We use the CVODE code [6-7] for solving the LLG equation. The relative performance of the Adams method, the BDF method and the BDF method with preconditioning changes depending on the microstructure, material parameters, and the finite element mesh. The Adams method seems to be attractive because of the low cost per time step. In contrast to the one-step methods (e.g. Runge-Kutta) multistep methods make use of the past values of the solution. At each time step a non linear system of equations has to be solved. The Adams method solves the nonlinear system with functional iteration and thus requires only the evaluation of the right hand side of equation (2.2). However, if the problem is stiff the convergence of the functional iterations is slow. For a stiff problem it is advisable to use an implicit method such as BDF. The nonlinear system is solved using a Newton method. Normally only a few Newton steps are required. Within CVODE the linear system for each Newton-step is solved either with a direct solver or with a Krylov subspace method. Krylov subspace methods have been explored in micromagnetics by Tsiantos et al. [20,21]. The solution is approximated iteratively by a linear combination of the basis vectors of the Krylov subspace. At each iteration step one orthonormal basis vector is added which increases the subspace dimension by one. If the Krylov subspace dimension is equal to the number of unknowns the exact solution is found. For practical applications a very good approximation is obtained for a Krylov subspace dimension much smaller than the number of unknowns. The default value for the maximum Krylov subspace dimension in CVODE is 5. As discussed in the next section the computation time drastically decreases when this value is increased to about 300. An additional parameter in the CVODE package is the maximum order of the time integration method. Especially for small damping constants, we found that a maximum order, $qu_{\max} = 2$, improves the stability of the solution.

The BDF method leads to the nonlinear system [14]

$$F(\mathbf{y}_n) = \mathbf{y}_n - \mathbf{a}_n - h\beta_0 \mathbf{f}(t_n, \mathbf{y}_n) = 0 \tag{2.52}$$

which is solved by Newton iterations. \mathbf{a}_n and β_0 are constants which depend on the order of the time integration method and on the previous time step size. Equation (2.52) is successively solved by adding corrections $\Delta\mathbf{y}$ to the solution vector. $\Delta\mathbf{y}$ is the solution of the linear system,

$$\frac{\partial F(\mathbf{y}_{n-1})}{\partial \mathbf{y}} \Delta \mathbf{y} = A \Delta \mathbf{y} = -\mathbf{F}(\mathbf{y}_{n-1}) \quad , \quad (2.53)$$

with

$$A = 1 - h\beta_0 J \text{ and } J = \frac{\partial f}{\partial \mathbf{y}}. \quad (2.54)$$

Equation (2.53) is solved with a Krylov method. It starts with a guess \mathbf{x}_0 for $\Delta \mathbf{y}$, and corrects it successively to get iterates $\mathbf{x}_1, \mathbf{x}_2, \dots$. After a few iterations a good approximation for $\Delta \mathbf{y}$ is found. In every iteration only the product $A\mathbf{x}_i$ has to be calculated. So the large matrix A has to be neither explicitly constructed nor stored. In micromagnetics A is fully populated owing to the long range magnetostatic interaction. $A\Delta \mathbf{y}$ is approximated using finite differences,

$$A(\mathbf{y}_{n-1})\mathbf{v} \approx \frac{\mathbf{F}(\mathbf{y}_{n-1} + \varepsilon \mathbf{v}) - \mathbf{F}(\mathbf{y}_{n-1})}{\varepsilon}. \quad (2.55)$$

However the number of Krylov iterations strongly depends on the matrix A . For some matrices A the Krylov methods converge slowly.

2.3.1 Preconditioning

The above problem of the slow convergence can be overcome by preconditioning. Instead of the system

$$A\Delta \mathbf{y} = \mathbf{b} \quad (2.56)$$

the equivalent system

$$(AP^{-1})(P\Delta \mathbf{y}) = A'\mathbf{x}' = \mathbf{b} \quad (2.57)$$

is solved. The matrix P should be an approximation to A . Then AP^{-1} is close to the identity matrix and the system $A'\mathbf{x}' = \mathbf{b}$ can be solved very efficiently with only a few Krylov iterations. The matrix AP^{-1} cannot be calculated directly since generally the matrix A is not explicitly constructed. To calculate the matrix vector product, $\mathbf{s} := AP^{-1}\mathbf{x}$, which is needed in every Krylov iteration, the following procedure is applied. Instead of the calculation of \mathbf{s} from

$$s = AP^{-1}x, \tag{2.58}$$

we multiply equation (2.58) by A^{-1} and calculate w from

$$A^{-1}s = P^{-1}x =: w \tag{2.59}$$

w is calculated by solving the linear system

$$Pw = x \tag{2.60}$$

with an efficient iterative solver, since the inversion of a matrix is very time consuming. Once w has been calculated, s follows from equation (2.59) simply by the matrix vector product

$$s = Aw \tag{2.61}$$

$$A = 1 - h\beta_0 J \tag{2.62}$$

We found that the solution of equation (2.60) is the most time consuming part in our micromagnetic simulation. We tested different methods to solve equation (2.60) (see section 2.4.2). The linear system of equations (2.60) is sparse. As the number of unknowns is large, the use of an iterative method is more appropriate than solving (2.60) with a direct method. Among different generalized minimum residual methods (GMRES), the Bi-Conjugate Gradient method was found to be the most efficient one. For some problems it is important to apply a preconditioner to the linear system (equation 2.60) to achieve good convergence. A good choice is the incomplete factorization technique RILU [4].

2.3.2 Error control

In the CVODE code the local truncation error ϵ is estimated. The tolerance parameters *reltol* and the vector *abstol*, which can be defined for every solution component separately, can be used to control the error. The time step of the integration is determined so that the error satisfies the inequality

$$\sqrt{\frac{\sum_{i=1}^N \left(e_i \frac{1}{reltol|u_i| + abstol_i} \right)^2}{N}} \leq 1. \quad (2.63)$$

In micromagnetics a useful error indicator follows from the structure of the LLG equation. The LLG equation maintains the magnitudes of the magnetic polarization. However the discretization of the LLG equation using the BDF formula violates this relation. For example for the implicit Euler method with time step h (BDF method or Adams method of order one) follows,

$$\frac{\mathbf{J}_{i+1} - \mathbf{J}_i}{h} = -\frac{|\gamma|}{1 + \alpha^2} \mathbf{J}_{i+1} \times \mathbf{H}_{eff}(\mathbf{J}_{i+1}) - \frac{\alpha}{1 + \alpha^2} \frac{|\gamma|}{J_s} \mathbf{J}_{i+1} \times (\mathbf{J}_{i+1} \times \mathbf{H}_{eff}(\mathbf{J}_{i+1})). \quad (2.64)$$

If equation (2.64) is multiplied by \mathbf{J}_{i+1} the right hand side vanishes.

$$\left(\frac{\mathbf{J}_{i+1} - \mathbf{J}_i}{h} \right) \mathbf{J}_{i+1} = 0. \quad (2.65)$$

Substituting $\mathbf{J}_i \mathbf{J}_{i+1}$ by $\frac{1}{2}(\mathbf{J}_i^2 + \mathbf{J}_{i+1}^2 - (\mathbf{J}_i - \mathbf{J}_{i+1})^2)$ in equation (2.65) it follows,

$$(\mathbf{J}_{i+1})^2 = (\mathbf{J}_i)^2 + (\mathbf{J}_{i+1} - \mathbf{J}_i)^2. \quad (2.66)$$

As a consequence $(\mathbf{J}_{i+1})^2 \neq \mathbf{J}_0^2$ for $i > 0$. To guarantee that the norm of the magnetic polarization does not drift away, we normalize the magnetic polarization on every node if on at least one node the deviation becomes larger than the specified tolerance *rentol*. To determine the accuracy of an integration method we use the number of renormalization steps during the simulation as well as the deviation norm of the spontaneous polarization,

$$DN = \frac{1}{J_s} \max(|\mathbf{J}|_i - J_s) \quad , \quad (2.67)$$

where $|\mathbf{J}|_i$ is the magnitude of the polarization vector on node i .

2.3.3 Storage requirements

The size of the workspace required for the scaled preconditioned GMRES iterative solver for the linear system is

$$n(l_{max} + 5) + l_{max}(l_{max} + 4) + 1, \tag{2.68}$$

where $n = 3N$ is the number of unknowns, l_{max} the maximum dimension of the Krylov subspace and N the number of nodes of the finite element mesh. For our micromagnetic simulations the storage requirement of the GMRES solver does not dominate the total memory. For example the simulation for a granular element (Section 2.4.2) with 3512 nodes and 2466 boundary nodes requires 48Mb for the storage of the $N_S \times N_S$ boundary matrix B (equation 2.31), where N_S is the number of nodal points on the surface. An increase of l_{max} from 5 to 300 increases the storage requirement for the GMRES solver from 0.2 Mb to 9.2 MB. However the CPU time decreases by one order of magnitude when l_{max} is changed from 5 to 300. For thin samples where all nodes are located on the surface $N_S = N$ the storage requirements of the B-matrix scales with N^2 . However, the Krylov subspace only scales with N . The situation slightly changes if the magnetic sample has almost the same lateral dimension in all three directions in space. For a sphere, which is discretized with tetrahedrons inside and triangles on the surface, the number of node points inside and the number of points on the surface is $N_V \sim l^3(16\pi/\sqrt{2})$ and $N_S \sim l^2(8\pi/\sqrt{3})$, respectively. l is the ratio between the radius of the sphere and the edge length of one tetrahedron. The storage requirement for the B matrix is $(N_S)^2$, so it scales with l^4 . However, the workspace needed for the Krylov method only scales with l^3 . So even for the case where the boundary matrix is relatively small it requires much more storage than the GMRES iterative solver.

2.4 Performance of time integration scheme

In the following two sections different time integration schemes are tested for their performance and accuracy. Since the efficiency of the time integration strongly depends on the investigated system the reversal process of two different magnetic samples was calculated. The first sample has simple geometry, no granular structure and flat surfaces are taken into account. As a second sample the dynamic response of realistically shaped patterned element is calculated. Taking into account surface roughness and grain structures requires an inhomogeneous computational grid which in turn causes very small time steps for explicit time integration schemes. In section 2.4.2 we show that especially for granular elements sophisticated time integration schemes have to be used to be able to integrate the Gilbert equation efficiently.

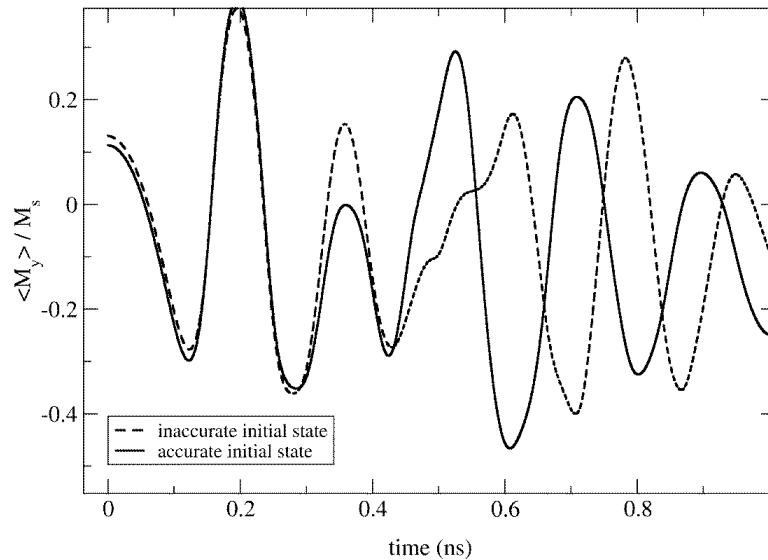


Figure 2.2: Time evolution of the y -component of the magnetic polarization of the μ MAG Problem # 4. The initial state for the simulation was calculated with a stopping criterion $r_e=10^{-6}$ (solid line) and $r_e=10^{-3}$ (dashed line)

2.4.1 μ MAG Problem # 4

The μ MAG standard problem number 4 is used to compare the efficiency of different time integration schemes. In the μ MAG problem the reversal process of a permalloy film with the dimensions $x = 500$ nm, $y = 125$ nm and $z = 3$ nm has to be calculated. We used $A = 1.2 \times 10^{-11}$ J/m, $J_s = 1$ T and zero magnetocrystalline anisotropy. We focused our investigation on the reversal process when the field $\mu_0 H_x = -35.5$ mT, $\mu_0 H_y = -6.3$ mT, $\mu_0 H_z = 0.0$ is applied instantaneously to the initial S-state. The S-state is obtained after applying a saturating field along the [1,1,1] direction which is slowly reduced to zero. The mesh size of the finite element mesh is 5 nm, in the following calculations. The reversal process obtained from a simulation with a mesh size of 3 nm is very similar. So we conclude that in our model a mesh size of 5 nm is sufficient to resolve the micromagnetic details. Figure 2.2 shows the time evolution of the y -component of the magnetic polarization. The time evolution significantly depends on the initial state. A small difference in the initial state leads to a different time evo-

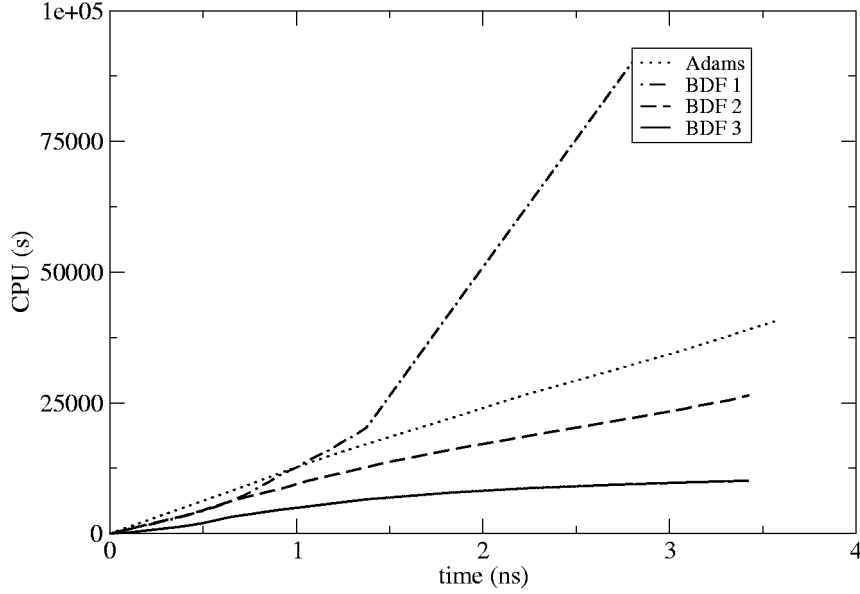


Figure 2.3: CPU time (Digital EV6 - 523 MHz) versus the simulation time for different time integration schemes for the μ MAG Problem # 4. (Adams) Adams method; (BDF1) BDF-method with maximum integration order $qu_{\max} = 3$, Krylov Subspace dimension $l_{\max}=400$; (BDF2) BDF with $qu_{\max} = 2$ and $l_{\max} = 400$; (BDF3) BDF-method with preconditioning, $l_{\max} = 400$, $qu_{\max} = 2$.

lution. Thus the initial equilibrium state has to be calculated with a very strict stopping criterion. For the solid line in Figure 2.2 the magnetization configuration of the S-state was calculated using a stopping criterion

$$r_e = \frac{1}{J_s} \left| \frac{\Delta \mathbf{J}}{\Delta t} \right| < 10^{-6}. \quad (2.69)$$

This quantity is proportional to the torque. For the dashed line in Figure 2.2 $r_e < 10^{-3}$. Starting from the accurate initial state the reversal process is calculated with different options and methods of the CVODE package. In the following simulation the accuracy of the time integration was defined with the *abstol* parameter of CVODE. We set $abstol = 10^{-3}$ and $reltol = 0$. To be able to compare the accuracy of the different methods we use the number of renormalization steps which were required to keep $DN < rentol$. This number of renormalization steps, *nrn*, serves as an error criterion. The smaller *nrn* the more accurate is the time integration method. Figure 2.3 shows the CPU time as a function of the simulation time. The

calculations are performed on a Digital EV6 workstation (523 MHz). The CPU time of the Adams method as a function of the simulation time is linear because the time step is constant (0.21 ps) during the whole simulation. The small time step provides a high accuracy. The number of renormalization steps is $nrn = 1$. Besides the Adams method the performance of the BDF method with different options is investigated. For the BDF method the default value for the maximum integration order, $qu_{\max} = 5$, leads to a very bad performance as shown in figure 2.3 (BDF: $qu_{\max} = 5$). A restriction of the maximum integration order to 2 drastically improves the performance (Figure 2.3 BDF 2). Although in other micromagnetic simulations the maximum dimension of the Krylov subspace dimension l_{\max} was found to be a very crucial parameter the default value, $l_{\max} = 5$, leads to the same CPU consumption as $l_{\max} = 400$. For $l_{\max} = 15$ the average time step is smaller than for $l_{\max} = 400$. Figure 2.4

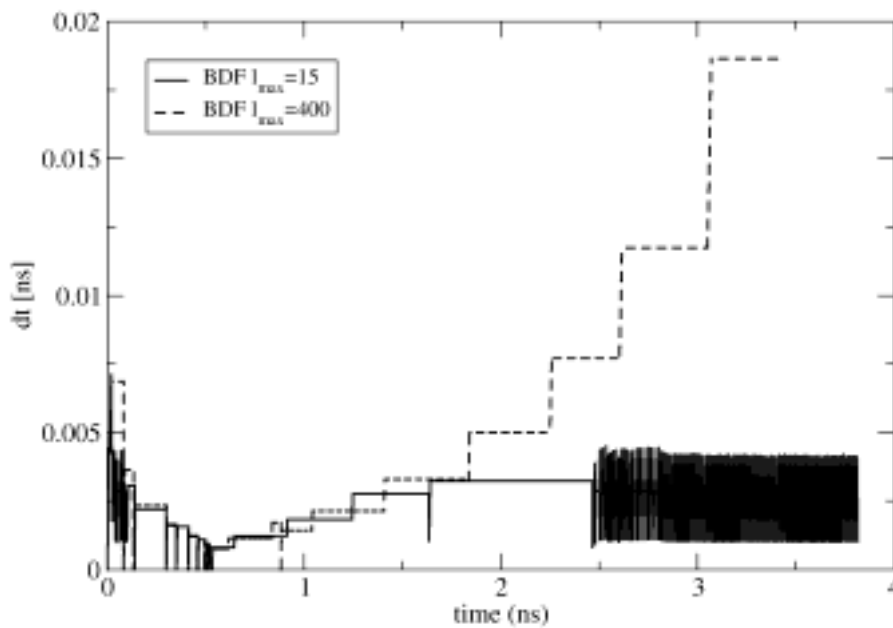


Figure 2.4: Comparison of the time step as a function of the simulated time of two simulations with a maximum Krylov subspace dimension $l_{\max} = 15$ and $l_{\max} = 400$. The maximum order of the time integration scheme was $qu_{\max} = 2$ in both simulations.

shows a significant difference in the time step for the simulation with $l_{\max} = 15$ and $l_{\max} = 400$ at the end of the simulation. If the maximum number of Krylov iterations is restricted to $l_{\max} = 15$ the linear system equation (2.53) cannot be solved with the desired accuracy. As a

consequence the time step is reduced to obey equation (2.63). However the overall CPU time consumption for $l_{\max} = 15$ is approximately the same as for $l_{\max} = 400$. In this example large time steps with a large cost per time step ($l_{\max} = 400$) gives the same amount of work as small time steps with a low cost per time step ($l_{\max} = 5$). The solid line in figure 2.3 shows that the BDF method with proper preconditioning yields the best performance during the whole simulation. Preconditioning speeds up the simulations by a factor of 2.5 as compared to BDF without preconditioning with the same parameters. A very time consuming part for preconditioning is the solution of the linear system (equation 2.60). It requires almost one half of the total CPU time. Figure 2.5 shows that preconditioning drastically decreases the number of

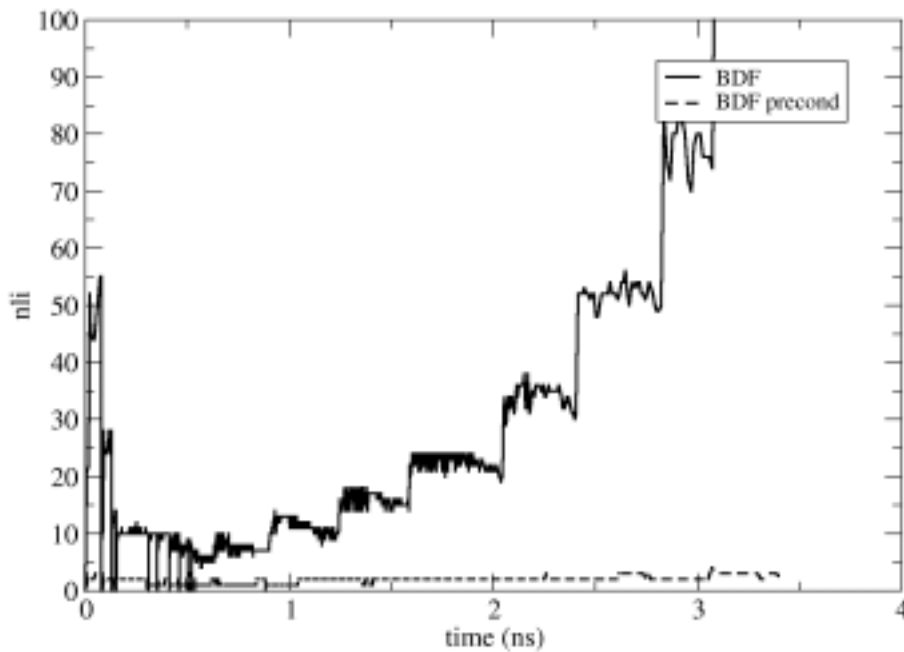


Figure 2.5: The number of Krylov iterations per time step for the BDF method with and without preconditioning. The dimension of the Krylov subspace $l_{\max} = 400$. The maximum integration order $qu_{\max} = 2$.

Krylov iterations which are required to solve the linear system (equation 2.56). Without preconditioning the number of linear iterations increases with time because the time step becomes larger when the system gets closer to equilibrium (figure 2.5). For a large time step the resulting linear system requires more linear iterations for its solution. For $t > 3$ ns the number of linear iterations decreases from more than 100 without preconditioning to 2 with a preconditioner. Fewer linear iterations require a smaller number of function evaluations. Thus

preconditioning reduces the number of function evaluations, in this example by a factor of 6.5. The BDF method with $l_{\max} = 15$, $l_{\max} = 400$ and with preconditioning has comparable accuracy. The number of renormalization steps, which serves as an error indicator, are 9, 7 and 10 for $l_{\max} = 15$, $l_{\max} = 400$ and $l_{\max} = 400$ with preconditioning, respectively. Table 2.1 summarizes the key performance parameters of the different integration methods

Table 2.1 Summary of statistical data for different time integration schemes after 3 ns of simulated time. **(Adams)** Adams method $qu_{\max} = 15$. **(BDF 1)** BDF-method with maximum integration order $qu_{\max} = 3$, Krylov subspace dimension $l_{\max} = 400$. **(BDF 2)** BDF-method with $qu_{\max} = 2$ and $l_{\max} = 400$. **(BDF 3)** BDF-method with preconditioning, $qu_{\max} = 2$ and $l_{\max} = 400$. **(BDF 4)** BDF with $qu_{\max} = 2$ and $l_{\max} = 15$.

	Adams	BDF 1	BDF 2	BDF 3	BDF 4
Total CPU time (s)	3.43×10^4	9.9×10^4	2.33×10^4	9.7×10^3	2.37×10^4
average CPU per time step (s)	2.37	4.58	19.1	7.87	11.1
average CPU for equation (2.60) per time step (s)	-	-	-	3.1	-
average number of iteration to solve equation (2.60)	-	-	-	7.1	-
average number of Krylov subspace iterations per Newton step	-	1.3	11.26	1.47	9.88
average time step (ps)	0.21	0.14	2.47	2.48	2.03
number of function evaluations	30 774	88 963	19 243	3 134	19 798
number of renormalization steps nrn (error indicator)	1	115	9	10	7

2.4.2 Granular media

As a second test case we have calculated the hysteresis loop for a Co element with a rough surface. The precise understanding of the switching process of thin film nanomagnets is important for sensor and spin electronic applications. Surface irregularities and grain structure drastically change the reversal mechanism of thin film elements [18,10]. Edge roughness and an irregular grain structure may cause small computational cells which leads to a small time step when an explicit time integration method is applied to solve the LLG equation.

The geometry of the investigated sample is shown in figure 2.6. To create a rough surface the element was built up of 8 nm wide columnar grains. The basal planes of the grains are irregular, constructed from voronoi cells. These grains lead to edge irregularities of the same size. Each grain consists in average of 26 finite elements. The grain structure leads to an inhomogeneous finite element grid. Since the time step for explicit time integration schemes has to be proportional to h^2 , where h is the size of the spatial grid, an inhomogeneous grid causes

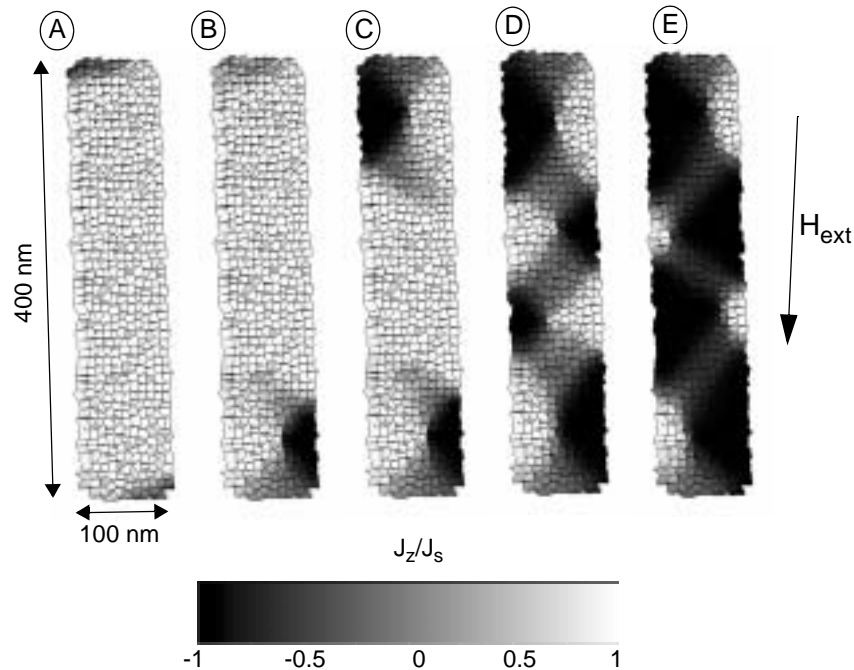


Figure 2.6: Equilibrium states during the demagnetization process for a Co-grain with granular structure. The film thickness is 25 nm. The letters identify the states marked on the demagnetization curve in figure 2.7.

very small time steps. The investigated element is 400 nm long, 100 nm wide and 25 nm thick. No uniaxial anisotropy is assumed. The spontaneous polarization $J_s = 1.76$ T and the exchange constant $A = 1.3 \times 10^{-11}$ J/m. The damping constant α was set to 0.1. Figure 2.6 shows magnetization states during the demagnetization process. The angle between the external field and the long axis of the Co element is 1° . The letters in figure 2.6 identify states marked on the hysteresis loop in figure 2.7. The nucleation of reversed domains starts at edge irregularities.

For the comparison of different time integration schemes we simulated the switching process under the action of an external field. An external field of 100 kA/m is applied instantaneously to the remanent state 1° off the easy axis. After 0.76 ns the normalized magnetization parallel to the external field direction becomes smaller than -0.99. Then we regard the particle to be switched.

Figure 2.8 shows the efficiency of different time integration schemes. The CPU time is plotted as a function of the simulated time. It clearly shows that the Adams method (A) is not suitable to solve the LLG equation for samples with granular structure. In all simulations with

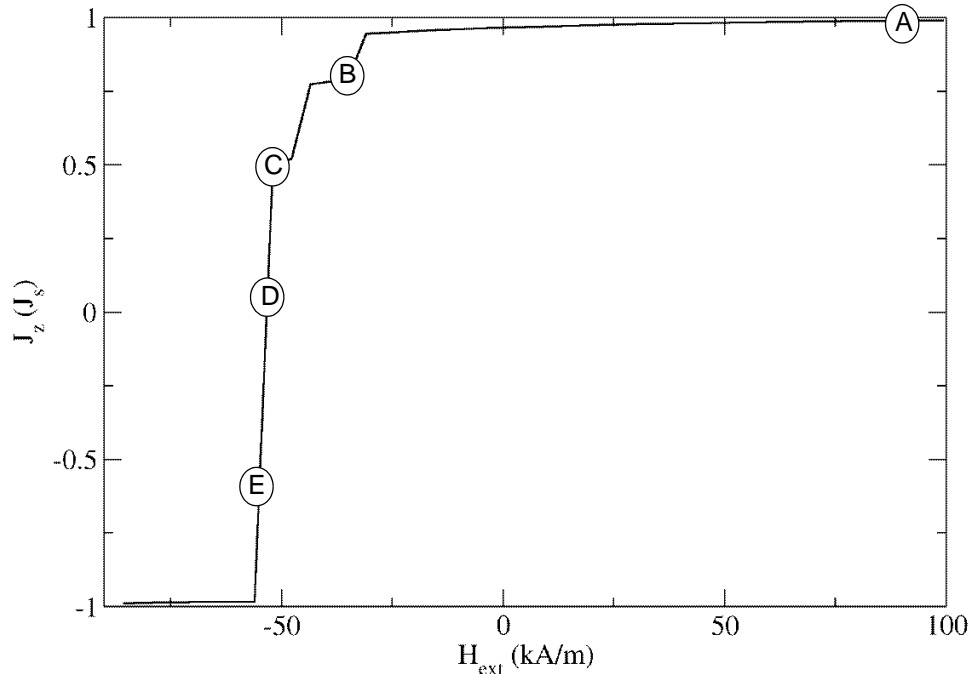


Figure 2.7: Hysteresis loop for the granular Co-particle. The field step is 4 kA/m.

the BDF method the maximum integration order, $qu_{\max} = 2$, was used. The BDF method shows a very bad performance if the dimension of the Krylov subspace is restricted ($l_{\max} = 5$ or $l_{\max} = 15$). The maximum dimension of the Krylov subspace restricts the number of iterations to solve the linear system (equation 2.56), which has to be solved in every Newton step. The linear iteration stops if the desired accuracy or l_{\max} is reached. If l_{\max} is large enough, so that the number of iterations does not reach l_{\max} , the ratio nli/nni (nli = number of linear iterations, nni = number of nonlinear iterations) gives the average number of linear iterations per Newton step. From Table 2.2 it follows that the average number of linear iterations for the BDF method without preconditioning is 64. Figure 2.8 shows that the efficiency of the time integration scheme increases with increasing l_{\max} . With higher dimension of the Krylov subspace, the linear system can be solved more accurately which in turn enables a larger time step. The maximum number of Krylov iterations is 162. So a further increase of $l_{\max} > 162$ has no influence on the simulation. It is interesting to note that the CPU time decreases when the absolute tolerance of the time integration scheme *abstol* is enhanced from 10^{-4} (curve D in

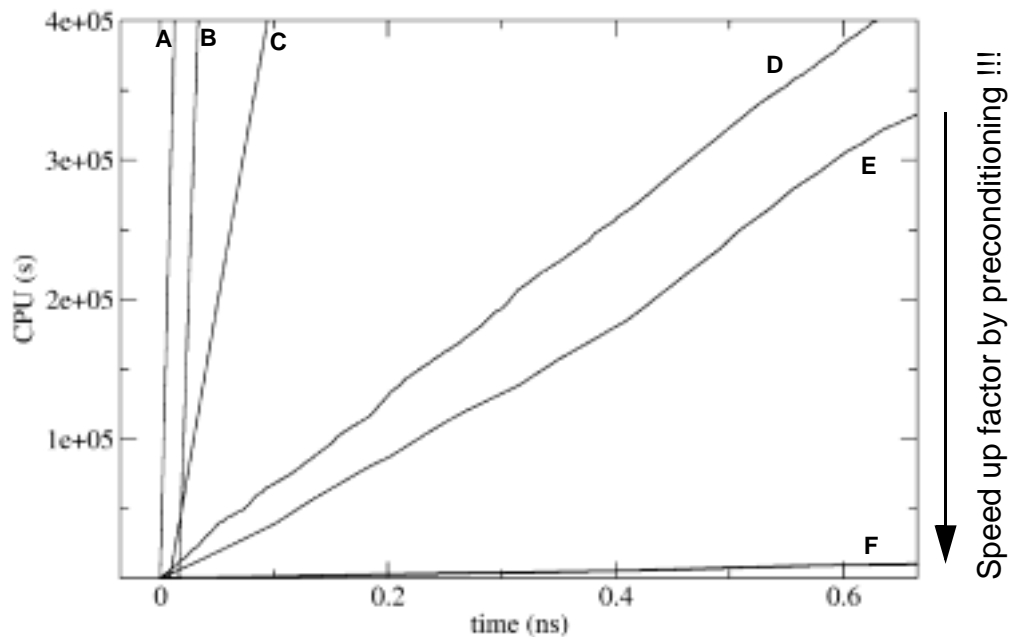


Figure 2.8: CPU time (Digital EV6 - 523 MHz) versus the simulated time for different time integration schemes for a Co element with a grain structure. (A) Adams method (B-D) BDF method without preconditioning for different dimension of the Krylov subspace. (B) Krylov subspace dimension $l_{\max} = 5$, (C) $l_{\max} = 15$, (D) $l_{\max} = 400$, (E) $l_{\max} = 400$ and high accuracy ($abstol = 10^{-5}$). (F) BDF-method with preconditioning, $l_{\max} = 15$.

fig. 3.14) to 10^{-5} (E). A smaller tolerance keeps the norm of the magnetization vector constant for a longer time period. Thus less renormalization steps which also require to restart the time integration algorithm are required. Restarting the BDF method requires some pre-computation steps like factorizing the matrices for the linear systems. In addition the initial time step is small.

The curve marked with (F) in figure 2.8 shows that the CPU time is drastically decreased if preconditioning for the time integration is used. For preconditioning the solution of equation (2.60) is the most time consuming part. We have tested different solvers for the solution of equation (2.60). The Methods of *Orthomin*, *GCR* and *MinRes* which belong to the family of nonsymmetric Krylov solvers were found to be less efficient than the Bi-Conjugate Gradient method. We emphasize that also the Bi-Conjugate Gradient method has to be combined with

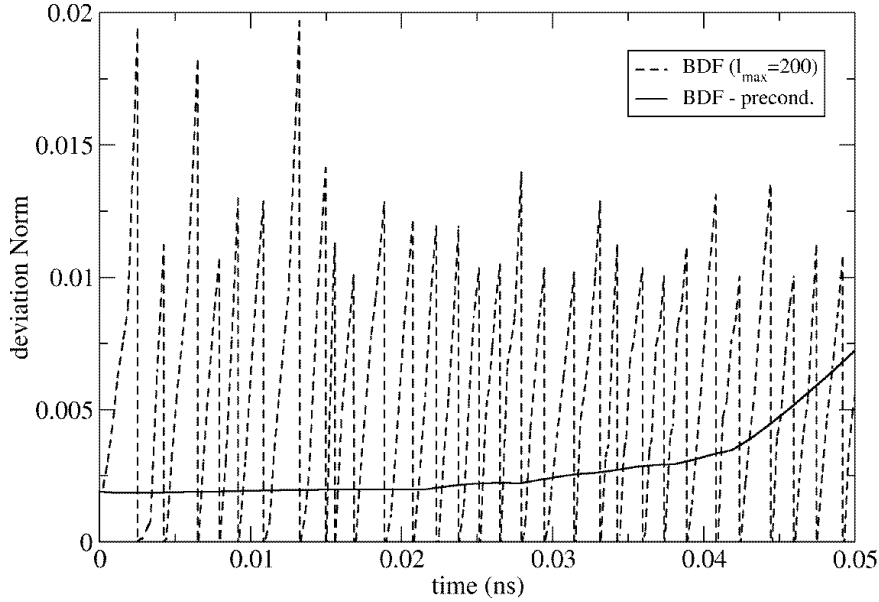


Figure 2.9: The deviation of the magnitude of the magnetic polarization vector from J_s indicates the quality of the time integration method. Comparison of the deviation norm DN for the BDF method with and without preconditioning. The maximum order of the time integration was $qu_{\max}=2$.

a preconditioner in order to speed up the convergence rate. We apply the incomplete factorization technique *RILU*. The fill-in entries during the incomplete factorization process are multiplied by a factor ω before adding them to the main diagonal. The reduction of the parameter ω from the all-round choice of $\omega = 0.95$ to $\omega = 0$ is sometimes necessary to avoid convergence problems. For the investigated sample RILU preconditioner was absolutely necessary to achieve convergence. Although we have tried different options of the linear solver it is still the most time consuming part in the simulations. The solution of the linear system needs almost 50% of the total CPU time. Figure 2.9 shows the deviation norm DN (equation 2.67) as a function of the simulated time for a calculation with and without preconditioning. In both calculations l_{\max} is 400. A large deviation norm indicates a large error. Although for both simulations the same values for the error tolerances, $abstol = 10^{-4}$ and $reltol = 0$ were used, the accuracy is much better if preconditioning is performed. Table 2.2 summarizes the statistical data after 0.76 ns of simulated time.

Table 2.2 Comparison of statistical data for the BDF method with and without preconditioning after 0.76 ns of simulated time. The maximum integration order qu_{\max} is 2. The Krylov subspace dimension $l_{\max} = 400$ in both calculations.

	BDF 400	BDF Precond
Total CPU time (s)	27.8×10^4	1.48×10^4
average CPU per timestep (s)	69.4	9.69
average CPU for equation (2.60) per timestep (s)	-	4.75
average number of iteration within to solve equation (2.60)	-	8.4
average number of Krylov subspace iterations per Newton step	64.3	1.18
average timestep (ps)	0.18	0.50
number of function evaluations	451 937	3 475
number of renormalization steps <i>nrn</i> (error indicator)	216	6

2.5 Conclusions

Both, for the soft magnetic thin film with perfect microstructure and a granular media with surface roughness the BDF method is faster than the Adams method. In both cases preconditioning speeds up the computational time. The solution of the linear system which has to be solved for preconditioning is very time consuming. Approximately 50% of the total CPU time is spent to solve the linear system. Nevertheless the overall speed up as compared to the Adams method is three orders of magnitude. The accuracy is higher with preconditioning.

References

- [1] G. Albuquerque, J. Miltat and A Thiaville, "Self-consistency based control scheme for magnetization dynamics," *J. Appl. Phys.*, vol. 89, 6719, 2001.
- [2] W. F. Brown, *Phys. Rev.*, vol. 58, pp. 736, 1940.
- [3] W. F. Brown Jr., *Micromagnetism*, New York: Interscience, 1963.
- [4] A. M. Bruaset, *Krylov subspace iterations for sparse linear systems in Numerical Methods and Software Tools in Industrial Mathematics*, Eds. Morten Daehlen and Aslak Tveito, Birkhauser, Boston, 21, 1997.
- [5] R. L. Burden J. D. Faires, *Numerical Analysis*, sixth edition, Brooks/Cole Publ. Co., Pasific Grove, 1997.
- [6] S. D. Cohen and A. C. Hindmarsh, *CVODE User Guide*, Lawrence Livermore National Laboratory report UCRL-MA-118618, Sept. 1994.
- [7] S. D. Cohen and A. C. Hindmarsh, "CVODE, A Stiff/Nonstiff ODE Solver in C," *Computers in Physics*, vol. 10, pp. 138, 1996.
- [8] W. E and X.-P. Wang, *SIAM Journal on Numerical Analysis*, vol. 38, pp. 1647, 2000.
- [9] D.R. Fredkin and T. R. Koehler, "Numerical micromagnetics of small particles," *IEEE Trans. Magn.*, vol. 24, pp. 2361, 1988.
- [10] J. Gadbois and J. G. Zhu, "Effect of edge roughness in nano-scale magnetic bar switching," *IEEE Trans. Magn.*, vol. 31, pp. 3802, 1995.
- [11] C. W. Gardiner, *Handbook of Stochastic Methods*, Berlin, Springer, 1985.
- [12] C. W. Gear, *Numerical Initial Value Problems in Ordinary Differential Equations*, Prentice-Hall: Englewood Cliffs, 1971.
- [13] N. Hayashi, Y. Nakatani, "Numerical calculation of magnetic bubble domain wall motion based on a lumped-constant model of vertical Bloch lines," *Jpn. J. Appl. Phys.*, vol. 25, pp. 406, 1986.
- [14] A. C. Hindmarsh and L. R. Petzold, "Algorithms and Software for Ordinary Differential Equations and Differential-Algebraic Equations," *Computers in Physics* vol. 9, pp. 148, 1995.
- [15] M Jones and J. J. Miles, "An accurate and efficient 3-D micromagnetic simulation of metal evaporated tape," *J. Magn. Magn. Mater.*, vol. 171, pp. 190, 1997.
- [16] M. Mansuripur, "Magnetization reversal dynamics in the media of magneto-optical recording," *J. Appl. Phys.*, vol. 63, pp. 5809, 1988.
- [17] R. D. McMichael M. J. Donahue, "Head to head domain wall structures in thin magnetic strips," *IEEE Trans. Magn.*, vol. 33, pp. 4167, 1997.

- [18] T. Schrefl, J. Fidler, C. Kirk, and J. N. Chapman, "Simulation of magnetization reversal in polycrystalline patterned Co elements," *J. Appl. Phys.*, vol. 85, pp. 6169, 1999.
- [19] K. M. Tako, K.M., M. A. Wongsam. and R. W. Chantrell, "Numerical Simulation of 2D Thin Films Using a Finite Element Method," *J. Magn. Magn. Mater.*, vol. 155, pp. 40, 1996.
- [20] V. Tsiantos, "Numerical methods for ordinary differential equations in micromagnetic simulations," Ph.D. Thesis, University of Manchester, 2000.
- [21] V. D. Tsiantos, T. Schrefl, J. Fidler, and A. Bratsos, "Cost-Effective Way to Speed-up Micromagnetic Simulations in Granular media," *Applied Numerical Mathematics*, in press.
- [22] J. C. Toussaint, B. Kevorkian, D. Givord, and M. F. Rossignol, in *Proceedings of the 9th International Symposium Magnetic Anisotropy and Coercivity In Rare-Earth Transition Metal Alloys* (World Scientific, Singapore , 1996), p. 59-68.
- [23] R. A. Victora,"Quantitative theory for hysteretic phenomena in CoNi magnetic thin films," *Phys. Rev. Lett.*, vol. 58, pp. 1788, 1987.
- [24] D. Weller and A. Moser, "Thermal effect limits in ultrahigh-density magnetic recording," *IEEE Trans. Magn.*, vol. 35, pp. 4423, 1999.
- [25] B. Yang and D. R. Fredkin, "Dynamical micromagnetics by the finite element method ," *IEEE Trans. Magn.* vol. 34, pp. 3842, 1998.
- [26] J. G. Zhu and H. N. Bertram,"Magnetization reversal in CoCr perpendicular thin films," *J. Appl. Phys.*, vol. 66, pp. 1291, 1989.

3

MICROMAGNETISM FOR PERPENDICULAR
RECORDING MEDIA

Micromagnetic simulations are performed to investigate the reversal process and the thermal stability of a grain of a typical perpendicular recording medium (Co-Cr). The integration of the LLG equation shows that the reversal process changes slowly and steadily from coherent rotation to nucleation with increasing column length (film thickness). The region between homogeneous rotation and nucleation becomes smaller and is shifted to smaller column lengths if the damping constant is reduced from $\alpha=1$ to $\alpha=0.02$.

Using solutions of LLG simulations, energy barriers between the two stable states at zero field are estimated. For column lengths larger than 30 nm the energy barriers for inhomogeneous reversal processes are smaller than for coherent rotation.

In the weakly damped case very fast switching modes exist if the switching field is only slightly larger than the coercive field. For fields slightly larger than the smallest possible switching field, the switching time increases with increasing field. The switching time reaches a maximum at an external field close to the Stoner-Wohlfarth coercivity. For larger external fields the expected decrease of the switching time with increasing field is obtained. The solution of the Langevin-equation shows that thermal fluctuations do not significantly influence the dependence of the switching time on the field strength.

3.1 Introduction

In recent years there has been a renewed interest in perpendicular recording since an improvement of the areal density in longitudinal recording is getting increasingly difficult. For longitudinal recording the demagnetization fields increases with increasing bit density, leading to a reduction in thermal stability. In contrast the demagnetizing fields for perpendicular recording continuously reduces with bit density.

Another advantage of perpendicular recording is that the areal density can be increased without reducing the volume of the magnetic bit. A large volume of the magnetic domain can be realized with an increased column length l_c (film thickness). For coherent rotation a higher grain volume leads to a higher energy barrier and hence to an improved thermal stability.

Thus twice the exchange length $2R_0$, which is assumed to be the limit between coherent rotation and inhomogeneous reversal processes, is the upper bound for the column length in perpendicular recording media [21]. For Co-Cr, a typical perpendicular recording material,

$$2R_0 = 2M_s \sqrt{4\pi A/\mu_0} \approx 50 \text{ nm} \quad (3.1)$$

We have performed micromagnetic simulations to investigate in detail the reversal modes in perpendicular recording media. The simulations at zero temperature are based on the integration of the LLG equation. The energy barrier between two stable magnetization states is estimated from LLG solutions. Langevin dynamics simulations give information about the switching process at finite temperature. In section 3.2 the reversal mode of a single grain of a perpendicular recording medium is investigated for different film thicknesses and two different damping constants. Estimated energy barriers for the two states of a perpendicular recording grain are calculated in section 3.3. Section 3.3 also deals with reversal modes at finite temperature. The switching time of single domain particles as a function of the field strength is calculated in section 3.4.

3.2 Reversal modes

The reversal process is calculated for one Co-Cr grain ($J_c = 0.5 \text{ T}$, $A = 10^{-11} \text{ J/m}$, $K_1 = 3 \times 10^5 \text{ J/m}^3$). The basal plane of the grain is an irregular pentagon with a diameter of about 12 nm. The easy axis is perpendicular to the basal plane. The external field is always applied 1° off the easy axis. The average element size of the finite element mesh is 2 nm, small enough to resolve domain walls which have a typical width of

$$d_w = \sqrt{A/K_1} \approx 6 \text{ nm}. \quad (3.2)$$

3.2.1 High damping reversal ($\alpha = 1$)

If the external field reaches the coercive field H_c which increases linearly from 0.97 ($2K_1/J_c$) for $l_c = 20 \text{ nm}$ to 1.03 ($2K_1/J_c$) for $l_c = 70 \text{ nm}$, the magnetization state becomes unstable and reversal starts. Figure 3.1 shows the maximum value of the exchange energy during reversal for different column lengths. The exchange energy measures the uniformity of the magnetization during reversal. The exchange energy remains zero if the reversal mode is

homogeneous rotation. It increases as the reversal mode becomes more inhomogeneous. The exchange energy is normalized to the domain wall energy.

$$E_w = 4A_{\text{end}}\sqrt{AK_1}. \quad (3.3)$$

A_{end} measures the area of the basal plane. It can be seen that nucleation does not occur at a critical length, but the transition is smooth from coherent rotation to nucleation. Below 40 nm coherent rotation dominates. Figure 3.2 shows non-equilibrium states of the magnetization during reversal for different column lengths at a time when $J_z = 0$. With increasing column length (>40 nm) the magnetization at the top and bottom of the grain becomes increasingly misaligned to the magnetization in the middle. Above 80 nm the magnetization at the top and bottom points antiparallel to the magnetization in the middle and the magnetic exchange energy reaches its maximum. In this regime on both ends a domain wall is formed. The maximum exchange energy during reversal is equal to the domain wall energy E_w .

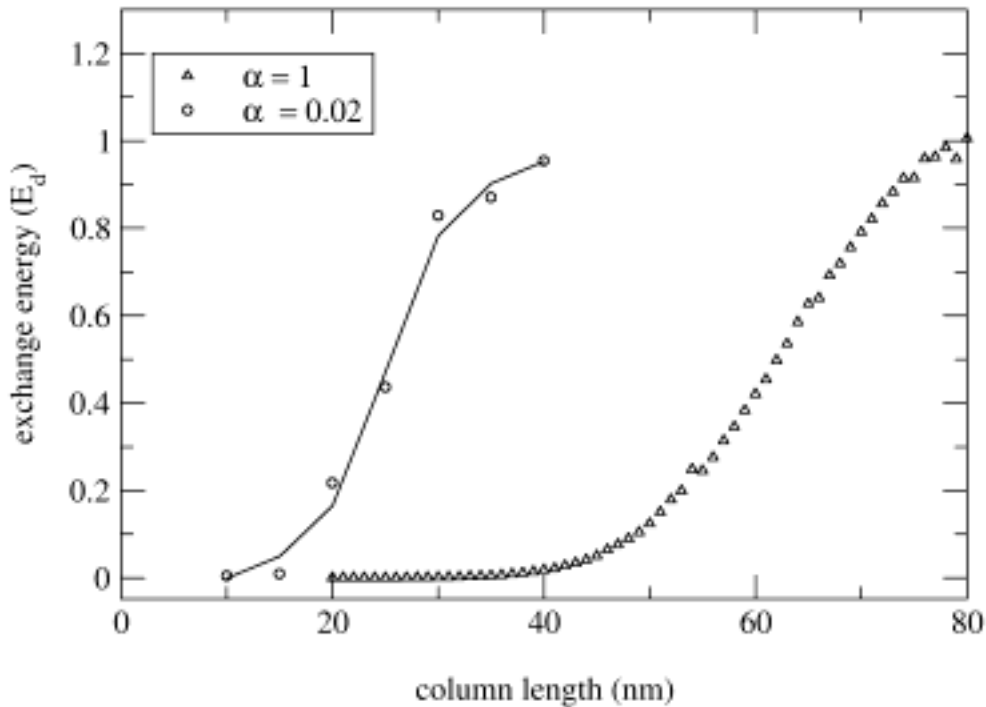


Figure 3.1: Maximum value of the exchange energy during reversal as a function of the column length for two different damping constants. A value of the exchange energy close to the domain wall energy E_d indicates nucleation processes at the particle ends.

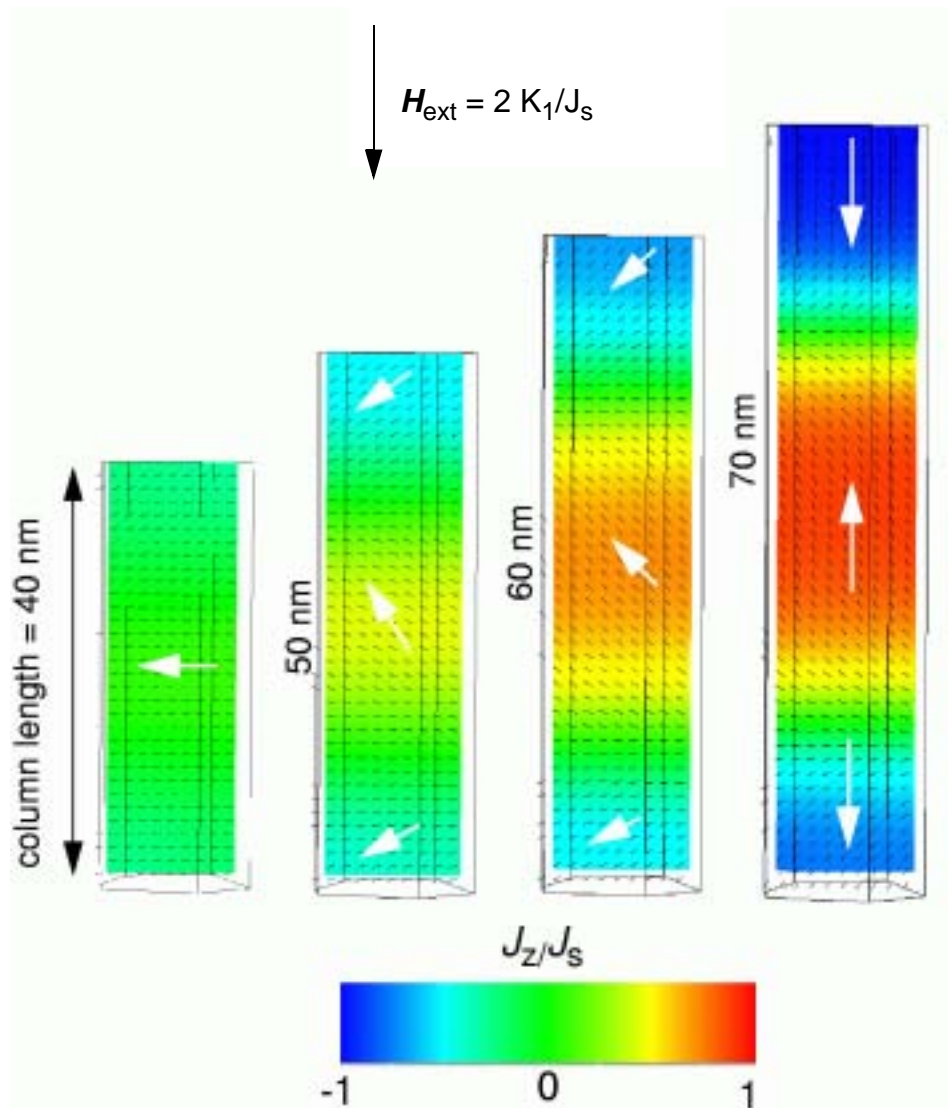


Figure 3.2: Non-equilibrium states at $J_z = 0$ during reversal for different column lengths after the coercive field was applied. The damping constant $\alpha = 1$. The z -component of the magnetization is color coded.

3.2.2 Low damping reversal ($\alpha = 0.02$)

The transition from coherent rotation to nucleation is shifted to smaller column length when the damping constant is reduced to $\alpha = 0.02$. The magnetization becomes already incoherent during reversal, for $l_c > 20$ nm. The transition from coherent rotation to nucleation is represented by the solid line in figure 3.1.

The top image in figure 3.3 shows the exchange energy during reversal for a granular grain with $l_c = 20$ nm. It shows that the exchange energy increases when the magnetization is per-

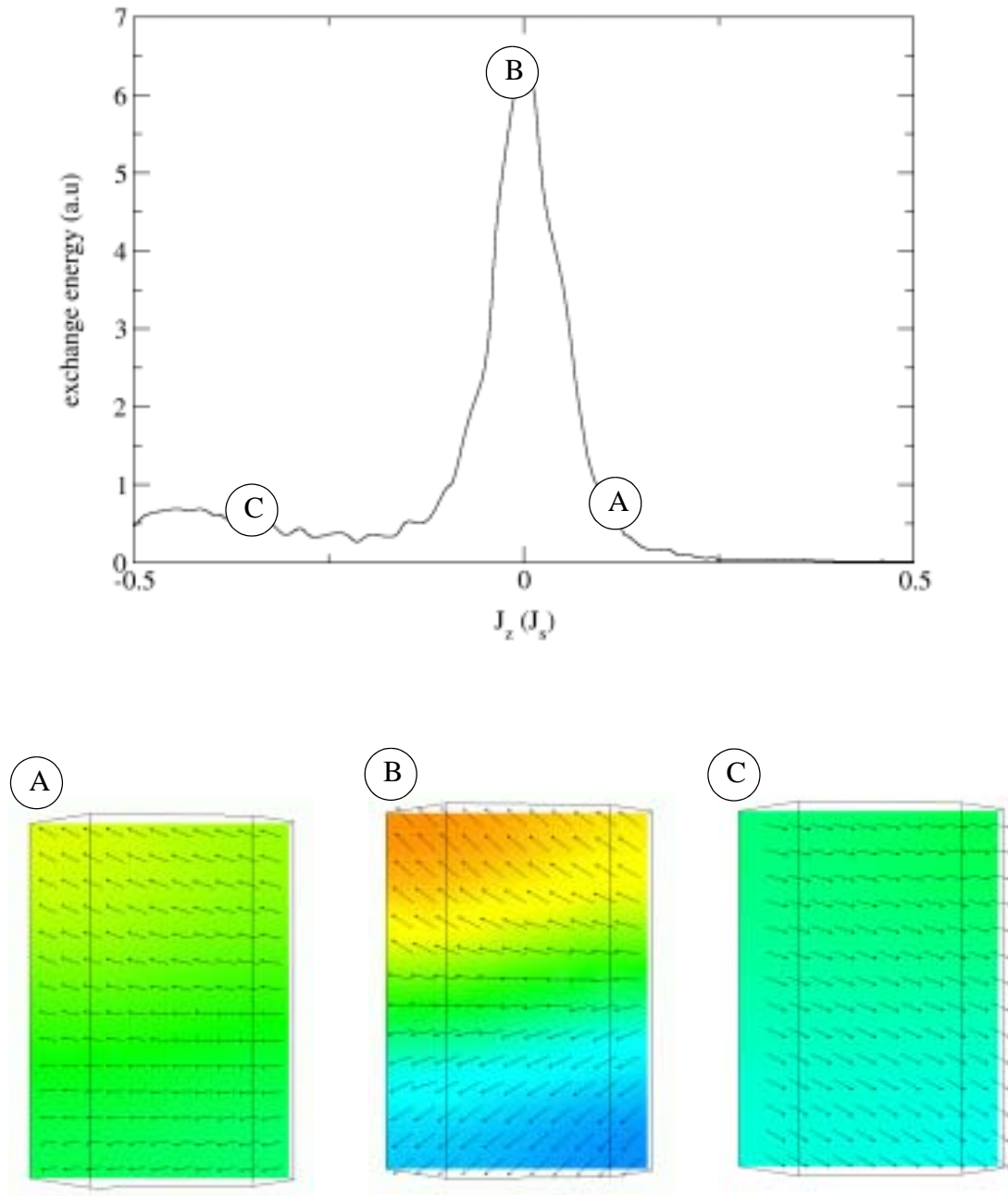


Figure 3.3: (top image) Exchange energy as a function of the z -component of the magnetization for a column length of 20 nm. ($\alpha = 0.02$). When the magnetization points perpendicular to the easy axis the exchange energy is largest. (bottom image) Transient magnetization states during reversal. The z -component of the magnetization is color coded. (A) $J_z/J_s = 0.1$, (B) $J_z/J_s = 0$ and (C) $J_z/J_s = -0.3$.

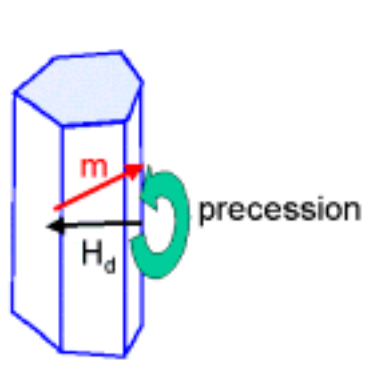


Figure 3.4: When the magnetization rotates out of the long axis a high stray field occurs. Owing to gyromagnetic precession the magnetization rotates around the stray field direction.

pendicular to the long axis. For a magnetization perpendicular to the long axis surface charges occur at the surfaces normal to the basal plane. These surface charges cause a large stray field that forms a flower state of the magnetization. The flower state can be seen in the middle picture in figure 3.3. The flower state transforms to a more homogeneous state again, when J_z/J_s becomes smaller than ~ -0.2 as shown by the right picture in figure 3.3.

Thus the maximum exchange energy occurs, when the magnetization is perpendicular to the long axis. In order to decrease surface charges and hence stray field energy an inhomogeneous state is formed.

For a low damping constant the precession term in the Landau-Lifshitz-Gilbert equation becomes important. Owing to gyromagnetic precession a domain wall that is formed does not propagate with constant velocity through the grain. An almost constant propagation of the domain wall can be observed for $\alpha=1$. Because the magnetization in the center of the domain wall points perpendicular to the long axis a stray field perpendicular to the long axis occurs as shown in figure 3.4. The magnetization starts to rotate around the stray field owing to gyromagnetic precession. As a consequence the domain wall oscillates leading to oscillations in the z -component of the magnetization as a function of time.

3.3 Energy barriers and thermally activated reversal modes

The information in hard disk media is stored in the magnetization state of the magnetic grains. Ideally, in perpendicular recording one bit is represented by two possible magnetization states - the magnetization points up or down. To guarantee that the information is per-

manently stored these two magnetization states have to be separated by an energy barrier that should be as large as possible. With decreasing energy barrier thermal fluctuations, that may induce reversal, become increasingly important. Street and Wooley [26] first discussed thermally activated reversal processes by pointing out that the thermal energy k_bT initiates magnetization reversal. Starting from the classical Arrhenius formula of chemical reaction theory, Néel [19] expressed the probability of magnetization reversal as,

$$f = f_0 \exp\left(-\frac{\Delta E}{k_b T}\right), \quad (3.4)$$

where f is the reversal rate between states that are separated by the energy barrier ΔE . f_0 is the attempt frequency of the order of 10^{10} Hz. For single domain particles the energy barrier can be simply calculated by the model of coherent rotation. If the particle has a uniaxial anisotropy the energy barrier is

$$\Delta E = K_1 V, \quad (3.5)$$

where K_1 is the anisotropy constant and V the volume of the particle. Inspecting equation (3.4) one finds that for an energy barrier of $\Delta E = 40k_bT$ the relaxation time is about 10 years.

For larger particles the application of the coercive field initiates incoherent magnetization reversal. This indicates that also the thermally activated switching process may be non uniform. In this case the energy barrier will differ from equation (3.5). The calculation of the energy barriers is a sophisticated problem. Depending on whether the final state is known or not different methods were proposed.

Most schemes for finding the saddle point and the final configuration start from the initial state and then trace stepwise a path of slowest ascent [20,6]. However, these methods find paths that do not necessarily pass through the saddle point.

If the initial and final state are given, more reliable methods can be applied. Berkov [2] applied the path integral method to find the minimum energy path of a system of interacting single domain particles. However, Berkov also showed that this method gives paths through local maxima, that have to be excluded.

A very promising method to find minimum energy paths and hence saddle points is the nudged elastic band method, that was proposed by Henkelman and Jónson [15]. This method

was successfully applied to micromagnetics by Dittrich et al. [7]. Using the nudged elastic band method together with the finite element method energy barriers for complex micromagnetic systems such as granular recording media can be calculated.

In the following we use magnetization states from hysteresis loop calculations to estimate energy barriers. We calculate energy barriers for different column lengths. Particularly, we are interested in the critical column length below which the lowest energy barrier correspond to coherent rotation.

To estimate the energy barrier between the two stable states (magnetization up and down) for vanishing external field we assume that the reversal process at zero temperature triggered by the external field is similar to the reversal process at zero field and finite temperature. Hysteresis loop calculations using the LLG equation provide the magnetization states during reversal. Figure 3.5 shows two possible paths in configuration space from the saturated state towards the reversed state. The z -axis shows the energy of the states. The magnetization states (1) to (4) follow from hysteresis loop calculation with $\alpha = 1$. The white line in the upper picture of figure 3.5 ($\alpha = 1$) shows a path in configuration space including the states (1) to (4). The energies of these states at zero external field is shown by the white line in the upper picture of figure 3.5.

Along the path for $\alpha = 0.02$ in figure 3.5 the magnetization states follow from a hysteresis loop calculation with $\alpha = 0.02$. Since the hysteresis loop calculation with $\alpha = 0.02$ leads to a different reversal mode than the hysteresis loop calculation with $\alpha = 1$ we find two different paths from the initial state to the reversed states. Since both paths do not necessarily pass through the saddle point, we can only determine an upper limit for the energy barrier. On the basis of such a path the elastic band method can be used to find the saddle point [18].

The path corresponding to $\alpha = 0.02$ contains inhomogeneous states when the column length exceeds 20 nm (figure 3.1).

For column lengths smaller than 30 nm the paths $\alpha = 0.02$ and $\alpha = 1$ yield the same energy barrier which increases with the column length linearly as predicted by Stoner-Wohlfarth theory (Figure 3.6). When the column length exceeds 30 nm the path following from hysteresis calculation with $\alpha = 0.02$ leads to smaller energy barriers. It proves that at least for column lengths $l_c > 30$ nm inhomogeneous reversal processes have a lower energy barrier than homogenous rotation. As discussed in section 3.2 the inhomogeneous reversal mode is

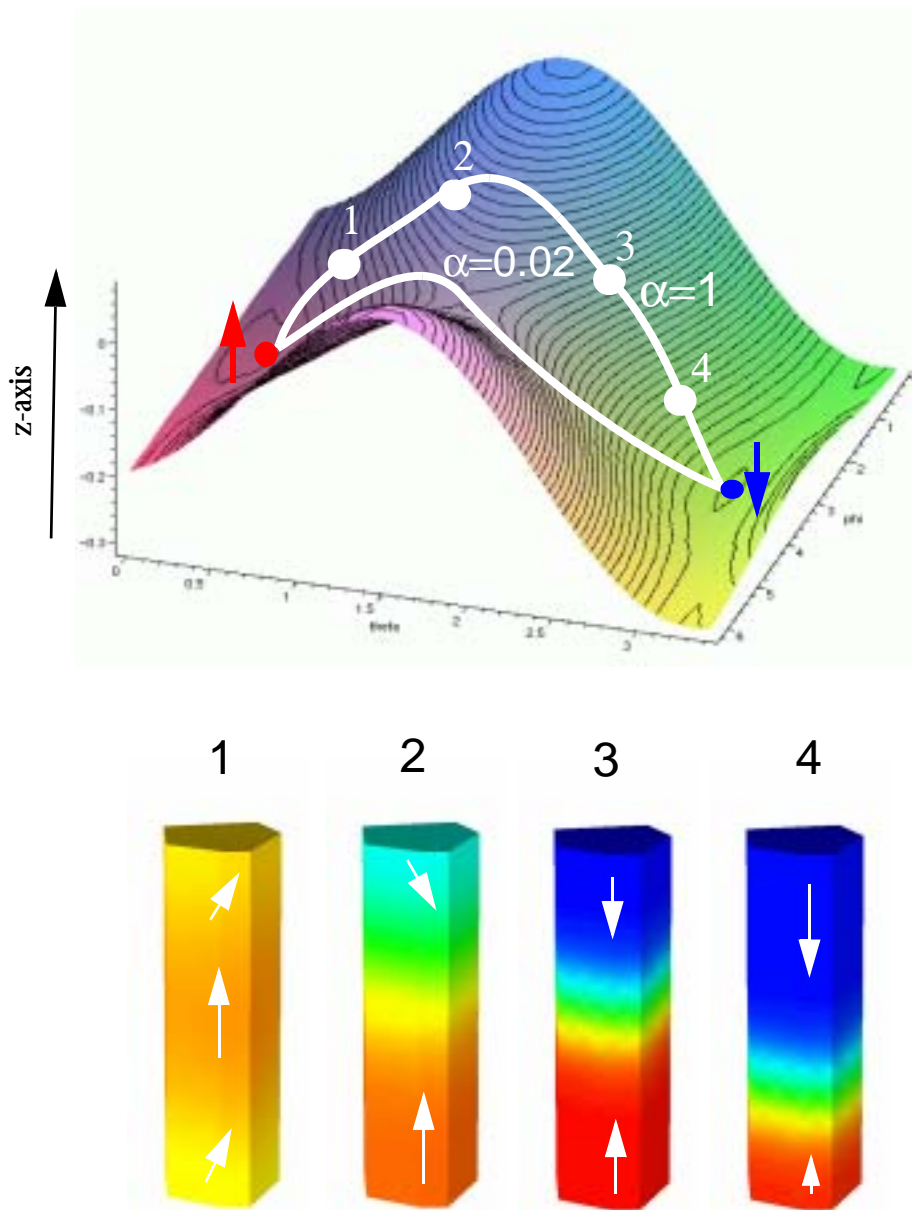


Figure 3.5: (top) The energy landscape shows the two minima, that correspond to the initial magnetization state and the switched state. An energy barrier separates these two states. The white lines show possible paths from the initial state towards the reversed state.

(bottom) Shows magnetization states along one possible path from the initial state towards the reversed. These states follow from a hysteresis loop calculation with $\alpha = 1$.

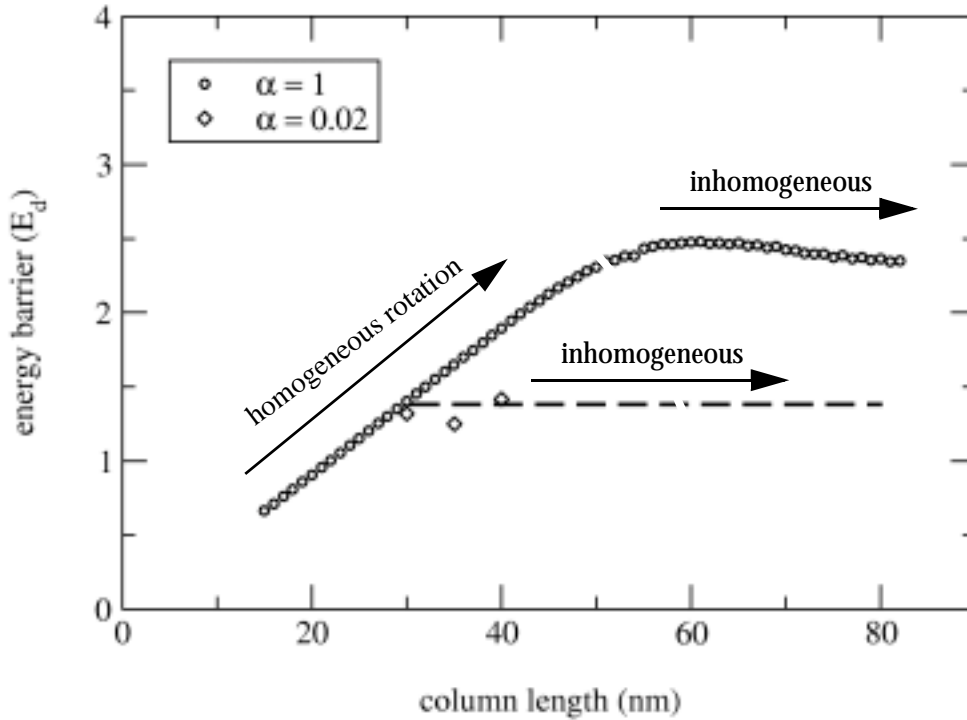


Figure 3.6: Upper limit of the energy barrier as a function of the column length. For l_c larger than 30 nm the estimation of the upper limit on the basis of LLG simulation with $\alpha = 0.02$ leads to smaller energy barriers (diamonds).

not necessarily nucleation. There is a variety of different inhomogeneous reversal modes in the transition from coherent rotation to nucleation.

In the limit of nucleation Braun [3] calculated the energy of forming a nucleus at the end of a wire as $\Delta E = 4A_{end}\sqrt{A(K_1 + J_s^2/(4\mu_0))}$. In Braun's calculation one of the two assumptions have to be fulfilled. Either $d < \sqrt{AK_1}$ or $K_1 > J_s^2/(4\mu_0)$.

The circles in figure 3.6 for $l_c > 60$ nm represent upper limits for energy barriers which are more than twice as large as the prediction by Braun. The reason is that the reversal process at $T=0$ and $\alpha = 1$, which is used as a trial path in configuration space, is symmetric with respect to the long axis. Hence nucleations occur on both ends of the particle. Therefore the energy which is required for nucleation is counted twice. Simulations with $\alpha = 0.02$ at $T=0$ show only one nucleation at the particle end. Therefore energy barrier estimations on the basis of these simulations yield much smaller values (squares and the extrapolated dotted line in figure 3.6).

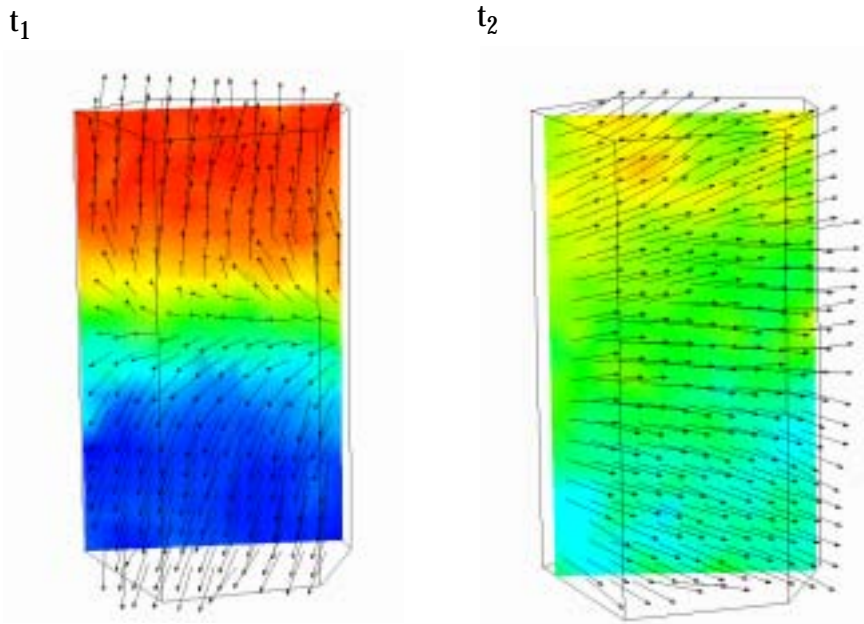


Figure 3.7: Thermally activated switching process of a grain with a column length of 15 nm at $T=300\text{K}$. (t_1) H_{ext} is 90% of the anisotropy field H_{ani} . (t_2) $H_{\text{ext}} = 0.96 H_{\text{ani}}$, $\beta = 1^\circ$, $\alpha=0.02$.

Beside the estimation of the energy barrier we investigated the thermal activated switching process using Langevin dynamic simulations. Details of finite element calculations at finite temperature can be found in [23].

In the following calculation a temperature of $T = 300\text{ K}$ is assumed. The edge length of one finite element is 2 nm. The damping constant $\alpha = 0.02$. An external field smaller than the coercive field is applied to the saturated state under an angle of 1° with respect to the uniaxial easy axis. This external field decreases the energy barrier and switching occurs within a time which can be calculated with our numerical approach, which is limited to several ns. The time step h is fixed to 3.7 fs. As a function of the strength of the field the thermally activated reversal mode may change. Figure 3.7 shows two typical reversal processes for an columnar grain with column length $l_c = 15\text{ nm}$. In figure 3.7 (t_1) the external field is, $H_{\text{ext}}=0.9 \times H_a$. If the external field is increased to $H_{\text{ext}}=0.96 \times H_a$ most realizations switch by quasi homogeneous rotation as shown in figure 3.7 (t_2). The switching time decreases from about 2 ns to 1.3 ns. Thus for high external fields that lead to a small energy barrier the reversal mode is almost homogeneous rotation. For low external fields the thermally activated switching process is nucleation.

For column lengths smaller than 20 nm we have observed quasi homogeneous rotation for all investigated field strengths ($H_{\text{ext}} = 85\%$, 90% and 95% of H_a).

3.4 Switching times of small magnetic particles

In the previous section the thermal stability was investigated that is important for the improvement of the areal density. In addition to the improvement of the areal density of magnetic recording media, the data rate becomes increasingly important [24]. For different types of magnetic memories ranging from magnetic core memory, hard discs, magneto-optical media to MRAMS the switching time is an important factor [10]. Kikuchi [12] investigated the reversal time of a single domain sphere and a single domain thin film. He reported a minimum reversal time for $\alpha = 1$ and $\alpha = 0.01$ for the sphere and the thin film, respectively. He and Doyle [13] solved the Landau-Lifshitz equation numerically, in order to investigate switching with very short field pulses. They conclude that switching times in the order of about 100 picoseconds are possible if the external field is applied 90° with respect to the anisotropy axis.

Doyle and co-workers [14] found that if the rise time of the pulse field is less than a few nanosecond and the Gilbert damping constant $\alpha < 1$, switching can occur well below the Stoner-Wohlfarth limit. Mallinson [16,17] derived the switching time as a function of the field strength for a field parallel to the anisotropy direction. The switching time decreases with increasing external field.

In the following the switching time of a grain of a perpendicular recording medium is investigated. The results show that a small angle of the external field with respect to the anisotropy axis significantly changes the dependence of the switching time as a function of the field strength. Fast switching also occurs at fields well below the Stoner-Wohlfarth limit.

3.4.1 Columnar grain

Consider a grain of a perpendicular recording medium (inset of figure 3.8) with the material parameters of Co-Cr ($J_s = 0.5$ T, $A = 10^{-11}$ J/m, $K_1 = 3 \cdot 10^5$ J/m³). The basal plane of the grain is an irregular pentagon with a diameter of about 13 nm. The easy axis is perpendicular to the basal plane (along the z -axis). After saturating the grain along the $+z$ -axis the remanent state is calculated. An external field is applied instantaneously at an angle β between the field and the minus z -axis. Depending on the damping constant and the height of the grain (=col-

umn length l_c) the reversal process changes from coherent rotation to inhomogeneous reversal as discussed in section 3.2. For a damping constant $\alpha=0.02$ homogeneous rotation only occurs for column lengths l_c smaller than 20 nm. For a column of this length we investigated the influence of the strength of the external field on the switching time. We distinguish between two switching times. We define the theoretical switching time as the minimum length of a field pulse to switch the particle. However, for longer field pulses the magnetization may precess back and no switching occurs. A suitable definition of a practical switching time is the critical duration of the field pulse, t_p , so that all field pulses longer than t_p will switch the particle. Figure 3.8 shows the time evolution of the average magnetization parallel to the z -axis. The magnetization oscillates owing to gyromagnetic precession. This effect is more pronounced with larger angle β . The arrows in figure 3.8 show the theoretical switching time t_{th} and the practical switching time t_p .

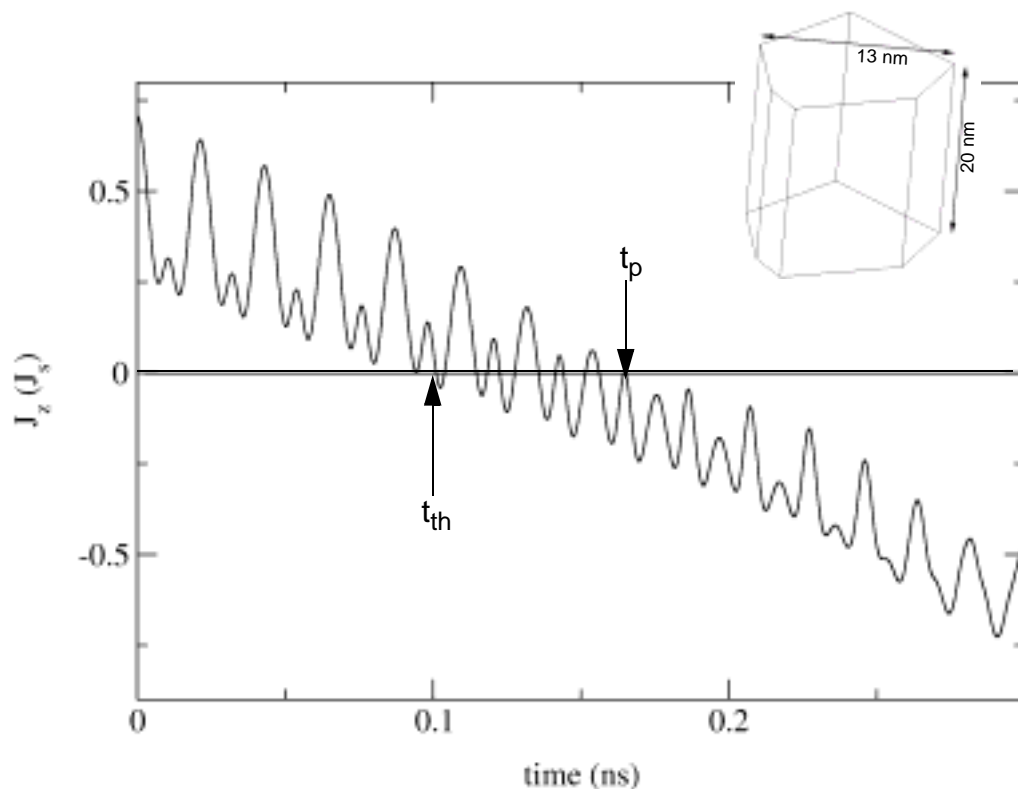


Figure 3.8: The average magnetization parallel to the long-axis as a function of time for $\beta = 1^\circ$. The theoretical switching time t_{th} and the practical switching time t_p are marked. The inset shows the shape of the columnar grain.

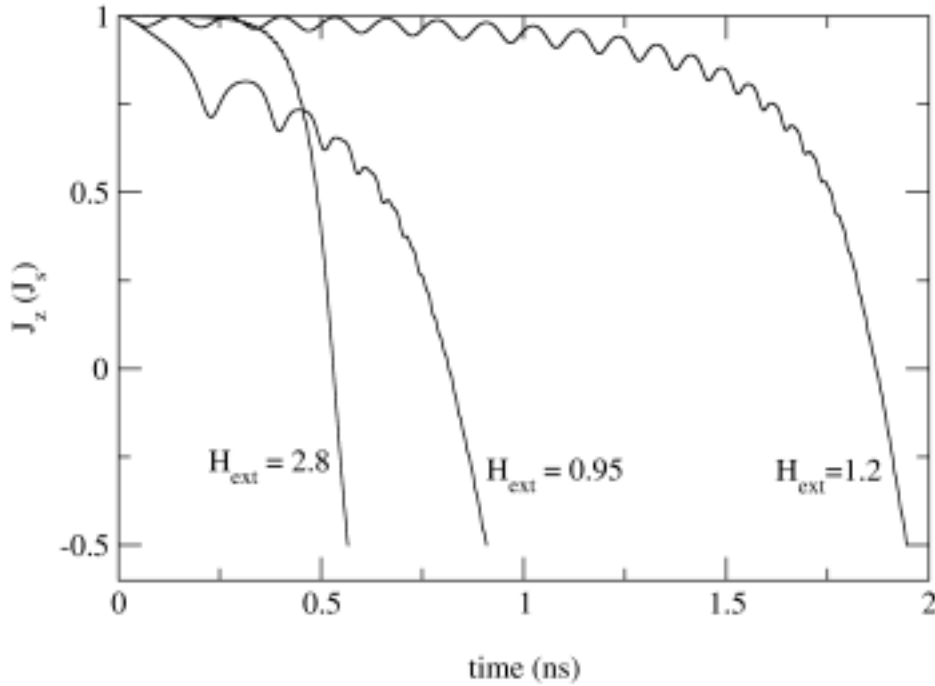


Figure 3.9: J_z as a functions of time after different external fields (0.95, 1.2 and 2.8 times $2K_1/J_s$) are instantaneously applied to the saturated state. The column length of the grain is 20 nm. ($\alpha = 0.02$)

Figure 3.9 shows the time dependence of the magnetization for different strengths of the external field. At $t = 0$ an external field of 0.95, 1.2 and 2.8 ($2 K_1/J_s$) is applied. For small values of the external field the z -component does not decrease monotonically but shows oscillations, which correspond to the precession of the magnetization around the effective field. This effect can only be found if the axial symmetry is broken (easy axis does not point exactly parallel to field direction) and an increase of J_z does not necessarily lead to an increase of the energy. With increasing damping constant the relaxation towards the minimum dominates the motion of the magnetization and the oscillations of the magnetization vanish for every strength of the external field.

Figure 3.10 shows the switching time t_p as a function of the strength of the external field. It is evident that the switching time does not decrease with increasing external field in the whole regime but shows a maximum slightly above the anisotropy field. For a further clarification of the correlation between field strength and switching time we simplified the model and investigated the reversal dynamics of a single magnetic moment.

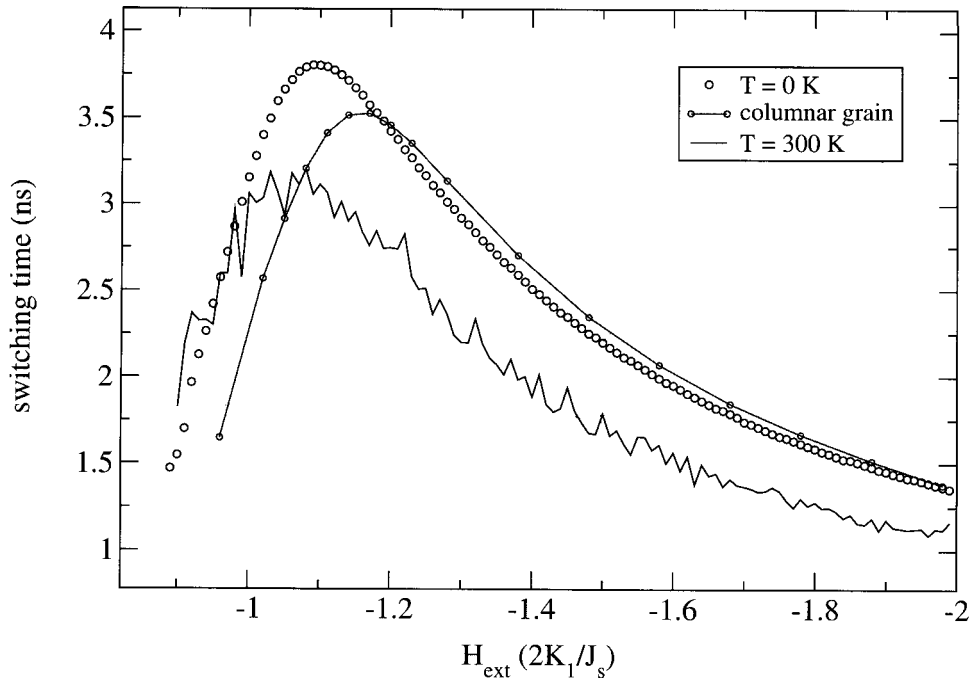


Figure 3.10: The switching time of the columnar grain as a function of the magnitude of the external field ($\beta = 1^\circ$).

3.4.2 Single magnetic moment

Again we assumed a uniaxial anisotropy along the z -axis. Initially, the magnetization points parallel to the positive z -axis. Then the external field is applied instantaneously at an angle β to the negative z -axis. Figure 3.10 shows that the dependence of the switching time as a function of the field strength is very similar for the granular grain and the single magnetic moment. Thus we assume that the reversal process of a columnar grain can be compared with that of a single magnetic moment. The path which the system follows through the energy landscape may explain the switching behavior more clearly. Figure 3.11 and figure 3.12 show the path of the magnetization through the energy landscape and the locus of the magnetization just after the application of the field $H_{\text{ext}} = 0.9 (2K_l/J_d)$ and $H_{\text{ext}} = 1.3 (2K_l/J_d)$, respectively. Before the application of the external field, the system is in equilibrium at $J_x = J_y = 0$ marked with a dark dot in (A) and (B) in figure 3.11 and figure 3.12. If a field of $1.3 (2K_l/J_d)$ is applied the energy landscape suddenly changes. The system is no longer in equilibrium. A well defined maximum is formed due to the Zeeman energy which contributes most to the total energy. The current state is close to the maximum. Due to the precession term in the

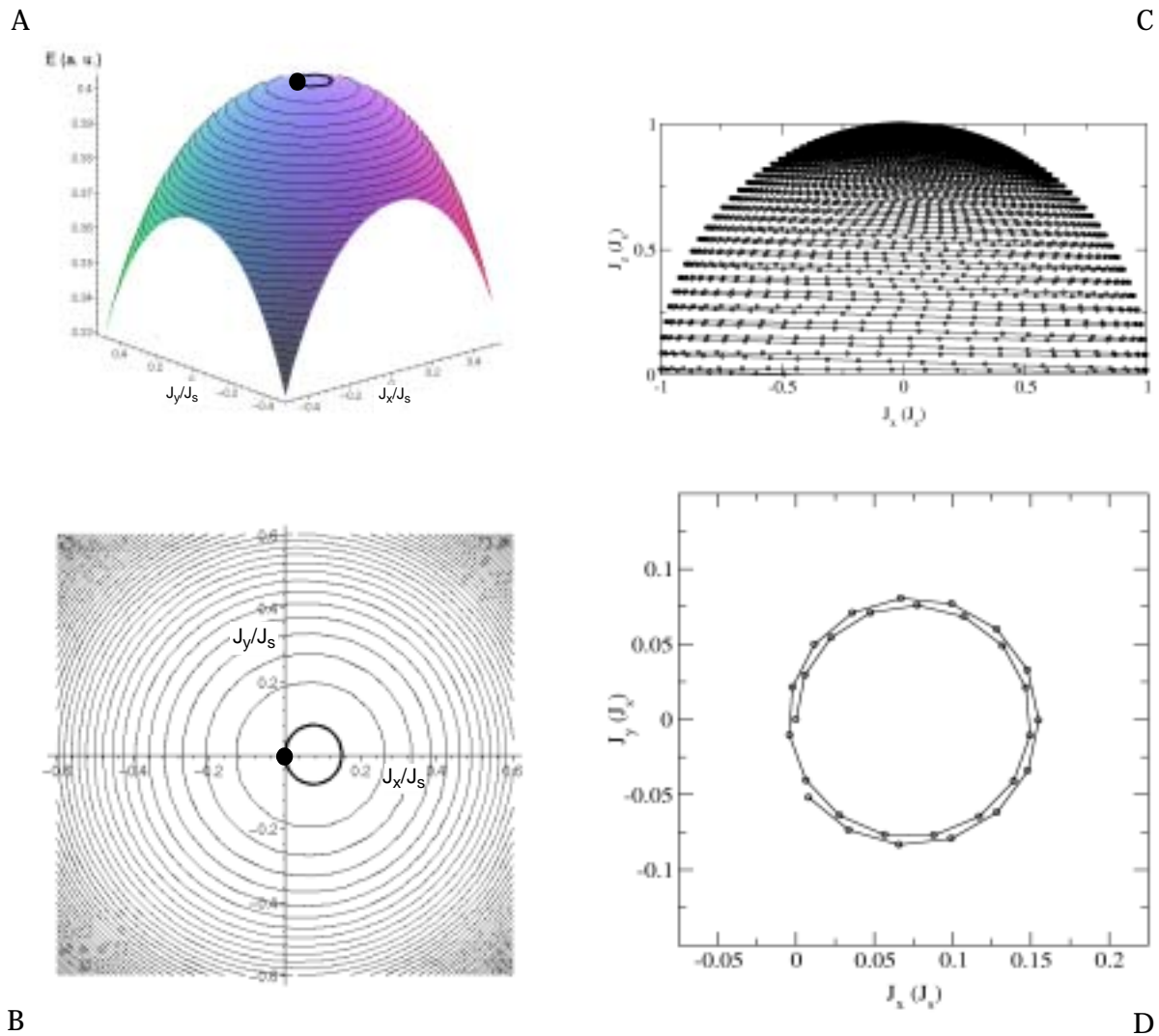


Figure 3.11: Energy landscape and paths of the magnetic polarization towards the switched state when an external field of $1.3 (2K_1/J_s)$ is applied.

(A) and (B) show the energy landscape and the contour plot in terms of its normalized magnetic polarization, respectively.

(C) and (D): Locus of the polarization as a function of time. The circles are plotted every 0.005 ns. (D) shows only the first 0.15 ns after applying of the external field.

LLG equation, the magnetization moves along a path with almost constant energy as shown in figure 3.11 (D). If the damping constant is small the magnetization will initially follow this path, indicated by the bold line in figure 3.11 (A and B). During this motion the angle between the magnetization and the effective field remains small and it precesses several times around the effective field, with J_z almost 1 (Figure 3.11 C). Since for J_z almost 1 the torque J

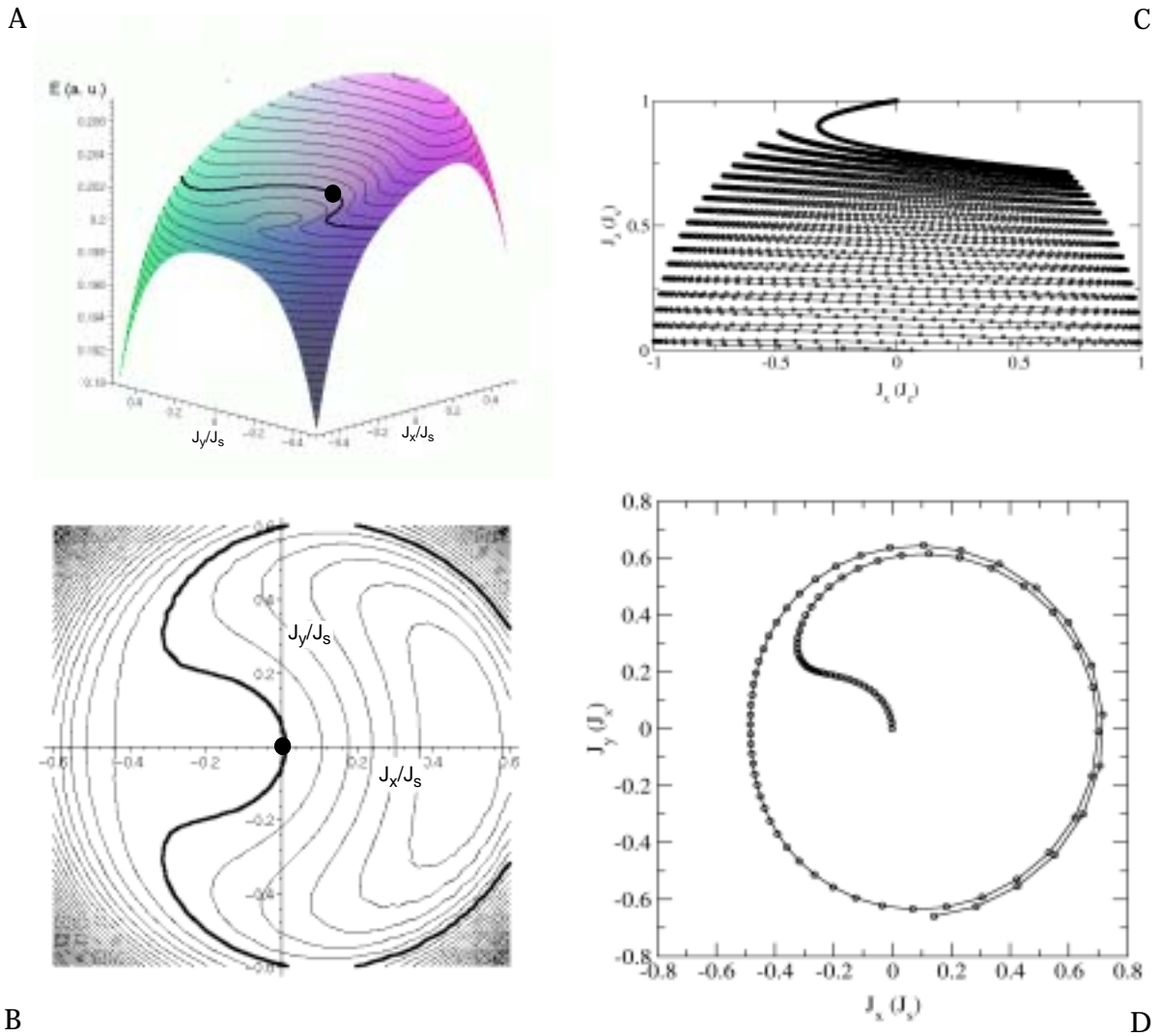


Figure 3.12: Energy landscape and paths of the magnetic polarization towards the switched state when an external field of $0.9 (2K_1/J_s)$ is applied.

(A) and (B) show the energy landscape and the contour plot in terms of its normalized magnetic polarization, respectively.

(C) and (D): Locus of the polarization as a function of time. The circles are plotted every 0.005 ns. (D) shows only the first 0.5 ns after applying of the external field.

$x H$ is small the relaxation towards the reversed state is slow. A large switching time occurs. Only for fields exceeding 1.1 times the anisotropy field the switching time decreases. This is due to the linear increase of the torque with the strength of the external field.

If the external field is comparable with the anisotropy field a more complex energy landscape is obtained, because anisotropy energy and Zeeman energy contribute in the same order of magnitude to the total energy. The bold line in the contour plot in figure 3.12 (B)

gives the path of the magnetization for an external field of $0.9 (2K_1/J_2)$. The precession drives the magnetization away from the effective field (Figure 3.12 D) which leads to a high torque. Fast switching occurs when the magnetization does not relax back to the local minimum shown in figure 3.12 (A) but moves towards the local minimum which corresponds to the reversed state. For an external field $H_{\text{ext}} \geq 0.89 (2K_1/J_2)$ the initial motion of the magnetization along a path with nearly constant energy leads to magnetization reversal. The minimum switching time was 1.4 ns for $H_{\text{ext}} = 0.89 (2K_1/J_2)$, whereas a field of $H_{\text{ext}} > 1.9 (2K_1/J_2)$ is required to switch within the same time for large external fields.

Figure 3.13 gives the switching time t_p for an angle β of 45° between the field and the neg-

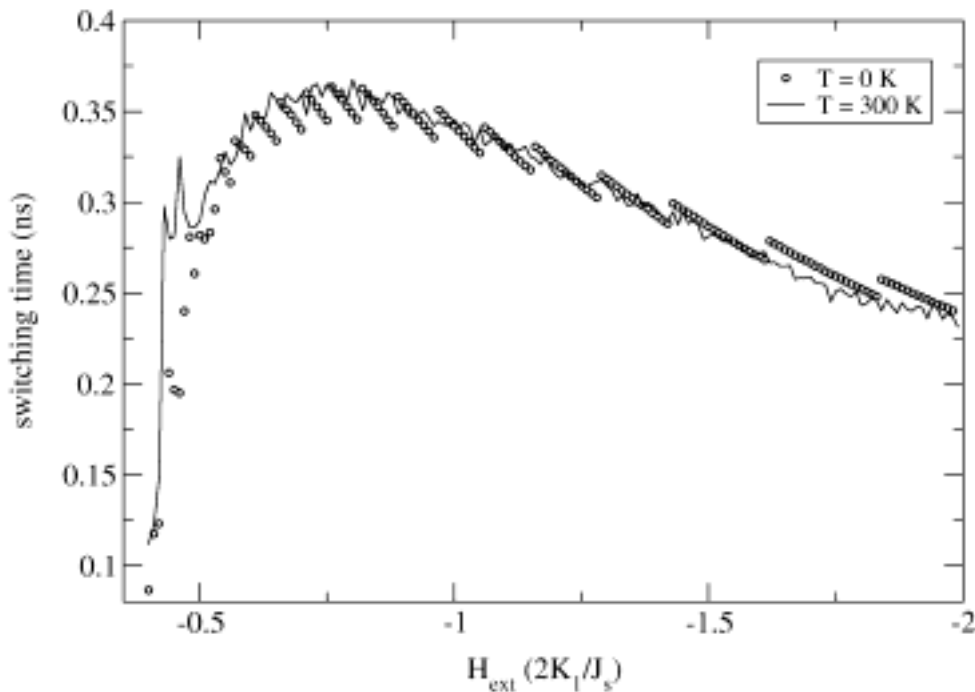


Figure 3.13: Switching time as a function of the field strength.(circles): $\beta = 45^\circ$, $T = 0 \text{ K}$, (solid line): $\beta = 45^\circ$, $T = 300 \text{ K}$.

ative z-axis. Again the switching time shows a maximum close to the coercive field obtained from the Stoner-Wohlfarth theory. Owing to the gyromagnetic precession the switching time shows jumps as a function of the field strength. Again a complex energy landscape causes fast switching at low fields. Different fields cause different paths through the energy landscape. It is interesting to note that at some specific fields for example at $H_{\text{ext}} = 0.43 (2K_1/J_2)$ switching does not occur. The magnetization rotates back towards the local minimum which corresponds to the non-switched state after precessing one complete circle. However, at lower

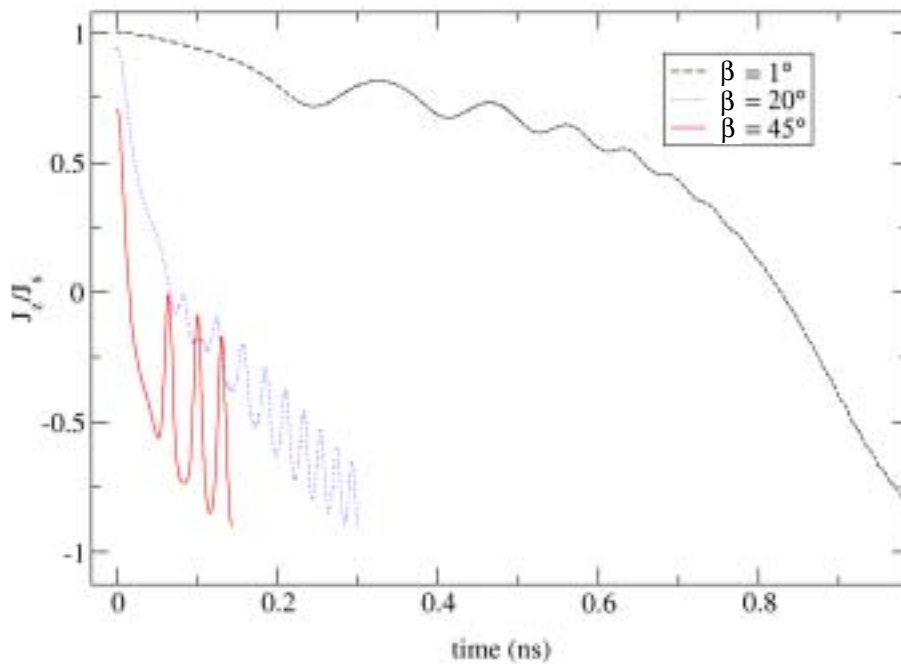


Figure 3.14: z -component of the magnetization as a function of time after applying the coercive field. The external field is applied at an angle of $\beta = 1^\circ$, 20° and 45° with respect to the z -axis.

fields switching is possible again provided $H_{\text{ext}} \geq 0.4 (2K_1/J_s)$. The observed switching times for $\beta = 45^\circ$ are smaller by about a factor of 1/10 as compared to the switching times obtained for $\beta = 1^\circ$.

Figure 3.14 compares the time evolution of the z -component of the magnetization after the application for different angles between the external field and the easy axis. Again it can be seen that fastest switching occurs for a field angle $\beta=45^\circ$. For $\beta=45^\circ$ the ringing of the magnetization is most pronounced.

3.4.3 Switching times at finite temperature

The above simulations were repeated using Langevin dynamics for room temperature. In order to take care of finite temperature for a single magnetic moment a stochastic, thermal field, H_{th} , is added to the effective field, H_{eff} . It accounts for the interaction of the magnetic polarization with the microscopic degrees of freedom which causes the fluctuation of the magnetization distribution. The Langevin equation [4]

$$\frac{\partial \mathbf{J}}{\partial t} = -|\gamma| \mathbf{J} \times (\mathbf{H}_{eff} + \mathbf{H}_{th}) + \frac{\alpha}{J_s} \mathbf{J} \times \frac{\partial \mathbf{J}}{\partial t} \quad (3.6)$$

is believed to give the random motion of the magnetization at finite temperatures. The effective field is the sum of the anisotropy field and the external field.

The thermal field is assumed to be a Gaussian random process with the following statistical properties:

$$\langle \mathbf{H}_{th,i} \mathbf{H}_{th,j} \rangle = 2D \delta_{ij} \delta(t - t') \quad (3.7)$$

The average of the thermal field taken over different realizations vanishes in each direction i in space. The thermal field is uncorrelated in time. The strength of the thermal fluctuations follows from the fluctuation-dissipation theorem:

$$D = \frac{\alpha k_B T}{\gamma J_s V} \quad (3.8)$$

where k_B is the Boltzmann constant and V the volume of the magnetic grain. Garcia-Palacios and Lazaro [11] showed that the equation has to be interpreted in the sense of Stratonovic, in order to obtain the correct thermal equilibrium properties. The numerical integration is performed using the method of Heun.

The results show that thermal effects do not change the dependence of the switching time on the strength of the external field as shown in figure 3.10. However, at low external fields thermal fluctuations may drive the magnetization towards the local minimum corresponding to the non-switched state and thus may prevent the particle from switching. On the other hand, thermal fluctuations may induce switching for fields where switching is impossible at $T = 0$ K. For each field 100 calculations were performed. Figure 3.15 shows the probability of not-switching as a function of the field. If the particle does not switch, the magnetization will relax back to the local minimum corresponding to the non-reversed state. The thermal relaxation time to escape this minimum is several orders of magnitudes larger than the switching time. Figure 3.16 gives the time evolution of the z -component of the magnetization for three different realization of the stochastic process. The external field was $\mathbf{H}_{ext} = 0.43 (2K_1/J_s)$. The results show that thermal fluctuations may completely change the path of the magnetization and thus induce switching.

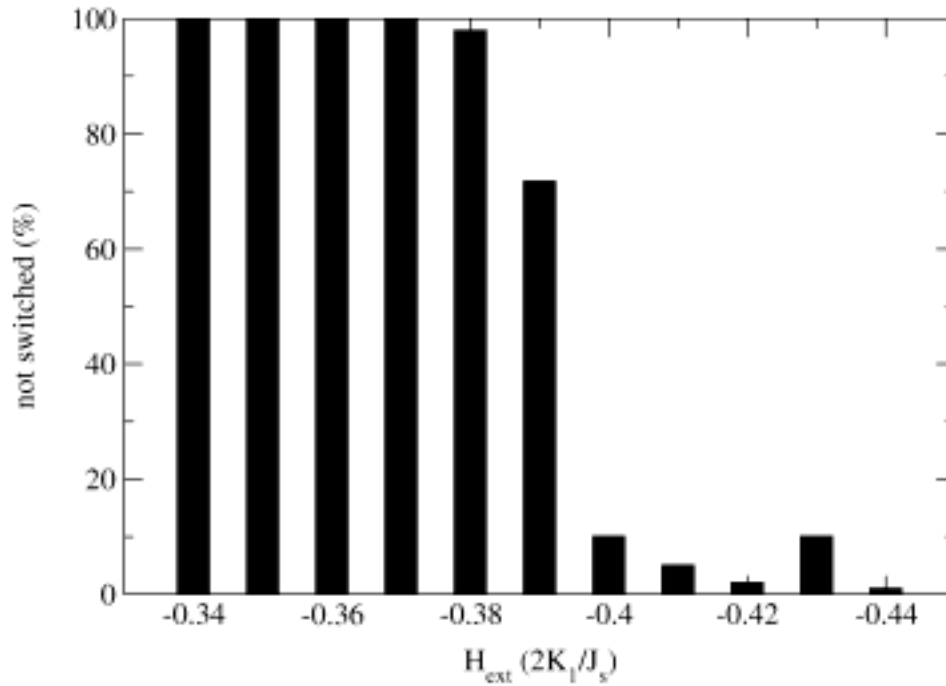


Figure 3.15: Probability of not-switching as a function of the strength of the external field. ($\beta = 45^\circ$)

When the external field is much larger than the Stoner-Wohlfarth switching field a well defined energy maximum is formed after the application of the external field. Thermal fluctuations just perturbed the deterministic path. Figure 3.17 compares a typical trajectory of a single magnetic moment during reversal at $T=50$ K and its path at zero temperature ($\alpha = 0.1$). At $T=0$ the number of precessional circles (until $J_z=0$) is smaller than at $T=50$. This indicates that the system at $T=50$ is effectively stronger damped. To explain this behavior we assume that the system is in the state s (black dot in figure 3.17). The thermal field causes fluctuations of the magnetic moment orientation. If the magnetic moment is perturbed into a state within the region T1 this state is closer to final state ($J_z=-1$). Since the area T1 is larger than the area T2 thermal fluctuations favour the relaxation of the system. This effect is pronounced when the effective field points almost antiparallel to the magnetic moment. In this case thermal fluctuations always increase the angle between the magnetic moment and the effective field which causes a higher torque. Thus fluctuations of the magnetization cause a

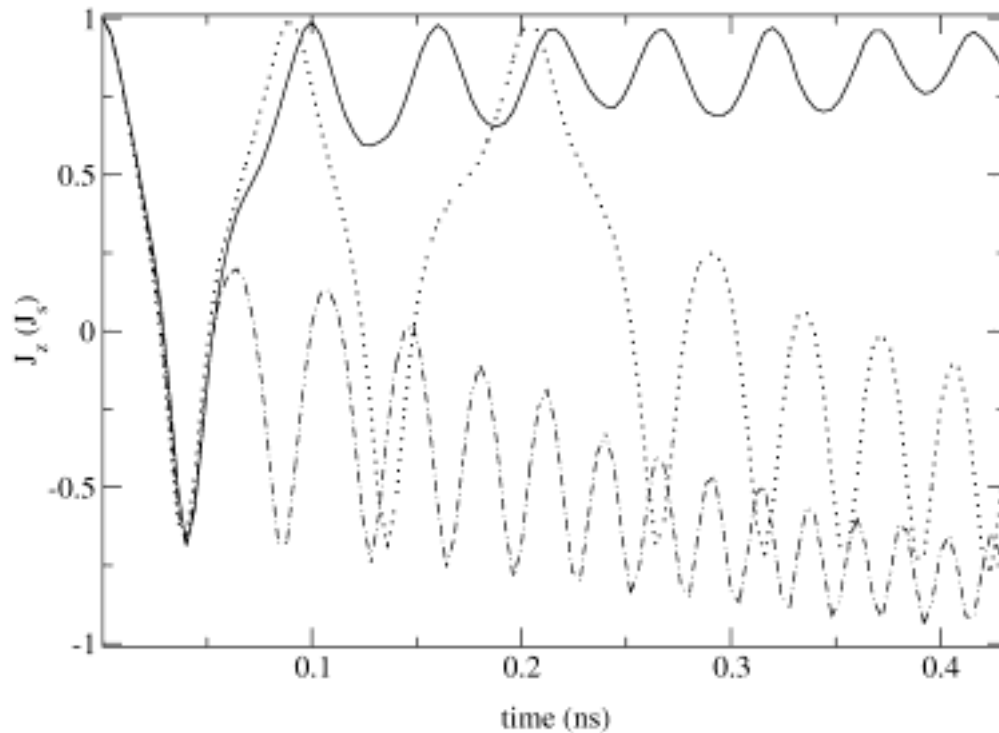


Figure 3.16: Time evolution of the magnetic polarization for three different realizations of the stochastic process. The solid line shows a realization which does not switch. The dotted and the dashed lines show two different paths towards the reversed state.

faster switching at higher temperature. With increasing angle between the magnetic moment and the effective field the effect vanishes. If the external field is for example applied 45° off the easy axis the switching time does not significantly change with temperature.

Figure 3.18 shows the switching time after the application of a field of $H_{\text{ext}} = 1.5 \times 2K_1/J_s$ as a function of temperature. The angle between the easy axis and the external field is 1° . In the investigated temperature range (0K - 400K) the switching time increases almost linearly as the temperature is increased

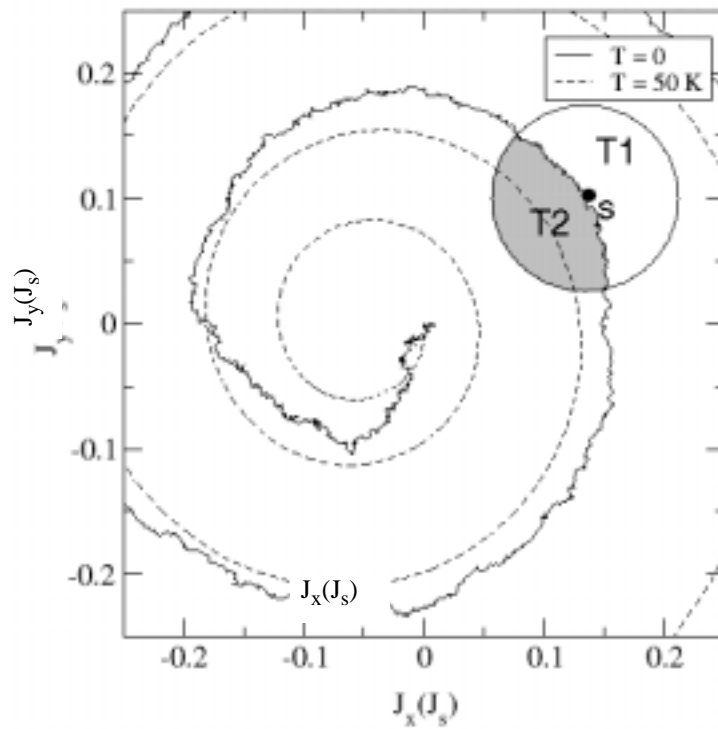


Figure 3.17: Comparison of the path of one magnetic moment at $T=0$ and $T=50\text{K}$. The projections of the time-evolution of the magnetic moment onto a plane perpendicular to the anisotropy axis. The external field of $H_{\text{ext}} = 1.5 (2K_1/J_s)$ is applied 1° off the easy axis.

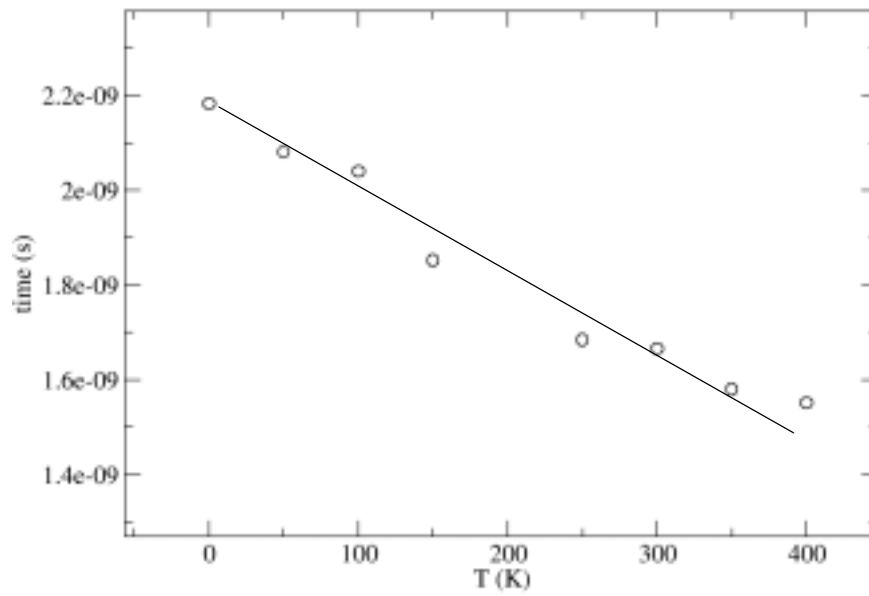


Figure 3.18: The switching time of a single magnetic moment for different temperatures. The angle between the external field ($H_{\text{ext}} = 1.5 \times 2K_1/J_s$) and the uniaxial easy axis $\beta = 1^\circ$.

3.5 Conclusions

For Co-Cr as perpendicular recording media the thermal stability increases with larger film thickness. However for films thicker than $l_c=30$ nm the thermal stability does not increase further with layer thickness. The reason is that for $l_c>30$ nm the most probable reversal mode is nucleation. For nucleation the energy barrier does not change with film thickness. The transition from homogeneous rotation to nucleation with increasing column length does not occur at a critical value of the column length. The reversal process becomes steadily more inhomogeneous as the column length is increased. The transition from homogeneous rotation to nucleation is shifted to smaller column lengths as the damping constant is reduced. That implies that the reversal mode changes as the value of the damping constant is changed.

Langevin dynamics simulations showed that the thermally activated switching process changes with the strength of the external field. Without external field the switching process is more inhomogeneous than with an external field that helps to reverse the particle.

The numerical solution of the LLG equation shows that fast switching is possible at low external field. The switching time decreases with smaller magnitude of the external field if the field is smaller than a critical value. This fast switching occurs for quasi-uniform rotation of the magnetization in small particles with small damping constant and at low fields. Non-uniform demagnetizing fields of irregular particles and thermal fluctuation does not significantly change the field dependence of the switched time. With increasing temperature the switching time decreases linearly. Fast switching modes are possible if the rise time of the external field is shorter than the relaxation of the magnetization towards the local minimum close to the initial state. Then the external field, which has to be small enough to create a complex energy landscape, drives the magnetization far away from its initial state at nearby constant energy. The large angle between the effective field and the magnetization creates a large torque which reduces the switching time.

References

- [1] A. Aharoni, "Introduction to the Theory of Ferromagnetism", Clarendon Press Oxford, 1996.
- [2] D. V. Berkov, "Numerical calculation of the energy barrier distribution in disordered many-particle systems: the path integral method," *J. Magn. Magn. Mater.*, vol. 186, pp. 199, 1998.
- [3] H. B. Braun, "Nucleation in ferromagnetic nanowires-magnetostatics and topology," *J. Appl. Phys.*, vol. 85, pp. 6172-6174, Apr. 1999.
- [4] W. F. Brown Jr., *Micromagnetics*. New York: Wiley, 1963.
- [5] P. N. Brown and A. C. Hindmarsh, "Reduced Storage Matrix Methods in Stiff ODE Systems," *J. Appl. Math. Comp.*, vol. 31, pp. 40, 1989.
- [6] C. J. Cerjan and W. H. Miller, "On finding transition states," *J. Chem. Phys.*, vol. 75, pp. 2800, 1981.
- [7] R. Dittrich, T. Schrefl, D. Suess, W. Schoz, H. Forster, J. Fidler, "A path method for finding energy barriers and minimum energy paths in complex micromagnetic systems," *J. Magn. Magn. Mater.*, in press.
- [8] D. R. Fredkin and T.R. Koehler, "Hybrid method for computing demagnetizing fields," *IEEE Trans. Magn.*, vol. 26, pp. 415, 1990.
- [9] T. L. Gilbert, *Phys. Rev.*, "A Lagrangian Formulation of the Gyromagnetic Equation of the Magnetization Field," vol. 100, pp. 1243, 1955.
- [10] R. H. Koch, J. G. Deak, D. W. Abraham, P. L. Trouilloud, R. A. Altman, Y. Lu, W. J. Gallagher, R. E. Scheuerlein, K. P. Roche, and S. S. P. Parkin, *Phys. Rev. Lett.*, 81 (1998) 4512.
- [11] L.P. E. Kloeden and E. Platen, *Numerical Solution of Stochastic Differential Equations*. Berlin, Heidelberg: Springer, 1995.
- [12] R. Kikuchi, "On the minimum of magnetization reversal time" *J. Appl. Phys.*, vol. 27, pp. 1452, 1956.
- [13] L. He and Doyle, "A theoretical description of magnetic switching experiments in picosecond field pulses," *J. Appl. Phys.*, vol. 79, pp. 6489, 1996.
- [14] L. He, W. D. Doyle, L. Varga, H. Fujiwara, P.J. Flanders, "High-speed switching in magnetic recording media," *J. Magn. Magn. Mater.*, vol. 155, pp. 6, 1996.
- [15] G. Henkelman and H. Jónsson, "Improved tangent estimate in the nudged elastic band method for finding minimum energy paths and saddle points" *J. Chem. Phys.*, vol. 113, pp. 9978, 2000.
- [16] J. C. Mallinson, "On damped gyro-magnetic precession," *IEEE Trans. Magn.*, vol. 23, pp. 2003, 1981.

- [17] J.C. Mallinson, "Damped gyromagnetic switching," *IEEE Trans. Magn.*, vol. 36, pp. 1976, 2000.
- [18] G. Mills and H. Jónson, "Quantum and thermal effects in H₂ dissociative adsorption: evaluation of free energy barriers in multidimensional quantum systems," *Phys. Rev. Letters*, vol. 72, pp. 1124, 1994.
- [19] L. Néel, "Influence des fluctuations thermiques sur l'aimantation de grains ferromagnétique très fins," *Compt. Rend., Acad. Sci. Paris*, vol. 228, pp. 664, 1949.
- [20] W. Quapp, "A gradient-only algorithm for tracing a reaction path uphill to the saddle of a potential energy surface", *Chem. Phys. Lett.*, vol. 253, pp. 286, 1996.
- [21] H. J. Richter, "Recent advances in the recording physics of thin-film media," *J. Phys. D: Appl. Phys.*, vol. 32, pp. 147, 1999.
- [22] Y. Saad; M.H. Schultz, *SIAM J. Sci. Stat. Comp*, 7 (1986) 856.
- [23] W. Scholz, T. Schrefl and J. Fidler, "Micromagnetic simulation of thermally activated switching in fine particles," *J. Magn. Magn. Mat.*, vol. 233, pp. 296, 2001.
- [24] D. Spisák and J. Hafner, "Frustrated exchange interaction at the interface of antiferromagnetic films with ferromagnetic substrates," *Phys. Rev. B*, vol. 168, pp. 257 - 268, 1997.
- [25] D. Spisák and J. Hafner, "Theory of bilinear and biquadratic exchange interactions in iron: bulk and surface," *J. Magn. Magn. Mat.*, vol. 168, pp. 257 - 268, 1997.
- [26] R. Street and J. C. Woolley, "A study on magnetic viscosity," *Proc. R. Soc. A*, vol. 62, pp. 562, 1949.
- [27] D. Suess, T. Schrefl, and J. Fidler, "Reversal modes, thermal stability and exchange length in perpendicular recording media," *IEEE Trans. Magn.*, vol. 36, pp. 1664, 2001.
- [28] D. Weller and A. Moser, "Thermal effect limits in ultrahigh-density magnetic recording," *IEEE Trans. Magn.*, vol. 35, pp 4423, 1999.

4

MAGNETIC REVERSAL PROCESSES IN FE-PT NANOPARTICLE ARRAYS

Magnetic measurements on arrays of chemically synthesized FePt nanoparticles show J_r/J_s ratios of 0.6 which is greater than that predicted for a series of non-interacting Stoner-Wohlfarth particles. The samples also display a high component of reversible magnetization and open recoil loops, all of which are reminiscent of exchange coupling between particles or grains. However, the particles in the arrays are well separated and so micromagnetic modeling was performed in order to understand the source of these interactions. It was found that when assuming no exchange coupling between nanoparticles the experimental behavior could only be replicated within the micromagnetic model when inhomogeneous magnetization occurred within the FePt Nanoparticles. This occurred only when there were both multiple c-axes within the FePt nanoparticles and a reduction of the exchange stiffness A compared to literature values of bulk FePt.

4.1 Introduction

Small magnetic particles are the basic structural units of magnetic recording media. To achieve a high storage density and obtain a high thermal stability a small particle size and high magneto-crystalline anisotropy are required. Recently, Sun and coworkers [9,10] fabricated monodisperse FePt nanoparticles. The particles were chemically synthesized with various compositions and sizes. The particles selfassemble into a three-dimensional superlattice when deposited onto a suitably prepared substrate. The particles can be made with sizes varying from 3 to 10 nm with very narrow size range distributions. The magneto-crystalline anisotropy of the particles after annealing was found to be of the order of 10^6 J/m³. The large anisotropy, the small particle size, and the high packing fraction make self assembled FePt superlattices an ideal candidate for future high-density information storage media with an areal density in the Tb/in² regime.

In section 4.2 magnetic measurements on FePt particles are presented. In section 4.3 micro-

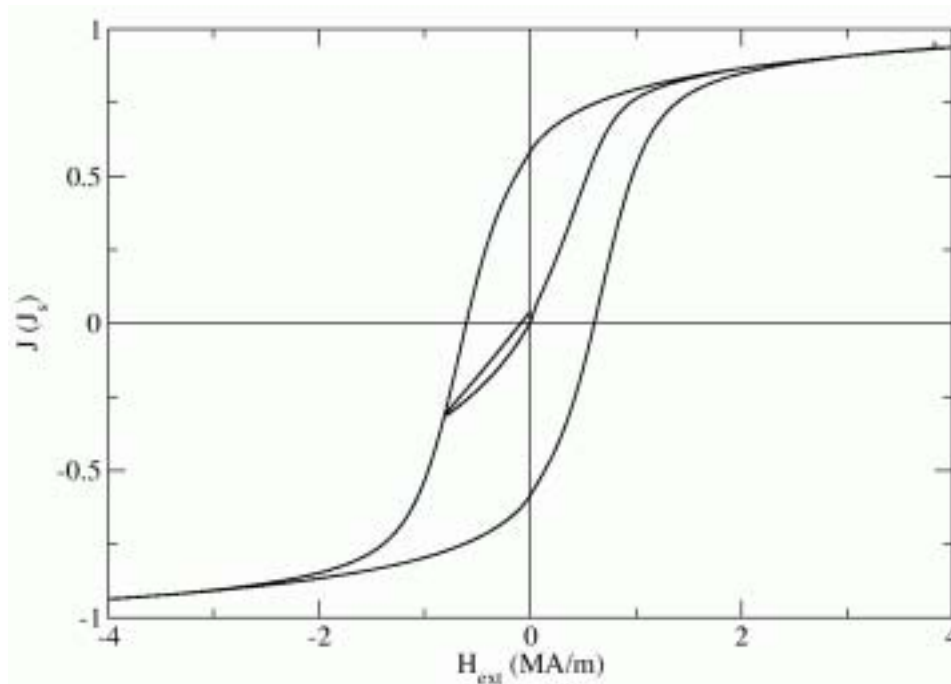


Figure 4.1: Hysteresis loop, recoil curve and recoil loop for FePt nanoparticle array at 290 K.

magnetic simulations of magnetization processes of a three dimensional matrix of FePt nanoparticles are performed.

4.2 Experimental data

Figure 4.1 shows a hysteresis loop, recoil curve and recoil loop taken at 290 K for monodisperse FePt nanoparticles [8]. The samples were prepared in accordance with the method outlined in [9,10]. The composition of the FePt nanoparticles was $\text{Fe}_{56}\text{Pt}_{44}$, with a particle diameter of 4 nm. A solution containing the monodisperse FePt nanoparticles was allowed to evaporate and the subsequent powder heat-treated at 560°C for 30 minutes.

The value of J_s for the FePt nanoparticles was 1.31 T. The literature value for bulk FePt is approximately 1.44 T [12]. The J_r/J_s ratio (J_s measured in a field of 9.5 MA/m) is 0.6 and the coercivity is around 0.6 MA/m. The recoil curve shows a high reversible component whilst the recoil loop is open. These effects and the high J_r/J_s ratio are often associated with the presence of exchange coupling between particles or grains [5]. However, the TEM work of Sun et al [9] suggests that the nanoparticles are well separated by a carbonaceous matrix. It

seems unlikely that there would be exchange coupling across the carbonaceous material, which separates the nanoparticles at room temperature and so the source of these exchange interactions is unknown.

In order to elucidate the magnetic behaviour, we have performed a series of micromagnetic calculations, based on the assumption of well-separated particles, from which we have explored other possible explanations for the observed magnetic properties

4.3 Micromagnetic simulations of the hysteresis loop

To simulate the hysteresis loop and the reversal process for FePt nanoparticles we have applied a micromagnetic approach. In this modeling we have assumed that the particles are isolated and only coupled to each other by dipolar interactions. The hysteresis loops are obtained by solving the Landau-Lifshitz-Gilbert equation for different external fields around the loop. For each field the LLG equation is integrated using a BDF formula [4]. When a steady state is reached, the field is stepped to the next value of the external field. We define our system to be in a steady state if the change of the normalized magnetization divided by the time step, $|\mathbf{du}/dt|$, becomes smaller than 10^{-4} on every node.

4.3.1 Single c-axis

Figure 4.2 shows the arrangement of the FePt nanoparticles we have used for our simulations. The particles form a cubic array. The diameter of the particles is 4 nm and the space between nearest neighbors is 2 nm. The intrinsic properties of the FePt spheres are $A = 10.8 \times 10^{-12}$ J/m [1], $J_s = 1.31$ T and $K_1 = 5.9 \times 10^6$ J/m³ [9]. One uniaxial easy axis is assigned to each FePt particle. The direction of the easy axis is randomly oriented over all the particles. The average mesh size is about 0.5 nm, which leads to about 65000 finite elements for the whole model.

The configuration shown in figure 4.2 (a) and (b) are the stable states for remanence ($H_{\text{ext}} = 0$) and for a point just past coercivity ($H_{\text{ext}} = 4.8$ MA/m), respectively. The normalized z -component of the magnetic polarization is grayscale-coded.

Figure 4.3 shows the hysteresis loop and a recoil curve for this FePt-array. The calculated hysteresis loop is very similar to that of an ensemble of non-interacting uniaxial particles with random orientation of the easy axes. In agreement with the predictions of the model of

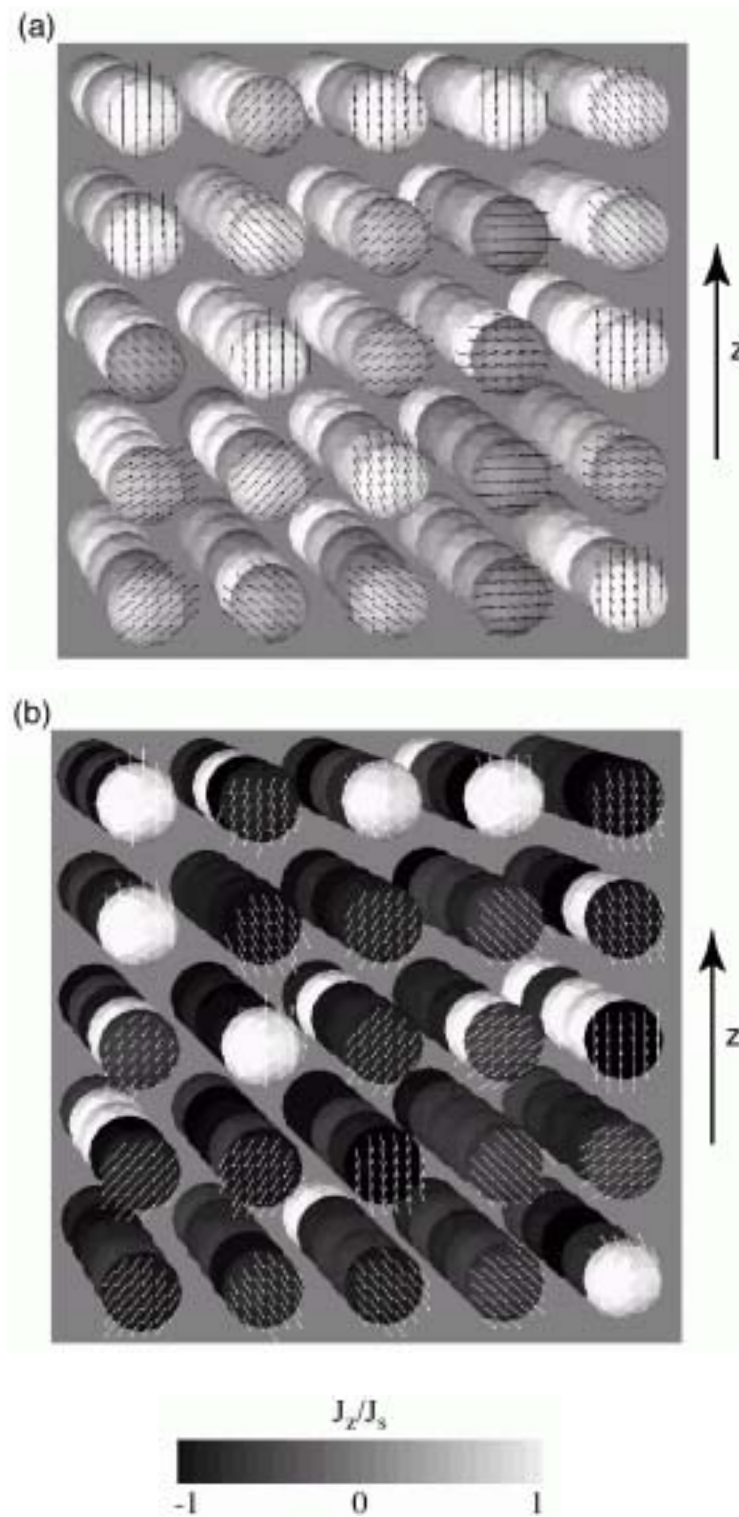


Figure 4.2: Micromagnetic modeling of the transient states during reversal. Every FePt particle has one easy axis, randomly orientation. The images (a) and (b) correspond to states marked in figure 4.3.

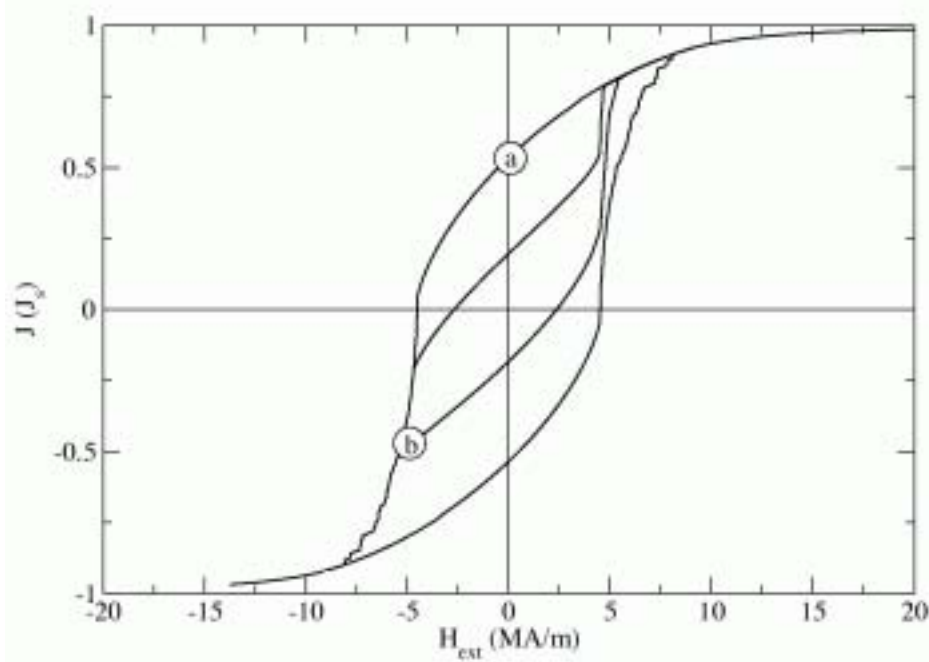


Figure 4.3: Hysteresis loop and recoil curve obtained from micromagnetic modeling of an array of FePt particles with a single easy axis orientated at random.

non-interacting single domain particles the hysteresis loop in figure 4.3 has a remanence of $J_r/J_s = 0.5$ and a coercivity of $0.48 H_A$, where H_A is the anisotropy field [7].

In order to prove that the stray field interactions between the FePt particles are negligible we have performed two sets of hysteresis loop calculations, with and without the calculation of stray field interaction. The hysteresis loops are almost the same and the coercive fields differ by less than 0.05%. It appears therefore that the stray field interaction between the FePt particles does not significantly influence the switching process.

If the results according to this simple model are compared with the earlier experiments significant differences can be found.

- The coercive field of the computer simulations (4.3 MA/m) is about 8 times larger than the experimentally measured values (0.6 MA/m).
- The model does not lead to the measured remanence enhancement of $J_r/J_s = 0.6$
- The slope of the recoil curve in figure 4.3 is much smaller than those observed in the experiment (figure 4.1)

4.3.2 Multiple c-axis

In order to obtain a better agreement with the experimental results we have assumed that the nanoparticles may consist of three independent c-axes oriented at 90° to each other. Such a distribution of the c-axis has been observed in a slightly different system by Bian et al. [2]. HREM images show an ordered $L1_0$ FePt nanoparticle, with a diameter of $\sim 6-8$ nm, in a $\alpha\text{-Al}_2\text{O}_3$ matrix with three different c-axes within the nanoparticle. Other complex FePt nanoparticles have also been observed by Watanabe et al. [9]. The multiple c-axes within a single nanoparticle are orthogonal to each other because of the transformation between the face centered cubic A1 phase and the tetragonal $L1_0$ phase. Where the c-axis in the $L1_0$ phase is along one of the $\langle 100 \rangle$ directions in the face centered cubic structure [11]. Other complex states within a nanoparticle including surface anisotropies are possible but may be better modeled using alternative techniques.

To consider multiple c-axes within each nanoparticle we subdivide every sphere into 8 octants ($o_{k,i}$). For every sphere (k), three orthogonal directions (a_k, b_k, c_k) are calculated, however the orientation of this triple is chosen at random. To every octant $o_{k,i}$ one of the axes a_k, b_k or c_k is assigned randomly. Figure 4.4 shows the distribution of the c-axes for one FePt

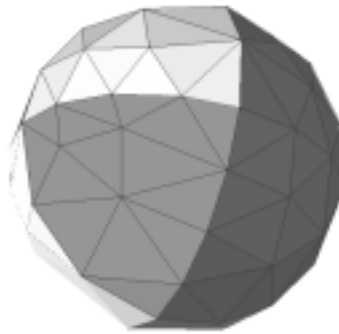


Figure 4.4: One possible distribution of the c-axes within one FePt particle. The different grey tones correspond to regions with different c-axes orientations.

particle. The different grey tones show different directions of the c-axes within each octant.

The hysteresis loop and recoil loop for a set of particles with multiple c-axes is given in figure 4.5. The coercive field decreases by a factor of 9 as compared to the model with only one easy axis within each particle. The relative slope of the initial part of the recoil loop is margin-

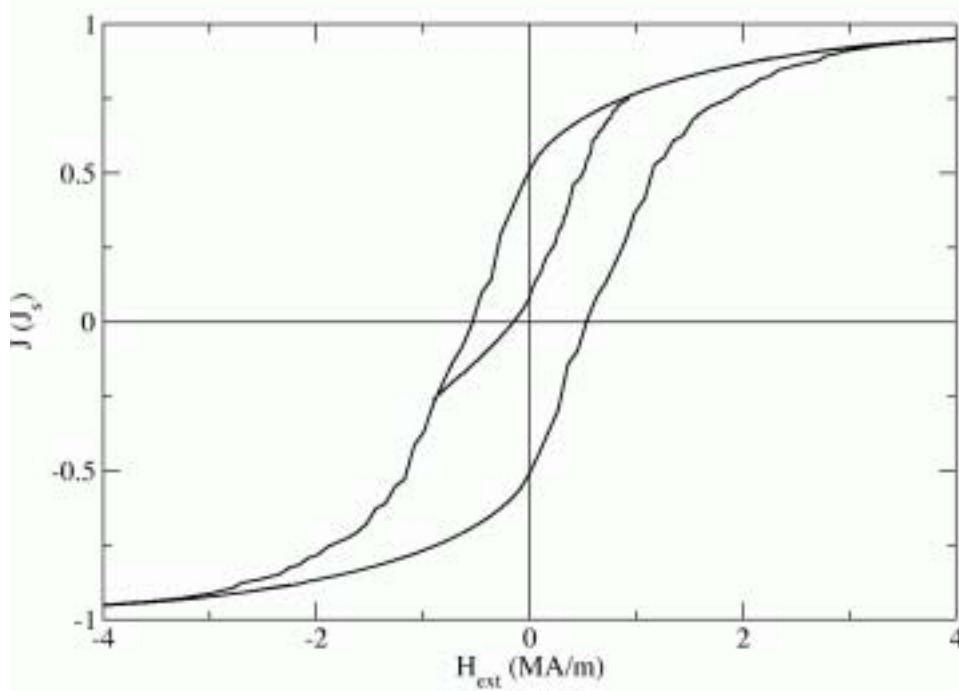


Figure 4.5: Hysteresis loop and recoil curve obtained from micromagnetic modeling of an array of FePt particles with multiple c-axes within each particle.

ally higher than the single c-axis model, shown in figure 4.3, but still well below that observed experimentally. The magnetization reverses coherently at all stages of the reversal process so that the distribution of magnetization in the model looks exactly the same as seen in figure 4.2 for the case of a single c-axis per particle. There is no remanence enhancement using an exchange stiffness, $A = 10.8 \cdot 10^{-12}$ J/m, and the FePt superlattice behaves like a Stoner-Wohlfarth system, but with a reduced effective anisotropy.

If the magnetization within each particle remains homogenous all the time, the anisotropy energy for one particle can be expressed as,

$$E_{tot} = E_o - K_1 \sum_{i=1}^3 (\mathbf{u}_i \cdot \mathbf{k}_i)^2 V_i \quad (4.1)$$

where \mathbf{u}_i and \mathbf{k}_i are the unit vectors of the magnetization and the easy axis in the region i , respectively. If the directions of \mathbf{k} are orthogonal in the three regions within one particle (e.g. $\mathbf{k}_1=(1,0,0)$, $\mathbf{k}_2=(0,1,0)$ and $\mathbf{k}_3=(0,0,1)$), equation (4.1) becomes

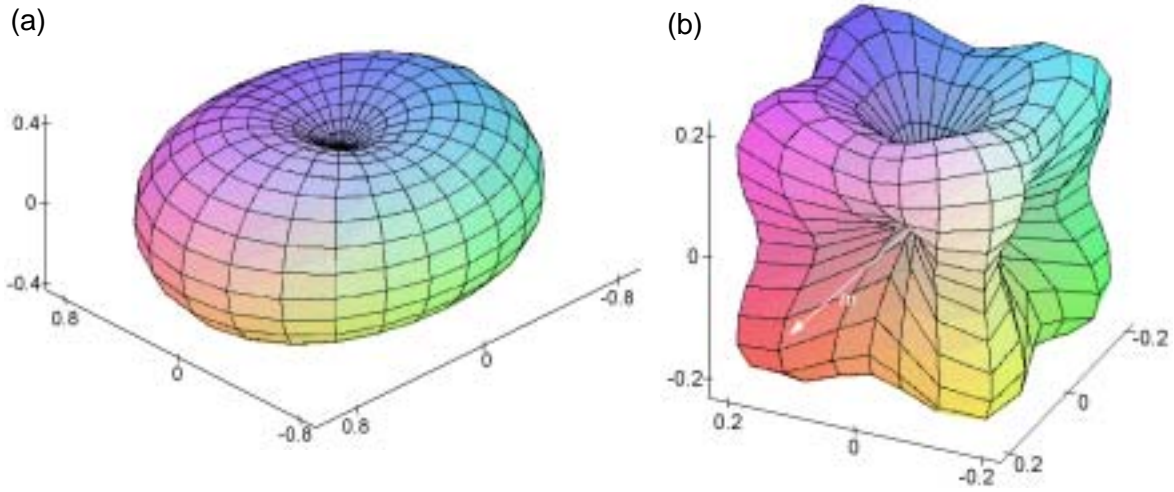


Figure 4.6: Energy density plots of the crystalline anisotropy in arbitrary units. The left image (a) shows the crystalline anisotropy energy density for the case that three orthogonal c-axes occur within one grain. The right picture (b) shows the energy density for cubic anisotropy.

$$E_{tot} = E_o - K_1(V_1u_x^2 + V_2u_y^2 + V_3u_z^2) \quad (4.2)$$

Figure 4.6. shows energy density surfaces. For every direction of the magnetization \mathbf{m} , the corresponding crystalline energy density is the distance from the origin to the point of the surface lying along the direction \mathbf{m} . Figure 4.6 (a) shows the energy surface for the case that the fractions of V_1 , V_2 and V_3 to the total volume are 5%, 20% and 70%, respectively. For comparison, figure 4.6 (b) shows the energy surface for a cubic anisotropy. Note if the three volumes are the same, no anisotropy occurs.

Even with the reduced effective anisotropy, which produces a coercivity of the same order as seen in the experimental system, the effect of the stray field interactions is small. The stray field interactions have little or no effect over loop shape and do not result in remanence enhancement. The variation of the coercivity with and without stray fields is less than 1 %.

4.3.3 Reduction in exchange stiffness

In order to produce remanence enhancement in the multiple c-axes nanoparticles we investigated the effect of changes in the exchange stiffness, A . With smaller exchange stiffness the

coercive field increases (Table 4.1) due to the formation of inhomogeneous states within one particle and remanence enhancement can be observed. It has been suggested that a reduction the exchange interactions in ultra fine particles can be caused by the lower coordination of near surface atoms [6].

Table 4.1 Coercive field and remanence obtained from micromagnetic modeling of an array of FePt particles with multiple c -axes for different values of exchange stiffness, A

A (J/m)	H_c (kA/m)	J_r/J_s
0.1×10^{-11}	1441	0.62
0.36×10^{-11}	901	0.58
1.08×10^{-11}	504	0.51

For zero exchange, there would be no coupling between the regions with different easy axes. The coercive field would increase to that of non-interacting Stoner-Wohlfarth particles.

In the case of strong coupling, the magnetization within one nanoparticle remains homogeneous looking similar to figure 4.2 but with a reduced effective anisotropy. The effective anisotropy of the particle, as mentioned above, is related to the volume fractions of the three orthogonal components, V_1 , V_2 and V_3 , and can be calculated according to equation (4.1). The effective anisotropy (Figure 4.6 (a)) is uniaxial but smaller in magnitude than the anisotropy of a particle with only one c -axis direction.

An array of FePt particles with multiple c -axes and a strong exchange coupling then behaves like an ensemble of non-interacting Stoner-Wohlfarth particles with a reduced anisotropy. As a consequence $J_r/J_s = 0.5$, and there is no observable remanence enhancement.

Remanence enhancement is only observed when the magnetization becomes inhomogeneous within one spherical FePt particle. This is observed when the exchange stiffness is reduced as shown in figure 4.7., where the exchange stiffness has been reduced to $A = 0.1 \times 10^{-11}$ J/m. At zero external field the magnetization tends to point parallel to the different easy axes within one nanoparticle, but the exchange coupling between regions with different easy axes results in deviations of the magnetization from the easy direction and the production of remanence enhancement. As well as displaying remanence enhancement the multiple c -axis model with reduced exchange stiffness also shows steeper recoil curves (Figure 4.8.), which are similar to those seen in the experimental system.

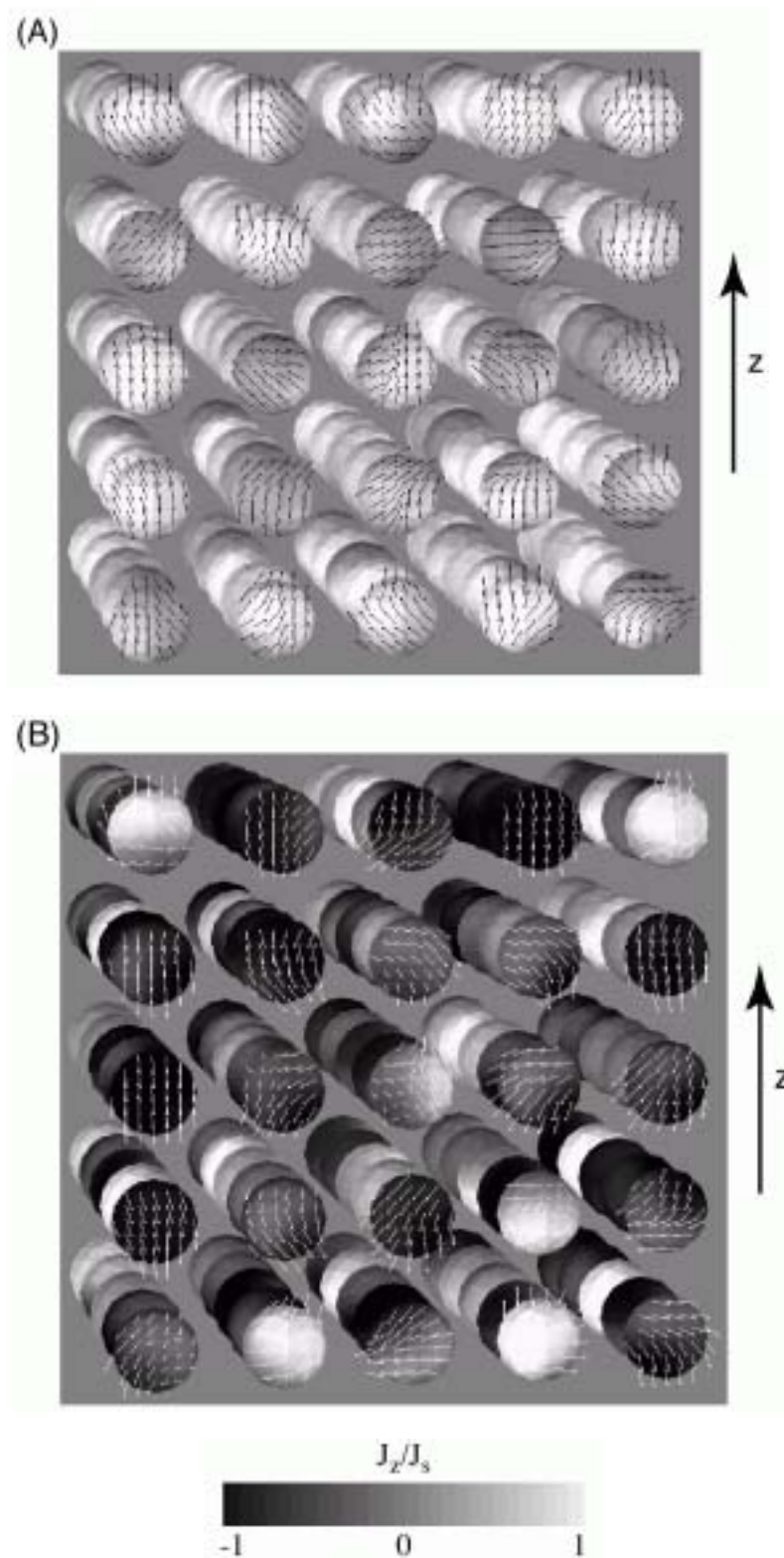


Figure 4.7: Micromagnetic modeling of the transient states during reversal. Every FePt particle has multiple orthogonal c-axes, randomly oriented. The images (A) and (B) correspond to applied fields and magnetization marked in figure 4.4.

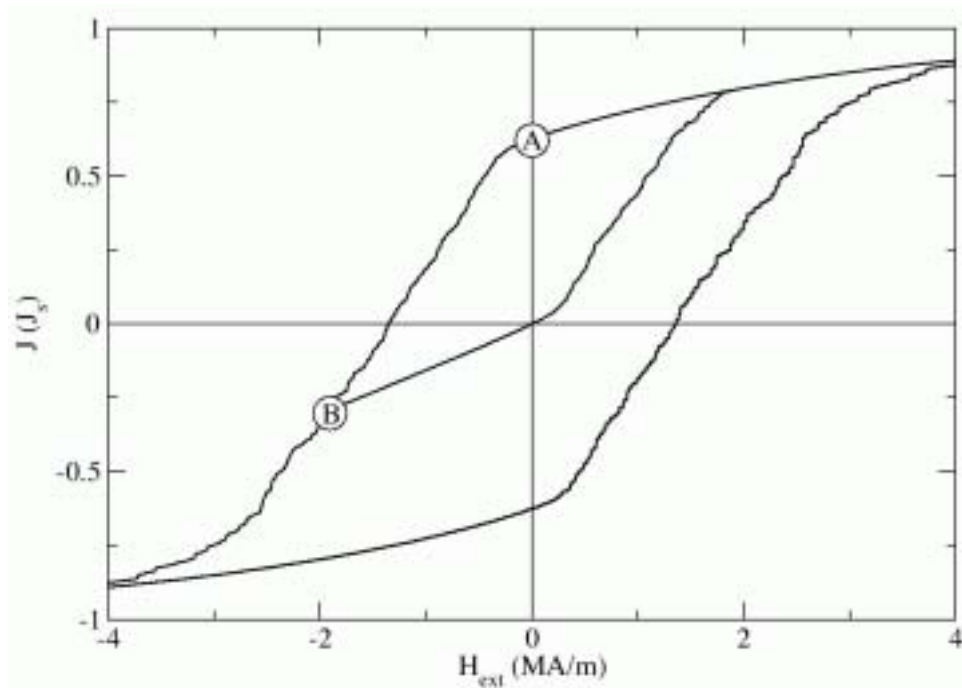


Figure 4.8: Hysteresis loops and recoil curve obtained from micromagnetic modeling of an array of FePt particles with multiple c -axes within each particle exchange stiffness $A = 0.1 \times 10^{-11}$ J/m.

Again, reference calculations without any magnetostatic simulations lead to only small variations in the coercivity with the general shape of the hysteresis loop and recoil curve are essentially unchanged. Thus, it can be concluded that the remanence enhancement and steep recoil behavior observed in the simulations as well as in the experiments are solely due to inhomogeneous magnetization processes within the FePt nanoparticles.

4.4 Conclusions

Experimental observations of FePt nanoparticles arrays show remanence enhancement and reversible magnetization behavior reminiscent of materials with significant exchange coupling between magnetic grains. The modeling results presented here show that magnetostatic interactions have very little effect on the magnetization behavior of the nanoparticle arrays. Assuming that the particles have not agglomerated or are in some other way exchange coupled together the modeling shows that remanence enhancement and reversible magnetization behavior was only reproduced when the magnetization within the FePt nanoparticles was inhomogeneous. To achieve inhomogeneous reversal of the magnetization within the FePt nanoparticle model both multiple c-axes within a nanoparticle and reduced exchange stiffness in comparison to literature values for FePt bulk alloys are required. The coercivity calculated for these particles, which reverse inhomogeneously, was similar to that observed experimentally.

REFERENCES

- [1] Estimated from the Curie temperature and published values of A in CoPt in "Permanent Magnetism" R. Skomski and J. M. D. Coey, IOP Publishing, Bristol 1999.
- [2] B. Bian, K. Sato, Y. Hirotsu, A. Makino, "Ordering of island-like FePt crystallites with orientations", *Appl. Phys. Lett.*, vol. 75, pp. 1999, 3686. and magnetic properties of FePt–Al–O granular thin films" *Appl. Phys.*
- [3] D. R. Fredkin, T. R. Koehler, "Hybrid method for computing demagnetizing fields" *IEEE Trans. Magn.*, vol. 26, pp. 415, 1990.
- [4] A. C. Hindmarsh, L. R. Petzold, "Algorithms and software for ordinary differential equations and differential-algebraic equations. II. Higherorder methods and software packages" *Computers in Physics*, vol. 9, pp. 148, 1995.
- [5] E. F. Kneller K Hawig, "The exchange-spring magnet: A new material principle for permanent magnets", *IEEE Trans. Magn.*, vol. 27, pp. 3588, 1991.
- [6] F.T. Parker, M.W. Foster, D.T. Margulies and A.E. Berkowitz, "Spin canting, surface magnetization, and finite-size effects in α -Fe₂O₃ particles", *Phys. Rev. B*, vol. 47, pp. 7885, 1993.
- [7] E. C. Stoner and E. P. Wohlfarth, "A mechanism of magnetic hysteresis in heterogeneous alloys", *Philos. Trans. R. Soc. London*, vol. A240, pp. 599, 1948.
- [8] D. Suess, T. Schrefl, J. Fidler, R. C. Woodward, T. G. St. Pierre, R. Street, S. Sun, C. Murray, L. Folds and B. Terris, "Reversal Processes in FePt Nanoparticle Arrays," submitted to *J. Magn. Magn. Mater.*
- [9] S. Sun, C. B. Murray, D. Weller, L. Folks, A. Moser, "Monodisperse FePt Nanoparticles and Ferromagnetic FePt Nanocrystal Superlattices", *Science*, vol. 287, pp. 1989, 2000.
- [10] S. Sun, E F Fullerton, D Weller CB Murray, "Compositionally controlled FePt nanoparticle materials", *IEEE Trans. Magn.*, vol. 37, pp. 1239, 2001.
- [11] Y. Tanaka, N. Kimura, K. Hono, K. Yasuda and T. Sakurai, "Microstructures and magnetic properties of Fe-Pt permanent magnets", *J. Magn. Magn. Mater.*, vol. 170, pp. 289, 1997.
- [12] N. I. Vlasova, G. S. Kandaurova, N. N. Shchegoleva, "Effect of polytwinned microstructure on the magnetic domain structure and hysteresis properties of the CoPt-type alloys", *J. Magn. Magn. Mater.*, vol. 222, pp. 138, 2000.
- [9] M. Watanabe, T. Masumoto, D. H. Ping, and K. Hono, *Microstructure Lett.*, vol. 76, pp. 3971, 2000.

5

HIGH COERCIVE PARTICLES

Micromagnetic simulations were performed to study magnetic reversal mechanism of $\text{Nd}_2\text{Fe}_{14}\text{B}$ particles. The simulations are compared with magnetization measurements on $\text{Nd}_2\text{Fe}_{14}\text{B}$ particles that are diluted in a Nd matrix. Experiments show that in the initial state a substantial proportion of grains contains domain walls. Micromagnetic simulations show that the single domain state is the lowest energy state. Thus it is concluded that thermal demagnetization does not drive the system into the global energy minimum, but rather the system remains in a local metastable energy minimum. Micromagnetic calculations showed that the state that is formed after annealing is not necessarily a single domain state. Once a domain wall within the grain is formed there is a significant energy barrier for the removal of the domain wall.

5.1 Introduction

The study of interaction effects in magnetic systems consisting of small particles is of interest from the point of view of using such systems as a probe of the fundamental physics of magnetic interactions as well as from the technological standpoint of understanding interacting fine particle systems such as magnetic recording media.

Experiments on $\text{Nd}_2\text{Fe}_{14}\text{B}$ particles diluted in a Nd-rich matrix were performed [1] to investigate how close the ideal non-interacting small particle limit, typified by the theory of Stoner and Wohlfarth [6], could be approached.

While behavior displaying all aspects of the ideal limit was not observed, the deviation from the idealized behavior in the sample of greatest dilution is explained with the aid of micromagnetic calculations. It was found that thermal demagnetization of the most dilute sample did not result in a global energy minimum state being reached, but rather a metastable equilibrium was established, separated from the global energy minimum by a significant energy barrier.

Room temperature hysteresis loops for the 4 samples, together with an idealized hysteresis loop for isotropic particles of $\text{Nd}_2\text{Fe}_{14}\text{B}$ reversing by coherent rotation, are shown in figure

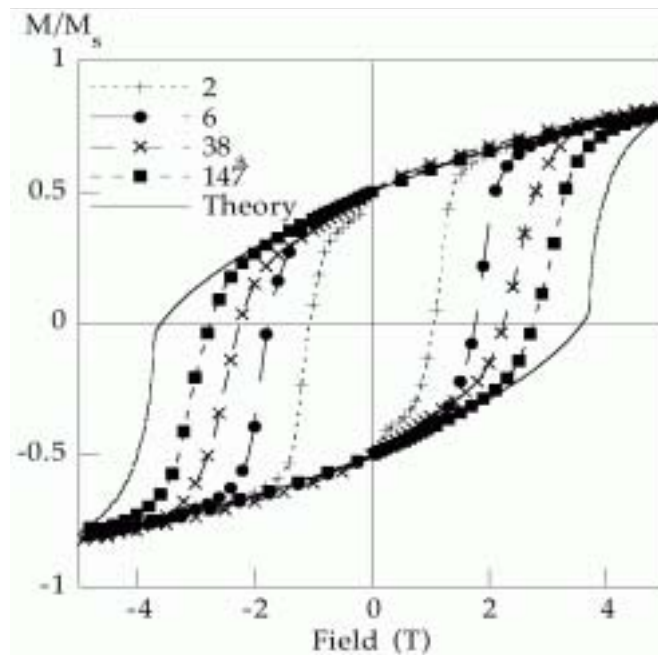


Figure 5.1: Hysteresis loops [1] at room temperature for four samples with different dilution are shown. The numbers 2, 6, 38 and 147 denotes the amount of Nd in $\text{Nd}_x\text{Fe}_{13.1}\text{B}$. With increasing number the dilution increases. The amount of Nd ranges from slightly Nd rich as compared with the stoichiometric composition to containing over 90% Nd atomically. The curve denoted with “theory” is obtained by assuming coherent rotation for the particles.

5.1. The idealized hysteresis loop assumes isolated particles and accounts only for the magneto-crystalline anisotropy, neglecting shape effects. It can be observed that as the degree of dilution increases, and the mean particle separation increases, the hysteresis loop approaches more closely that of idealized coherent rotation. However even in the most dilute sample the coercivity is some 0.8 T below that of idealized $\text{Nd}_2\text{Fe}_{14}\text{B}$ particles.

The initial magnetization curves for the samples, including the idealized curve for comparison, are shown in figure 5.2. On the initial magnetization curve the behavior of all the samples is very different to that of the idealized theory. The initial curves show a rapid increase in magnetization in low fields. For samples 2 and 6 these curves resemble those measured in melt-quenched NdFeB magnets [2] with 2 steps on the curve, associated with single and multi-domain grains reversing. For samples 38 and 147 the curves resemble those of sintered NdFeB [2] with a large low field step, although a small second high field step is also present.

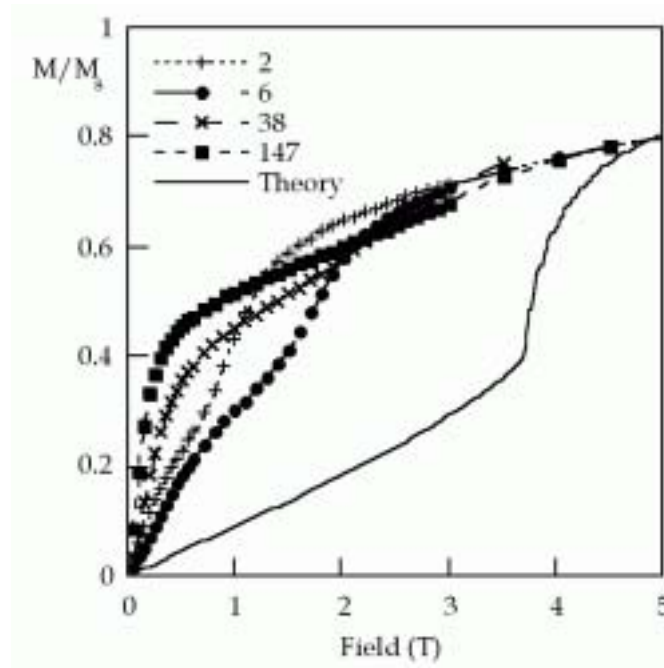


Figure 5.2: Initial magnetization curves at room temperature from the thermally demagnetized state of the samples shown in figure 1, along with the idealized theoretical Stoner-Wohlfarth curve for an isotropic ensemble of particles.

From small slope in the initial magnetization curves it can be determined that in all samples domain walls are present in at least some of the grains in the thermally demagnetized state.

Previous TEM work [4] has shown that for nearly single phase $\text{Nd}_2\text{Fe}_{14}\text{B}$ the grains are randomly oriented, polyhedral and with a size between 50 and 70 nm. However, sample 2 is expected to have a larger grain size because of the higher annealing temperature used, evidenced by the differing initial curve behavior measured. Higher Nd content promotes the growth of the $\text{Nd}_2\text{Fe}_{14}\text{B}$ grains into an elongated shape [4]. For the less dilute samples, 2 and 6, many grains are close to each other and intergranular contact at grain boundaries is common. For the more dilute samples, 38 and 147, the grains are elongated, of typical dimensions 100 x 40 x 25 nm with the easy axis parallel to the short side of the grain. The grains are still randomly oriented and most are isolated from neighboring grains by the Nd matrix, with only the occasional cluster of grains observed, less so in sample 147 than in sample 38.

These previous results on grain size and distribution suggest that the grains in the most dilute samples are too small to support domain walls in the thermally demagnetized state. Lorentz microscopy was performed [1] in a Philips CM200 FEG microscope using the

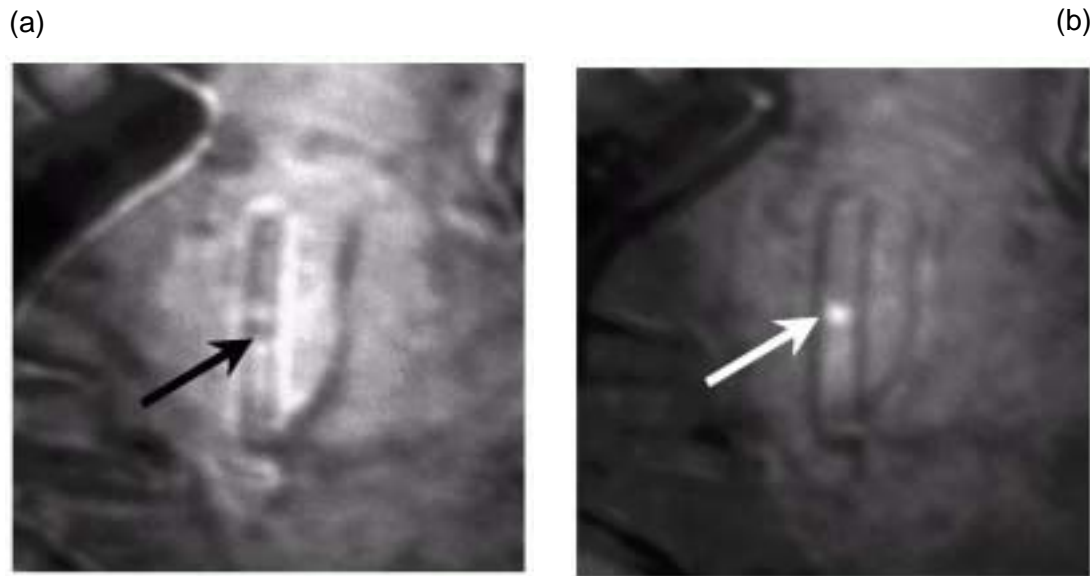


Figure 5.3: Lorentz TEM image, using the Fresnel imaging method, of a grain showing a domain wall within the grain in the thermally demagnetized condition (marked by the arrows). (a) Underfocussed image (b) Overfocussed image. Fresnel imaging involves slightly under or overfocussing the image to reveal magnetic domain wall contrast so the grain image is slightly blurred in both cases.

Fresnel imaging method to investigate the multi-domain structure deduced to be present on the initial curve of the most dilute samples. The imaging was performed with the objective lens switched off to minimize the magnetic field in the sample area. In order to obtain high magnification, a Gatan Imaging Filter (GIF) with a CCD camera was used instead of the objective lens. In figure 5.3 are shown Fresnel images of the multidomain structure of $\text{Nd}_2\text{Fe}_{14}\text{B}$ grains in sample 147. The domain wall is formed perpendicular to the longest side of the platelet like grain. Note that the domain wall width is less than 5 nm and is close to the resolution of the microscope. Despite this figure 5.3 clearly shows the multi-domain structure of these grains.

5.2 Calculation of the initial curve and coercivity

Micromagnetic simulations were performed to study the reversal process of one NdFeB grain. The following material parameters were used for the simulations: $A = 10^{-11}$ J/m, $J_s = 1.6$ T and $K_1 = 5.6 \times 10^6$ J/m³. The grain size was 100 x 40 x 25 nm. An easy axis parallel to the short axis (z-axis) of the particle was assumed. The process of reversal in the micromag-

netic model is shown in the series of micromagnetic states in figure 5.4. This figure is a time series of the reversal in a constant field and the states shown are not equilibrium states. In figure 5.4 an external field is applied in the $H_x = -1$, $H_y = 0$ and $H_z = -6$ direction. The time $t = 0$ is immediately after the field was increased from 4.787 T to 4.866 T, which is equal to the coercive field for this particle. Figure 5.4 shows the non-ideal nature of the reversal, with nucleation of a reverse domain occurring at the top and bottom surfaces of the particle. The reversal process is initiated by the stray field that is largest at the top and bottom surfaces of the particle. The reversal process is not coherent rotation although the single domain state, as shown in the following, is the lowest energy state in equilibrium.

The presence of domain walls on the initial magnetization curve for all samples is somewhat in contradiction to the small particle size observed by transmission electron microscopy [4]. In the less dilute samples, 2 and 6, the $\text{Nd}_2\text{Fe}_{14}\text{B}$ grains are between 50 and 70 nm in diameter. This is well below the single domain limit of 200 - 300 nm in $\text{Nd}_2\text{Fe}_{14}\text{B}$ [5,7]. However, similar to other fine-grained NdFeB magnets, domain walls can be supported across a number of grains because of the intergranular interactions which are present [3]. The domains which are formed in this way are known as interaction domains. For the most dilute samples, 38 and 147, strong intergranular interactions are absent and a different explanation is required for the observed presence of domain walls on the initial curve.

Using the micromagnetic model it is possible to calculate the energy of particles similar in size and shape to those in samples 38 and 147 with and without the presence of the domain wall. The magnetostatic energy of a particle without a domain wall is 53×10^{-18} J. While the presence of a domain wall in the configuration shown in figure 5.3 lowers this magnetostatic energy to 39×10^{-18} J the domain wall energy of 27 mJ/m^2 multiplied by the area gives a final total energy of 66×10^{-18} J, which is larger than that of a single domain particle. Thus the single domain state is the global minimum energy state. To remove a domain wall from a particle however requires overcoming an energy barrier resulting from the increase in magnetostatic energy as the wall is translated. This energy barrier can be estimated by the difference in magnetostatic energy between the two domain and single domain states of 14×10^{-18} J. This is equivalent to 3400 kT at room temperature, which means that a particle in the metastable state containing a domain wall is remarkably stable. At higher temperatures however this energy barrier drops sharply (e.g. the barrier is 900 kT at 500 K) because it scales with M_s^2 as well as the temperature.

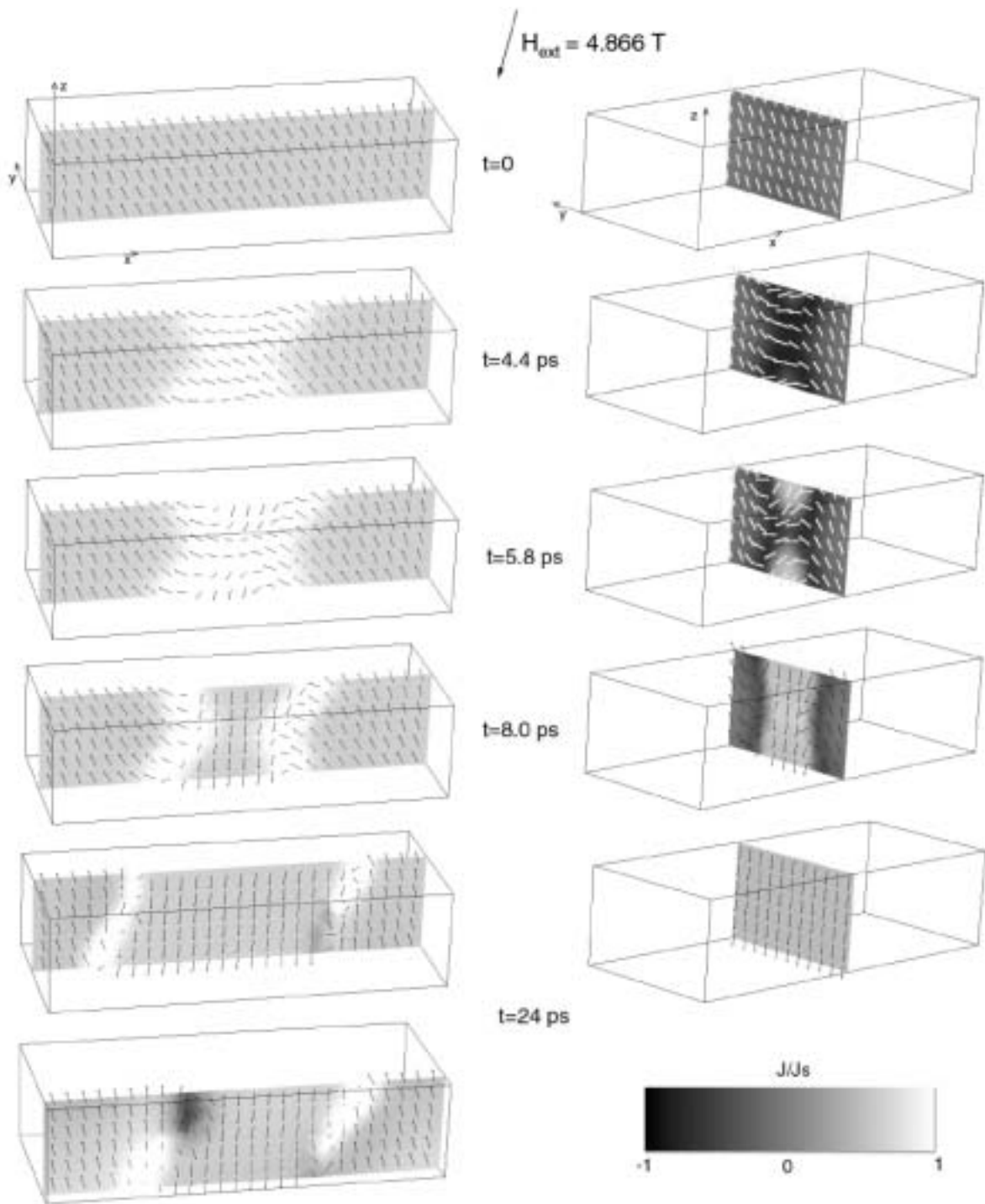


Figure 5.4: An external field is applied in the $H_x=-1$, $H_y=0$ and $H_z=-6$ direction. The two upper pictures show the magnetic polarization immediately after the field was increased from 4.787 T to 4.866 T, which is equal to the coercive field. The arrows show the projection of the magnetization onto the shaded plane. The perpendicular component of the magnetization is shaded according to the key at bottom right.

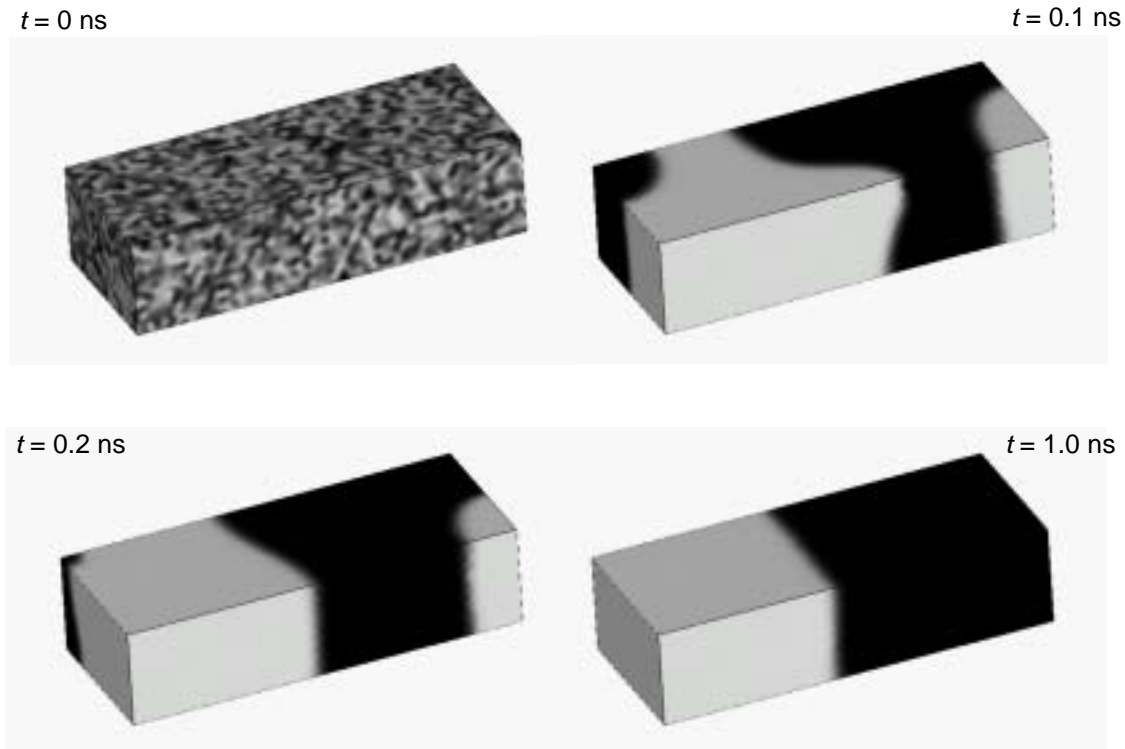


Figure 5.5: Four pictures of a simulation of the approach to a stable state. The micromagnetic elements are initially assigned a direction randomly and the system allowed to evolve until a stable state is reached. For this particular run a two domain state is found to be stable, even though a single domain state has a lower energy. The pictures correspond to the initial state and 0.1, 0.2 and 1 ns after commencing the simulation. The last picture is the stable state. The z -component of magnetization is shaded according to the key in figure 5.4

An estimate of the field stability of the two domain state can be made by calculating the field required such that the Zeeman energy is equivalent to the energy barrier. This results in a calculated stability field of 0.23 T, which is similar to the value found from applying successively larger fields to a two domain particle using the micromagnetic model.

To investigate the likelihood of the multi-domain state arising during cooling from the Curie temperature, a simulated annealing procedure was undertaken using the three dimensional micromagnetic model in which the micromagnetic elements were initially assigned direction randomly and the system allowed to evolve to a stable configuration. The evolution of the magnetization configuration for one such run is shown in figure 5.5. From the result of 20 simulated runs it was determined that the single domain state was reached in only 35% of the simulations. The rest of the simulations (65%) became stable in a multi-domain state, with the vast majority being a two domain state (50%) although some 3 (10%) and 4 (5%) domain

configurations were also found. The proportion of single domain states observed from the simulation is higher than that seen on the initial magnetization curve, but this is a result of allowing the system to come to stable configuration in the simulation using room temperature material properties rather than using a true simulated cooling from the Curie Temperature. The energy barrier between the single domain and multi-domain states is much higher at room temperature than at higher temperatures and thus using room temperature properties in the simulation will more favorably predispose the system to stabilize in the single domain state compared with the experimental cooling regimen.

5.3 Conclusions

Thermal demagnetization of magnetic samples does not guarantee that the system is in a global energy minimum state. This has implications on the interpretation of initial magnetization curves because the system may be in a metastable state, rather than a global minimum of energy. Micromagnetic calculations revealed a significant energy barrier for the removal of a domain wall within the grain once it is formed.

References

- [1] D.C. Crew, E. Girt, D. Suess, T. Schrefl, K.M. Krishnan, G. Thomas and M. Guilot, "The effect of magnetic interactions between grains on reversal behavior in diluted $\text{Nd}_2\text{Fe}_{14}\text{B}$," Phys. Rev. B, submitted.
- [2] D.C. Crew, P.G. McCormick and R. Street, "An investigation of reversible magnetization in NdFeB ," J. Appl. Phys., vol. 86, pp. 3278, 1999.
- [3] D.C. Crew and L.H. Lewis, "Effect of grain alignment on magnetic structure in nanoscale material," IEEE Trans. Magn, vol. 37, pp. 2512, 2001.
- [4] Er. Girt, K.M. Krishnan, G. Thomas, E. Girt and Z. Altounian, "Coercivity limits and mechanism in nanocomposite Nd_Fe_B alloys," J. Magn. Magn. Mater., vol. 231, pp. 219, 2001.
- [5] L. Néel, C. R. Acad. Sci. Paris, vol. 224, pp. 1550, 1947.
- [6] E.C. Stoner and E.P. Wohlfarth, "A mechanism of magnetic hysteresis in heterogeneous alloys," Phil. Trans. Roy. Soc., vol. 240A, pp. 599, 1948
- [7] E.P. Wohlfarth, Proc Roy Soc, vol. A 232, pp. 208, 1955.

6

MAGNETIC NANODOTS

The demagnetizing process of isotropic, single crystal magnetic cylinders ("nanodots") was studied using finite element micromagnetic simulations. The exchange energy was used as a measure for the degree of disorder during the demagnetizing process. The reversal process strongly depends on the thickness of the circular nanomagnet which was varied from 6 nm to 15 nm. The reversal mode changes from uniform rotation to an inhomogeneous reversal process when the diameter is increased from 27.5 nm to 275 nm. Vortex nucleation occurs for nanodots with a diameter greater than 165 nm and a thickness of 15 nm.

For an array of interacting nanodots magnetic interactions lead to non-uniformity during reversal, that limits the switching time of magnetic logic gates.

6.1 Introduction

Circular nanomagnets may be the basic structural units of magnetic sensors and magneto-electronic devices [6,1]. The reversal process of the magnetic nanodots is of importance for applications as the switching field and the reversal time may depend on the specific way the magnetization reverses. Cowburn and co-workers [2] investigated the hysteresis properties of circular nanomagnets as a function of diameter and thickness using magneto-optical magnetometry. If measured parallel to the uniaxial anisotropy axis they find two types of hysteresis loops. Square hysteresis loops, which indicate uniform rotation, occur for samples with a diameter of 100 nm and a thickness of 15 nm to samples with a diameter of 300 nm and a thickness of 6 nm. Wider and thicker samples show a drop of the magnetization at a critical field which is induced by the formation of a vortex. Kirk and co-workers [4] showed that the presence of vortices significantly lowers the switching field of rectangular NiFe elements. The influence of magnetostatic interactions on the hysteresis of an array of circular nanomagnets was demonstrated in [1]. A reduction of the lattice spacing gives rise to shape anisotropy which increases the coercivity measured parallel to the long axis of the chain.

In section 6.2 the switching process of isolated circular nanomagnets is investigated. The results provide details of the magnetization distribution during irreversible switching. Section 6.3 deals with interacting magnetic nanoelement that may be used as logic gates.

6.2 Reversal modes for a single dot

To investigate the reversal process of an isolated magnetic nanoelement the particle is discretized using the finite element method. Figure 6.1 shows the finite element mesh at the sur-

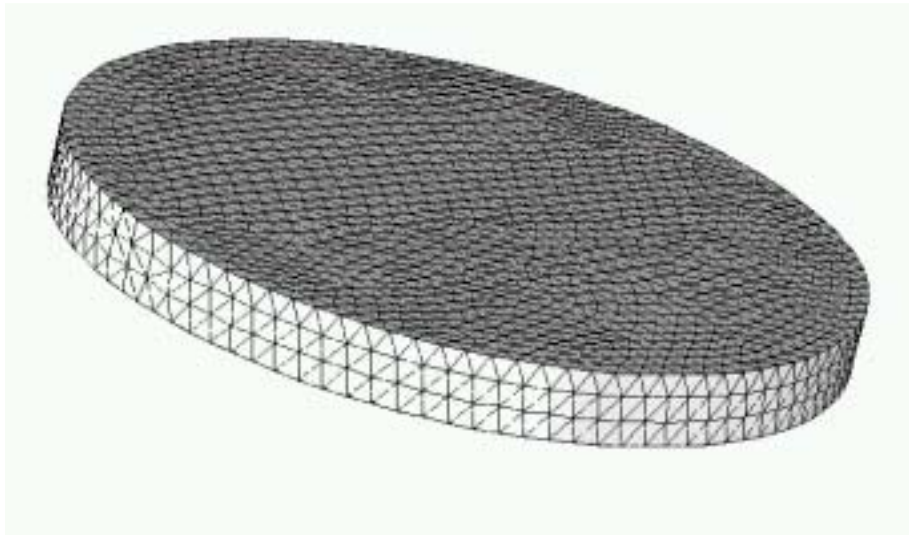


Figure 6.1: Finite element model of one circular nanodot. The triangles show the surface mesh used for the boundary element method.

face of one nanodot. The mesh size is 5 nm, which corresponds to the exchange length of NiFe ($J_s = 1$ T, $A = 10$ pJ/m). The diameter of the dot was varied in computer simulations from 27.5 nm to 275 nm, the thickness from 6 nm to 15 nm. In the initial state, the nanodot is completely magnetized in the positive x -direction, which is the direction of the external field. To obtain the remanent state the external field is reduced step by step until zero. After each step the LLG equation is integrated. The external field is decreased when equilibrium is reached. We define our system to be in equilibrium if the change of the normalized magnetization divided by the time step, $|\mathbf{d}\mathbf{u}/dt|$, becomes smaller than 10^{-4} on every node. The magnetization reversal process was investigated using the magnetization distribution for zero applied field as the initial state. An external field of $H_{\text{ext}} = -8$ kA/m is applied instantaneously to the remanent state.

Figure 6.2 shows transient states during reversal for different sizes of the magnetic nanodot. A damping constant $\alpha = 1$ was used. The left dot has a diameter of 55 nm and a thickness of 10 nm. For this small volume of the particle the reversal process is homogeneous rotation. The middle dot shows the reversal process of a dot with $d = 110$ nm and a thickness

of 10 nm. To reduce magnetic surface charges and hence stray field energy s-state is formed. If the thickness exceeds 15 nm, as in the right picture, a vortex state has smaller energy than an s-state. Two reasons can be mentioned why thicker samples favor the formation of a vortex state. First, in the core of a vortex state the magnetization points perpendicular to the surface and produces a demagnetizing field parallel to the surface. With increasing thickness the demagnetizing field decreases which reduces the stray field energy. Secondly, the surface charges which lead to a high stray field energy become dominant with increasing thickness. Figure 6.3 summarizes the different reversal modes in a phase diagram. The damping constant was set to $\alpha = 1$. It must be emphasized that the phase diagram will change if the damping constant changes.

Figure 6.4 shows the formation of a vortex for a sample with $d = 220$ nm and $t = 15$ nm. Figure 6.5 gives the exchange energy during reversal as a function of time. The exchange energy measures the homogeneity of the state. It is zero if the state is uniform and increases as the state becomes more inhomogeneous. The external field points from right to left. In the

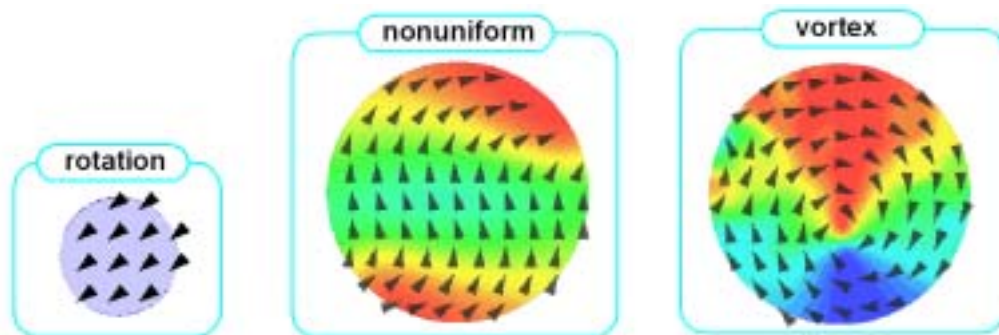


Figure 6.2: Three different reversal modes of permalloy nanodots are shown. (left) diameter of the dot $d = 55$ nm and the thickness is $t = 10$ nm. (middle) $d = 110$ nm, $t = 10$ nm. (right) $d = 110$ nm, $t = 15$ nm.

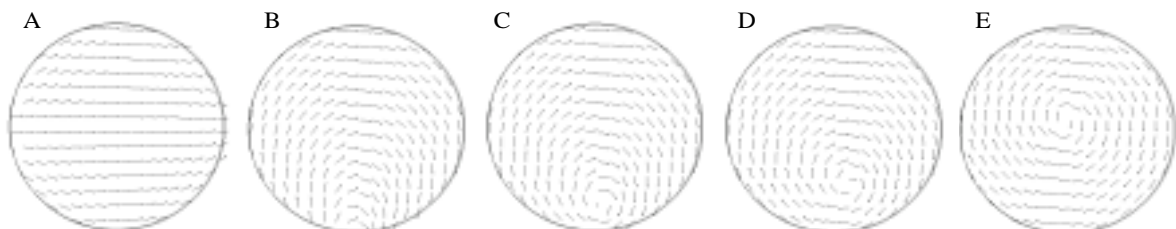


Figure 6.4: Magnetic states during reversal for a magnetic dot with a diameter of 165 nm and a thickness of 15 nm. The letters A - E correspond to the states marked in figure 6.5

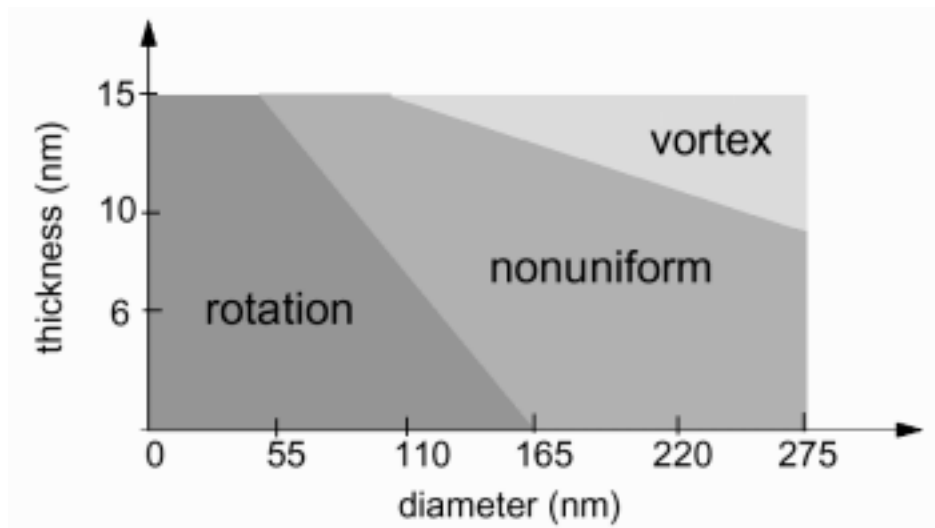


Figure 6.3: Phase diagram of the different reversal processes.

beginning a c-state is formed. This c-state transforms to a vortex state, whereas only one vortex occurs with the center close to the surface. The letters B and C in figure 5 correspond to the c-state and the vortex state, respectively. Figure 5 shows that these two states have almost the same exchange energy and it takes a while (2 ns) until the vortex state is formed. With increasing time the center of the vortex moves to the center of the sample. The dotted line in figure 5 corresponds to a sample with a diameter of 165 nm. Again a vortex state is formed. The time until the vortex is formed increases to 12 ns. Edge roughness favors the formation of vortices in real samples. The influence of defects on switching time and switching field was investigated by J. Deak and R. Koch [3].

In addition, we investigated the influence of the damping constant on the switching process. Figure 6.6 compares the time evolution of the magnetic component parallel to the field for $\alpha = 1$ and $\alpha = 0.01$ ($d = 220$ nm and $t = 10$ nm). After the application of a field $H_{\text{ext}} = -8$ kA/m, 1° off the x-direction, the torque $|J \times H_{\text{eff}}|$ remains small. For $\alpha = 1$ the nanodot starts to switch only after a waiting time of about 3 ns. For $\alpha = 0.01$ the waiting time reduces to about 0.5 ns. Leineweber und Kronmüller [5] observed that a certain waiting time is required before switching is initiated in hard magnetic spheres. Figure 6.7 shows that the reversal process changes if the damping constant is decreased. For $\alpha=1$ inhomogeneous rotation occurs. For $\alpha=0.01$ vortices are formed during reversal. Whereas in simulations with

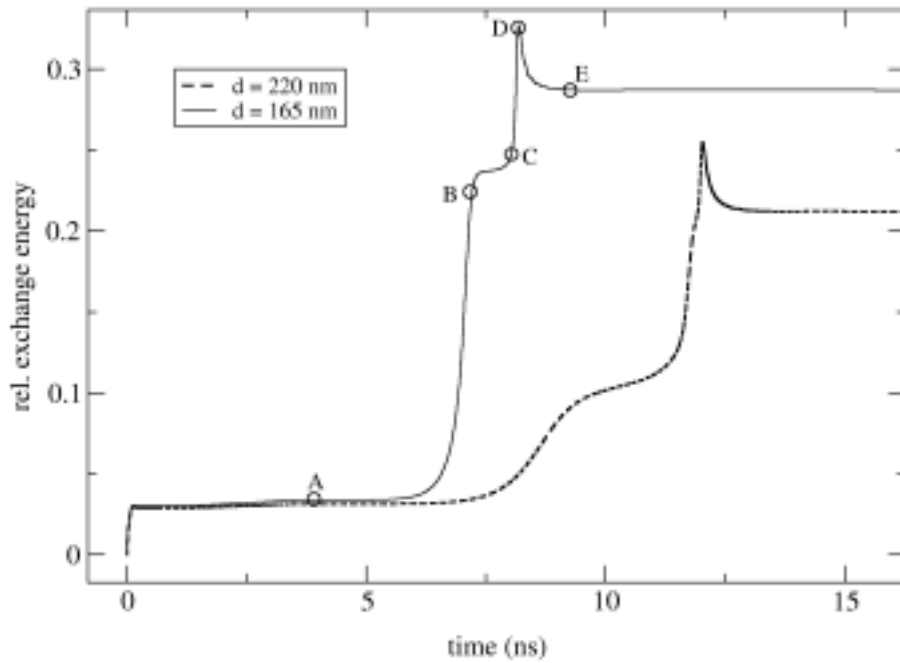


Figure 6.5: Time evolution of the relative exchange energy during reversal for two different diameters of the magnetic nanodot. The relative exchange energy measures the homogeneity of the reversal process.

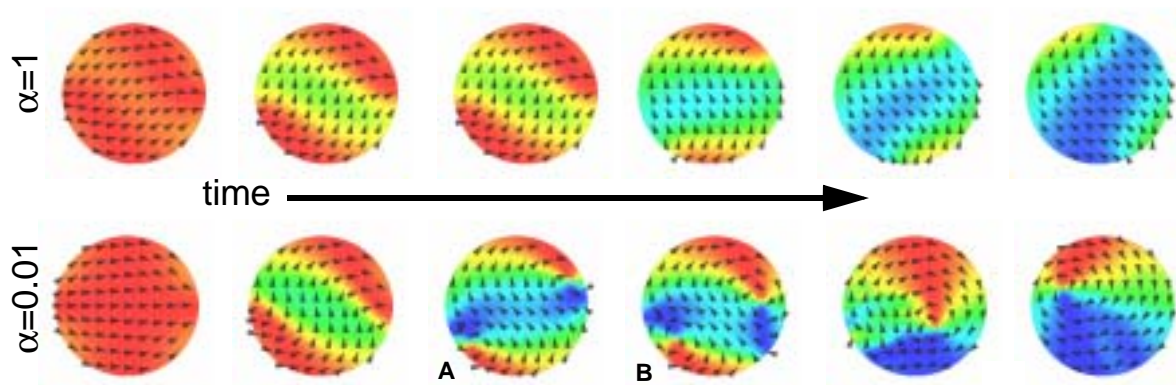


Figure 6.7: Transient states during reversal after the application of the external field for different values of the damping constant. The simulation time increases from the left to the right.

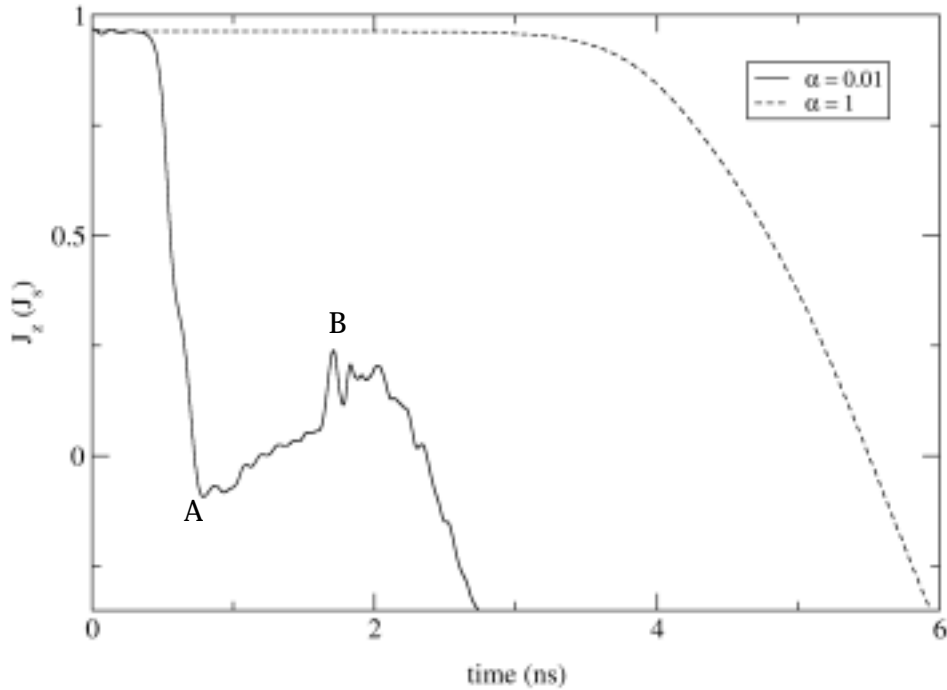


Figure 6.6: Time evolution of the magnetic polarization parallel to the external field for different values of the damping constant α .

$\alpha=1$ only one vortex occurs (provided the samples have a large enough diameter and thickness), for $\alpha=0.01$ two vortices are formed at the beginning (A in figure 6.6 and figure 6.7). These two vortices combine to one vortex after 1 ns. As a consequence the magnetic polarization increases until one big vortex is formed (B in figure 6.6 and figure 6.7).

The maximum reduced exchange energy during reversal for $\alpha = 0.01$ is about a factor 6 larger than for a damping constant $\alpha = 1$ which indicates highly uniform reversal for low damping.

6.3 Logic gates

R. Cowburn and M. Willand [1] suggested to use networks of interacting magnetic nanodots to perform logic operations. The logic states are signaled by the magnetization direction of a single-domain magnetic dot. The information is carried through the network by domain wall motion (magnetic solitons). The advantage of the proposed technique as com-

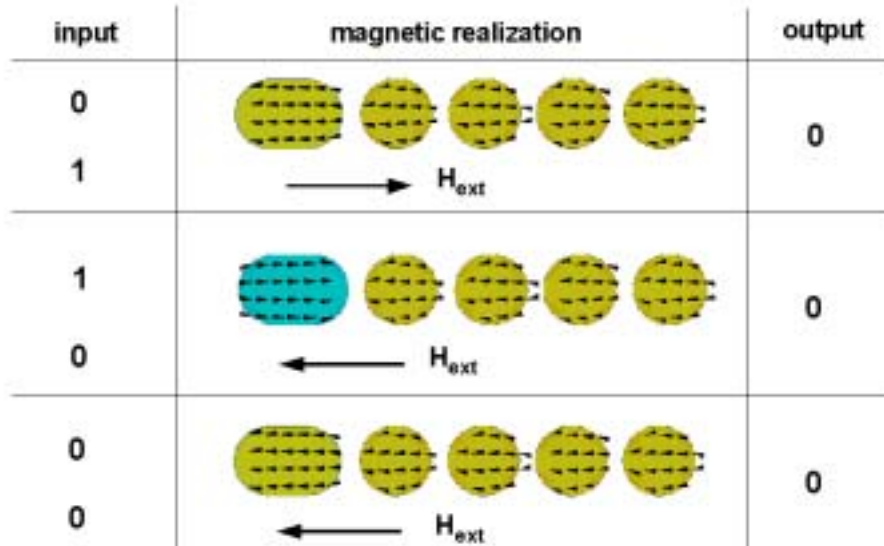


Figure 6.8: Three basic logic function of an AND gate are shown. Magnetic nanoelements together with the external field direction act as an AND gate.

pared to the common CMOS technology is an increased integration density and a hundred-fold reduction in power dissipation.

To explain the principle of logic AND gate let us assume a chain of dots as shown in figure 6.8. The magnetization direction of the first elongated dot acts as an input for the device. A magnetization to the left corresponds to the logic zero, a magnetization state to the right corresponds to a logic one. The state of the input dot can be set by a local external field. The second input of the device is the direction of the external field (left 0, right 1). The output of the system is the magnetization state of the right most dot.

The system is initialized by an external field to the left. The field has to be large enough to align all dots to the left.

Figure 6.8 shows three possible input configurations. In the first network the magnetization of the input dot points to the left (0) and the external field direction to the right (1). Because of the shape anisotropy of the system it is in a minimum energy state. For small external field strength no dot can be reversed. As a consequence the magnetization direction of the output dot remains to the left (0). It is obvious that for an external field to the left (0)

the output dot will remain to the left, independent of the state of the input dot. The three presented basic logic functions describe three of the four basic logic functions of an AND-gate.

To investigate the fourth basic logic function micromagnetic simulations are performed. The simulated system consists of an elongated nanoelement and 4 circular permalloy nanomagnets, as shown in 6.9. The diameter of the dots is 110 nm placed on a pitch of 135 nm. The thickness is 10 nm.

To simulate the fourth possible input configuration the magnetization of the input dot was set to the right, antiparallel to the magnetization of the circular elements. Then the system was relaxed to equilibrium. After the system relaxed to equilibrium an external field of 5.57 kA/m was applied to the right. A smaller field causes a strongly inhomogeneous magnetic state in the circular nanomagnet placed next to the already reversed input dot but it does not provide enough energy to propagate the soliton to the right. Thus all dots except the input dot (that initially points to the right) remain magnetized to the left. However for an external field of 5.57 kA/m and a damping constant of $\alpha=0.1$ the soliton propagates to the right as shown in figure 6.9. During reversal of the magnetic dots neighboring elements rotate in opposite directions, forming partial flux closure structures during the reversal process. It is important to note that the stray field interaction is responsible for the formation of inhomogeneous magnetic states during reversal. Isolated elements of the same size rotate homogeneous. Figure 6.10 compares the time evolution of the magnetization component parallel to the long axis, obtained for different values of the Gilbert damping constant. A uniform reversed field of $H_{\text{ext}} = 5.57$ kA/m was applied instantaneously with an angle of 1 degree with respect to the long axis of the chain. With decreasing damping constant the switching time decreases drastically. The slope of the $J_z(t)$ curve changes considerably as the damping constant is increased from $\alpha = 0.1$ to $\alpha = 1$. In regimes where the change of J_z with time is small non-uniform magnetic states with low magnetostatic energy form.

6.4 Conclusion

Micromagnetic simulations of magnetization reversal in circular nanomagnets clearly show that the reversal process strongly depends on the thickness of the elements. With increasing thickness demagnetizing field becomes important leading to partial flux-closure structures during reversal, if the diameter of the nanodot is greater or equal 110 nm. For the very same reason vortices form during the reversal process for a thickness of 15 nm and a diameter

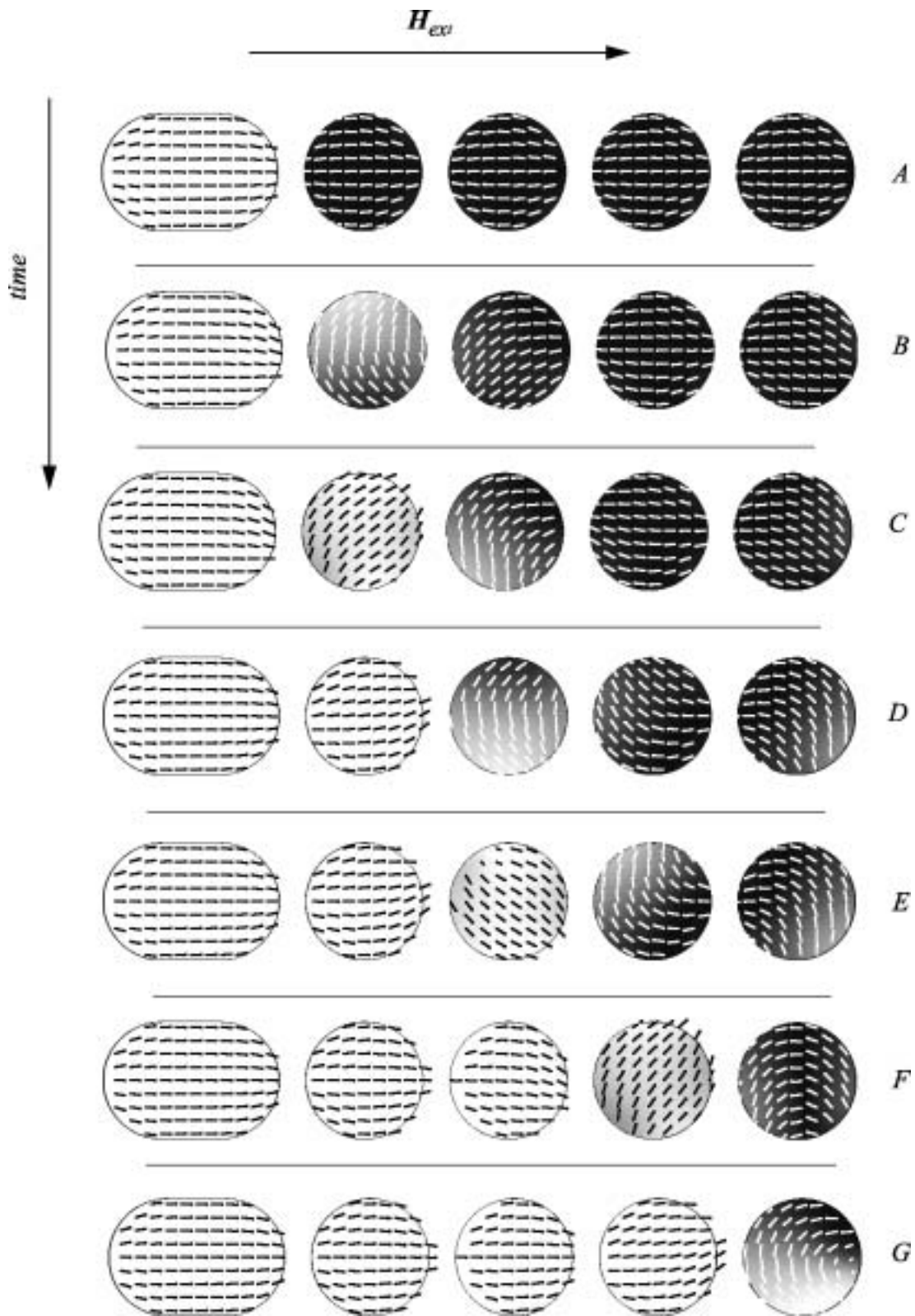


Figure 6.9: Initial state and transient states during irreversible switching of the array of circular nanomagnets. The greyscale maps the magnetization component parallel to the long axis. The simulation time increases from the top to the bottom.

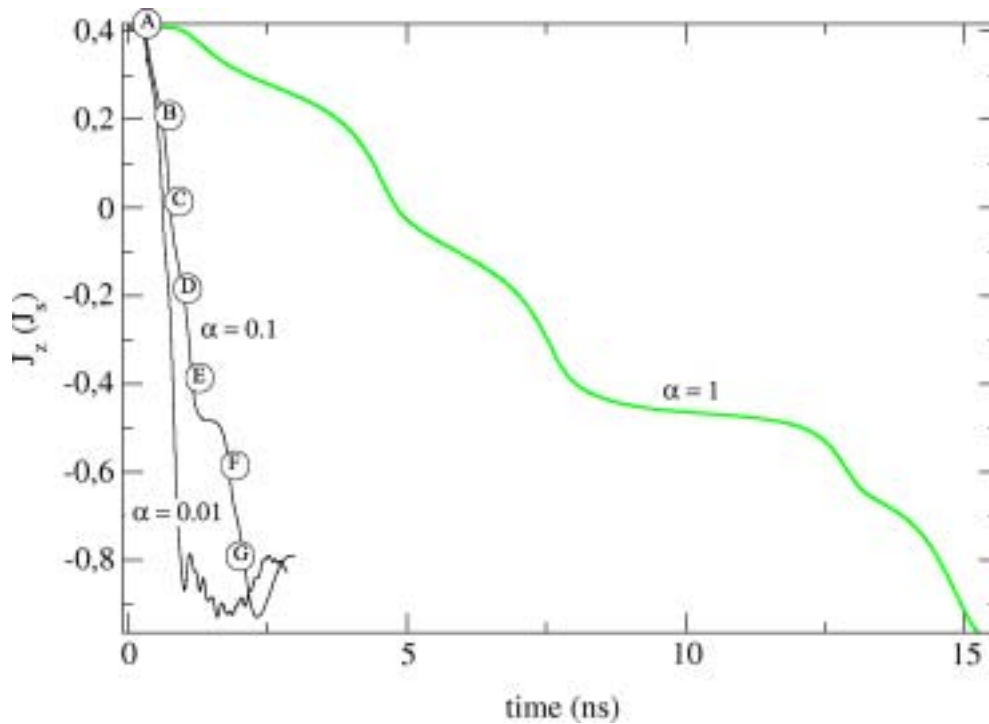


Figure 6.10: Magnetization component parallel to the long axis of the array as a function of time for three different values of the Gilbert damping constant. The circles refer to the magnetization patterns of figure 6.9.

greater or equal 165 nm. The damping constant changes the reversal mode. With decreasing damping constant the reversal process becomes more inhomogeneous.

Isolated circular nanomagnets with a diameter smaller of 110 nm and a thickness of 10 nm reverse almost homogeneously. Nevertheless, highly nonuniform magnetic states form during switching of an array of interacting nanomagnets with the same size owing to magnetostatic interactions. A small Gilbert damping constant decreases the reversal time as compared to the reversal time obtained for $\alpha = 1$ by a factor 15. However for all investigated damping constants partial flux closer states are formed that slow down the switching process and may limit the processing speed of magnetic logic gates.

References

- [1] R. P. Cowburn, M. E. Welland, "Room temperature magnetic quantum cellular automata," *Science*, vol. 287, pp. 1466, 2000.
- [2] R. P. Cowburn, D. K. Koltsov, A. O. Adeyeye, M. E. Welland, D. M. Tricker, "Single-Domain Circular Nanomagnets," *Phys. Rev. Lett.*, vol. 83, pp. 1042, 1999.
- [3] J. G. Deak and R. H. Koch, "The effect of edge roughness on magnetization reversal in micron-sized permalloy thin films," *J. Magn. Magn. Mater.*, vol. 213, pp. 25, 2000.
- [4] K. J. Kirk, M. R. Scheinfein, J. N. Chapman, S. McVitie, M.F. Gillies, B. R. Ward and J. G. Tennant, "Role of vortices in magnetisation reversal of rectangular Ni Fe elements," *J. Phys. D: Appl. Phys.*, vol. 34, pp. 160, 2001.
- [5] T. Leineweber, H. Kronmüller, "Dynamics of magnetisation states," *J. Magn. Magn. Mater.*, vol. 192, pp. 575, 1999.
- [6] G. A. Prinz, "Magnetoelectronics applications," *J. Magn. Magn. Mater.*, vol. 200, pp. 57, 1999.

EXCHANGE BIAS

A novel approach for solving the Landau-Lifshitz-Gilbert equation for antiferromagnets with the finite element method is presented. The antiferromagnet is treated in a continuum theory which allows to explore the domain structure on a mesoscopic length scale. The finite element method is suitable to treat antiferromagnets with arbitrarily shaped grains as well as exchange coupled antiferromagnetic / ferromagnetic structures. The simulations confirm a 90° coupling between the antiferromagnet and the ferromagnet at fully compensated interfaces.

Most important this model explains exchange bias and training effect in fully compensated antiferromagnet/ferromagnet bilayers. Unlike previous partial wall models, the energy associated with the unidirectional anisotropy is stored in lateral domain walls located between antiferromagnetic grains. Furthermore it is shown that the mechanism leads naturally to a training effect, that denotes the decrease of the bias effect and coercivity with increasing number of hysteresis cycles.

7.1 Introduction

When a ferromagnet is coupled to an antiferromagnet a shift of the hysteresis loop along the magnetic field axis can occur. Thus the antiferromagnet pins the ferromagnet along one direction. Usually the shift in the hysteresis loop requires that the whole system (ferromagnet and antiferromagnet) is cooled through the Néel temperature of the antiferromagnet in the presence of an applied field. The shift in the hysteresis loop is called exchange bias effect. It was discovered by Meiklejohn and Bean [6].

The phenomenon of exchange bias is not well understood however it is used in various applications. The application of the exchange bias effect ranges from the use of antiferromagnets in hard magnets to recording heads and recording media.

Already Meiklejohn and Bean [6] proposed to use the exchange bias effect in hard magnetic materials to improve its energy product. High end permanent magnets are characterized by large energy products.

The thermal stability of longitudinal magnetic recording media can be increased by antiferromagnetically coupling of two ferromagnetic layers via a thin polarization layer [1,10].

Another application is to use an antiferromagnetic layer in recording heads to stabilize the domain in the head [46].

The most important application of the exchange bias effect is to use an antiferromagnet to stabilize the pinned layer in spin valve GMR sensors [4]. In GMR sensors the magnetoresistance (GMR) is due to spin-dependent scattering in ferromagnet/non-magnetic metal multilayers. Commonly used materials are bilayers of FeMn/FeCo, IrMn/NiFe, IrMn/FeCo [30]. In these multilayer systems, both the antiferromagnet and the ferromagnet are polycrystalline. A successful model for exchange bias should therefore be able to describe loop shifts and coercivity of polycrystalline films.

Proposed mechanisms to explain exchange bias require exact information about the spin structure between the ferromagnet and antiferromagnet. Under the assumption that the spin structure at the interface is the same as in the bulk, the antiferromagnetic spins at the interface are either compensated or uncompensated.

At a completely uncompensated interface all the antiferromagnetic spins point in the same direction. These spins produce a net moment the ferromagnet can interact with.

The interface between a ferromagnet and an antiferromagnet is completely compensated, when the number of interfacial spins pointing in one direction (sublattice A) is the same as the number of interfacial spins pointing in the opposite direction (sublattice B). If the antiferromagnet moments were exactly antiparallel in the two sublattices, there would be no net moment's that couples the antiferromagnet to the ferromagnet. Thus all orientations of the ferromagnet would lead to the same interface energy.

Meiklejohn and Bean [6] assumed uncompensated spins and introduced phenomenologically a unidirectional anisotropy to explain the shift in the hysteresis loop of small Co particles with an antiferromagnetic CoO shell.

Contrary to the intuitive pictures of Meiklejohn and Bean the bias field was found to be almost independent of the type of the interface between the ferromagnet and the antiferromagnet [25,47,30]. Exchange bias was found for both uncompensated as well as for compensated interfaces [17,35].

Therefore a successful theory should be able to explain exchange bias in the case of compensated interfaces, and it should also account for the sometimes observed insensitivity of measured bias to supposed interface structure.

The simple model of Meiklejohn and Bean cannot give answers to most questions we are confronted with when investigating the exchange bias effect.

The realization that many complex processes contribute to exchange bias was first put forward by Néel in attempts to understand coercivity and training effects [27]. Additional developments were made by Malozemoff and Mauri by explaining the possibility of effects due to domain wall pinning, partial wall formation in the antiferromagnet, and spin order reconstruction at the interface of the antiferromagnet and ferromagnet [18,20].

For compensated interfaces Koon [17] suggested that the spins in the antiferromagnet are canted because of the coupling to the ferromagnet. Thus the ferromagnet generates a small magnetic moment parallel to the spin direction of the ferromagnetic spins at the interface. As a consequence the antiferromagnet aligns perpendicular to the easy axis in the antiferromagnet. Koon's model can explain exchange bias, when the antiferromagnetic spins are constrained to planes parallel to the interface and the interface coupling is strong. Schulthess and Butler [35] showed that partial domain walls which are essential to explain exchange bias in Koon's model are unstable owing to out of plane fluctuations.

Two of the most recent suggestions for bias mechanisms concentrate on the role of domain pinning by defects in semi-random antiferromagnets, and the formation of a lateral wall between steps at uncompensated interfaces. Morosov and Sigov [26] proposed a model in which exchange bias appears due to a magnetic configuration generated between steps at an uncompensated interface. The grain model discussed here involves the formation of narrow domain walls between grains, along the interface.

The second mechanism is called the domain state model, and has been proposed by Nowak et al.[32]. This model describes an exchange bias due to domain wall pinning by random defects. A net moment caused by uncompensated spins provides coupling across the interface, and the authors find a bias shift for directions parallel to the antiferromagnetic anisotropy axis for spins in a single crystal lattice.

A key element of all later developments has been the recognition of magnetization processes in the antiferromagnet on measurable features associated with the bias. Typically, the problem has been to understand exchange bias in the presence of imperfections and defects.

In section 7.1 we give a more detailed introduction of the developments of exchange bias during the last 40 years. In section 7.2 we present magnetization processes and theories of exchange bias in ferromagnetic/antiferromagnetic bilayers for compensated, uncompensated and mixed interfaces. The numerical results of section 7.2 are obtained by solving the micromagnetic equations using a finite element method. The simulations are based on a continuum model which is described in section 7.3. In section 7.4 a new mechanism is suggested by

which energy can be stored in the antiferromagnet which relies on a random distributions of grains. Most importantly, it is shown that a system with perfectly compensated interfaces, free of defects and other structural imperfections within grains, can still exhibit exchange bias. This is in contrast to previous theories of exchange which require some sort of imperfections, either at the interface or within the antiferromagnet, in order to produce exchange bias in a mostly compensated interface structure.

7.2 Mechanisms

7.2.1 Uncompensated interfaces

Meiklejohn and Bean explained phenomenologically the observed shift in the hysteresis loop of Co coupled to CoO with a unidirectional anisotropy. They considered that the surface between the Co and CoO is coherent with the (111) plane of CoO. If the spin structure on the surface of CoO is the same as in the bulk all spins on the surface (interface) will point parallel and in the same direction. Let us assume in the following the coupling between the ferromagnet (Co) and antiferromagnet (CoO) is ferromagnetically. If the system is initially heated above the ordering temperature of the antiferromagnet (Néel temperature) and then cooled below the Néel temperature under the action of an external field, the spins of the AF at the interface will align parallel to the ferromagnet as shown in figure 7.1 (I). This spin configuration minimizes the interface energy. In figure 7.1 only the spins of one sublattice in the antiferromagnet are drawn. The spins of the other sublattice point in the opposite direction.

Meiklejohn and Bean assumed that the large anisotropy of CoO freezes the spin structure of CoO. Thus the spins will stay aligned parallel to the crystallographic easy axis (parallel to x -axis in figure 7.1), independent of the state of the ferromagnet. If the ferromagnet is reversed the spins in the ferromagnet and antiferromagnet point in opposite directions (figure 7.1-B). The interface energy increases. The interface energy can be written as,

$$E_{ex,interface} = -2JS^2 \sum_{i=1}^N \mathbf{u}_i^F \mathbf{u}_i^A, \quad (7.1)$$

where \mathbf{u}_i^F and \mathbf{u}_i^A give the unit vector parallel to the spin direction in the ferromagnet and antiferromagnet, respectively. N is the number of interface spin pairs ($\mathbf{u}_i^F \mathbf{u}_i^A$). J and S

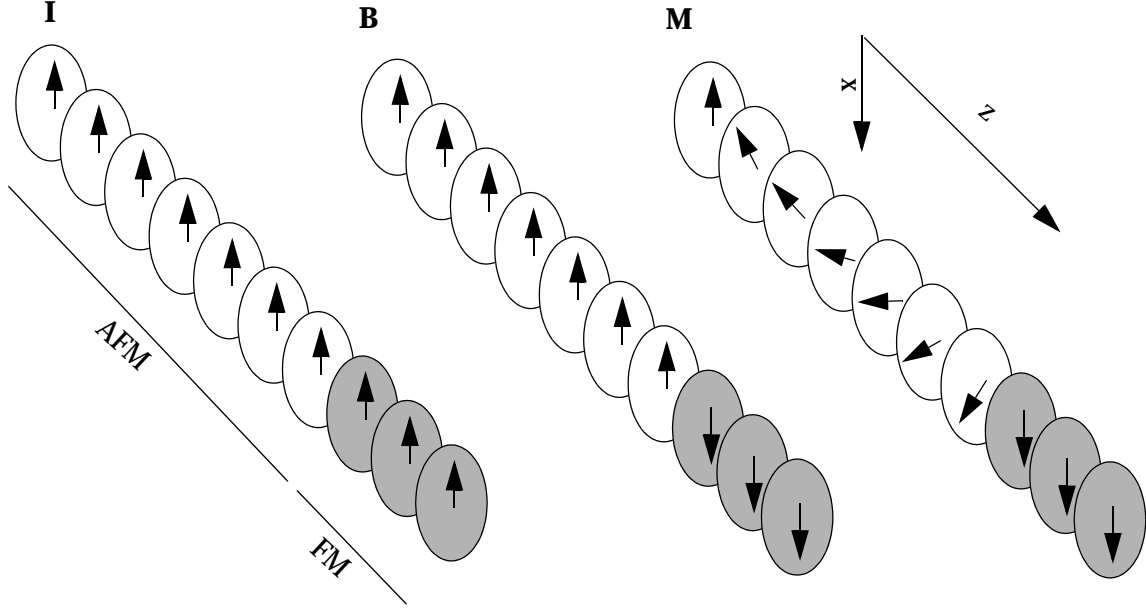


Figure 7.1: (I) The initial spin configuration (e.g. after field cooling) in the ferromagnet and antiferromagnet is shown. In the antiferromagnet only the sublattice that couples to the ferromagnet is drawn. (B) The spins in the ferromagnet are reversed. The spins in the antiferromagnet remain homogeneous. At the interface a high energy state is formed. [Meiklejohn and Bean's model]. (M) A partial domain wall is formed in the antiferromagnet in order to decrease the interface energy. [Model of Mauri].

denote the exchange integral and the total spin quantum number, respectively. In a continuum approach we can write

$$E_{ex,interface} = -n_o 2JS^2 \int_A \mathbf{u}^F \mathbf{u}^A dA, \quad (7.2)$$

where n_o is the number of spins per unit area at the interface. For a cubic lattice with lattice constant a , $n_o = \frac{1}{a^2}$. In the model of Meiklejohn and Bean \mathbf{u}^A points parallel to the uniaxial anisotropy of CoO and remains constant. Thus we can write equation (7.1) in the form

$$E_{ex,interface} = -J_s \int_V \mathbf{u}^F \mathbf{H}_E dV, \quad (7.3)$$

where J_s is the spontaneous polarization of the ferromagnet and

$$\mathbf{H}_E = \frac{2JS^2n_o}{t_F J_s} \mathbf{u}^A, \quad (7.4)$$

where t_F is the thickness of the ferromagnet. The integral in equation (7.3) is over the volume of the ferromagnet. The field \mathbf{H}_E is called bias field. Equation (7.3) can also be written in the form of

$$E_{ex,interface} = -K_{eb} \int_V \mathbf{u}^F \mathbf{u}^A dV = -K_{eb} \int_V \cos(\theta) dV, \quad (7.5)$$

where θ denotes the angle between the magnetization in the ferromagnet and the spin direction of the antiferromagnet at the interface. The anisotropy constant

$$K_{eb} = \frac{k_{eb}}{t_F} = \frac{2JS^2n_o}{t_F}, \quad (7.6)$$

leads to a uniaxial anisotropy. The uniaxial surface anisotropy k_{eb} or also called interface energy ΔE is,

$$k_{eb} = \Delta E = 2JS^2n_o. \quad (7.7)$$

The surface anisotropy k_{eb} is independent of the ferromagnetic layer thickness and the spontaneous magnetic polarization of the ferromagnet. Thus it is often used to compare the bias strength of different systems. Let us look at the predicted strength of the bias field according to Meiklejohn and Bean's model for a Permalloy/CoO bilayer. The thickness of the permalloy layer is 20 nm and J_s of permalloy is 1 T. In CoO the $\langle 111 \rangle$ planes are fully uncompensated. For the $\langle 111 \rangle$ plane $n_o = 4/\sqrt{3}a^2$, where $a = 0.427$ nm. For an exchange integral at the interface of $J = 2$ meV = $3,2 \times 10^{-22}$ J we get a bias field of 406 kA/m. The uniaxial surface anisotropy $k_{eb} = 8$ mJ/m² (= 8 erg/cm²). This value is about 10 or 100 times larger than all experimentally measured values. A compilation of measured interface energies for various exchange biased systems can be found in [30].

Mauri et al [20] suggested that a state with a perfectly rigid antiferromagnet and a perfectly homogeneous ferromagnet does not describe the lowest energy configuration near the interface. They proposed the formation of a planar domain wall at the interface as the ferromagnet is reversed. Mauri et al considered the case that the domain wall energy in the ferromagnet

is much larger than the domain wall energy in the antiferromagnet. Thus the domain wall will be formed in the antiferromagnet (figure 7.1-M) because it costs less energy than a domain wall in the ferromagnet. To derive an expression for the exchange field we consider a chain of spins in the ferromagnet and a chain of spins in the antiferromagnet. The exchange integral J couples the spin of the ferromagnet and the spin of the antiferromagnet at the interface. The total energy per unit area can be written as

$$e_{tot} = e_w - 2Jn_0 \cos(\theta - \phi) - J_s H t_F \cos(\theta - \theta_H), \quad (7.8)$$

where θ_H is the angle of the external field with respect to the x -axis. ϕ and θ are the angles of the interfacial spin relative to the x -axis in the antiferromagnet and ferromagnet, respectively. J_s is the magnetic polarization in the ferromagnet and t_F its thickness. e_w is the energy of the twist in the antiferromagnet, which is initiated by the rotation of the ferromagnet. Néel [28] calculated the domain wall energy per unit area of a continuum chain of spins along the z -axis as

$$e_w = \int_{-\infty}^{\infty} \left[A \left(\frac{\partial}{\partial z} \phi(z) \right)^2 + K_1 \sin^2 \phi(z) \right] dz. \quad (7.9)$$

The spins are restricted to planes perpendicular to the z -axis. The uniaxial anisotropy direction is parallel to the x -axis. A denotes the strength of the exchange coupling. Equation (7.9) is minimized by solving the Euler-Lagrange equation. For the domain wall energy follows,

$$e_w = 2\sqrt{AK_1} [1 - \cos(\phi)]. \quad (7.10)$$

Minimizing equation (7.8) using equation (7.10) with respect to ϕ and θ gives two nonlinear equations for ϕ and θ . The bias field is defined here as the magnitude of the external field H necessary to align the ferromagnet perpendicular to the applied field. Thus the bias field requires $\phi - \theta_H = 90^\circ$. For the bias field follows

$$H_B = -\frac{2Jn_0 \cos(\theta_H)}{J_s t \sqrt{\gamma^2 + \gamma |\sin \theta_H| + 1}}, \quad (7.11)$$

$$\text{where } \gamma = \frac{2Jn_0}{2\sqrt{AK_1}}, \quad (7.12)$$

is the ratio of the interface energy and the 90° domain wall energy in the antiferromagnet. In the limiting case, that the interface energy is much smaller than the domain wall energy, we get for $\theta_H = 0$ the expression of Meiklejohn and Bean (equation 7.4). In the other limit, where the interface energy is much larger than the domain wall energy, Mauri's formula follows

$$H_B = -\frac{2\sqrt{AK_1}}{J_s t}. \quad (7.13)$$

The partial domain wall as suggested by Mauri may become unstable when the twist exceeds a critical angle. Depending on the strength of the interface coupling the partial domain wall unwinds or the magnetization of the antiferromagnet switches irreversibly.

Large interface coupling:

Let us assume that the interface coupling $2A/a$ is larger than the domain wall energy $\sigma_w = 2\sqrt{A_{AF}K_{AF}}$. When the spins at the interface of the antiferromagnet pass the hard axis the twist becomes unstable. At a critical angle α_{crit} the AF structure makes a transition to another state, which has reversed ordering of the antiferromagnetic spins far from the interface. Néel first investigated this irreversible motion of the antiferromagnetic spins. Néel found that for AF thicker than $2\sqrt{A_{AF}/K_{AF}}$ the irreversible transitions occur at a critical angle between 90° and 180° . For an infinitely thick AF the critical angle reaches 180° .

The irreversible switching of the antiferromagnetic grains leads to the rotational hysteresis loss and a field shift in the isotropic ferromagnetic resonance [41].

Small interface coupling:

A different behavior occurs when the interface coupling $2A/a$ is smaller than the domain wall energy. When the spins at the interface rotate beyond a critical angle which is greater than 90° further winding of the structure generates a wall energy that cannot be sustained by the interfacial energy coupling. The twist unwinds and rotates back. Finally a new twist with opposite chirality is formed.

7.2.2 Compensated interfaces - Spin flop coupling

An interface between a ferromagnet and an antiferromagnet is completely compensated, when the number of interfacial spins of sublattice A is equal to the number of interfacial spins of sublattice B . If the antiferromagnet moments were rigidly antiparallel in the two sublattices, there would be no net moment for the ferromagnet to interact with. Thus all orientations of the ferromagnet would lead to the same interface energy. However, Koon [17] suggested that the spins in the antiferromagnet are canted because of the coupling to the ferromagnet. Thus the ferromagnet generates a small magnetic moment parallel to the spin direction of the ferromagnetic spins at the interface. As a consequence the antiferromagnet aligns perpendicular to the easy axis in the antiferromagnet. Figure 7.2 shows schematically

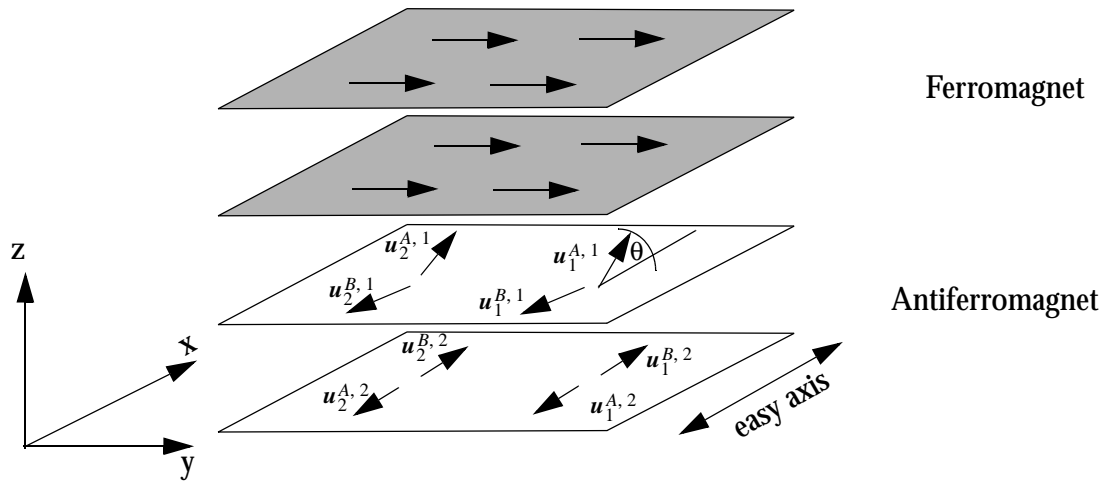


Figure 7.2: Spin flop coupling at the interface between a ferromagnet and antiferromagnet. The spins in the interface layer in the antiferromagnet are canted by an angle θ with respect to the easy axis in the antiferromagnet.

the spin flop coupling at the interface. The spins in the interface layer in the antiferromagnet are canted. The net moment is parallel to the ferromagnet and perpendicular to the easy axis in the antiferromagnet. The spin flop leads to a uniaxial anisotropy in the ferromagnet.

The spin flop coupling was confirmed by several measurements. Neutron diffraction measurements [14] show a perpendicular orientation between the ferrimagnetic Fe_3O_4 and the antiferromagnetic CoO . Hysteresis measurements along different directions for $\text{Ni}_{80}\text{Fe}_{20}/\text{Fe}_{50}\text{Mn}_{50}$ reveal a uniaxial anisotropy in the ferromagnetic layer, induced by the antiferromagnetic $\text{Fe}_{50}\text{Mn}_{50}$ layer [15]. Above the Néel temperature of the antiferromagnet the

imposed uniaxial anisotropy in the ferromagnet vanishes. Also for CoO single crystals spin flop coupling was found [24].

Figure 7.3 shows the net magnetic moment for planes parallel to the interface obtained by

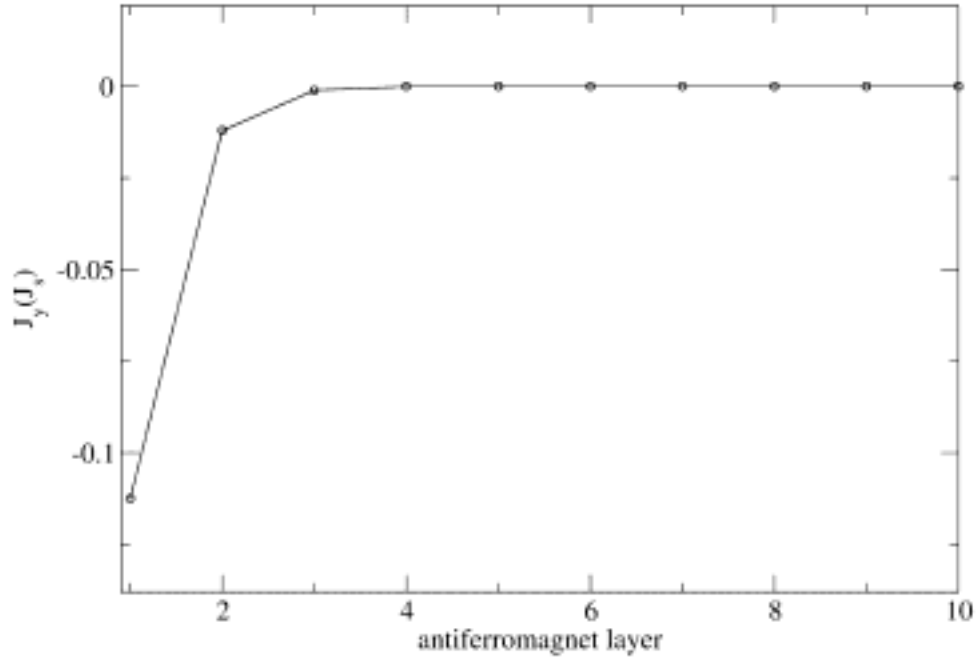


Figure 7.3: The net magnetic polarization in different layers in the antiferromagnet is shown as a function of the distance (in monolayers) from the interface. The component parallel to the magnetization of the ferromagnet is plotted.

computer simulations. The antiferromagnet layer 1 contains all interfacial spins ($\mathbf{u}_i^{A,1}$ and $\mathbf{u}_i^{B,1}$ of figure 7.2) of the antiferromagnet. The layer n contains the spins of the n -th monolayer ($\mathbf{u}_i^{A,n}$ and $\mathbf{u}_i^{B,n}$) in the antiferromagnet.

In the simulation the exchange energy follows from a Heisenberg Hamiltonian, where the spin operators are treated as vector quantities. Details of the simulations can be found in [16].

The exchange integral in the antiferromagnet and across the interface is $J = 1.7$ meV. The uniaxial anisotropy in the antiferromagnet is 0.034 meV/spin. Figure 7.3 shows that the angle between the spins of the antiferromagnet and the easy axis in the interface layer is about $\theta = -0.112$ ($= -6.4^\circ$). In the next monolayer the angle decreases by an approximately a factor 10. Thus the canted spin structure at the interfaces relaxes within a few monolayers to the spin structure of the bulk. Thus spin flop coupling is localized at the interface.

7.2.2.1 Spin flop coupling strength

To estimate the strength of the spin flop coupling we use a microscopic Heisenberg model. The exchange energy is given by,

$$E_{ex} = -S^2 \sum_{i=1}^N \sum_{j=1}^{nN} J_{ij} \mathbf{u}_i \mathbf{u}_j, \quad (7.14)$$

where nN is the number of nearest neighbors. We separate the exchange energy into an interface exchange energy

$$E_{ex,interface} = -2J^{int}S^2 \sum_{i=1}^{I_A} \mathbf{u}_i^F \mathbf{u}_i^{A,1} - 2J^{int}S^2 \sum_{i=1}^{I_B} \mathbf{u}_i^F \mathbf{u}_i^{B,1}, \quad (7.15)$$

and a bulk exchange energy in the antiferromagnet.

$$\begin{aligned} E_{ex,anti} = & -4J^{AF}S^2 \sum_{i=1}^{I_A} \mathbf{u}_i^{A,1} \mathbf{u}_i^{B,1} - 4J^{AF}S^2 \sum_{i=1}^{I_B} \mathbf{u}_i^{B,1} \mathbf{u}_i^{A,1} \\ & - J^{AF}S^2 \sum_{i=1}^{I_A} \mathbf{u}_i^{A,1} \mathbf{u}_i^{B,2} - J^{AF}S^2 \sum_{i=1}^{I_B} \mathbf{u}_i^{B,1} \mathbf{u}_i^{A,2}. \end{aligned} \quad (7.16)$$

The unit vectors $\mathbf{u}_i^{A,1}$ and $\mathbf{u}_i^{B,1}$ describe the spin directions of sublattice A and sublattice B in the interface layer of the antiferromagnet. (figure 7.2). I_A and I_B is the number of interface spins of sublattice A and B respectively. The factor 2 in equation (7.15) arises since both, the coupling of the spins in the ferromagnet to the spins in the antiferromagnet and the coupling of spins in the antiferromagnet to the spins in the ferromagnet, contribute to the interface exchange energy. The third and fourth term in equation (7.16) denote the coupling of the interface layer to the second monolayer away from the interface.

If we assume that the canted state relaxes within one monolayer (thus already $\mathbf{u}_i^{A,2}$ and $\mathbf{u}_i^{B,2}$ are parallel to the easy axis in the antiferromagnet) and that the ferromagnet points perpendicular to the easy axis, for the exchange energy follows

$$E_{ex} = 2NJ^{int}S^2 \sin \theta + 4NJ^{AF}S^2 \cos 2\theta + NJ^{AF}S^2 \cos \theta, \quad (7.17)$$

where θ is the angle between the spins at the interface of the antiferromagnet and the easy axis, as shown in figure 7.3. N is the number of the interfacial spins, $N=I_A + I_B$. A uniaxial anisotropy in the antiferromagnet can be considered by adding

$$E_{ani} = -NK_1 \cos^2 \theta \quad (7.18)$$

to the total energy $E_{tot}(\theta) = E_{ani} + E_{ex}$. Linearizing the equation which follows from the equilibrium condition $\partial E_{tot}(\theta)/\partial \theta = 0$, with respect to θ we get

$$\theta \approx \frac{2S^2 J^{int}}{17J^{AF}S^2 - 2K_1}. \quad (7.19)$$

Using the same material parameters as in the simulations used for figure 7.3 we get $\theta = -0.112$. The difference of the angle θ between the computer simulation and the analytic estimation is less than 5%. The uniaxial anisotropy changes θ by less than 0.3%. Thus the canted angle θ is determined by the ratio of the interface exchange integral J_{int} to the bulk exchange integral J_{AF} .

$$\theta \approx \frac{J^{int}}{8.5J^{AF}}. \quad (7.20)$$

When the ferromagnet points perpendicular to the easy axis of the antiferromagnet the AF spins at the interface cant by an angle θ that reduces the interface energy by,

$$\Delta E_{inter} = 2NJ^{int}S^2 \sin \frac{J^{int}}{8.5J^{AF}} \quad (7.21)$$

7.2.2.2 Interface energy term for spin flop coupling

The perpendicular orientation between the ferromagnet and the antiferromagnet for a perfectly compensated interface is closely related to the principle of biquadratic coupling proposed by Slonczewski [37]. Slonczewski investigated ferromagnetic multilayers with a varying sign of the coupling constant along the interface. The observed perpendicular orientation of the films was described with an biquadratic energy term.

Stiles and McMichael [41] and Stamps [40] suggested a biquadratic energy term at a compensated interface between a ferromagnet and an antiferromagnet.

$$\frac{E}{Na^2} = \frac{J_{sf}}{a^2} (\mathbf{u}_{AF} \mathbf{u}_F)^2, \quad (7.22)$$

where \mathbf{u}_{AF} and \mathbf{u}_F denotes the direction of the magnetization in the antiferromagnet and the ferromagnet, respectively. a denotes the lattice constant and N the number of spins at the interface. J_{sf} , the spin flop coupling constant, can be approximated by equation (7.20).

$$J_{sf} = \frac{\Delta E_{inter}}{N} \quad (7.23)$$

7.2.2.3 Partial domain walls in the antiferromagnet

Let us assume that the spin flop coupling is so strong that the moments at the interface in the antiferromagnet are locked to minimize the interface energy. Thus the rotation of the ferromagnetic spins rotate the antiferromagnetic spins at the interface. If the thickness of the antiferromagnet is larger than the domain wall width spins at the bottom of the antiferromagnet will point parallel to the easy axis. Thus partial domain walls are formed in the antiferromagnet. If the partial domain is wound past a critical angle the spins at the interface rotate out of the interface plane. The critical angle is reached when the energy of the twist exceeds the interface energy. The partial domain in the antiferromagnet unwinds owing to the out of plane rotation of the interfacial spins. Figure 7.4 shows the unwinding of the antiferromagnetic domain wall. Initially the ferromagnet points perpendicular to the easy axis of the antiferromagnet. No partial domain wall is formed, solely the spins at the interface are canted owing to spin flop coupling (image (1) in figure (7.4)). In image (3) the ferromagnet is rotated above the critical angle. Images (4-6) show the out of plane rotation of the antiferromagnetic spins. The out of plane component of the magnetization is black-white coded. In image (7) again a stable twist is formed. The twist angle never exceeds 90° . The ferromagnet irreversibly unwinds and winds up with opposite chirality. No bias but an enhanced coercivity occurs.

In the model originally studied by Koon the antiferromagnetic spins were restricted to planes parallel to the interface. As a consequence the antiferromagnetic spins are hindered to rotate out of plane and partial domain walls up to 180° can be formed. The partial domain wall does not irreversibly unwind. Exchange bias occurs.

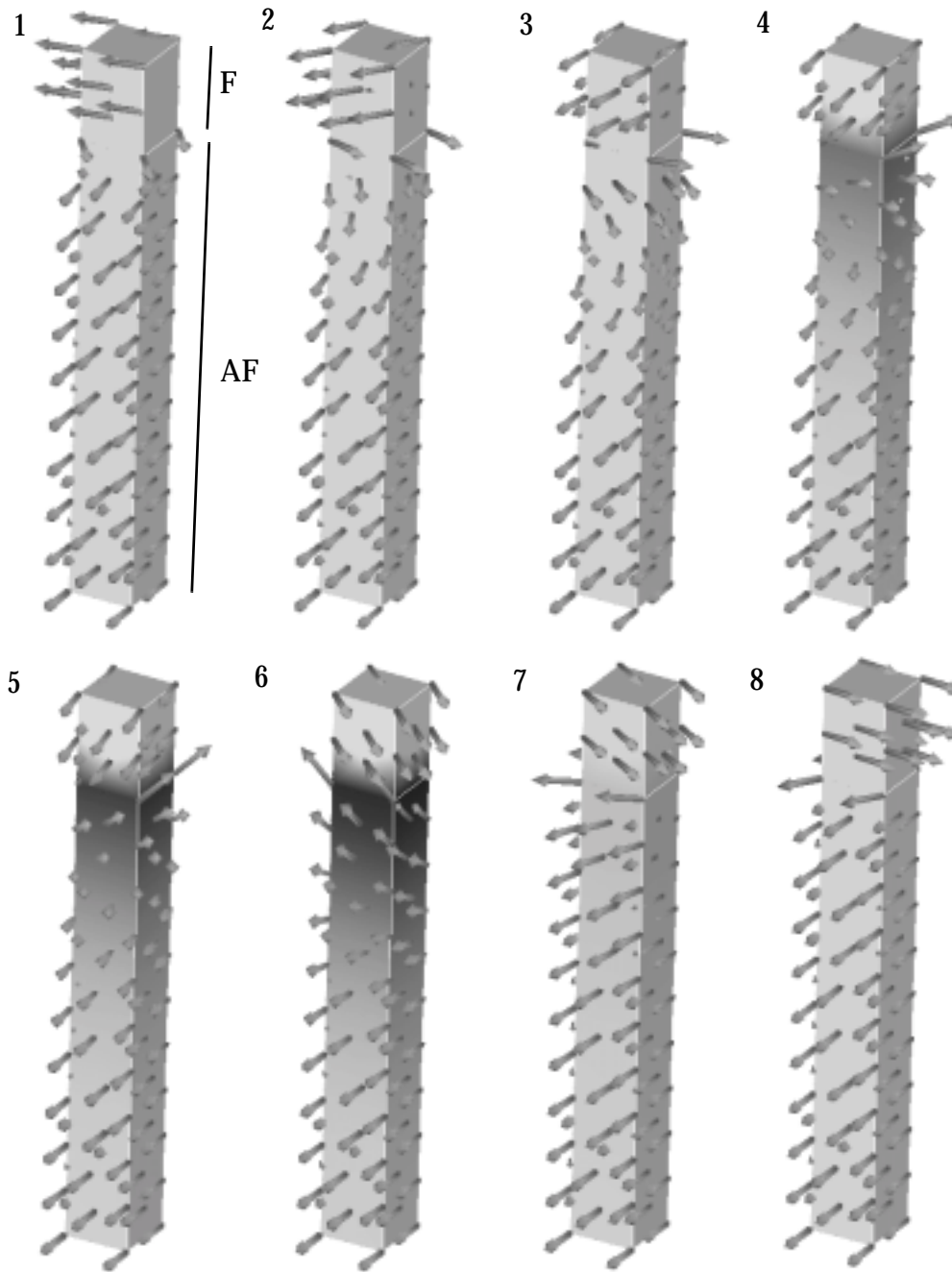


Figure 7.4: Unwinding of domain walls in the antiferromagnet as predicted by Schulthess and Butler [35]. The interface is perfectly compensated. The AF thickness is $l = 10$ nm. The uniaxial anisotropy in the antiferromagnet is, $K_1 = 1.0$ MJ/m³.

A second mechanism which increases the coercivity of the ferromagnet occurs for thin antiferromagnets. If the thickness of the antiferromagnet is smaller than the domain wall width the rotation of the ferromagnet will irreversibly switch the antiferromagnet.

Easy axis in the AF is parallel to the interface:

In order to investigate the transition between switching and not switching of antiferromagnetic grains computer simulations were performed. Ferromagnetic/antiferromagnetic bilayers are simulated. The thickness and the anisotropy constant in the antiferromagnet are varied. The interface is perfectly compensated. The exchange constant at the interface and in the bulk of the antiferromagnet is $A = -1 \times 10^{-11}$ J/m.

In the initial state the magnetization in the ferromagnet points in y -direction as shown in figure 7.5. A uniaxial easy axis parallel to the x -axis is assumed in the antiferromagnet. Thus the ferromagnet initially orients perpendicular to the easy axis of the antiferromagnet, as predicted by the model of 90° coupling for compensated interfaces. The external field initially points in x -direction. In the following the angle α , that is the angle between the external field and the x -axis, is increased from 0° to 360° in increments of 10° . The direction of the external field is always parallel to the interface. For a non zero angle α the magnetization in the AF forms a twist. This twist winds further as the spins at the interface of the AF try to follow the spins in the ferromagnet, which point in the case of an infinite large field in the field direction. The middle image in figure 7.5 shows the domain configuration in the AF/F bilayer when the external field is rotated by 90° . The anisotropy constant in the antiferromagnet is $K_1 = 0.1$ MJ/m³. The AF thickness is 40 nm. A partial domain wall can be formed although the thickness of the antiferromagnetic film is only 10 nm when the anisotropy constant is increased to $K_1 = 0.2$ MJ/m³, as shown in the right picture in figure 7.5. The large anisotropy constant decreases the domain wall width.

For both samples the partial domain wall unwinds and forms a twist with opposite chirality, when the ferromagnet is rotated beyond 90° . Thus the rotation of the ferromagnet does not irreversibly switch the antiferromagnet. The spins far away from the interface remain approximately in the easy direction during a 360° rotation of the ferromagnet.

If the thickness of the antiferromagnet or the anisotropy constant is reduced a rotation of the ferromagnet beyond 90° switches the antiferromagnet irreversibly.

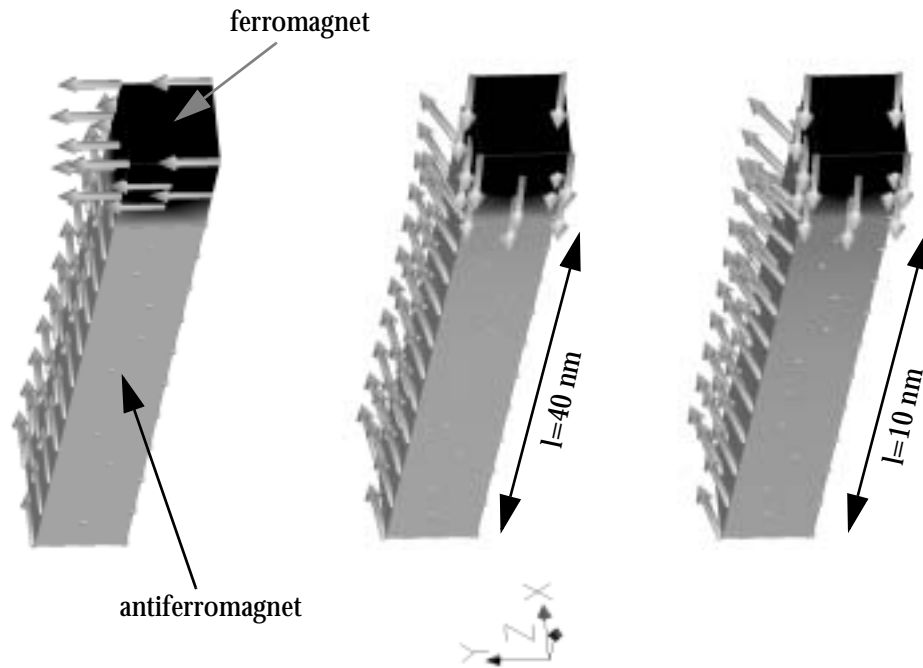


Figure 7.5: (left) In the initial state the ferromagnet points in y - direction. The antiferromagnet points in x - direction. The interface is perfectly compensated. (middle) The spin structure after rotating the ferromagnet by 90° is shown. The anisotropy constant of the antiferromagnet is, $K_1 = 0.1 \text{ MJ/m}^3$. The thickness of the AF is $l = 40 \text{ nm}$. (right) $K_1 = 0.2 \text{ MJ/m}^3$. $l = 10 \text{ nm}$.

Table 7.1 compiles the information whether the antiferromagnet can be switched or not

Tabelle 7.1 $A = -1 \times 10^{-11} \text{ J/m}$, and $J_s^A = J_s^B = 1.1 \text{ T}$. The easy axis in the antiferromagnet is parallel to the interface.

	$K=2$	$K=5$	$K=10$	$K=12$	$K=20$	$K=100$
L=10nm	switched	switched	switched	switched	NOT switched	NOT switched
L=40nm	switched	switched	NOT switched	NOT switched	NOT switched	NOT switched

for different antiferromagnetic film thicknesses and different values of the anisotropy constant.

Both processes involve irreversible changes of the magnetization.

When the antiferromagnet switches the magnetization in the antiferromagnet makes an irreversible transition to another state, which has approximately reversed antiferromagnetic order far from the interface.

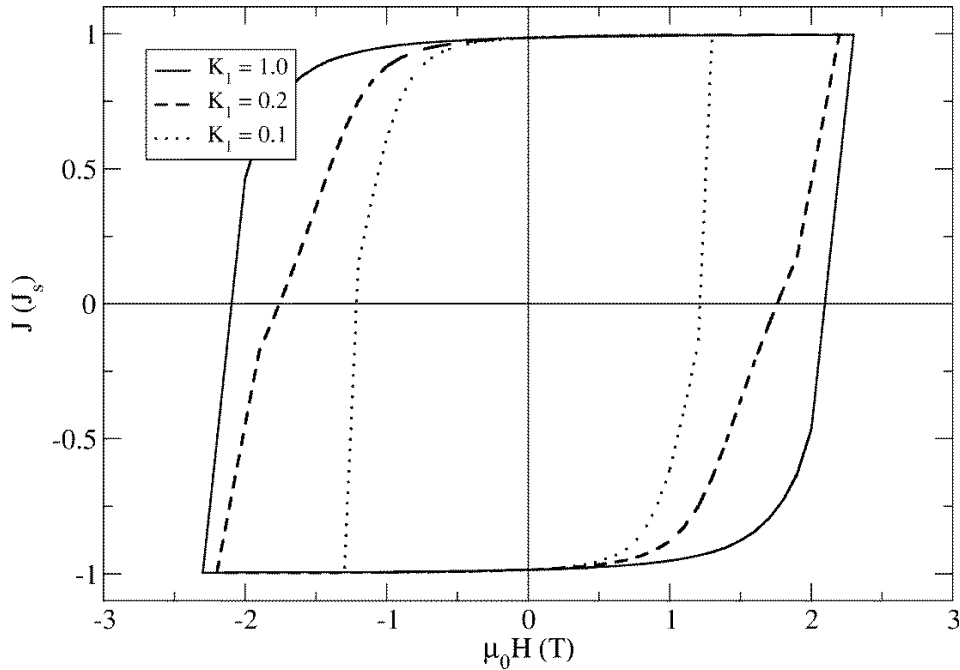


Figure 7.6: Hysteresis loop of a F/AF bilayer. The thickness of the ferromagnetic and antiferromagnetic layer is 1nm and 10nm, respectively. The anisotropy constant in the AF is varied. K_1 is measured in MJ/m^3 .

When the partial domain wall becomes unstable it irreversibly unwinds. The antiferromagnet does not switch. Spins at the bottom of the antiferromagnet remain almost parallel to the easy axis during the whole reversal of the ferromagnet.

Both processes lead to an enhanced coercivity of the ferromagnet owing to irreversible spin reorientation. Figure 7.6 compares the hysteresis loops for different values of the anisotropy constant in the antiferromagnet. The thickness of the antiferromagnet is 10 nm. For an anisotropy constant of $K_1 = 0.1 \text{ MJ}/\text{m}^3$ a rotation of the ferromagnet beyond 90° reverses the antiferromagnet. For $K_1 = 0.2 \text{ MJ}/\text{m}^3$ and $K_1 = 1.0 \text{ MJ}/\text{m}^3$ the antiferromagnet does not switch when the ferromagnet is reversed. An increase of the anisotropy constant from $K_1 = 0.2 \text{ MJ}/\text{m}^3$ to $K_1 = 1.0 \text{ MJ}/\text{m}^3$ increases the coercivity by only 20%. The small change of the coercivity is because the interface energy determines the partial wall energy. For a smaller domain wall energy a larger twist angle is formed. However in both samples the twist unwinds when the

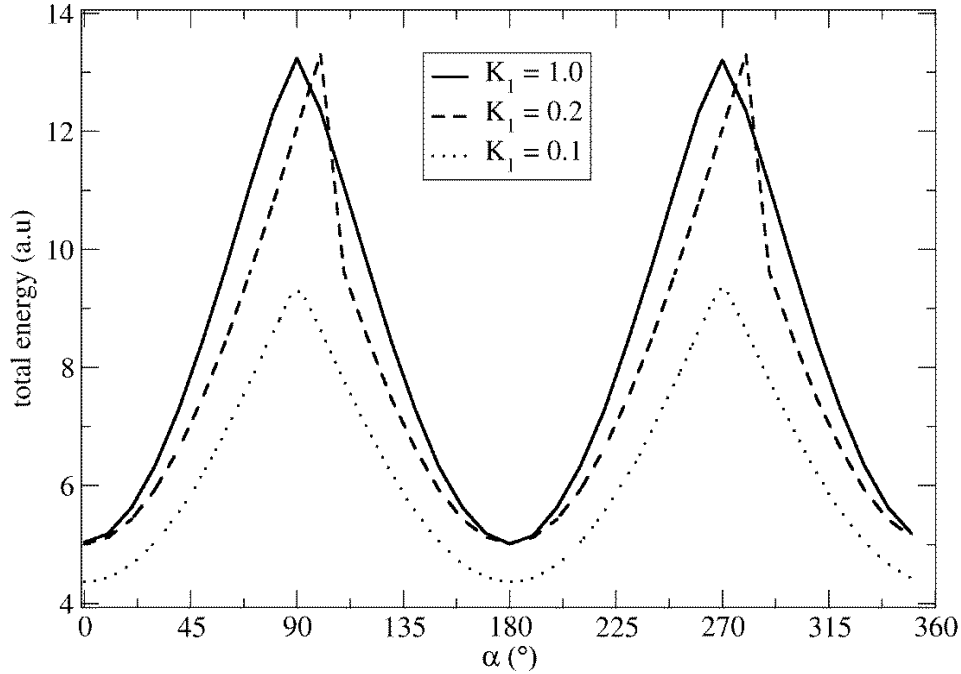


Figure 7.7: Total energy as a function of α , which denotes the angle between the external field and the hard axis of the antiferromagnet. The F/AF interface is perfectly compensated. The film thickness of the AF is, $l = 10$ nm.

twist energy exceeds the interface energy. Since the interface energy is the same in both samples the coercivity depends only little on the anisotropy constant in the antiferromagnet.

In figure 7.7 the total energy is plotted as a function of the angle between the external field and the x -axis (α). The external field strength is sufficiently large to saturate the particle. For $K_1 = 0.1$ MJ/m³ the major contribution to the total energy is the anisotropy energy. All other energy terms remain almost constant as the angle α is increased. Thus the dependence of the total energy on α , $E(\alpha)$ is determined by the anisotropy energy.

If the anisotropy constant is sufficient large to hinder switching of the antiferromagnet the interface energy determines the dependence of the total energy on α . For $K_1 = 0.2$ MJ/m³ and $K_1 = 1.0$ MJ/m³ the antiferromagnetic spins remain approximately parallel to the easy axis. As the ferromagnet is rotated by the external field the angle between the interfacial spins in the antiferromagnet and ferromagnet changes. Thus the dependence of the interface

energy on α , $E_{\text{inter}}(\alpha)$ is approximately given by $E(\alpha)$. If we compare $E_{\text{inter}}(\theta_H) \cong E(\theta_H)_H$ with the interface energy following from the biquadratic form (7.22) differences can be found. Although the positions of the maxima predicted by the biquadratic form of the interface energy (7.22) are the same as in the plots in figure 7.7, equation (7.22) does not predict sharp peaks in the energy.

The external field direction and the magnetization in the ferromagnet do not rotate in phase because of the finite external field strength. As a consequence the maxima of $E(\alpha)$ are not exactly at 90° and 270° .

Arbitrary orientation of the easy axis in the AF:

The sequence of magnetic states in figure 7.8 shows the magnetization configuration of one sublattice in the antiferromagnet and in the ferromagnet, when the ferromagnet is rotated.

The exchange constant of the antiferromagnet is $A = -1 \times 10^{-11}$ J/m. The anisotropy constants of sublattice A and B are $K_1^A = K_1^B = 1 \times 10^5$ J/m³, the magnetic polarization of the two sublattices are $J_s^A = J_s^B = 1.1$ T and the lattice constant $a = 3.76 \times 10^{-10}$ m. The ferromagnet is permalloy with $A = 1 \times 10^{-11}$ J/m, $J_s = 1$ T and $a = 4.27 \times 10^{-10}$ m. The thickness of the permalloy and of the antiferromagnetic layer is 2 nm and 10 nm, respectively. The angle between the uniaxial easy axis in the antiferromagnet and the interface plane is 5° . Initially the magnetization in the antiferromagnet points parallel to the easy axis as shown in image 1 of figure 7.8. The ferromagnet points perpendicular owing to spin flop coupling. A rotational external field rotates the ferromagnet.

Figure 7.9 shows the total energy, the exchange energy and the interface energy as a function of α . In contrast to the results in the previous section, where the uniaxial anisotropy direction was exactly parallel to the interface plane, the interface energy shows a dependence of the angle α , similar to the predictions of the biquadratic energy model (7.22).

Figure 7.8 shows magnetization configurations in the bilayer when the external field is rotated. The angle of the field direction α increases from image (1) to image (8) in figure 7.8. When the magnetization of the ferromagnet points parallel to the easy axis of the antiferromagnet (image 5) the magnetization in the antiferromagnet rotates out of the planes parallel to the interface. This out of plane rotation of the antiferromagnet is caused by a slight misorientation of the easy axis of the antiferromagnet. Contrary to the case, when the easy axis is

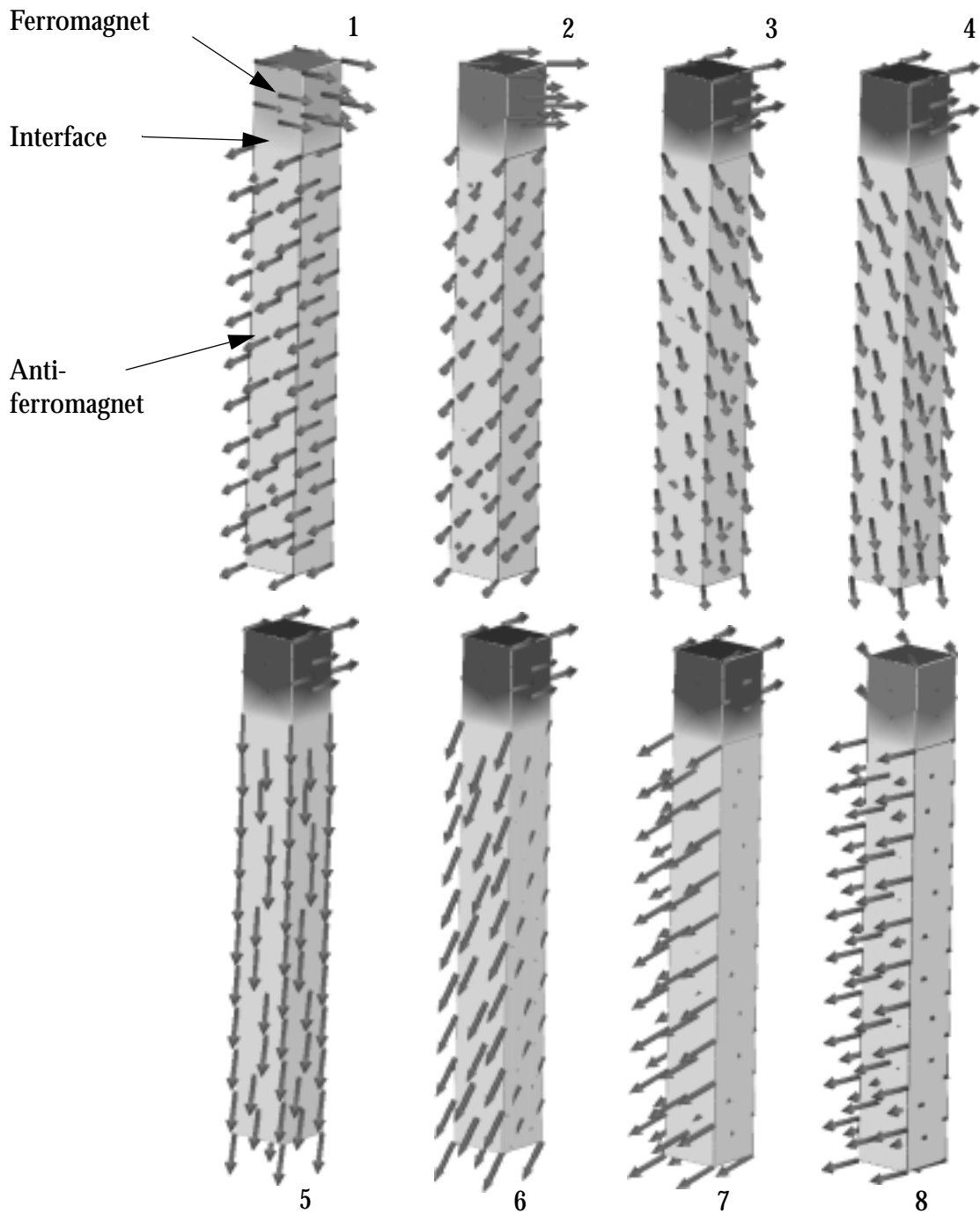


Figure 7.8: Out of plane rotation of the antiferromagnet with an easy axis not parallel to the interface. The ferromagnet thickness is 2 nm the antiferromagnet thickness is 10 nm. The angle between the easy axis in the antiferromagnet and the interface plane is 5° . The easy axis of the antiferromagnetic grain is parallel to the spins in the antiferromagnet in image 1. The interface is completely compensated. After a 180° rotation of the ferromagnet the antiferromagnet did not switch. The magnetization in the antiferromagnet in the last image (8) points in the same direction as in the first image (1).

exactly parallel to the interface plane, as investigated in the last section, it is not possible to switch a single crystal antiferromagnet with an arbitrary easy axis.

The out of plane rotation of the spins during switching of the ferromagnet reminds of the out of plane rotation Schulthess and Butler [35] found. They showed that out of plane rotations of the canted spins at the interface unwinds partial domain walls in the antiferromagnet.

7.2.3 Interface defects

In the previous section it was pointed out that the spin structure at the interface strongly influences the mechanisms leading to exchange bias. Uncompensated interfaces give rise to exchange bias as originally suggested by Meikeljohn and Bean in their intuitive picture. Compensated interfaces basically lead to an increase of the coercivity of the ferromagnet. Only under very special conditions it can give rise to exchange bias as proposed by Koon [17].

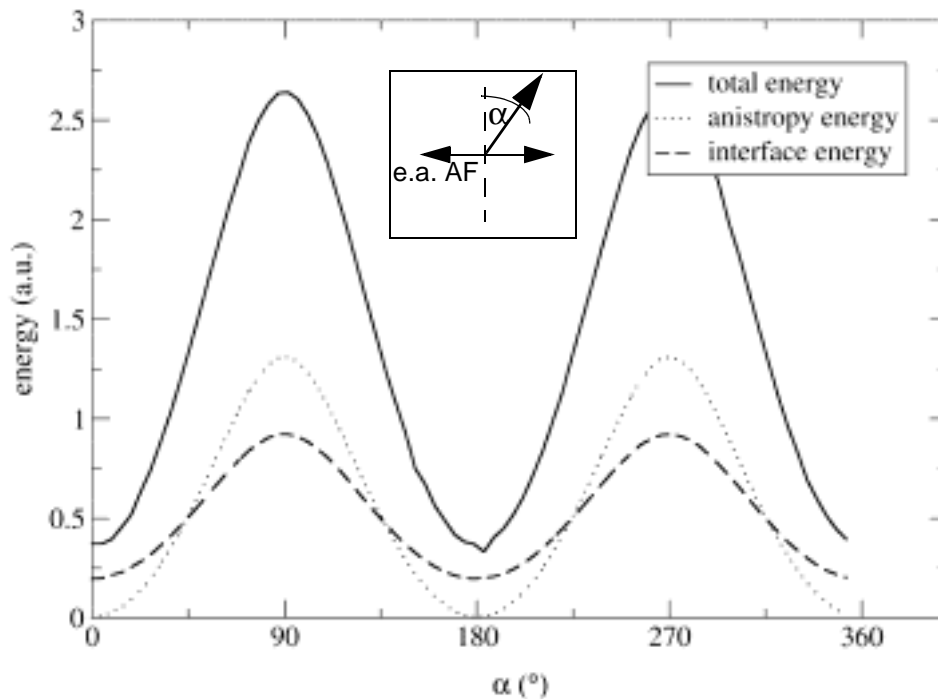


Figure 7.9: Total energy, anisotropy energy and interface energy as a function of α , which denotes the angle between the external field and the hard axis of the antiferromagnet. The angle between the easy axis and the interface plane is 5° . The inset shows the definition of the angle α which denotes the angle between the magnetization of the ferromagnet and the hard axis of the antiferromagnet (dashed line).

In real ferromagnetic/antiferromagnetic bilayers the interface is neither perfectly compensated nor perfectly uncompensated. Depending on the crystallographic orientation of grains the interface spin structure changes. Takano et al. [45] calculated the density of interfacial uncompensated spins as a function of the orientation of the grains in polycrystalline AFM films.

Another contribution to locally uncompensated regions is interface roughness. The interface roughness can be changed by controlling e.g. substrate temperature, sputtering power, sputtering rate, sputtering pressure or substrate bias. However, usually not only the interface roughness is influenced by these parameters but also the grain size or crystallinity will change in polycrystals. Thus measurements of the exchange bias field for different interface roughness are influenced by other contributions, which are difficult to separate. This problem can be reduced by measurements on antiferromagnetic single crystals.

Most measurements in textured thin films seem to agree that the exchange bias field decreases with increasing roughness [8,31,33,39]. This behavior was found for uncompensated [39] as well as for compensated [8,31,33] interfaces. It is reasonable for uncompensated interfaces because interface roughness decreases the net moment at the interface, which is commonly supposed to be responsible for exchange bias.

7.2.3.4 “Random field” Model

Equation (7.4) gives the exchange bias field when the number of uncompensated spins per unit area at the interface is given by n_0 . Using $A = \frac{JS^2}{a}$ equation (7.4) can be written as,

$$\mathbf{H}_E = \frac{2Aan_o}{t_F J_s} \mathbf{u}^A, \quad (7.24)$$

In the case of a perfectly flat compensated interface n_0 is zero. However for a rough interface that is random on an atomistic scale locally uncompensated regions occur. If the antiferromagnet remains in a single domain state, in average the number of interfacial spins in the antiferromagnet pointing in one direction will be the same as the number of spins pointing in the opposite direction. The bias field would be zero since there is no net magnetic moment at the interface in the antiferromagnet.

The random field model predicts that the antiferromagnet breaks up into domains. The spins in the antiferromagnet of one domain arrange in such a way that the net moment of the

antiferromagnetic spins at the interface point in the same direction as the ferromagnet. (Here we have assumed a positive exchange integral across the interface). The domain walls are perpendicular to the interface. The formation of a large number of small domains would be energetically favorable to minimize interface energy. However, the formation of domains costs domain wall energy. Malozemoff [18] showed that the balance between domain wall energy and interface energy is attained when the size l_w of the antiferromagnetic domains is,

$$l_w \approx \pi \sqrt{\frac{A}{K_1}}, \quad (7.25)$$

To calculate the number of uncompensated spins for perfectly rough interfaces Malozemoff applied the random field theory. At a perfectly rough interfaces the interfacial spins in the ferromagnet point completely random in one or in the opposite direction. For perfectly rough interfaces random field theory predicted that in a region with N spins on average $z\sqrt{N}$ spins are uncompensated. For a flat interface z would be one. Because of the increased number of bounds for rough interfaces z is larger than one but in the order of unity.

The number of spins in the area l_w^2 is $N = l_w^2/a^2$, where a is the lattice constant.

For the number of uncompensated spins per unit area follows,

$$n_o = \frac{z\sqrt{N}}{l_w^2} = \frac{z}{al_w} = \frac{z}{\pi a} \sqrt{\frac{K_1}{A}} \quad (7.26)$$

Substituting equation (7.26) into equation (7.24) one gets for the bias field,

$$\mathbf{H}_E = \frac{2z\sqrt{AK_1}}{\pi t_F J_s} \mathbf{u}^A. \quad (7.27)$$

It is interesting to note that the Malozemoff formula is very similar to Mauri's planar interfacial antiferromagnet domain model given by equation (7.13), although the origin of the exchange bias field is completely different.

7.2.3.5 Transition from spin flop coupling to collinear coupling

Let us assume a rough compensated interface between a ferromagnet and an antiferromagnet. If the exchange integral in the antiferromagnet and across the interface are approximately the same equation (7.20) predicts a net moment due to the spin flop coupling of

$$\mu_{net} \approx 0.1 \times \mu_{AF} \times N, \quad (7.28)$$

where N is the number of interface spins and μ_{AF} the magnetic moment of one atom at the interface in the antiferromagnet.

Let us compare the spin flop coupling strength with the coupling strength according to the random field model. For a perfectly rough region with N atoms, where $N = l_w^2/a^2$, the random field model predicts a net moment,

$$\mu_{net} = z \times \mu_{AF} \times \sqrt{N}. \quad (7.29)$$

For realistic domain wall widths the net moment owing to spin flop coupling is much larger than the net moment according to the random field model. This estimation proposes that spin flop coupling is much stronger than the direct coupling.

A detailed analysis of the transition from spin flop coupling to collinear coupling can be found in the appendix.

7.3 Continuum theory for antiferromagnets

A simple theory which was used to describe magnetic processes in magnetic particles was developed by Stoner and Wohlfarth [43]. The theory describes magnetization reversal of non interacting single domain particles. The Stoner-Wohlfarth theory successfully predicts the critical fields and the dependence of the magnetization as a function of field strength and field angle. Although the Stoner-Wohlfarth theory is widely applicable and it was even successful applied for exchange bias systems by T. Mewes et al. [22] it breaks down when domain processes dominate the reversal mechanism of the considered sample. The continuum theory of micromagnetics, developed by Brown [2], is suitable to calculate the magnetic configuration on a mesoscopic length scale. In the continuum theory of micromagnetics the spontaneous polarization is assumed to be a continuous function of space $\mathbf{J}(\mathbf{x})$. The magnetic polarization is the magnetic moment per unit volume times μ_0 . The magnetic moment at a lattice point \mathbf{x}_a of the magnet is the value of the function $\mathbf{J}(\mathbf{x})$ at the point \mathbf{x}_a divided by n , where n is the number of spins per volume (for a simple cubic lattice $n=1/a^3$; a = lattice constant). The stable equilibrium state of the specimen's magnetization is found by minimizing an expression for the total free energy. The total free energy is the sum of the exchange energy, the Zeeman energy, the stray field energy, the crystalline anisotropy energy, and the magnetostrictive energy. In the following we neglect the magnetostrictive energy. Magnetic domains, which originally were proposed by Weiss in order to account for the observed magnetization and hysteresis curves, are formed due to the interplay between the different energies. Since for various applications (e.g. hard disc media, MRAMs...) the question of interest is not only the equilibrium distribution of the magnetization but the relaxation of the system to equilibrium, the theory had to be extended to describe the time evolution of the magnetization. The Gilbert equation of motion

$$\frac{\partial \mathbf{J}}{\partial t} = -\gamma \mathbf{J} \times \mathbf{H}_{eff} + \frac{\alpha}{J_s} \mathbf{J} \times \frac{\partial \mathbf{J}}{\partial t}, \quad (7.30)$$

is believed to describe the relaxation of the spontaneous polarization \mathbf{J} towards equilibrium. α is the phenomenologically introduced damping constant. The effective field is the negative functional derivative of the total free energy with respect to the spontaneous polarization \mathbf{J} .

$$\mathbf{H}_{eff} = -\frac{\delta E_{tot}}{\delta \mathbf{J}}, \quad (7.31)$$

The Gilbert equation (2.1) is mathematically equivalent to the Landau-Lifshitz-Gilbert (LLG) equation

$$\frac{\partial \mathbf{J}}{\partial t} = -\frac{|\gamma|}{1 + \alpha^2} \mathbf{J} \times \mathbf{H}_{eff} - \frac{\alpha}{1 + \alpha^2} \frac{|\gamma|}{J_s} \mathbf{J} \times (\mathbf{J} \times \mathbf{H}_{eff}). \quad (7.32)$$

The continuum theory of micromagnetics is an efficient starting point for describing dynamic or static processes in a magnetic sample numerically. For numerical calculations the spontaneous polarization has to be discretized. However, the discretization size is usually much larger than the atomic lattice constant, which means that an equivalent physical system can be described with less variables. This is possible because the spins do not change significantly from lattice point to lattice point owing to ferromagnetic exchange coupling. The length over which the magnetic polarization changes from one domain to the next depends on the material parameters. The so-called domain wall width is, $l_{dw} = \pi \sqrt{A/K_1}$, where A is the exchange constant and K_1 the uniaxial anisotropy constant. For hard magnetic materials the domain wall length is in the order of some nanometers, for soft magnetic materials it is even one or two orders of magnitude larger. Due to the slowly varying spin directions on a length scale of $l_c = \min(\sqrt{A/K_1}, \sqrt{2\mu_0 A/J_s^2})$ the discretization error of the numerical method remains small if the discretization is smaller than l_c .

At first glance it seems that this concept cannot be applied to antiferromagnetic materials, since the direction of the spins usually changes from lattice point to lattice point, which would result in a discretization length equal to the atomic lattice constant. However, if the antiferromagnet is subdivided into sublattices, again the magnetic moments vary slowly in space within each sublattice. Figure 7.10 shows a domain wall in an antiferromagnet. The subdivision of the system into a sublattice A and a sublattice B yields a distribution of the magnetic moments similar to that of a ferromagnet for both sublattices. Hence it seems reasonable to develop a continuum theory for antiferromagnets which is similar to that for ferromagnets.

Zeeman Energy: The Zeeman energy for a ferromagnet is given by

$$E_{H,ferro} = -\int \mathbf{J} \mathbf{H}_{ext} dV. \quad (7.33)$$

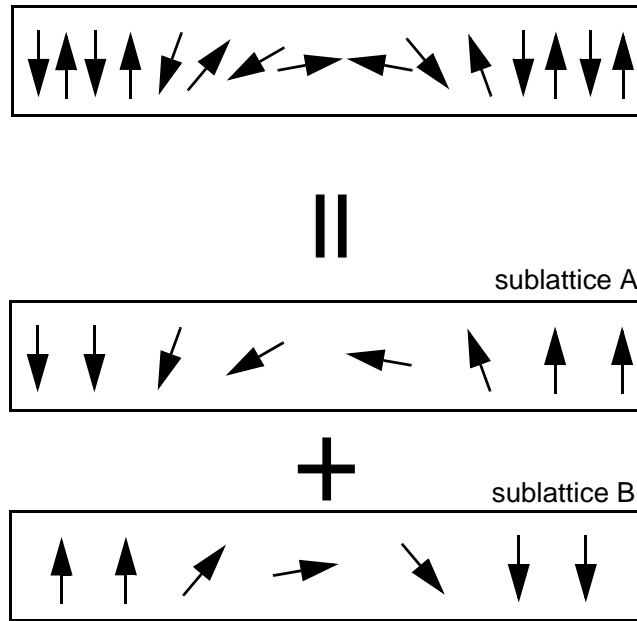


Figure 7.10: Schematic diagram that shows the subdivision of an antiferromagnet into two sublattices. The antiferromagnetic wall structure can be represented in a continuum model by two walls, one in each sublattice.

If the Zeeman energy is calculated for both sublattices separately, it follows for the antiferromagnet

$$E_{H, \text{antiferro}} = - \int \mathbf{J}^A \mathbf{H}_{\text{ext}} dV - \int \mathbf{J}^B \mathbf{H}_{\text{ext}} dV \quad , \quad (7.34)$$

where $\mathbf{J}^A = J_s^A \mathbf{u}$ and $\mathbf{J}^B = J_s^B \mathbf{u}$ denote the spontaneous polarization for sublattice A and sublattice B , respectively. The unit vector \mathbf{u} points in the direction of the spontaneous magnetic polarization. For a ferromagnet $J_s = \mu_0 g n \mu_B S$, where n is the number of spins per volume (for a simple cubic lattice $n=1/a^3$), S the total spin quantum number of one atom, g the Landé factor and μ_B the Bohr magneton. The subdivision of the antiferromagnet into two sublattices decreases the number of spins per volume (n^A or n^B) for every sublattice by a factor 2. As a consequence the spontaneous polarization of each sublattice (provided the atomic moment is the same for both sublattices, which has not necessarily to be the case) is half the spontaneous polarization of the undivided system

$$J_s^A = \frac{\mu_0 g n \mu_B S^A}{2}, \quad (7.35)$$

$$J_s^B = \frac{\mu_0 g n \mu_B S^B}{2} \quad (7.36)$$

For example, $J_s^A = \mu_0 g n^A \mu_B S$ and n^A denotes the number of spins in sublattice A per volume.

Anisotropy Energy: If the in-plane anisotropy is neglected, the anisotropy energy for crystals with uniaxial symmetry can be expressed as,

$$E_{K,ferro} = \int K_1 [1 - (\mathbf{u}\mathbf{k})^2] dV = \int K_1 \sin^2 \theta dV, \quad (7.37)$$

where θ is the angle between the magnetization and the easy axis \mathbf{k} . K_1 denotes the first anisotropy constant. If the angle between the magnetic polarization and the easy axis is 90° , K_1 gives the anisotropy energy per volume. Another equivalent form, which will be used later, is

$$E_{K,ferro} = \int \mathbf{u} M \mathbf{u} dV + const, \quad (7.38)$$

where M is a tensor with

$$M_{lm} = K_1 k_l k_m, \quad (7.39)$$

If \tilde{K}_1 is the anisotropy energy of one spin and n the number of spins per volume, $K_1 = n \tilde{K}_1$. Because of the argument mentioned above in the description of the Zeeman energy,

$$K_1^A = K_1^B = \frac{K_1}{2} \quad (7.40)$$

In an antiferromagnet the anisotropy energy may be different in the different sublattices. The general form of the anisotropy energy of a uniaxial antiferromagnet is

$$E_{K, antiferro} = - \int K_1^A (\mathbf{u}^A \mathbf{k}^A)^2 dV - \int K_1^B (\mathbf{u}^B \mathbf{k}^B)^2 dV + const. \quad (7.41)$$

Exchange Energy: When the spin operators are approximated as classical vectors the exchange energy can be written in the form

$$E_{ex} = - \sum_{i=1}^N \sum_{j \neq i}^N J_{ij} \mathbf{S}_i \cdot \mathbf{S}_j, \quad (7.42)$$

where J_{ij} is the exchange integral, which can be calculated using quantum mechanics [24]. To derive a continuum expression one has to distinguish between different lattice structures.

• **Antiferromagnetic ordering on a simple cubic lattice:**

If the nearest neighbor interaction is responsible for the magnetic ordering, the six nearest neighbors (nN) point antiparallel to the spin in the middle as shown in figure 7.11 (a). The local moments fall on two interpenetrating face-centered cubic sublattices. Within each sublattice the spins vary only slowly with space. If both sublattices have the same number of spins ($N/2$) equation (7.42) can be written in the form.

$$E_{ex, antiferro} = \left(-J \sum_{i=1}^{N/2} \mathbf{S}_i^A \cdot \sum_j^{nN} \mathbf{S}_j^B \right) + \left(-J \sum_{i=1}^{N/2} \mathbf{S}_i^B \cdot \sum_j^{nN} \mathbf{S}_j^A \right) = -2J \sum_{i=1}^{N/2} \mathbf{S}_i^A \cdot \sum_j^{nN} \mathbf{S}_j^B \quad (7.43)$$

$$= -2J \sum_{i=1}^{N/2} \mathbf{S}^A(\mathbf{x}_i) \cdot \sum_j^{nN} \mathbf{S}^B(\mathbf{x}_j) = -2J \sum_{i=1}^{N/2} \mathbf{S}^A(\mathbf{x}_i) \cdot \sum_{k=1}^6 \mathbf{S}^B(\mathbf{x}_i + \delta_k). \quad (7.44)$$

In a continuum limit, we want all our variables to be evaluated at the same point. Thus we expand $\mathbf{S}^B(\mathbf{x}_j)$ about \mathbf{x}_i . For a cubic lattice with lattice constant a ,

$$\delta_k = \begin{bmatrix} a \\ 0 \\ 0 \end{bmatrix}_{k=1}, \begin{bmatrix} -a \\ 0 \\ 0 \end{bmatrix}_{k=2}, \begin{bmatrix} 0 \\ a \\ 0 \end{bmatrix}_{k=3}, \begin{bmatrix} 0 \\ -a \\ 0 \end{bmatrix}_{k=4}, \begin{bmatrix} 0 \\ 0 \\ a \end{bmatrix}_{k=5}, \begin{bmatrix} 0 \\ 0 \\ -a \end{bmatrix}_{k=6}. \quad (7.45)$$

The k -th component of the spin can be expanded as,

$$S_k^B(\mathbf{x}_j) \approx S_k^B(\mathbf{x}_i) + \left(\frac{\partial S_k^B}{\partial x} \delta_x + \frac{\partial S_k^B}{\partial y} \delta_y + \frac{\partial S_k^B}{\partial z} \delta_z \right) + \frac{1}{2} \left(\frac{\partial^2 S_k^B}{\partial^2 x} \delta_x^2 + \frac{\partial^2 S_k^B}{\partial^2 y} \delta_y^2 + \frac{\partial^2 S_k^B}{\partial^2 z} \delta_z^2 \right). \quad (7.46)$$

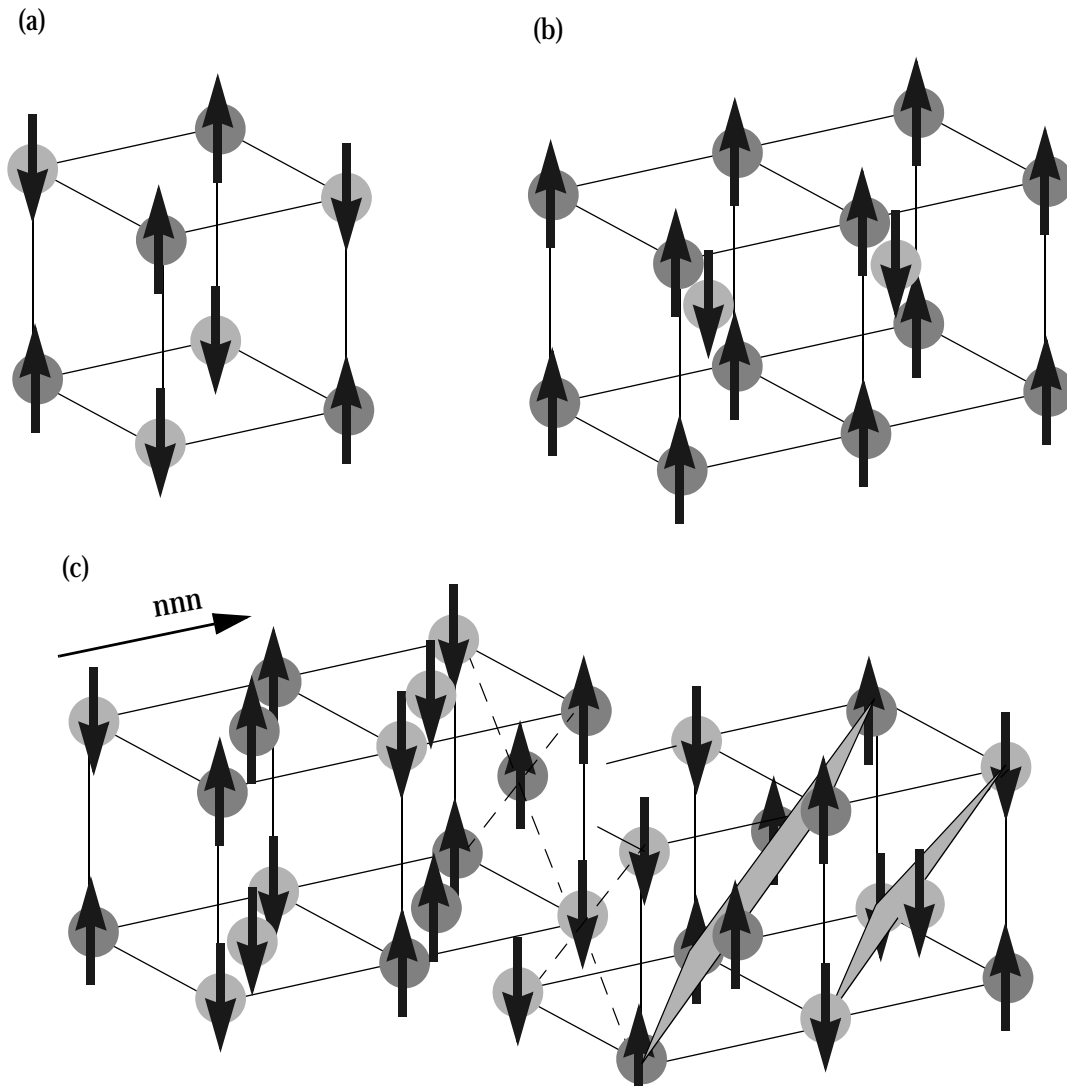


Figure 7.11: (a) Antiferromagnetic ordering on a simple cubic lattice. Spins of the same kind form two interpenetrating face-centered cubic lattices (b) Antiferromagnetic ordering on a body-centered cubic lattice. Spins of the same kind form two interpenetrating simple cubic lattices. (c) Antiferromagnetic ordering on an fcc lattice for the case of a negative next nearest neighbor interaction (e.g. CoO). The fcc lattice consists of four interpenetrating simple cubic lattices. The vector *nnn* connects next nearest neighbors.

The first-order terms and second order cross terms vanish in the sum over nearest neighbors because of the symmetry of the cubic lattice. That is why they are omitted in the expansion of equation (7.46). Using equation (7.46),

$$\sum_j^{nN} S^B(\mathbf{x}_j) = 6S^B(\mathbf{x}_i) + a^2 \Delta S^B(\mathbf{x}_i). \quad (7.47)$$

To obtain the continuum expression (7.47), some assumptions have been used. In the summation over all position vectors δ_k it was assumed that all of them are inside the crystal. However, on a surface the number of neighbors is reduced and the sum may come up different than at internal points. To compensate this error, an additional term to the surface anisotropy can be added. Using equation (7.47) equation (7.44) can be written in the continuum limit as

$$\begin{aligned} E_{ex,antiferro} &= -\frac{12JS^2}{a^3} \sum_{i=1}^{14} \mathbf{u}^A(\mathbf{x}_i) \mathbf{u}^B(\mathbf{x}_i) a^3 - \frac{2JS^2}{a} \sum_{i=1}^{14} \mathbf{u}^A(\mathbf{x}_i) \Delta \mathbf{u}^B(\mathbf{x}_i) a^3 \\ &= -\frac{12JS^2}{a^3} \frac{1}{2} \int_V \mathbf{u}^A(\mathbf{x}_i) \mathbf{u}^B(\mathbf{x}_i) dV - \frac{2JS^2}{a} \frac{1}{2} \int_V \mathbf{u}^A(\mathbf{x}_i) \Delta \mathbf{u}^B(\mathbf{x}_i) dV, \end{aligned} \quad (7.48)$$

where $\mathbf{S} \cdot \mathbf{u}^B(\mathbf{x}_i) = S^B(\mathbf{x}_i)$. Applying Greens first identity and the condition that the normal derivative of the magnetic polarization at the surface vanishes, equation (7.48) transforms to

$$\begin{aligned} E_{ex,antiferro} &= -6 \frac{A}{a^2} \int_V \mathbf{u}^A(\mathbf{x}_i) \mathbf{u}^B(\mathbf{x}_i) dV + \\ &A \int_V (\nabla u_x^A(\mathbf{x}_i) \nabla u_x^B(\mathbf{x}_i) + \nabla u_y^A(\mathbf{x}_i) \nabla u_y^B(\mathbf{x}_i) + \nabla u_z^A(\mathbf{x}_i) \nabla u_z^B(\mathbf{x}_i)) dV, \end{aligned} \quad (7.49)$$

where $A = \frac{JS^2}{a}$.

• **Antiferromagnetic ordering on a body-centered cubic lattice:**

For a dominating nearest neighbor interaction all eight nearest neighbors of one atom point antiparallel. The derivation of the exchange energy is very similar to the previous deriva-

tion, only the number of nearest neighbors changes from 6 to 8, and the distance between nearest neighbors changes from a to $\sqrt{3}a/2$. The sum over the nearest neighbors yield,

$$\sum_{j=1}^8 S^B(\mathbf{x}_j) = 8S^B(\mathbf{x}_i) + 3a^2\Delta S^B(\mathbf{x}_i). \quad (7.50)$$

Hence we get for the exchange energy

$$E_{ex,antiferro} = -8\frac{A}{a^2} \int_V \mathbf{u}^A(\mathbf{x}_i)\mathbf{u}^B(\mathbf{x}_i)dV +$$

$$3A \int_V (\nabla u_x^A(\mathbf{x}_i)\nabla u_x^B(\mathbf{x}_i) + \nabla u_y^A(\mathbf{x}_i)\nabla u_y^B(\mathbf{x}_i) + \nabla u_z^A(\mathbf{x}_i)\nabla u_z^B(\mathbf{x}_i))dV, \quad (7.51)$$

where $A = \frac{JS^2}{a}$.

• Antiferromagnetic ordering on an fcc lattice

The face centered cubic lattice represents a more complicated situation, since it is not possible to arrange all nearest neighbors of one atom antiparallel. Neutron diffraction studies [36] revealed the structure of MnO, as shown in figure (7.11 c). All the next nearest neighbors point antiparallel. Hence the important interaction that produces the antiferromagnetic ordering must be the next nearest neighbor interaction (indirect exchange), which is in figure (7.11 c) along a cube edge and denoted with the vector mmn . In figure (7.11 c) the spins of two interpenetrating cubic sublattices are drawn separately. Four interpenetrating equivalent simple cubic lattices form on fcc lattice. If nearest neighbor interaction is neglected these four sublattices are not exchange coupled in the bulk, however they are indirectly exchange coupled via the interface to the ferromagnet. For all four sublattices equation (7.49) can be used for the calculation of the exchange energy.

Stray field energy:

For ferromagnets the stray field ${}^m H_{S,ferro}$ is obtained from a boundary value problem,

$$\Delta u = \frac{\nabla \mathbf{J}_s}{\mu_0} \text{ and } {}^m\mathbf{H}_{S,ferro} = -\nabla u \quad (7.52)$$

To apply the boundary condition $u = 0$ at infinity a hybrid finite element boundary element method [9] is used. For the stray field energy follows

$${}^mE_S = -\frac{1}{2} \int {}^m\mathbf{H}_{S,ferro} \mathbf{J} dV. \quad (7.53)$$

Equation (2.30) does not take care of the atomic structure of the material, since the magnetic moments are replaced by the continuum function of space $\mathbf{u}(\mathbf{x})$ for the normalized magnetization. The atomic structure leads to an additional field,

$${}^a\mathbf{H}_{S,ferro} = \frac{1}{\mu_0} \left(\frac{1}{3} \mathbf{J} + C\mathbf{J} \right), \quad (7.54)$$

where C is a tensor which depends on the crystalline symmetry. C vanishes for a cubic symmetry. So the total stray field is the sum,

$$\mathbf{H}_{S,ferro} = {}^a\mathbf{H}_{S,ferro} + {}^m\mathbf{H}_{S,ferro} \quad (7.55)$$

The atomic field leads to the additional energy

$${}^aE_{S,ferro} = -\frac{1}{\mu_0} \int \left(\frac{1}{3} \mathbf{J}^2 + \mathbf{J}C\mathbf{J} \right) dV. \quad (7.56)$$

The first term in equation (7.56) is constant. Therefore it can be omitted since it only shifts the zero level of energy. In equation (7.54) the first term does not change the dynamics of the system, since the effective field in the Landau-Lifshitz-Gilbert equation (2.2) only occurs in terms of $\mathbf{J} \times \mathbf{H}_{eff}$. Hence all field contributions parallel to \mathbf{J} vanish. The second term in equation (7.56) is of the form of the anisotropy energy (7.38). Thus this additional energy term can be added to the anisotropy constant. If the anisotropy constant is measured in experiments, the measurement cannot distinguish between the different origins to the anisotropy. So measured anisotropy constants already include this term.

Analogously, the stray field in antiferromagnets with two sublattices follows as,

$${}^a\mathbf{H}_{S, antiferro} = \frac{1}{\mu_0} \left(\frac{1}{3} \mathbf{J}^A + C^A \mathbf{J}^A \right) + \frac{1}{\mu_0} \left(\frac{1}{3} \mathbf{J}^B + C^B \mathbf{J}^B \right) \quad (7.57)$$

and

$$\Delta^a u = \frac{\nabla(\mathbf{J}^A + \mathbf{J}^B)}{\mu_0} \quad \text{and} \quad {}^m\mathbf{H}_{S, antiferro} = -\nabla^a u. \quad (7.58)$$

The atomic field ${}^a\mathbf{H}_{S, antiferro}$ leads to an additional contribution to the stray field energy

$$\begin{aligned} {}^aE_{S, antiferro} &= -\frac{1}{\mu_0} \int \left(\frac{1}{3} \mathbf{J}^A \mathbf{J}^A + \mathbf{J}^A C^A \mathbf{J}^A + \frac{1}{3} \mathbf{J}^A \mathbf{J}^B + \mathbf{J}^A C^B \mathbf{J}^B \right) dV. \\ &\quad -\frac{1}{\mu_0} \int \left(\frac{1}{3} \mathbf{J}^B \mathbf{J}^A + \mathbf{J}^B C^A \mathbf{J}^A + \frac{1}{3} \mathbf{J}^B \mathbf{J}^B + \mathbf{J}^B C^B \mathbf{J}^B \right) dV \end{aligned} \quad (7.59)$$

The terms $\mathbf{J}^A \mathbf{J}^A$ and $\mathbf{J}^B \mathbf{J}^B$ can be omitted since they only shift the zero level of energy. The scalar product $\mathbf{J}^A \mathbf{J}^B$ is a small correction to the exchange energy. The terms $\mathbf{J}^A C^A \mathbf{J}^A$ and $\mathbf{J}^B C^B \mathbf{J}^B$ are already taken into account in the anisotropy constant. The remaining terms are of the form $\mathbf{J}^A C^A \mathbf{J}^B$. They give rise to an anisotropic exchange interaction. The contribution of these term to the energy are smaller than the anisotropy energy or at most comparable with the anisotropy energy, because the matrix C^A is the same as in the term $\mathbf{J}^A C^A \mathbf{J}^A$. However from experiments follows that the exchange energy, $-\frac{A}{a^2} \int \mathbf{u}^A(\mathbf{x}_i) \mathbf{u}^B(\mathbf{x}_i) dV$, which is responsible for an antiparallel alignment in collinear antiferromagnets is usually two orders of magnitude larger than the anisotropy energy. Hence, we neglect the terms $\mathbf{J}^A C^A \mathbf{J}^B$ and consider only the magnetostatic field which arises from the Poisson equation (7.58). The stray field energy follows as,

$$E_{S, antiferro} = -\frac{1}{2} \int {}^m\mathbf{H}_{S, antiferro} (\mathbf{J}^A + \mathbf{J}^B) dV. \quad (7.60)$$

7.3.1 Coupling to a ferromagnet

In the following we derive the interface energy in continuum limit. We start from equation (2.34). If we separate the terms in the sum, which describe the energy across the interface between the ferromagnet and antiferromagnet, we can combine them in the interface exchange energy.

$$E_{ex,interface} = - \sum_{i=1}^N J_{ij} S_i^F S_i^{AF} - \sum_{i=1}^N J_{ij} S_i^{AF} S_i^F = -2 \sum_{i=1}^N J_{ij} S_i^{AF} S_i^F, \quad (7.61)$$

where S_i^F denotes the spin vector in the ferromagnet at node point i . S_i^A is the nearest neighbor to S_i^F in the antiferromagnet. The antiferromagnet splits into two sublattices A and B . If we assume I_A atoms of sublattice A at the interface and I_B atoms of sublattice B at the interface equation (7.61) becomes

$$E_{ex,interface} = -2JS^2 \sum_{i=1}^{I_A} \mathbf{u}^{A,F}(\mathbf{x}_i) \mathbf{u}^A(\mathbf{x}_i) - 2JS^2 \sum_{i=1}^{I_B} \mathbf{u}^{B,F}(\mathbf{x}_i) \mathbf{u}^B(\mathbf{x}_i) \quad (7.62)$$

Replacing the sum with an integral and introducing the number of interface atoms of sublattice A per unit area n_0^A and the number of interface atoms of sublattice B per unit area n_0^B we get,

$$E_{ex,interface} = -2JS^2 n_0^A \int_A \mathbf{u}^{A,F}(\mathbf{x}_i) \mathbf{u}^A(\mathbf{x}_i) dA - 2JS^2 n_0^B \int_A \mathbf{u}^{B,F}(\mathbf{x}_i) \mathbf{u}^B(\mathbf{x}_i) dA \quad (7.63)$$

If we assume a perfectly compensated interface ($I_A = I_B$) and a simple cubic lattice with lattice constant a we get,

$$n_0^A = n_0^B = \frac{1}{2a^2}. \quad (7.64)$$

The reduced number of nearest neighbors in the antiferromagnet changes the exchange energy in the antiferromagnet given by equation (7.49). If the interface is completely uncompensated, the spins of one sublattice which couples to the interface has 5 nearest neighbors in the antiferromagnet. Hence the exchange energy at the interface is

$$E_{ex,surface} = -5Aan_0^A \sum_{i=1}^{I_A} \mathbf{u}^A(\mathbf{x}_i) \mathbf{u}^B(\mathbf{x}_i) \quad (7.65)$$

Considering surface effects in equation (7.49), it changes to

$$\begin{aligned}
E_{ex} = & -5Aan_0^A \int_A \mathbf{u}^A(\mathbf{x}_i) \mathbf{u}^B(\mathbf{x}_i) dA \\
& -6 \frac{A}{a^2} \int_V \mathbf{u}^A(\mathbf{x}_i) \mathbf{u}^B(\mathbf{x}_i) dV + \\
& A \int_V (\nabla u_x^A(\mathbf{x}_i) \nabla u_x^B(\mathbf{x}_i) + \nabla u_y^A(\mathbf{x}_i) \nabla u_y^B(\mathbf{x}_i) + \nabla u_z^A(\mathbf{x}_i) \nabla u_z^B(\mathbf{x}_i)) dV \quad , \quad (7.66)
\end{aligned}$$

In the last term in (7.66) the surface effects have not been corrected. The justification will be given in the section 7.3.3.

For a cubic lattice, where all spins at the interface belong to sublattice A , $n_0^A = \frac{1}{a^2}$.

For a partly compensated interface the first term in equation (7.66) has to be changed to,

$$E_{ex} = -5JS^2 (n_0^A + n_0^B) a \int_A \mathbf{u}^A(\mathbf{x}_i) \mathbf{u}^B(\mathbf{x}_i) dA + \dots \quad (7.67)$$

7.3.2 Effective fields

Analogous to the calculation of the effective field in a ferromagnet, the k -th component of the effective field on node i of sublattice A is approximated, using the box scheme,

$$H_i^{k,A}{}_{eff} \approx -\frac{1}{m_i} \frac{\partial E_t}{\partial u_i^{k,A}}, \quad (7.68)$$

where m_i^A denotes the magnetic moment on the node point i of sublattice A . It follows from the integral

$$m_i^A = \int_{V_i} J_s^A(\mathbf{x}) dV, \quad (7.69)$$

where V_i satisfies

$$\sum_j V_j = V \text{ and } V_i \cap V_j = 0 \text{ for } i \neq j. \quad (7.70)$$

The total energy can be written within the finite element approach as (see section 1),

$$E_t = \int_{\Omega} e_t(\mathbf{J}^A, \mathbf{J}^B) dV \cong \sum_{e=1}^{N_e} \int_{\Omega_e} e_t \left(\mathbf{J}_{s,e}^A \sum_{i=1}^{N_b} u_{e,i}^{k,A} \varphi_{e,i}(\mathbf{x}), \mathbf{J}_{s,e}^B \sum_{i=1}^{N_b} u_{e,i}^{k,B} \varphi_{e,i}(\mathbf{x}) \right) dV \quad (7.71)$$

The magnetic polarization \mathbf{J} is approximated using standard linear basis function on tetrahedral elements.

The calculation of the stray field and anisotropy field is analogous to the calculation for ferromagnets.

The calculation of the exchange energy requires special consideration because of the two sublattice approach and the coupling to the ferromagnets.

Bulk: Let us start with the calculation of the exchange field in the bulk. The second term and the third term in equation (7.66) contribute to the exchange field. The contribution from the second term to the exchange field on node i is

$$H_{i,ex}^{k,A} = 6 \frac{A}{J_s a^2} \mathbf{u}^B(\mathbf{x}_i), \quad (7.72)$$

The contribution owing to the third term can be calculated on an element by element fashion. For the local derivative follows

$$\frac{\partial E_{ex}}{\partial u_{e,j}^{k,A}} = \sum_{\tilde{e}=1}^{N_e} \int_{\Omega_{\tilde{e}}} A \sum_l^{x,y,z} \frac{\partial}{\partial u_{e,j}^k} \left(\nabla \sum_{i=1}^{N_b} u_{\tilde{e},i}^{l,A} \varphi_{\tilde{e},i}(\mathbf{x}) \nabla \sum_{i=1}^{N_b} u_{\tilde{e},i}^{l,B} \varphi_{\tilde{e},i}(\mathbf{x}) \right) dV. \quad (7.73)$$

$$\frac{\partial E_{ex}}{\partial u_{e,j}^{k,A}} = A \left[\sum_{l=1}^{N_b} u_{e,l}^{k,B} M_{lj}^e \right], \quad (7.74)$$

where M_{lj}^e is the element matrix.

Interface: The exchange field on the interface to a ferromagnet follows from the derivative of the scalar product term (first term) in equation (7.66) plus the derivative of the gradient term (third term) in equation (7.66) plus the derivative of the interface energy (7.63) with respect to the node point on the surface. From the scalar product term in equation (7.66) follows,

$$H_i^{k,A}{}_{ex} = \frac{5JS^2 (n_0^A + n_0^B)a}{m_i^A} \mathbf{u}^B(\mathbf{x}_i) \Delta A_i, \quad (7.75)$$

where ΔA_i is the surrounding area of node i such that,

$$\sum_{i=1}^{sN} A_i = A \text{ and } A_i \cap A_j = 0 \text{ for } i \neq j. \quad (7.76)$$

sN is the number node points on the surface.

The contribution from the interface between antiferromagnet and ferromagnet to the exchange field is

$$H_i^{k,A}{}_{ex} = \frac{2JS^2 n_0^A}{m_i^A} \mathbf{u}^{A,F}(\mathbf{x}_i) \Delta A_i, \quad (7.77)$$

The derivative of the gradient term (third term) in equation (7.66) is the same as in the bulk. Hence it is given by equation (2.23).

7.3.3 Comparison with an atomistic model

In order to test the micromagnetic approach, we compared finite element calculations with an atomistic approach for an exchange coupled ferromagnet/antiferromagnet bilayer. The thickness of the ferromagnetic and the antiferromagnetic layer is 2 nm and 10 nm, respectively. The interface between the ferromagnet and the antiferromagnet, which is parallel to the x - y plane, is perfectly compensated. The layer is assumed to be infinitely in the x and y directions. In the atomistic approach the ferromagnet/antiferromagnet is modeled as a simple cubic structure. The total energy is calculated using a Heisenberg Hamiltonian,

$$H = -g\mu_0 n \mu_B \sum_{i=1}^N \mathbf{H}_{ext} \mathbf{S}_i - \sum_{i=1}^N \sum_{j \neq i}^N J_{ij} \mathbf{S}_i \mathbf{S}_j - \frac{K_1}{S^2} \sum_{i=1}^N (\mathbf{S}_i \cdot \mathbf{k})^2. \quad (7.78)$$

Details of the atomistic approach can be found in [16]. A uniaxial anisotropy along the y -axis, with $K_1^A = K_1^B = 5.45 \times 10^5 \text{ J/m}^3$, is assumed for the antiferromagnet. The exchange constant is $A = -2.725 \times 10^{-12} \text{ J/m}$, and $J_s^A = J_s^B = 0.5 \text{ T}$.

No uniaxial anisotropy is assumed in the ferromagnet. The exchange constant in the ferromagnet is $A = 3.6 \times 10^{-11}$ J/m and $J_s = 1$ T. Additionally an in plane anisotropy which favors spin rotation in the x - y plane is assumed in the ferromagnet and antiferromagnet. The in plane anisotropy is imposed with an energy term equal to that of a uniaxial anisotropy along the z axis, however the value of the anisotropy constant is chosen negative to $K_1 = -8 \times 10^7$ J/m³. The exchange constant across the interface is $A = -8.17 \times 10^{-12}$ J/m.

Linear basis functions are used to interpolate the magnetization. Tetrahedrons form the finite element mesh. The calculations were performed for different average edge lengths of one tetrahedron (1.5 nm, 1.0 nm and 0.6 nm). The external field is applied 10° off the x -axis in the x - y plane. The left picture of figure 7.12 shows the equilibrium state for a field strength of $\mu_0 H_{\text{ext}} = 2$ T. The magnetization in the ferromagnet points in positive x - direction. The magnetization of the antiferromagnet of sublattice A and sublattice B points in positive y and negative y direction respectively. When the external field is decreased the magnetization in the ferromagnet rotates reversibly towards the field direction. The middle image in figure 7.12 shows the equilibrium state for a field strength of $\mu_0 H_{\text{ext}} = -2.2$ T. If no inplane anisotropy is assumed in the antiferromagnet the twist angle (angle between the spins (of one sublattice) at the bottom and at the interface) never exceeds 90°. Above 90° the twist angle can be reduced or released through a 180° rotation through a plane normal to the interface [35]. In this process the antiferromagnet spins rotate out of the film plane. However the in plane anisotropy assumed in the presented calculation is sufficiently strong to keep the antiferromagnet spins in plane. Hence reversible exchange bias occurs. The right image in figure 7.12 shows the twist in the antiferromagnet, when the external field has saturated the ferromagnet in negative initial field direction.

Figure 7.13 compares the hysteresis loops of the finite element calculation with the atomistic model. With decreasing mesh size the finite element calculation converges toward the atomistic method. The exchange bias field of the atomistic calculation is $\mu_0 H_b = -2.12$ T. The finite element calculations with a mesh size of 1.5 nm and 0.6 nm lead to a bias field of $\mu_0 H_b = -2.22$ T and $\mu_0 H_b = -2.15$ T, respectively. Thus the bias field differs by less than 5% and 2% respectively. The results show that the finite element approach is suitable to model exchange coupled AF/F layers with a much smaller number of unknowns.

Figure 7.14 shows the profile of the domain wall, which is formed in the antiferromagnet after the reversal of the ferromagnet, for different mesh sizes. The x -component of the mag-

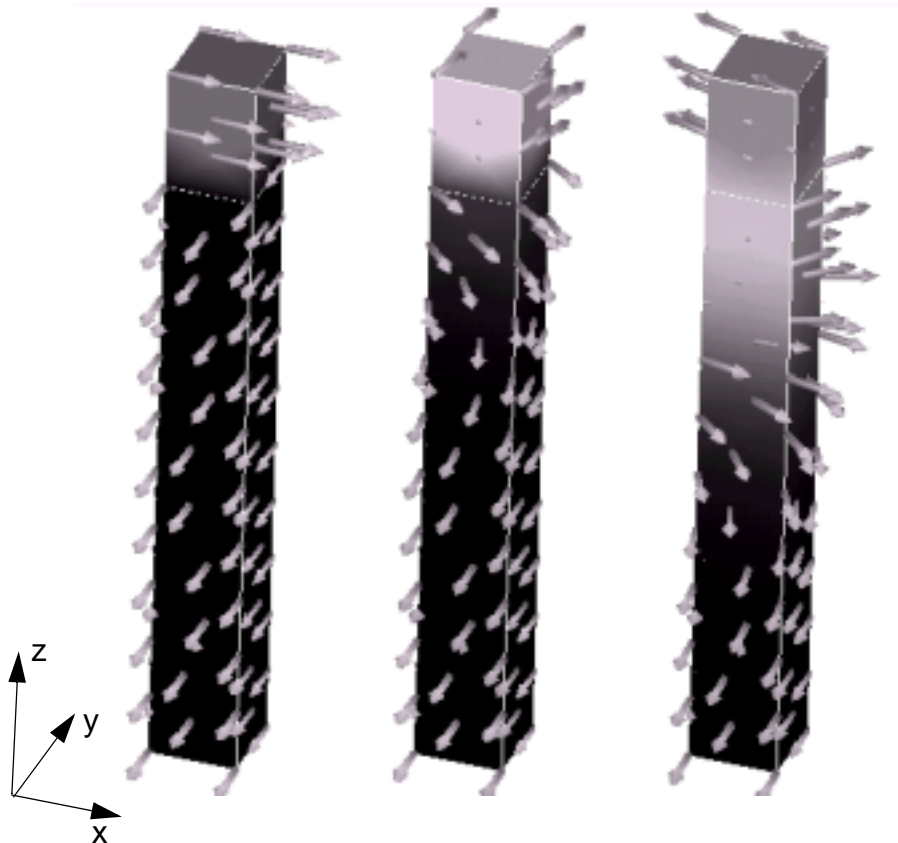


Figure 7.12: Equilibrium configurations of the magnetization in a ferromagnetic/antiferromagnetic interface. The top and the bottom portion of the slab refer to the ferromagnet and the antiferromagnet, respectively. In the antiferromagnet the magnetization of only one sublattice is shown. The left image shows the initial state for the calculation. The image in the middle shows an equilibrium state for $\mu_0 H_{\text{ext}} = -2.2$ T. The field in the right image is $\mu_0 H_{\text{ext}} = -6$ T.

netic polarization is plotted as a function of the distance of the interface. The discontinuity at $position = 0$ occurs owing to the 90° coupling between the ferromagnet and antiferromagnet. It is important to note that the 90° coupling cants the antiferromagnet spins at the interface. This canted state relaxes within one or two monolayers into the bulk spin structure (spins of sublattice A and spins of sublattice B are antiparallel in the bulk), as shown in figure 7.3. This change of the magnetization occurs on a length scale much smaller than the exchange length in the antiferromagnet. Usually the mesh size is chosen to equal the exchange length l_c , since the discretization error of the finite element simulation remains small when the elements are smaller than l_c . Thus the canted state decays on a distance smaller than one finite element. Figure 7.15 shows the projection of the antiferromagnet interface spins $u_y = \cos(\alpha/2)$

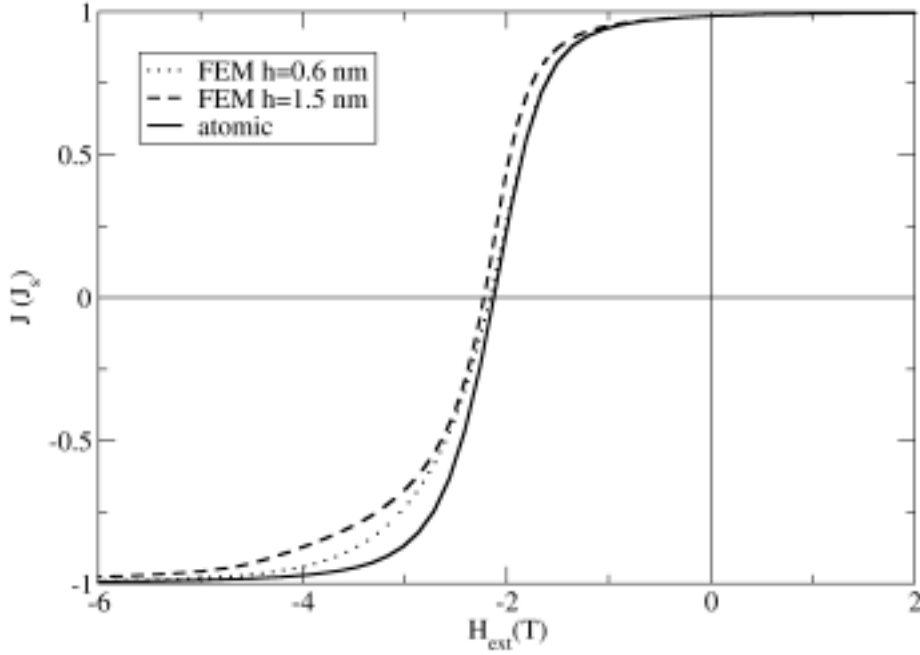


Figure 7.13: Comparison of the demagnetization curve for different finite element mesh sizes with the atomistic model. The lattice constant in the atomistic model is 0.1 nm. The interface is compensated.

onto the ferromagnet direction for different finite element mesh sizes. α is the angle between the spins of sublattice A and sublattice B . In bulk α is zero if no external field is applied. It can be seen that the canted angle is nearly independent of the finite element mesh size.

Let us investigate the dependence of the simulation on the mesh size in more detail. To show the influence of mesh effects we investigate the relative order of magnitudes of the different terms in equation (7.66). Rewriting the exchange energy in the antiferromagnet (equation 7.66) in the form of equation (7.48). By using Green's identity it follows,

$$E_{ex} = -5Aa(n_0^A + n_0^B) \int_A \mathbf{u}^A(\mathbf{x}_i) \mathbf{u}^B(\mathbf{x}_i) dA - \frac{2JS^2}{a} \frac{1}{2} \int_V \mathbf{u}^A(\mathbf{x}_i) \Delta \mathbf{u}^B(\mathbf{x}_i) dV. \quad (7.79)$$

In the finite element calculation the Laplace operator is discretized using a discretization length (finite element size) larger than the decay length of the canted state. Thus it is not obvious that equation (7.79) discretized with the finite element method is a good approximation for the exchange energy at the interface for 90° coupling. To investigate the approximation in

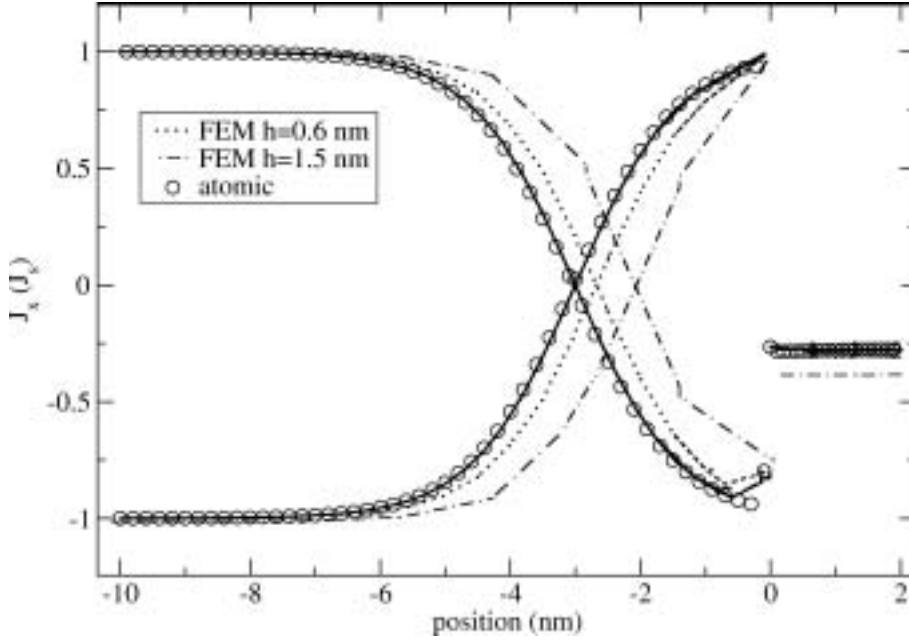


Figure 7.14: Comparison of the x -component of the normalized magnetization as a function of position within the slab for different finite element sizes with the atomistic model. The antiferromagnet ranges from $x = -10$ nm to $x = 0$. The ferromagnet from $x = 0$ to $x = 2$ nm. The lattice constant in the atomistic model is 0.1 nm. The interface is compensated.

more detail, let us discretize the Laplace term in equation (7.79) using finite differences with a lattice size Δx . For the Laplace term follows,

$$\Delta u^B(x_i) \approx \frac{\mathbf{u}_{i+1}^B - 2\mathbf{u}_i^B + \mathbf{u}_{i-1}^B}{(\Delta x)^2}. \quad (7.80)$$

If equation (7.80) is evaluated on an interface node ($i = 0$) boundary conditions have to be applied. The boundary condition that the normal derivative vanishes can be imposed by $\mathbf{u}_{-1} = \mathbf{u}_0$. For equation (7.79) follows at the interface node,

$$E_{ex, interface\ node} = -\frac{5A}{a} \mathbf{u}_0^A \mathbf{u}_0^B \Delta A_i - A \mathbf{u}_0^A \frac{\mathbf{u}_1^B - \mathbf{u}_0^B}{(\Delta x)^2} \Delta V_0. \quad (7.81)$$

Let us assume that the spins in the bulk of the ferromagnet point parallel to the x axis. If the exchange integral J between the ferromagnet (it points in y -direction) and the antiferromagnet is equal to the exchange in the antiferromagnet from equation (7.20) follows for the spins at the interface that $\mathbf{u}_0^A = (0.99, 0.12, 0)$ and $\mathbf{u}_0^B = (-0.99, 0.12, 0)$. If we assume that

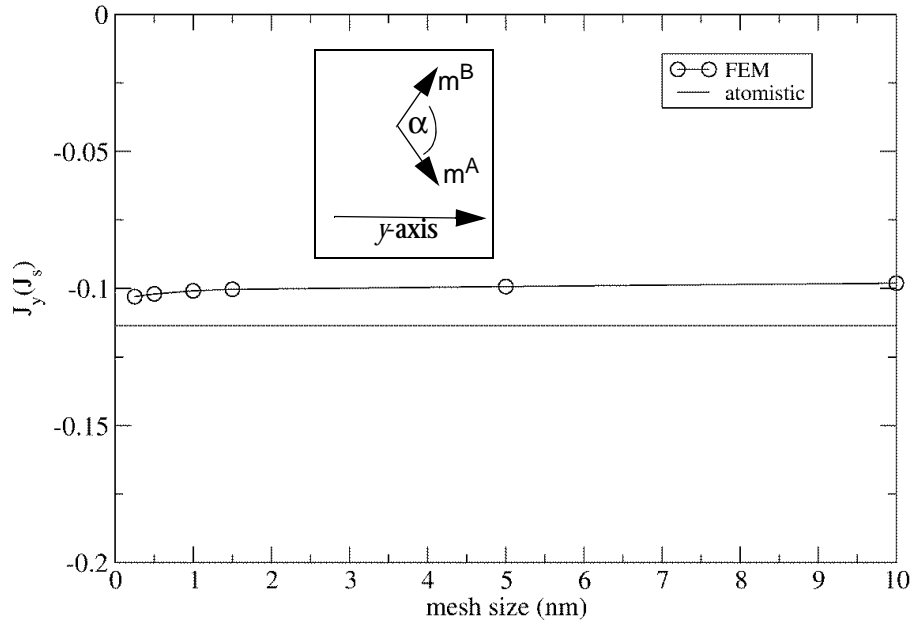


Figure 7.15: Comparison of the y -component of the antiferromagnet interface spins (canted angle) for different finite element mesh sizes. The inset shows the spins of the antiferromagnet of sublattice A and sublattice B at the interface.

the spin structure of the next monolayer is already the same as the spin structure of the bulk we get for the spin direction $\mathbf{u}_1^B = (1.0, 0, 0)$. The difference $\mathbf{u}_1^B - \mathbf{u}_0^B = (0.01, 0.12, 0)$. The product $\mathbf{u}_0^A (\mathbf{u}_1^B - \mathbf{u}_0^B)$ is about one hundredth.

If the discretization length Δx is equal to the atomic lattice constant a the second term in equation (7.81) is about 500 times smaller than the first term in equation (7.81). Thus the first term together with the exchange field caused by the ferromagnet determines the canted state. The second term can be neglected. If the discretization length Δx is increased the second term becomes even smaller.

7.4 Exchange bias at compensated interfaces

Consider a ferromagnetic film exchange coupled to an ensemble of antiferromagnetic grains. The interface is assumed to be perfectly compensated everywhere. Spin flop coupling at the interfaces of each grain provides a small net magnetic moment through which the ferromagnet and antiferromagnet moments are correlated. It has been shown that the spin flop configuration is not stable, and will not lead to exchange bias for realistic material parameters. The reason is that during magnetic reversal, the antiferromagnet attempts to follow the ferromagnet but the spin flop configuration reverses due to out of plane fluctuations. This can lead to coercivity, but not a shifted hysteresis loop characteristic of exchange bias.

We present a model for exchange bias at compensated interfaces where the loop shift arises due to randomness and domain formation in the antiferromagnet. In a global picture the exchange bias effect can be understood by the change of the total Gibbs' free energy after the reversal of the ferromagnet. After field cooling the total energy of the system is low. During field cooling the ferromagnetic spins are fixed in the field direction, the antiferromagnetic spins arrange in such a way that they occupy low energy states. Several experiments like rotational hysteresis measurements and ferromagnetic resonance studies suggest that irreversible processes occur in the antiferromagnet when the ferromagnet is reversed [41]. Many antiferromagnet / ferromagnetic systems show the so-called training effect [11]. The loop shift decreases with increasing number of hysteresis cycles. This suggests that after each cycle the system is in a different state.

After field cooling the system has low energy. The energy will increase if the system changes its state from the state after field cooling to a different state. If the ferromagnet is reversed, some antiferromagnetic grains switch irreversibly. These irreversible processes are initiated by the reversal of the ferromagnet. They occur for uncompensated as well as for compensated interfaces. Owing to the intergrain exchange coupling between antiferromagnetic grains the energy increases. Different mechanisms contribute to the partial switching of the antiferromagnetic grains. Xi and White [47] found a varying interface coupling in NiFe/CrMnP bilayers prepared by substrate bias sputtering. However, it is sufficient to take into account the random magnetocrystalline anisotropy in the AF grains to observe that some and not all AF grains switch irreversibly. To point out the mechanism which leads to a bias field for compensated interfaces in more detail, let us consider two antiferromagnetic grains (G_1 and G_2) and a single crystal ferromagnetic film as shown in figure 7.16. Two different direc-

tions of the easy axis are assumed in the antiferromagnet. Both easy axes are parallel to the image plane. The upper picture in figure 7.16 shows the spin configuration after field cooling. In the antiferromagnet only the spin direction of one sublattice is shown. The spins in the antiferromagnet arrange in such a way that the total energy is minimized. Consequently the spins in grain G_1 and G_2 are almost parallel. The 90° coupling at the interface results in a spin direction in the ferromagnet perpendicular to the spins in the antiferromagnet (perpendicular to the image plane). When the external field reaches the coercive field the ferromagnet switches. For a certain easy axis direction of the antiferromagnetic grain (e.g. easy axis parallel to the interface plane) the reversal of the ferromagnet causes the irreversible switching of the antiferromagnet. This mechanism occurs for the spins of grain G_2 in figure 7.16. The spins

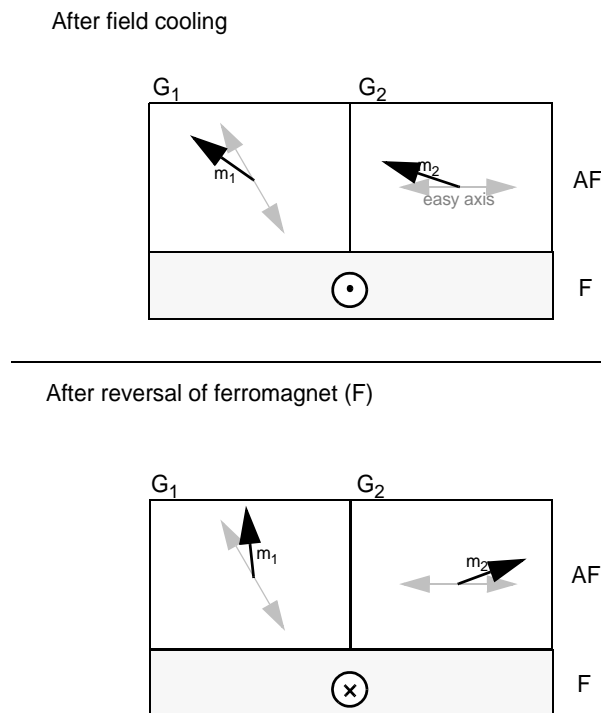


Figure 7.16: Spin configuration in the antiferromagnetic grains G_1 and G_2 and the ferromagnetic film F after field cooling and after the reversal of the ferromagnet, respectively. The angle between the magnetization m_1 and m_2 is larger after the reversal of the ferromagnet than after field cooling. Thus the state after field cooling has lower energy than the state after the reversal of the ferromagnet

make a transition from one local minimum of the anisotropy energy to the equivalent minimum with opposite magnetization direction.

For easy axes directions close to the film normal the switching of the ferromagnet reversibly rotates the antiferromagnet. The spins in grain G_1 remain in the same local minimum of

the anisotropy energy. As a consequence the state after field cooling and the state after the switching of the ferromagnet are not symmetric. The angle between the spins between neighboring grains will increase as the ferromagnet is reversed. The total energy increases owing to intergranular exchange coupling. Generally, we found that the field that is required to switch the ferromagnet from the low energy state to the high energy state is larger than the field required to switch the ferromagnet in the other direction. This explains the loop shift observed in antiferromagnetic / ferromagnetic structures.

This mechanism is investigated using the continuum approach. The finite element discretization allows to resolve nonuniform magnetic states within the grains. In these simulations the total number of grains is limited. In order to obtain better statistics we also perform simulations using a large scale model which assumes uniform magnetization within the grains.

7.4.1 Finite element model

The continuum model is suitable to calculate antiferromagnets with large domain wall width such as IrMn. It forms a disordered fcc (γ) phase [5]. We treat the system with a two lattice approach and assume the following intrinsic parameters: $A = -10^{-11}$ J/m, $K_1^A = K_1^B = 10^5$ J/m³, $J_s^A = J_s^B = 0.5$ T and lattice constant $a = 3.76 \times 10^{-10}$ m. For permalloy $K_1 = 2 \times 10^3$ J/m³, $A = 10^{-11}$ J/m, $J_s = 1$ T. The easy axis of the permalloy is along the x -axis. No inplane anisotropy is assumed in the ferromagnet and in the antiferromagnet. The thickness of the permalloy layer is 2 nm and of the IrMn layer 6 nm. The IrMn layer consists of 8×3 grains. The grain size is 8 nm. The basal planes of the grains are squares, equal in size. The easy axes are randomly oriented in space. The antiferromagnetic grains are weakly exchange coupled to each other. We assume an intergranular phase with a thickness of 1 nm with reduced exchange constant, $A = 5 \times 10^{-13}$ J/m or zero exchange. The interface between the permalloy layer and the IrMn layer is perfectly compensated.

The solid line of figure 7.17 gives the hysteresis loop for weak exchange between the antiferromagnetic grains. The loop shows bias, although the interface is completely compensated. In addition figure 7.17 gives the hysteresis loop for zero exchange between the antiferromagnetic grains. In this case no bias occurs. These results indicate that weak intergrain exchange interactions are required to obtain exchange bias. Intergranular coupling reduces the out of plane rotation. Thus it is possible to switch grains in an exchange coupled granular antiferro-

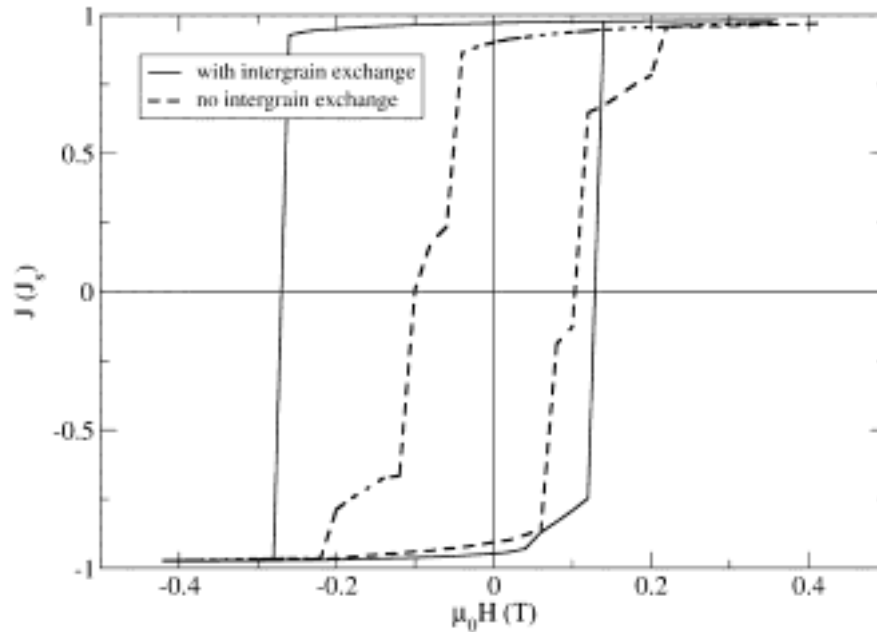


Figure 7.17 Hysteresis loops of a ferromagnet and an F/AF bilayer with compensated interface. The AF leads to an enhanced coercivity and to a loop shift.

magnet, as shown in figure 7.18. Figure 7.18 compares the magnetization configuration of the field cooled state and the reversed state.

Figure 7.19 shows a sequence of magnetization configurations during the reversal of the ferromagnet for weak exchange between the antiferromagnetic grains. From top to bottom the magnetization of the ferromagnet reverses its orientation. Initially the magnetization of the antiferromagnetic grains in the front point in the same direction. When the ferromagnet is reversed the AF grains on the left hand side switch, whereas the antiferromagnetic grains on the right hand side remain in their original direction. As a consequence a domain wall is formed in the antiferromagnet. The increase of the domain wall energy results in exchange bias.

For zero exchange coupling between the antiferromagnetic grain only a few antiferromagnetic grains are able to switch irreversibly when the ferromagnet is reversed. Figure 7.20 shows the field cooled state and the reversed state for zero exchange coupling between antiferromagnetic grains. Only grains with an easy axis almost parallel to the interface switch irre-

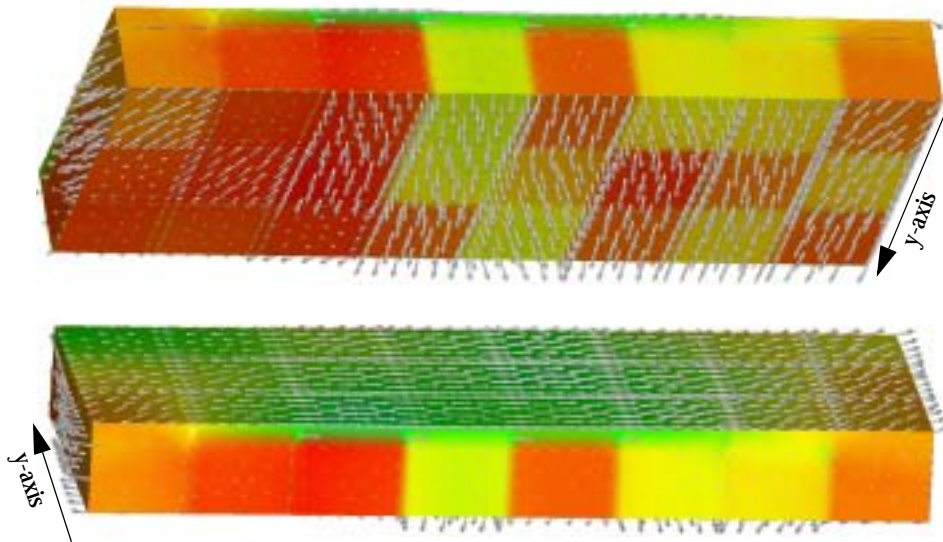
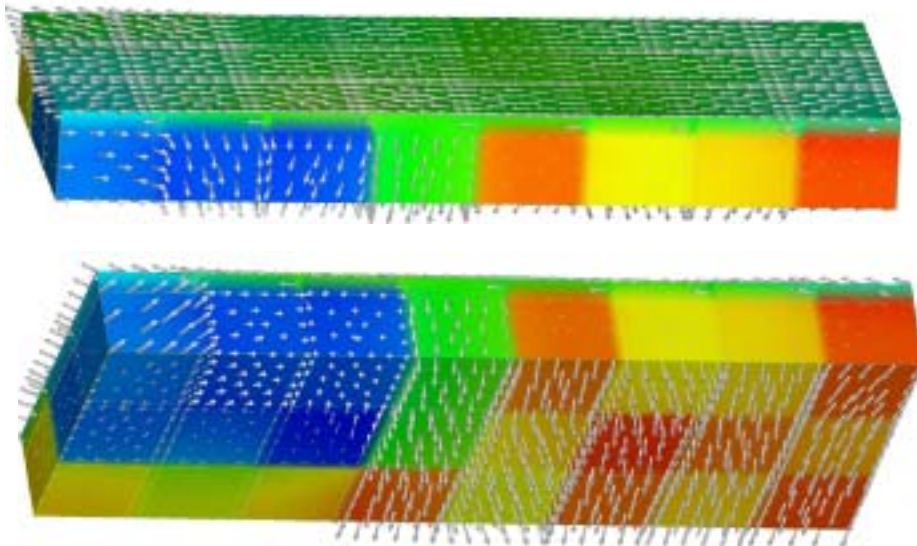
Field cooled state**Reversed ferromagnet**

Figure 7.18: Full micromagnetic calculation of a IrMn/Permalloy bilayer. The antiferromagnet (AF) consists of 8×3 grains. The size of each grain is $8 \times 8 \times 6 \text{ nm}^3$. Each grain is subdivided into about 400 finite elements. Non equilibrium states during switching of the ferromagnet are shown.

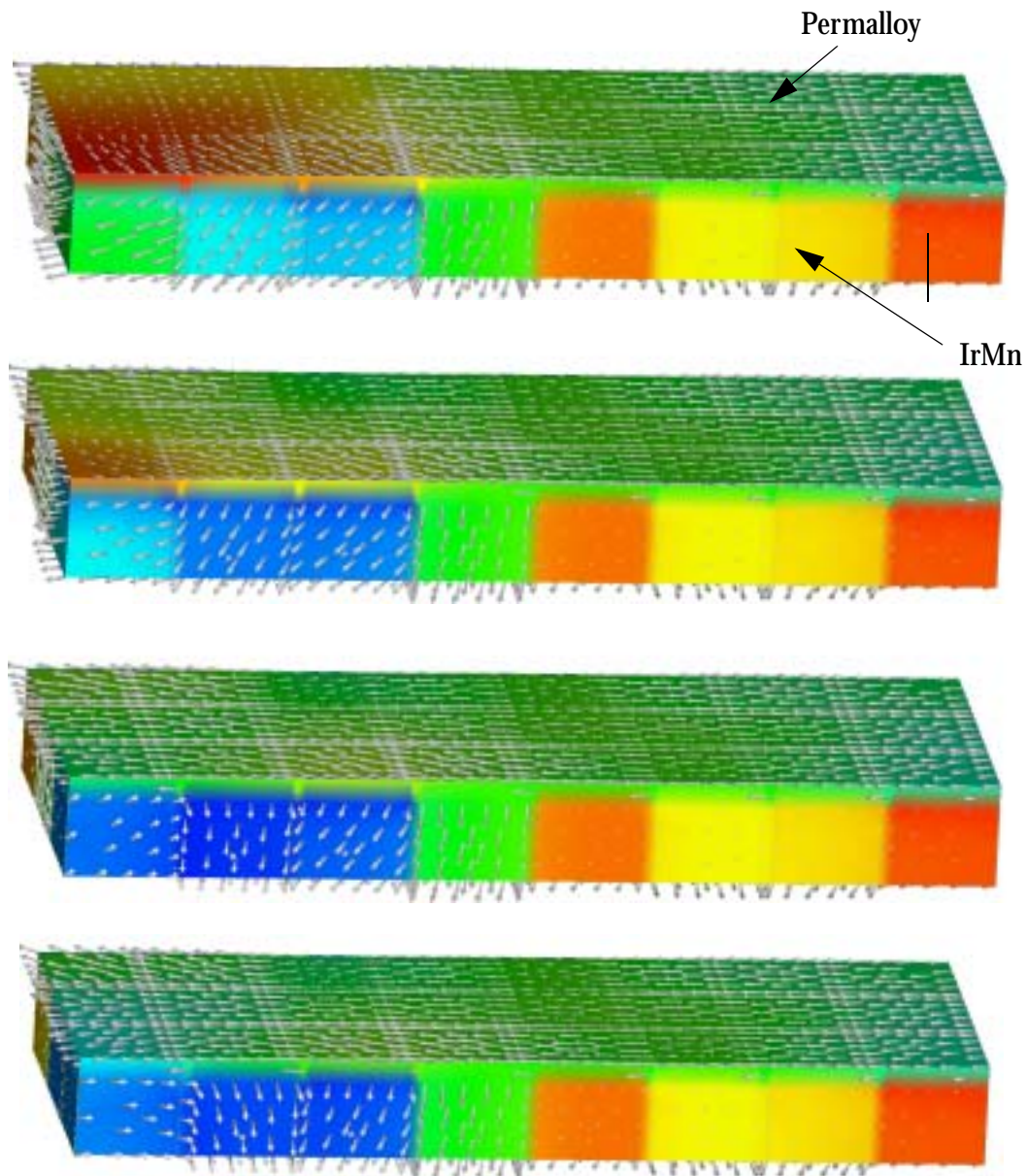


Figure 7.19: Time evolution of the magnetic configuration in the IrMn/Permalloy bilayer is shown for the reversal of the ferromagnet.

versibly. The switching of the antiferromagnetic grains does not change the exchange energy stored in the antiferromagnet. As a consequence no bias occurs as shown in figure 7.17.

Figure 7.21 shows the interface energy and the exchange energy during the hysteresis cycle for weak exchange between the antiferromagnetic grains. Whereas the interface energy slightly decreases as the ferromagnet is reversed, the exchange energy increases. This leads to

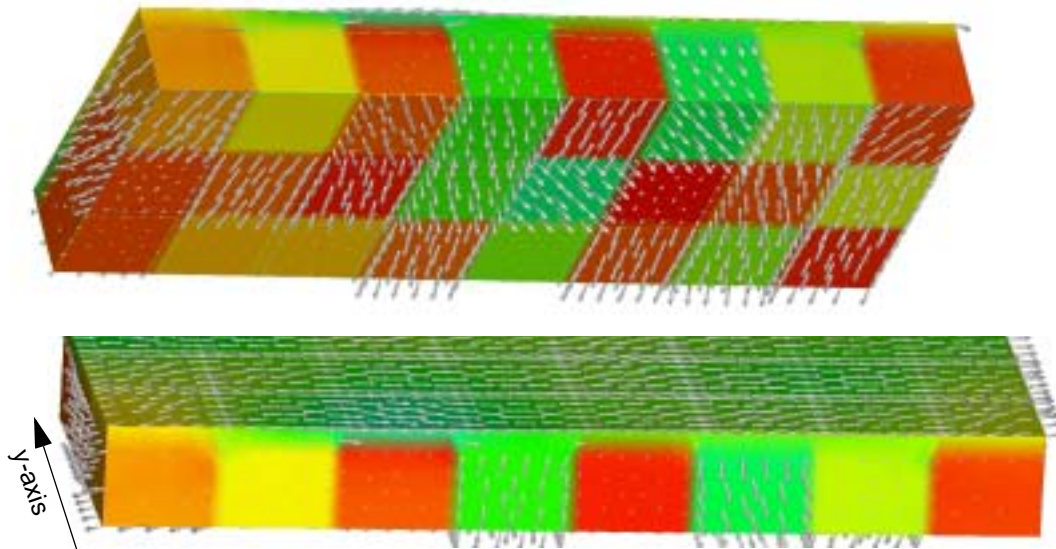
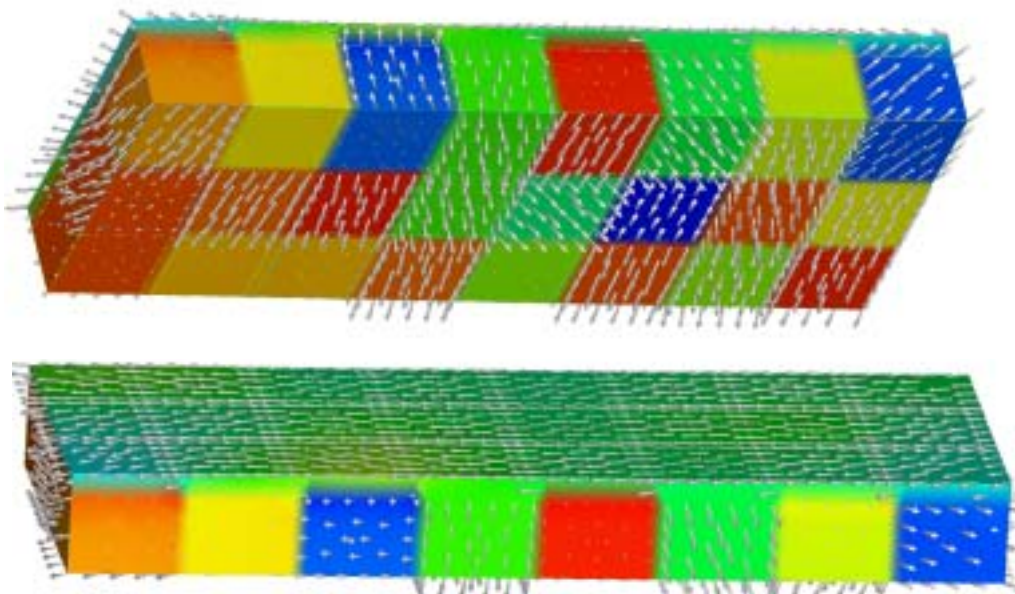
Field cooled state**Reversed ferromagnet**

Figure 7.20: No intergranular exchange coupling is assumed between the IrMn grains. Only grains where the angle between the easy axis and the interface plane is smaller than 10° switch.

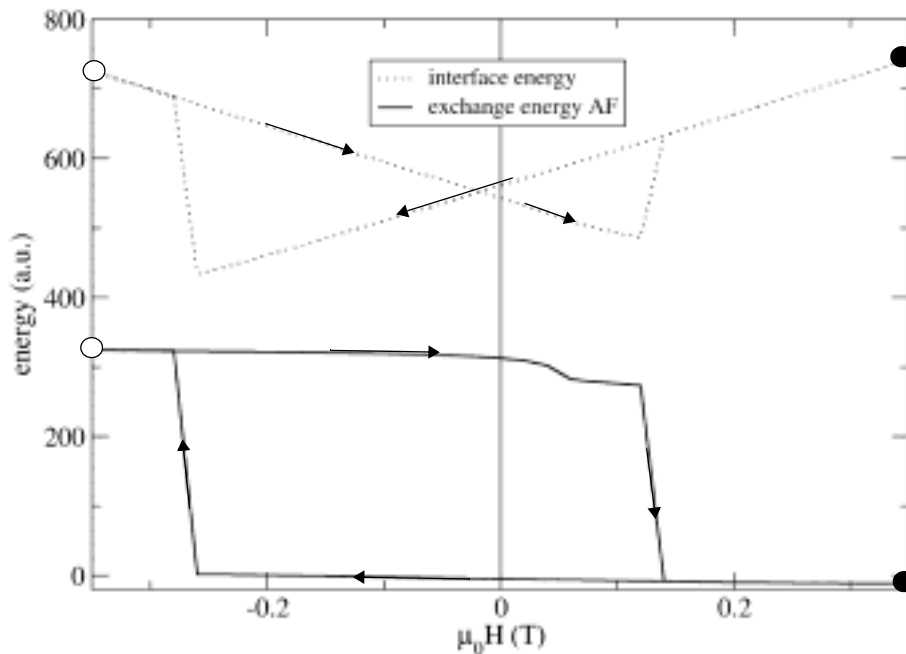


Figure 7.21: Different energy contributions for the F/AF bilayer. The energy is plotted as a function of the external field during one hysteresis loop. The dots mark the field cooled state. The open circle denote the reversed state.

an increase of the total energy when the ferromagnet is switched from the field cooled state to the reversed state.

The above results show that the increase in domain wall energy contributes to exchange bias. To observe a change of the antiferromagnetic domain configuration it is crucial that some and not all antiferromagnetic grains switch irreversibly as the ferromagnet is reversed.

7.4.2 Granular model

The magnetization configurations calculated with the finite element approach show that the magnetization remains mostly uniform within a grain. This justifies a numerical model where the grains are uniform within a grain. The granular model allows to model larger systems. Thus possible finite size effects can be avoided.

The model described by an energy for each grain is composed of anisotropy, Zeeman, and intergrain exchange energy terms. We assume a polycrystalline antiferromagnetic film of

thickness t_{AF} coupled to a polycrystalline ferromagnetic film of thickness t_F . For small grain size and low intergrain exchange coupling the magnetization within a grain remains nearly uniform. In the antiferromagnet the direction of the magnetization changes from grain to grain depending on the local anisotropy and the interface coupling with the ferromagnet. We assume a compensated interface and therefore introduce a 90° coupling between the AF layer and F layer following suggestions by Stiles and McMichael [41] and as derived by Stamps [40]. The total energy per grain j is

$$\begin{aligned}
 E^j = & \sum_{i=1}^{nN} [-J_F S^2 n_F t_F l \mathbf{u}_F^j \mathbf{u}_F^i - J_{AF} S^2 n_{AF} t_{AF} l \mathbf{u}_{AF}^j \mathbf{u}_{AF}^i] - J_{AF-F} S^2 n_I (\mathbf{u}_{AF}^j \mathbf{u}_F^j)^2 l^2 \\
 & - K_1 (\mathbf{k}_{AF}^j \mathbf{u}_{AF}^j)^2 t_{AF} l^2 + \frac{J_s^2}{\mu_0} (\mathbf{k}_F^j \mathbf{u}_F^j)^2 t_F l^2 - J_s \mathbf{H} \mathbf{u}_F^j t_F l^2
 \end{aligned} \tag{7.82}$$

The sum over i is over the nearest neighbor grains in the antiferromagnet. S is the total spin quantum number, l the grain diameter. J_F and J_{AF} denotes the exchange integral across ferromagnetic grains and antiferromagnetic grains, respectively. J_{AF-F} describes the total effective exchange interaction at the compensated interface. This includes a measure of the net moment due to spin flop coupling and additional factors due to energy involved in disturbing the spin configuration. The exchange energies depend on the number of spins at the interface, n_I , in the ferromagnetic grain, n_F , and in the antiferromagnet, n_{AF} . For a cubic lattice with lattice constant a , $n_F = n_{AF} = n_I = 1/a^2$. \mathbf{u}_{AF}^j and \mathbf{u}_F^j denote the unit vector of the spin direction in the grain j of the antiferromagnet and ferromagnet, respectively. Equation (7.82) implicitly takes into account the canted state which is formed at the interface [40]. Because the canted state is strongly localized to the interface, it is a good approximation to assume that in the bulk of the antiferromagnet the spins of the different sublattices are antiparallel for the typical fields applied in applications. This means that as long as the applied field is not larger than the antiferromagnetic exchange, as it is the case in most experiments, magnetic surface and volume charges cancel in the antiferromagnet. Any remaining contributions to magnetostatic energy for individual magnetic sublattices in the antiferromagnet can be taken into account through the anisotropy constant, K_1 . Shape effects for the ferromagnetic film are approximated with the fifth term in equation (7.82) by assuming an in plane anisotropy energy proportional to the square of the magnetization. In this term, k_F is a unit vector pointing perpendicular to the film plane. The antiferromagnet has a uniaxial anisot-

ropy of strength K_1 and the easy axis direction k_{AF} is assigned randomly for every grain. Finally, we assume that an external static magnetic field H only acts on the ferromagnet. This energy is given by the sixth term in equation (7.82) where J_s is the magnitude of the spontaneous magnetization.

Hysteresis loop calculations are made by first initializing the system by simulating field cooling and then following the evolution of the magnetization with changing applied magnetic field. An equilibrium configuration is found at each magnetic field value. The equilibrium state is obtained by the numerical integration of the Landau-Lifshitz-Gilbert equation [19] using effective fields determined from the energy in equation (7.82). The field acting on the antiferromagnet is found using

$$\mathbf{H}_{eff, AF}^j = -\frac{1}{J_s t_{AF} l^2} \frac{\partial E_{tot}}{\partial \mathbf{u}_{AF}^j} \quad (7.83)$$

where $J_s t_{AF} l^2$ is the total sublattice moment of the antiferromagnetic component of grain j . A similar expression is used to calculate the effective field acting on the ferromagnet. We assume the system to be in equilibrium if the change of the magnetization, $d\mathbf{u}/dt$, is smaller than $10^{-4}\mu_0$ on every node. A backward differentiation method [12] is used to integrate the LLG equation numerically.

Field cooling is simulated using a Metropolis Monte Carlo algorithm. The ferromagnet direction is fixed, and the magnetization of the antiferromagnet is set randomly. Three different trial steps [13] are used to efficiently sample the phase space of spin configurations. Each Monte Carlo step begins by randomly choosing an antiferromagnetic grain and making the following three tests, each chosen according to a Metropolis Monte Carlo algorithm: (1) A new magnetization direction is randomly chosen within a cone of angle of 3° such that the symmetry axis of the cone is parallel to the old magnetization direction; (2) within any orientation on a sphere; and (3) as a simple reversal. We start the cooling process at a temperature of $T = 800$ K and decrease the temperature to $T = 0$ in steps of $\Delta T = 25$ K. At each temperature we perform $2000 \times N_x \times N_y$ Monte Carlo steps. N_x and N_y are the numbers of grains in x and y direction, respectively.

Results are now presented using material parameters chosen to approximate materials used in GMR read-heads, such as IrMn. The parameters used in the following are as follows. In the antiferromagnet, $K_1 = 1 \times 10^5$ J/m³, $J_{AF} = 0.023$ meV (corresponding to an exchange stiff-

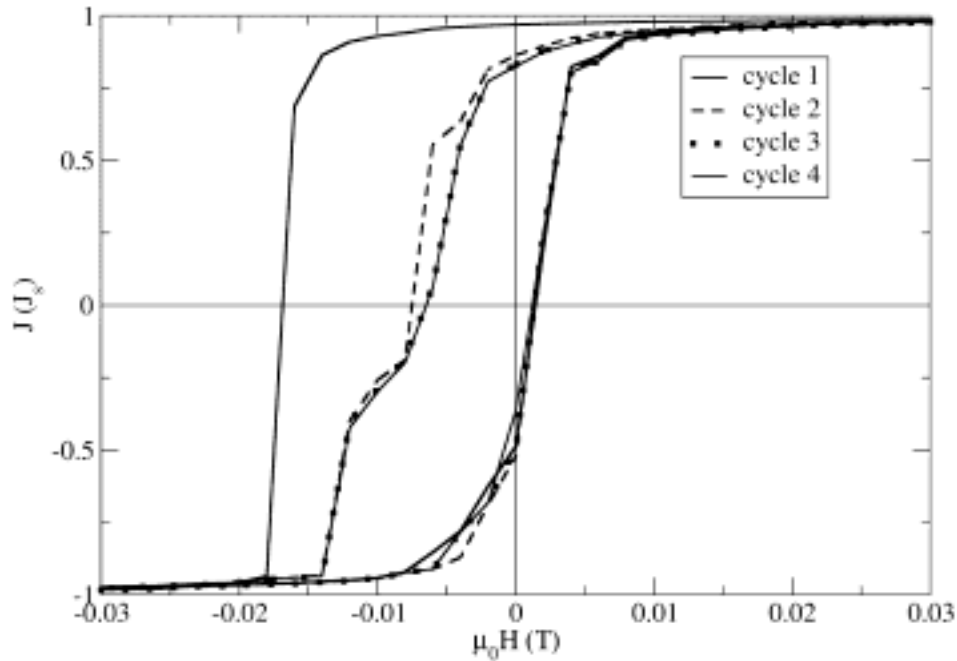


Figure 7.22: Calculated hysteresis loops for a IrMn/Permalloy bilayer. The IrMn thickness and the grain size is 20 nm and 10 nm, respectively. The thickness of the ferromagnet is 10 nm. The interface is completely compensated. The bias field decreases with the number of hysteresis cycles.

ness constant $A = 0.5 \times 10^{-13}$ J/m). The antiferromagnetic layer consists of 60×60 rectangular grains with basal plane area 10×10 nm². The grain structure in the ferromagnet is the same as in the antiferromagnet. The thickness of the ferromagnet is 10 nm in all cases. The intergrain interaction between ferromagnetic grains is $J_F = 0.45$ meV ($A = 10^{-12}$ J/m²). The coupling between the ferromagnet and antiferromagnet is completely compensated, with an effective interface exchange, $J_{AF-F} = -0.45$ eV.

Figure 7.22 shows the calculated hysteresis loops for a thickness of the antiferromagnet of 20 nm. The initial field strength is $\mu_0 H = 0.1$ T and is decreased in steps of $\mu_0 \Delta H = -0.002$ T. In order to investigate the training effect several hysteresis cycles are calculated. Cycle 1 of the loops in figure 7.22 is calculated starting from the field cooled state as initial configuration and has a bias field of ($\mu_0 H_b = 7.7$ mT). The next cycle (cycle 2) shows a reduction of the bias field by about 65 %. Note that this training effect occurs at zero temperature and appears because the domain configuration in the antiferromagnet is strongly field dependent through the orientation of the ferromagnet. The ferromagnet orientation does not change during

cooling. After cooling, the only equilibration process available to the antiferromagnet appears through changes in the state of the ferromagnet. Thus each cycle through the magnetization loop brings the antiferromagnet closer to a type of dynamic equilibrium in which the coercive field no longer changes with each additional cycle and the loop area remains constant. In our simulations, this equilibrium appeared after about four cycles.

Figure 7.23A shows the domain configuration after field cooling. The external field is $\mu_0 H_{\text{ext}} = 0.1$ T. The magnetization of one sublattice of the antiferromagnet parallel to the x -axis is indicated by a gray scale (left = black, right = white). Note the formation of large domains with diameters of several hundred nanometers. Figure 7.23 (B) shows the domain configuration at $\mu_0 H_{\text{ext}} = -0.1$ T. The initially large domains break up into a number of smaller domains. The formation of small domains costs domain wall energy, and eventually the size of domains stabilizes as the energy costs in forming the domains balance the energy gained by aligning with the ferromagnet. Figure 7.23 (C) and figure 7.23 (D) show the domain configuration at $\mu_0 H_{\text{ext}} = 0.1$ T and $\mu_0 H_{\text{ext}} = -0.1$ T after the first cycle. Note that the number of domains increases when the external field points antiparallel to the field cooling direction.

The exchange bias persists after cycling and is due to interplay between grains that remain fixed during the magnetization process, and grains that reverse. The energy involved in forming domain walls between antiferromagnetic grains is responsible for the exchange bias shift. This energy is plotted in figure 7.24 as a function of the applied field for several cycles. The minimum energy is always in the field cooling direction regardless of the cycle, and has its smallest value directly after field cooling and before cycling. The total energy increases when the ferromagnet switches. Figure 7.25 shows the bias field for different thicknesses of the antiferromagnet. The bias field was calculated for the 10-th hysteresis cycle. The bias field shows a maximum for a thickness of 22 nm. For decreasing antiferromagnetic thickness the domain wall energy approaches zero. For large thicknesses the high anisotropy energy hinders switching of the antiferromagnetic grains resulting in weak bias.

Figure 7.26 shows the hysteresis loop for different grain diameters in the ferromagnet and antiferromagnet. The interface exchange constant is $A_{\text{inter}} = -0.5 \times 10^{-12}$ J/m and the intergranular exchange constant in the ferromagnet and antiferromagnet is $A_{\text{F}} = 1 \times 10^{-12}$ J/m and $A_{\text{AF}} = 1 \times 10^{-13}$ J/m. The thickness of the antiferromagnet and ferromagnet is 15 nm and 10 nm. The largest bias field of $\mu_0 H_{\text{b}} = 3$ mT accrues for a grain diameter of 15 nm.

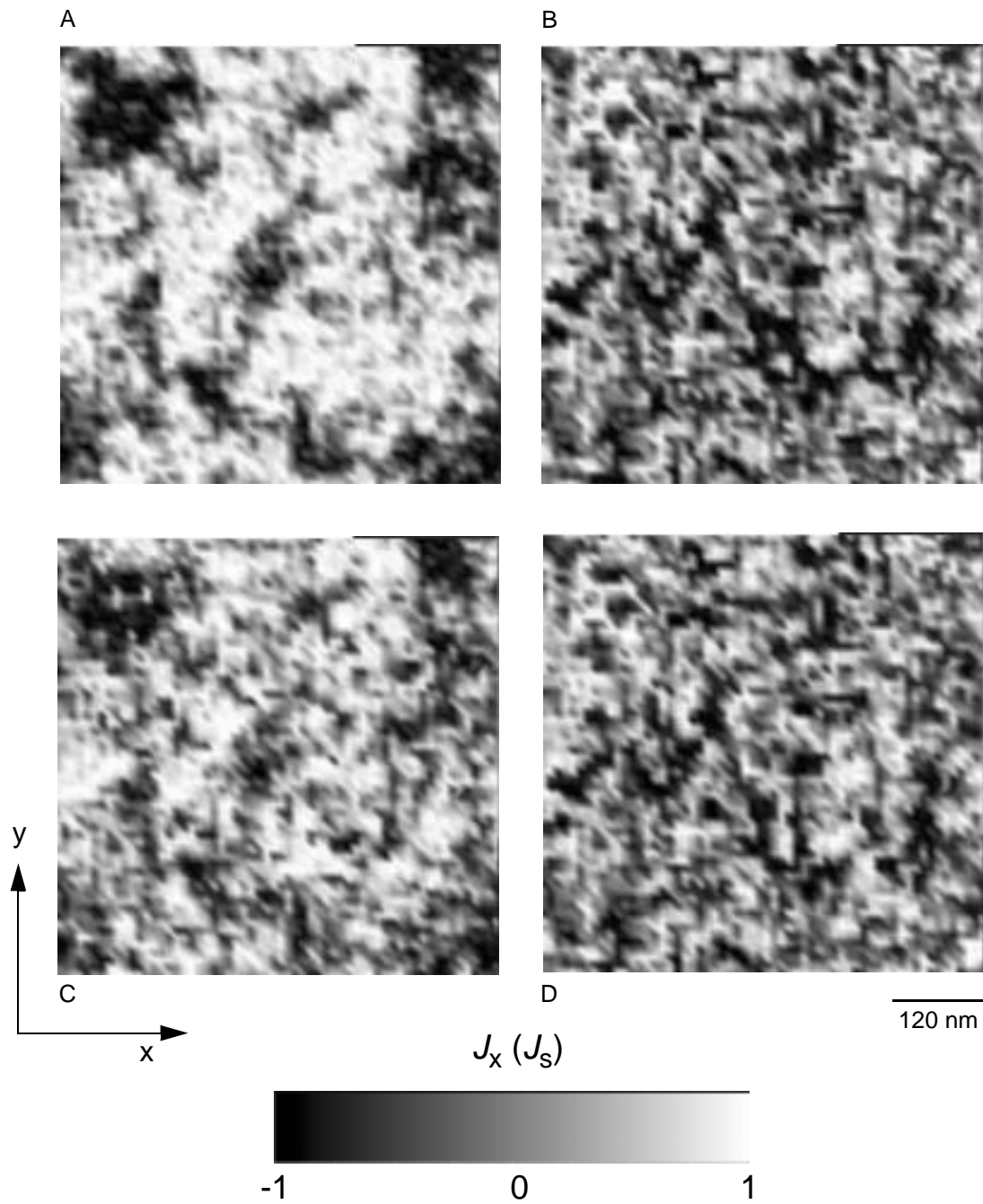


Figure 7.23: Domains in the antiferromagnet. The x -component of one sublattice of the antiferromagnet is color coded. The properties of the antiferromagnet are the same as in figure 7.22. (A) state after field cooling. The external field is $\mu_0 H_{\text{ext}} = 0.1$ T (B) Domain structure in the antiferromagnet after the switching of the ferromagnet. $\mu_0 H_{\text{ext}} = -0.1$ T (C) Domain structure after the first hysteresis cycle. $\mu_0 H_{\text{ext}} = 0.1$ T (D) After switching the ferromagnet again. $\mu_0 H_{\text{ext}} = -0.1$ T

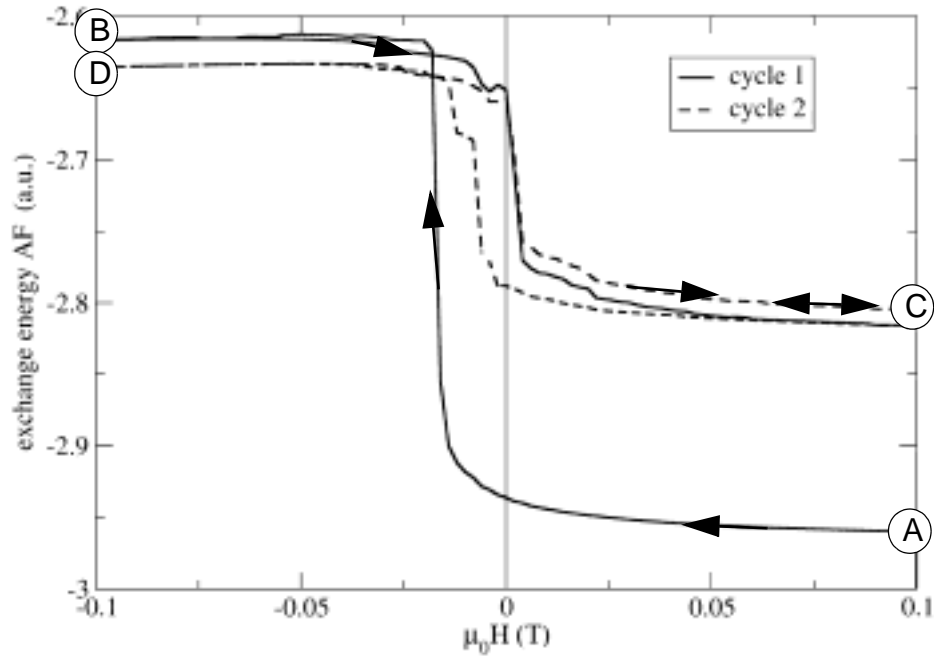


Figure 7.24: Exchange energy in the antiferromagnet as a function of the external field strength for the first and second hysteresis cycle. The states (A) - (D) are the same as in figure 7.23.

The hysteresis loops in figure 7.27 show the influence of the strength of the interface exchange coupling on the bias field and the coercivity. The grain size in the ferromagnet and antiferromagnet is 10 nm. The antiferromagnet thickness and ferromagnet thickness is 15 nm and 10 nm. $A_F = 1 \times 10^{-12}$ J/m and $A_{AF} = 2 \times 10^{-13}$ J/m. Figure 7.27 shows that for an interface exchange constant of $A = -0.1 \times 10^{-12}$ J/m no bias occurs. For that value of the exchange constant the interface energy is too small to switch antiferromagnetic grains irreversibly. Thus the domain structure in the antiferromagnet is the same in the field cooled and reversed state. With increasing interface exchange the bias field increases. For $A_{\text{inter}} = -2 \times 10^{-12}$ J/m the bias field is $\mu_0 H_b = 0.8$ mT.

Figure 7.28 shows the hysteresis loop for different values of the intergrain exchange constant in the ferromagnet. The other material parameters are: $A_{\text{inter}} = -1 \times 10^{-12}$ J/m, $A_{AF} = 0.5 \times 10^{-13}$ J/m, $t_F = 10$ nm and $t_{AF} = 15$ nm. The bias field is almost independent of the strength of the exchange constant of the ferromagnet. The bias field is $\mu_0 H_b = 1.4$ mT. The

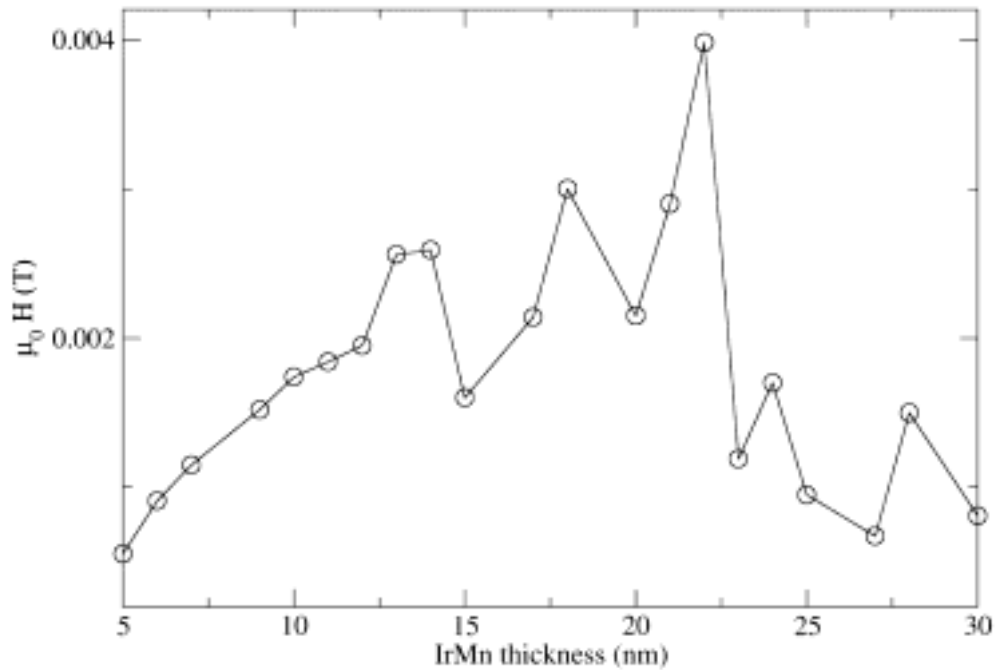


Figure 7.25: Bias field as a function of the thickness of the antiferromagnetic IrMn layer. The bias field is calculated for the 10-th hysteresis cycle.

coercive field increases with decreasing exchange constant of the ferromagnet. For $A_F = 0.1 \times 10^{-12} \text{ J/m}$ the coercive field is $\mu_0 H_c = 35 \text{ mT}$ whereas for $A_F = 1 \times 10^{-12} \text{ J/m}$ the coercive field is only $\mu_0 H_c = 3 \text{ mT}$. The increase of the coercive field of ferromagnetic/antiferromagnetic bilayers with decreasing exchange constant in the ferromagnet was also reported by Stiles and McMichael [42]. Experimentally an easy way to vary effectively the intergranular exchange constant is to vary the thickness of the ferromagnetic layer. Thus the coercive field and the bias field does not vary simply as inversely proportional to the thickness as predicted by the simple model given in equation (7.4), but there is a small correction that is proportional to one over the thickness squared.

In the following we will discuss the dependence of coercivity of the bilayer on the exchange constant in the ferromagnet. In polycrystalline ferromagnets with random easy axes distributions the coercivity vanishes if the magnetization is constrained to be uniform over the whole sample. For particles much smaller than the exchange length the magnetization is

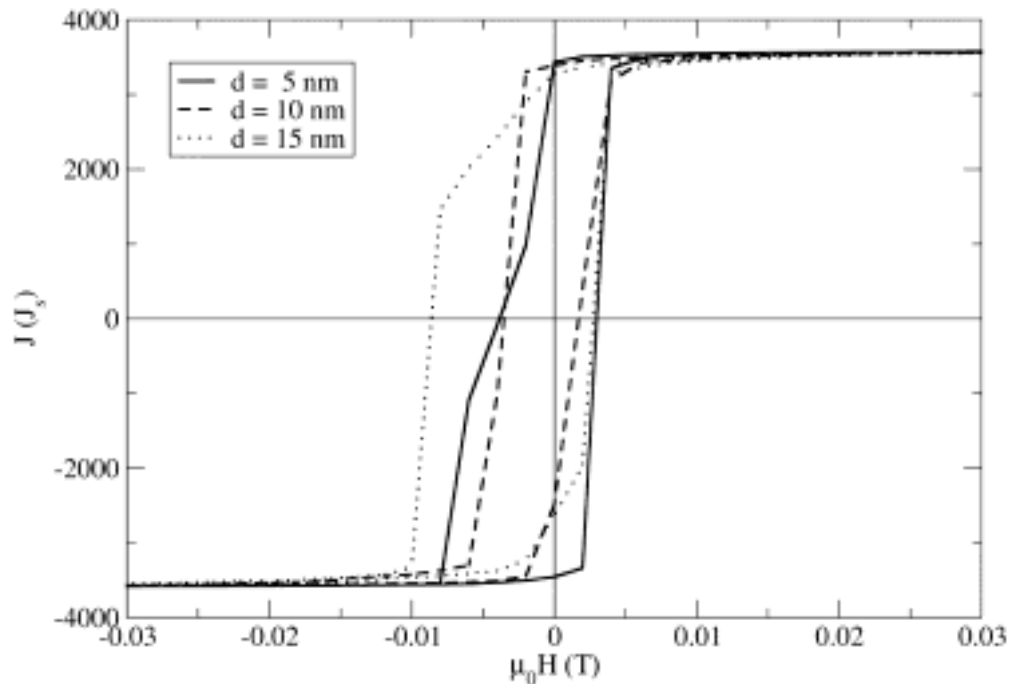


Figure 7.26: Hysteresis loop for different grain diameters in the ferromagnet and antiferromagnet.

indeed nearly uniform. The exchange length increases with increasing exchange constant. Thus in polycrystalline ferromagnets the coercivity vanishes for an infinitely large exchange constant. Zero coercivity indicates that no irreversible processes occur in the ferromagnet. To keep the magnetization for samples that are larger than the exchange length uniform during reversal a high rotating external field can be applied. These measurements are called rotational hysteresis measurements. For ferromagnets the rotational hysteresis loss is zero if the field is higher than the anisotropy field. This indicates that for high external fields or high exchange constants no irreversible processes occur in the ferromagnet.

However for ferromagnetic/antiferromagnetic bilayers even for arbitrarily large fields the rotational hysteresis loss does not vanish. Thus in ferromagnetic/antiferromagnetic bilayers irreversible processes occur during the reversal of the ferromagnet even if the exchange constant of the antiferromagnet is infinitely large. It is not obvious why the coercive field decreases with increasing exchange within the ferromagnetic layer.

Figure 7.29 shows the domain structure in the ferromagnet for small exchange constant in the ferromagnet ($A_F = 0.1 \times 10^{-12}$ J/m). The magnetization configurations (A-D) show equilibrium states for decreasing external field. The remanent state (Figure 7.29 B) clearly shows a

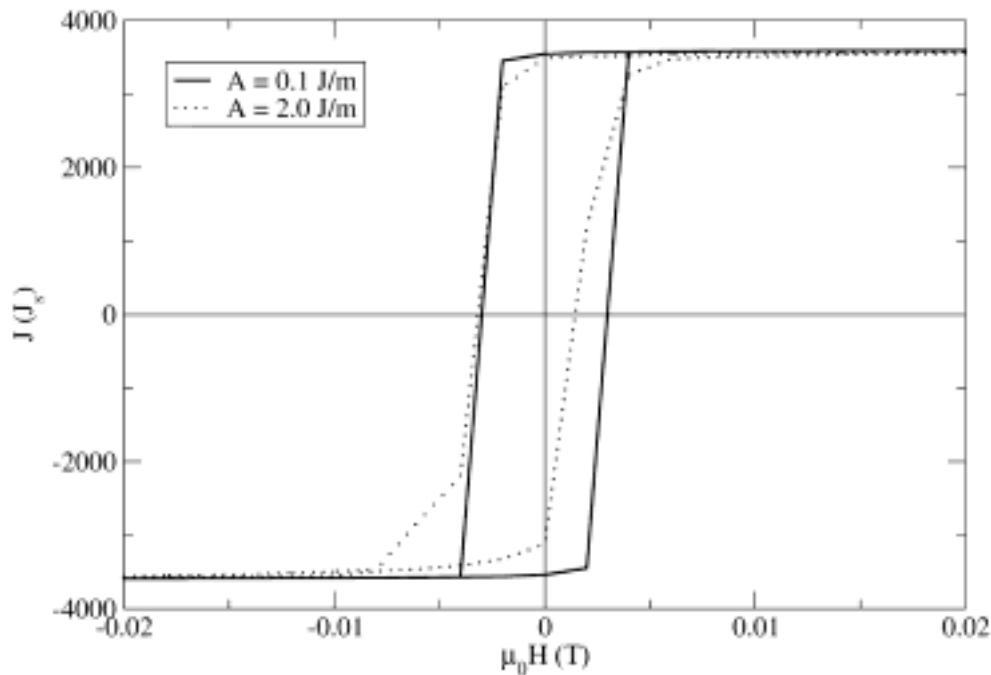


Figure 7.27 Hysteresis loop for different interface exchange constants.

ripple structure. If the external field is decreased further some regions in the ferromagnet rotate clockwise, other regions rotate counterclockwise. As a consequence it is possible to wind up partial domain walls in the antiferromagnet without exceeding a twist angle of 90° as the ferromagnet is reversed. This gives a possibility to get exchange bias at compensated interfaces as suggested by Koon.

If the spins in the antiferromagnet pointed exactly in the field direction the twist angle would exceed 90° as the external field is reversed. Figure 7.30 shows that neither in the field cooled state nor in the reversed state the twist in the antiferromagnet exceeds 90° owing to the ripple structure in the ferromagnet. For small ferromagnetic exchange both twists will unwind as the external field is decreased, resulting in a clockwise and counterclockwise rotation of the ferromagnetic spins, depending on different regions. After field cooling the antiferromagnetic spins far away from the interface will arrange in that direction parallel to the easy axis that leads to a smaller twist angle. Thus after field cooling the energy is lower than after the reversal of the ferromagnet. This suggested mechanism to exchange bias has to be further investigated.

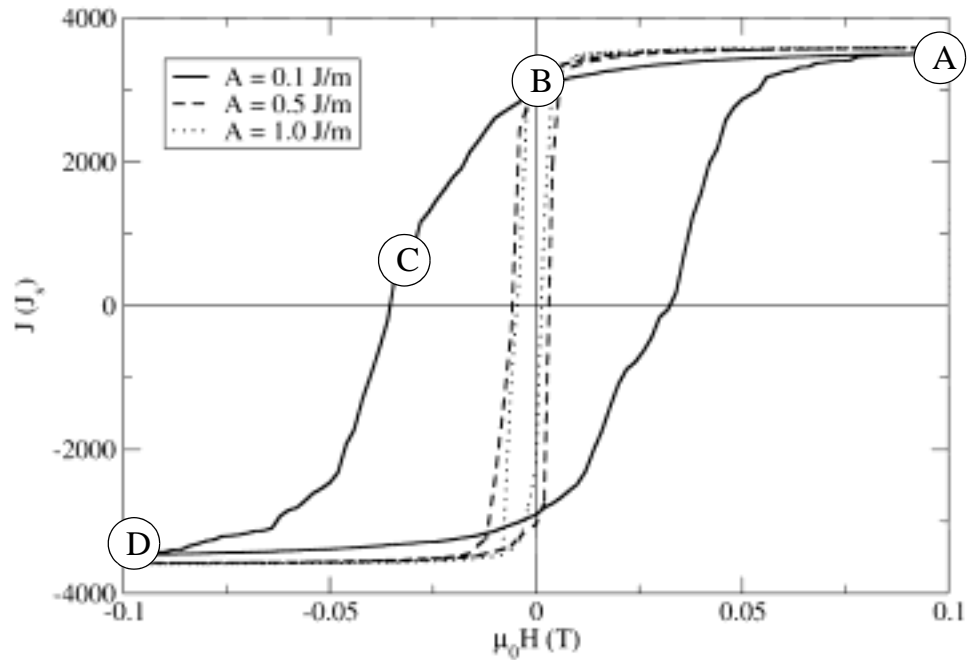


Figure 7.28: Hysteresis loops for different intergranular exchange in the ferromagnet. The spin configurations of the states marked with the letters (A-D) are shown in figure 7.29.

If the exchange in the ferromagnet is large the ferromagnetic spins rotate in the same direction, resulting in unwinding one twist and further winding up the other twist. In that mechanism one twist will exceed the critical angle that is at most 90° . As a consequence no bias but an increase in coercivity will occur.

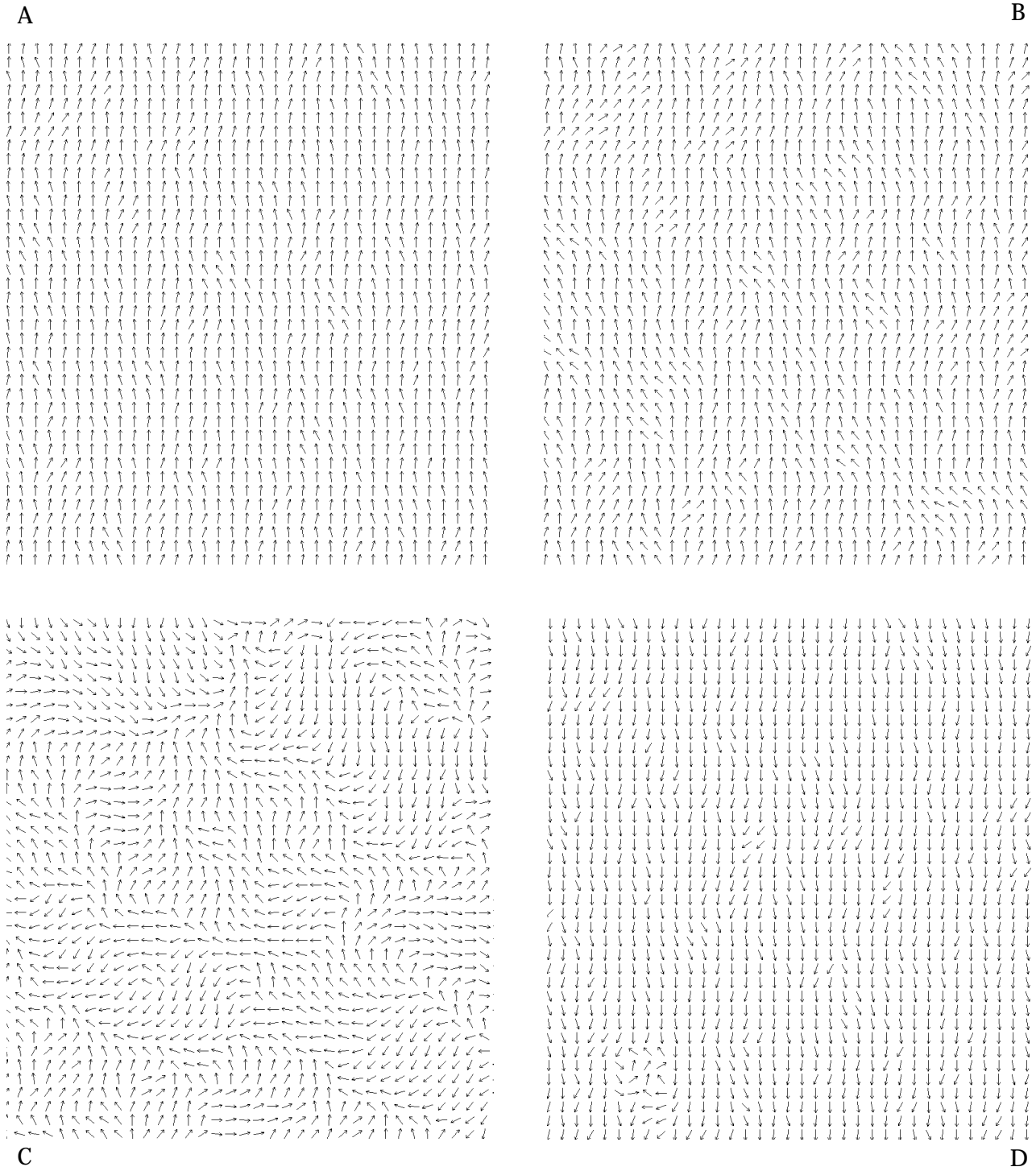


Figure 7.29 Magnetization configuration in the ferromagnet during the hysteresis loop. The exchange constant in the ferromagnet is $A = 0.1 \times 10^{-11}$ J/m.

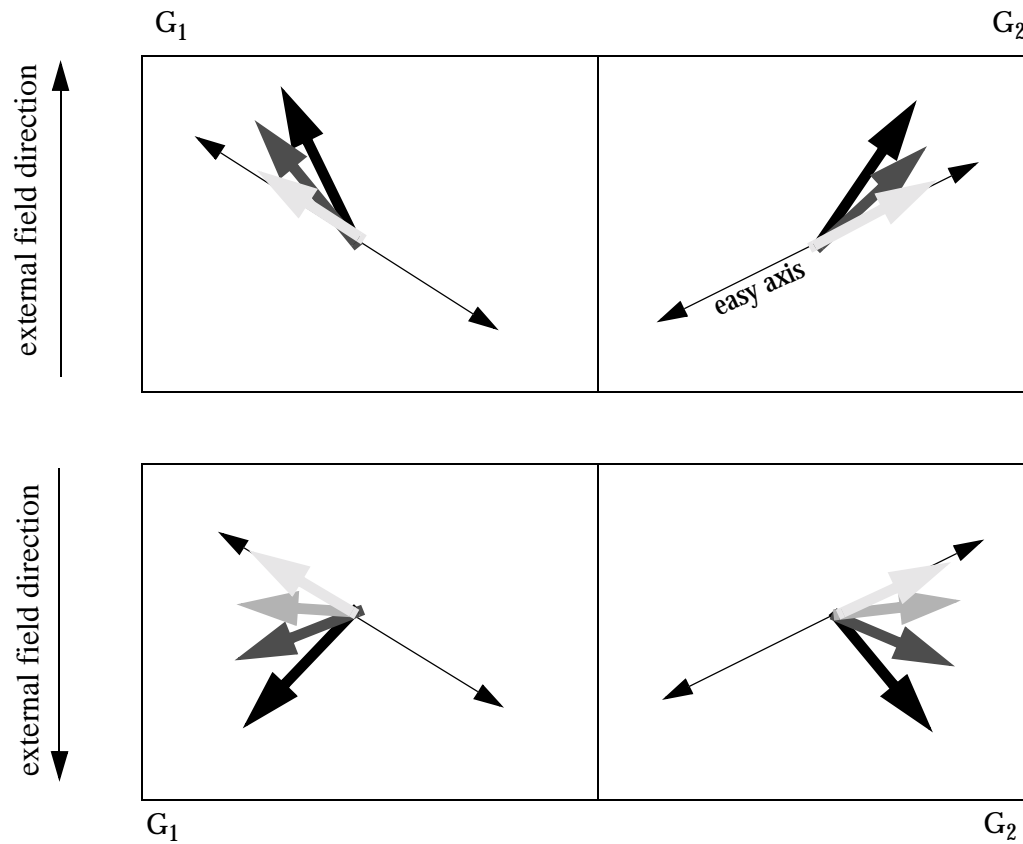


Figure 7.30: Partial domain wall in the antiferromagnet in grain G_1 and grain G_2 . The upper picture shows the state after field cooling. The picture below shows the state after reversal of the ferromagnet. The black arrows show the antiferromagnetic spins of one sublattice at the interface. We assume that the ferromagnetic spins point in the same direction as the antiferromagnetic spins at the interface. The brighter spins shows the magnetization of one sublattice in the antiferromagnet farther away from the interface. If the distance of the spins to the interface is much larger than the domain wall width the spins point parallel to the easy axis.

7.5 Conclusions

A continuum approach was developed to explore the dynamic magnetization processes in antiferromagnets/ferromagnetic bilayers on a mesoscopic length scale. The comparison with an atomistic calculation showed that the continuum approach is suitable to resolve the most important properties, such as spin canting of the two sublattices, domain wall formation and spin flop coupling at the interface to the ferromagnet. The finite element method was proved to be a suitable tool to discretize the micromagnetic equations for antiferromagnets. The finite element method is suitable to treat arbitrarily shaped grains in polycrystalline ferromagnetic antiferromagnetic bilayer.

The method was applied to calculate the exchange bias field in granular antiferromagnetic/ferromagnetic layers, that are used for spin valve sensors in read heads of hard disc drives. It is proposed that the important mechanism governing bias in the granular antiferromagnet with random easy axis distribution is the intergrain exchange coupling. The model assumes no defects except for grain boundaries, and coupling is due to spin flop at a perfect interface. The antiferromagnetic film is not a single crystal but instead a collection of small crystallites with randomly oriented axes. Because perfect compensation is assumed everywhere, there are no regions of uncompensated spins present at the interface. For such a system it is believed that bias does not occur. In the presented model exchange bias with spin flop coupling is found because the random distribution of granular axes is taken into account, that allows for the existence of two types of domains: one in which the antiferromagnet magnetization changes reversibly, and one in which the magnetization state changes irreversibly. It is the coupling between these two domain types that provides the exchange bias in the presented system. One consequence is that in the presented model the role of the interface energy is merely to provide coupling to the antiferromagnetic domains, and otherwise plays no role in the formation of bias.

In addition to the finite element method a granular model that assumes that every antiferromagnetic grain is a single domain particle was developed. With this model a larger number of grains could be calculated. The assumptions of that model could be justified by the finite element model. Field cooling was carefully simulated by a Metropolis Monte Carlo approach. The results of the granular model agree well with the finite element method. It was found that the bias field can be maximized by properly chosen antiferromagnetic thickness and average grain diameter.

References

- [1] E. N. Abarra, A. Inomata, H. Sato, I. Okamoto, and Y. Mizoshita, "Longitudinal recording media with thermal stabilization layers," *J. Appl. Phys. Lett.*, vol. 77, pp. 2581, 2000.
- [2] T. Ambrose, R.L. Sommer und C.L. Chien, "Angular dependence of exchange coupling in ferromagnetic/antiferromagnetic bilayers," *Phys. Rev. B*, vol. 56, pp. 83, 1997.
- [3] A. Aharoni, "Introduction to the Theory of Ferromagnetism", Clarendon Press Oxford, 1996.
- [4] M. N. Baibich, J. M. Broto, A. Fert, F. Nguyen Van Dau, F. Petroff, P. Eitenne, G. Creuzet, A. Friederich, and J. Chazelas, "Giant Magnetoresistance of (001)Fe/(001)Cr Magnetic Superlattices," *Phys. Rev. Lett.*, vol. 61, pp. 2472, 1988.
- [5] A. E. Berkowitz, J. H. Greiner, *J. Appl. Phys.*, vol. 36, pp. 3330, 1965.
- [6] H. B. Braun, "Nucleation in ferromagnetic nanowires-magnetostatics and topology," *J. Appl. Phys.*, vol. 85, pp. 6172, 1999.
- [7] W. F. Brown, *Phys. Rev.*, vol. 58, pp. 736, 1940.
- [8] A. M. Choukh, "Effect of interface on exchange coupling in NiFe/FeMn system," *IEEE Trans. Magn.*, vol. 33, pp. 3676, 1997.
- [9] D.R. Fredkin and T. R. Koehler, "Numerical micromagnetics of small particles," *IEEE Trans. Magn.*, vol. 24, pp. 2361, 1988.
- [10] E. Fullerton, D. Margulies, M. Schabes, M Carey, B Gurney, A. Moser, M Best, G. Zeltzer, K. Rubin, H. Rosen, M. Doerner, "Antiferromagnetically coupled magnetic media layers for thermally stable high density recording," *Appl. Phys. Lett.*, vol. 77, pp. 3806, 2000.
- [11] H. Fujiwara, K. Zhang, T. Kai, T. Zhao, "Effect of direct exchange coupling between antiferromagnetic grains on magnetic behavior of ferro/antiferromagnetic exchange coupled polycrystalline layer systems," *J. Magn. Mat.*, vol. 235, pp. 319, 2001.
- [12] A. C. Hindmarsh and L. R. Petzold, "Higher-Order Methods and Software Packages," *Computers in Physics*, vol. 9, pp. 148, 1995.
- [13] D. Hinzke and U. Nowak, "Magnetization switching in a Heisenberg model for small ferromagnetic particles," *Phys. Rev. B*, vol. 58, pp. 265, 1998.
- [14] Y. Iriji, J.A. Borchers, R.W. Erwin, S. H. Lee, P. J. van der Zaag, R.M. Wolf, "Perpendicular coupling in exchange-biased Fe₃O₄/CoO superlattices," *Phys. Rev. Lett.*, vol. 80, pp. 608, 1998.
- [15] R. Jungblut, R. Coehoorn, M.T. Johnson, Ch. Sauer, P.J. van der Zaag, A.R. Ball, Th.G.S.M. Rijks, J. aan de Stegge, and A. Reinders, "Exchange biasing in MBE-grown Ni₈₀Fe₂₀/Fe₅₀Mn₅₀ bilayers," *J. Magn. Magn. Mat.*, vol. 148, pp. 300, 1995.

- [16] J. V. Kim, R.L. Stamps, B.V. McGrath, and R.E. Camley, "Angular dependence and interfacial roughness in exchange-biased ferromagnetic/antiferromagnetic bilayers," *Phys. Rev. B*, vol. 61, pp. 8888, 2000.
- [17] N. C. Koon, "Calculation of Exchange Bias in Thin Films with Ferromagnetic/Antiferromagnetic Interfaces," *Phys. Rev. Lett.*, vol. 78, pp. 4865, 1997.
- [18] A. P. Malozemoff, "Mechanism of exchange anisotropy," *J. Appl. Phys.*, vol. 63, pp. 3874, 1988.
- [19] J. C. Mallinson, "On damped gyromagnetic equations," *IEEE Trans. Magn.*, vol. 30, pp. 62, 1987.
- [20] D. Mauri, H. C. Siegmann, P.S. Bagus und E. Kay, "Simple model for thin ferromagnetic films exchange coupled to an antiferromagnetic substrate," *J. Appl. Phys.*, vol. 62, pp. 3047, 1987.
- [21] W. H. Meiklejohn, C. P. Bean "New magnetic anisotropy," *Phys. Rev.*, vol. 102, pp. 1413, 1956
- [22] http://www.physik.uni-kl.de/w_hilleb/pdf/jb01/6-x/6-14.pdf
- [23] G. Mills and H. Jónson, "Quantum and thermal effects in H₂ dissociative adsorption: evaluation of free energy barriers in multidimensional quantum systems," *Phys. Rev. Lett.*, vol. 72, pp.1124, 1994.
- [24] T. J. Moran und I. Schuller, "Effects of cooling field strength on exhcange anisotropy at permalloy/CoO interfaces," *J. Appl. Phys.*, vol. 79, pp. 5109, 1996.
- [25] T. J. Moran, J. M. Gallego, I. K. Schuller, "Increased Exchange Anisotropy due to Interface Disorder in Permalloy/CoO," *J. Appl. Phys.*, vol. 78, pp. 1887, 1995.
- [26] A. I. Morosov, A. S. Sigov, "Interface roughness and unidirectional anisotropy of thin ferromagnetic film on uncompensated surface of antiferromagnet," *J. Magn. Magn. Mater.*, in press.
- [27] L. Néel, *Ann. Phys.*, vol. 2, pp. 61, 1967.
- [28] L. Néel and N. Kurti, "Selected Works of Louis Néel", Gordon and Breach, New York, 1988.
- [29] V. I. Nikitenko, V. S. Gornakov, L. M. Dedukh, Yu. P. Kabanov, and A. F. Khapikov, "Asymmetry of domain nucleation and enhanced coercivity inexchange-biased epitaxial NiO/NiFe bilayers," *Phys. Rev. B*, vol. 57, pp. 8111, 1998.
- [30] J. Nogués and K. Schuller, "Exchange bias," *J. Magn. Magn. Mater.*, vol. 192, pp. 203, 1999.
- [31] J. Nogués, D. Lederman, T.J. Moran, I. K. Schuller, K. V. Rao, "Large exchange bias and its connection to interface structure in FeF₂-Fe bilayers," *Appl. Phys. Lett.*, vol. 68, pp. 3186, 1996.
- [32] U. Nowak, A. Misra, and K.D. Usadel "Domain state model for exchange bias," *J. Appl. Phys.*, vol. 89, pp. 7269, 2001.

- [33] C. M. Park, K. I. Min, K. Shin, "Effects of surface topology and texture on exchange anisotropy in NiFe/Cu/NiFe/FeMn spin valves," *J. Appl. Phys.*, vol. 79, pp. 6228, 1996.
- [34] H. J. Richter, "Recent advances in the recording physics of thin-film media," *J. Phys. D: Appl. Phys.*, vol. 32, pp. 147, Aug. 1999
- [35] T. C. Schulthess and W. H. Butler "Consequenes of spin-flop coupling in exchange biased films," *Phys. Rev. Lett.*, vol. 81, pp. 4516, 1998.
- [36] C. G. Shull, W. A. Strauser, and E. O. Wollan, *Phys. Rev.*, vol. 83, pp. 333, 1951.
- [37] J. C. Slonczewski, "Fluctuation mechanism for biquadratic exchange coupling in magnetic multilayers," *Phys. Rev. Lett.*, vol. 67, pp 3172, 1991.
- [38] D. Spisák and J. Hafner, "Frustrated exchange interaction at the interface of antiferromagnetic films with ferromagnetic substrates," *Phys. Rev. B*, vol. 168, pp. 257, 1997.
- [39] S. Soeya, M Fuyama, S. Tadokoro, T. Imagawa, " NiO structure-exchange anisotropy relation in the Ni₈₁Fe₁₉/NiO films and thermal stability of its NiO film," *J. Appl. Phys.*, vol. 76, pp. 5356, 1996.
- [40] R. L. Stamps, "Mechanisms for exchange bias," *J. Phys. D:Appl. Phys.*, vol. 33, pp. 247, 2000.
- [41] M. D. Stiles and R. D. McMichael, "Model of exchange bias in polycrystalline ferromagnet-antiferromagnet bilayers," *Phys. Rev. B*, vol. 59, pp 3722, 1999.
- [42] M. D. Stiles and R. D. McMichael, "Coercivity in exchange-bias bilayers," *Phys. Rev. B*, vol. 63, pp. 64405, 2001.
- [43] E. C. Stoner und E.P. Wohlfarth, *Phil. Trans. Roy. Soc.*, vol. A 240, pp. 599, 1948.
- [44] D. Suess, T. Schrefl, J-V Kim, R. L. Stamps, J. Fidler, "Micromagnetic simulation of anti-ferromagnetic/ferromagnetic structures", *IEEE Trans. Magn.*, in press.
- [45] K. Takano, R.H. Kodama, A.E. Berkowitz, W. Cao and G. Thomas, "Interfacial uncompensated antiferromagnetic spins: Role in unidirectional anisotropy in polycrystalline Ni₈₁Fe₁₉/CoO bilayers," *Phys. Rev. Lett.*, vol. 79, pp. 1130, 1997.
- [46] C. Tang, *J. Appl. Phys.*, vol. 55, pp. 2226, 1984.
- [47]H. Xi and R. M. White, "Exchange coupling of NiFe/CrMnPt_x bilayers prepared by a substrate bias sputtering method," *J. Appl. Phys.*, vol. 87, pp. 410-415, 2000.A. E. Berkowitz, J. H. Greiner, *J. Appl. Phys.*, vol. 36, pp. 3330, 1965.

A

APPENDIX

A.1 Exchange coupling at mixed AF/F interfaces

In this appendix the transition from spin flop coupling to direct coupling by increasing the number of uncompensated spins is investigated in detail. Simulations are performed where it is assumed that 51%, 55%, 70% and 100% spins at the interface of sublattice A are present at the interface. Hence the percentage of the spins of the other sublattice B is 49%, 45%, 30% and 0%. The total energy is plotted as a function of the angle α (α denotes the angle between the ferromagnet and the hard axis of the antiferromagnet) in order to identify the direction of the ferromagnet with minimum energy. If the energy plots exhibit only one minimum a unidirectional anisotropy in the ferromagnet is imposed by the antiferromagnet. Two energy minima indicate spin flop coupling.

For the simulations the exchange constant of the antiferromagnet is, $A = -1 \times 10^{-11}$ J/m. The magnetic polarization of the two sublattices are $J_s^A = J_s^B = 1.1$ T and the lattice constant is, $a = 3.76 \times 10^{-10}$ m. The thickness of the permalloy layer is 2 nm and of the antiferromagnetic layer 10 nm, respectively. The uniaxial easy axis in the antiferromagnet is parallel to the interface plane. The anisotropy constants of sublattice A and B is varied in the calculations. The interface is compensated with an exchange constant $A = -1 \times 10^{-11}$ J/m.

In order to investigate the coupling mechanism between the ferromagnet and the antiferromagnet a rotational external field is applied. The total energy is plotted as a function of the angle α , which is the angle between the y -axis (normal to the easy axis in the antiferromagnet) and the field direction. In figure 7.31 the anisotropy constants of sublattice A and B are $K_1^A = K_1^B = 10 \times 10^5$ J/m³. If 70% and 100% of the interface spins are coupled to one sublattice in the antiferromagnet the coupling between the antiferromagnet and ferromagnet is collinear, as shown by the minima in figure 7.31. The total energy has a minimum when the angle α is 90°. Thus in the equilibrium state without external field the ferromagnet points parallel to the antiferromagnet. Figure 7.32 shows the magnetization configurations in the ferromagnet and antiferromagnet when the ferromagnet is rotated by a rotational external field. The image (1) in figure 7.32 shows that the interfacial spins in the ferromagnet and antiferromag-

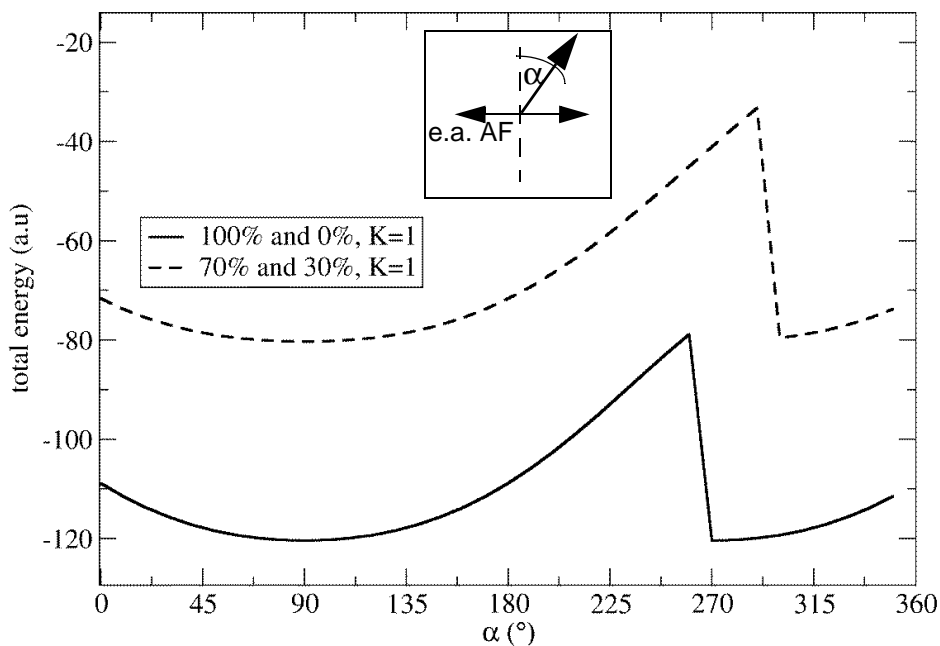


Figure 7.31: Total energy as a function of the angle between the external field and the hard axis in the antiferromagnet. A different percentage (100% and 70%) of the ferromagnetic interfacial spins are coupled to one sublattice of the antiferromagnet. The anisotropy constant is $K_1 = 10 \times 10^5 \text{ J/m}^3$.

net are arranged parallel. Although the interface is not completely uncompensated no spin-flop coupling occurs. Between image (5) and image (6) the antiferromagnet switches irreversibly. The irreversible switching can also be seen in the step in figure 7.31 at $\alpha = 290^\circ$.

When the interface between the ferromagnet and antiferromagnet becomes more compensated the interface coupling becomes weaker. In the simulation presented by the dashed line in figure 7.33, 51% and 49% of the interface spins are coupled to sublattice A and sublattice B , respectively. The antiferromagnet does not switch. Two energy minima, representing spin-flop coupling, occur. The angle between the ferromagnet and easy axis in the antiferromagnet is not exactly 90° owing to the uncompensated fraction of interfacial spins. At the interface in the antiferromagnet more spins point in positive x -axis direction than in negative x -axis direction. Thus in addition to the net moment from the spin-flop coupling a net moment in positive x -axis arises. Due to the negative exchange integral across the interface the spins in the antiferromagnet rotate a small angle into the negative x -axis direction. This

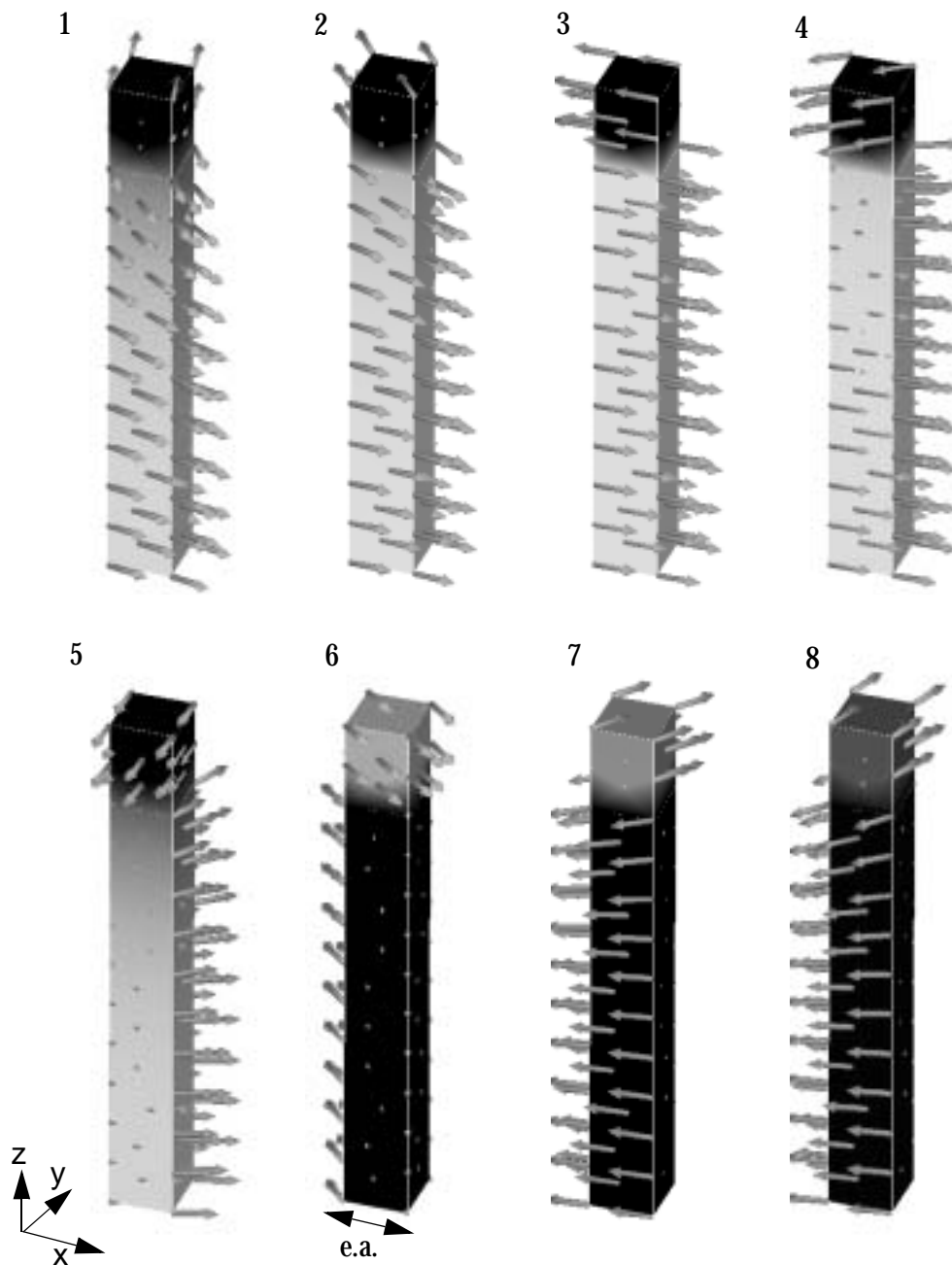


Figure 7.32: The magnetization configuration is shown when an rotational external field is applied. 70% and 30% of the interface spins are coupled to sublattice A and sublattice B, respectively. $K_1 = 10 \text{ MJ/m}^3$.

effect becomes more pronounced when the fraction of uncompensated spins is increased. The solid line in figure 7.33 shows the energy as a function of α when 55% of the ferromagnetic spins are coupled to one sublattice ($f=55\%$). The two energy minima become close to $\alpha = 90^\circ$. At $\alpha = 90^\circ$ the ferromagnet and antiferromagnet would be coupled collinear. Figure

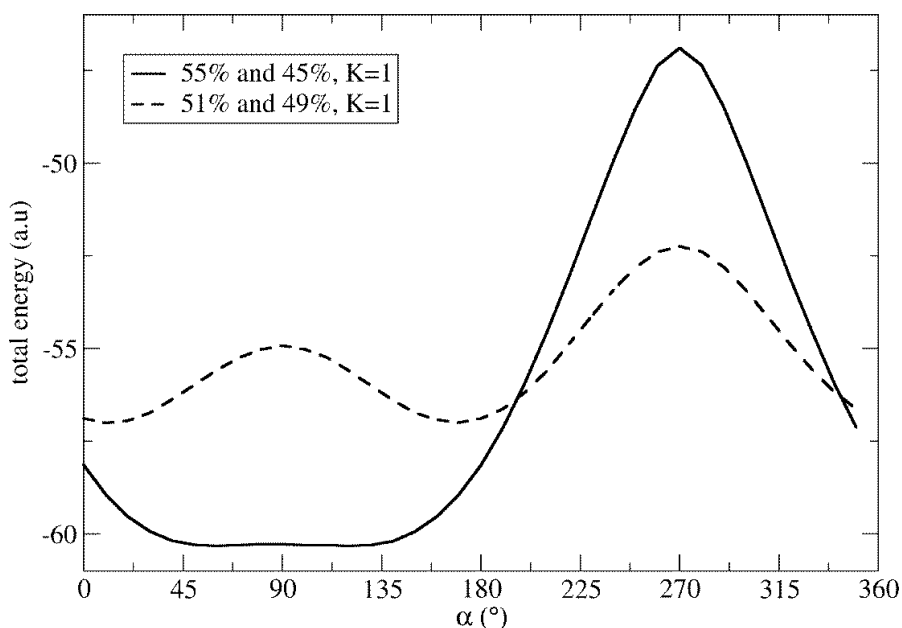


Figure 7.33: 55% and 51% of the ferromagnetic interfacial spins are coupled to one sublattice in the antiferromagnet, respectively. The anisotropy constant K is measured in MJ/m^3 . Spin-flop coupling occurs.

7.34 shows the magnetization configuration for $f=55\%$. The images (1) to (4) show that the antiferromagnet is less affected by the rotation of the ferromagnet. It indicates that in that range of the angle α the interface energy remains almost constant. The almost constant energy between $\alpha=45^\circ$ and $\alpha=135^\circ$ can be seen in the energy plot in figure 7.33.

Figure 7.35 shows the total energy as a function of α for an anisotropy constant in the antiferromagnet of $K_1 = 10 \times 10^5 \text{ J}/\text{m}^3$ and $K_1 = 20 \times 10^5 \text{ J}/\text{m}^3$. Figure 7.35 shows that the coupling between ferromagnet and antiferromagnet is collinear. For $f=70\%$ and $K_1 = 20 \times 10^5 \text{ J}/\text{m}^3$ (solid line) the antiferromagnet irreversibly switches when the angle α exceeds $\alpha = 220^\circ$. The antiferromagnet switches at smaller angle α when the anisotropy in the antiferromagnet is decreased. In the case of zero anisotropy the antiferromagnetic spins are locked to the ferromagnetic spins at the interface. The antiferromagnet would switch at $\alpha = 90^\circ$.

In the curves in figure 7.36 the fraction of uncompensated spins is reduced. Only in sample with $f=55\%$ $K_1 = 10 \times 10^5 \text{ J}/\text{m}^3$ the antiferromagnet switches irreversibly. In all the other samples twists in the antiferromagnet are formed and are unwound at some critical angles, which can be seen in the peaks in the energy in figure 7.36.

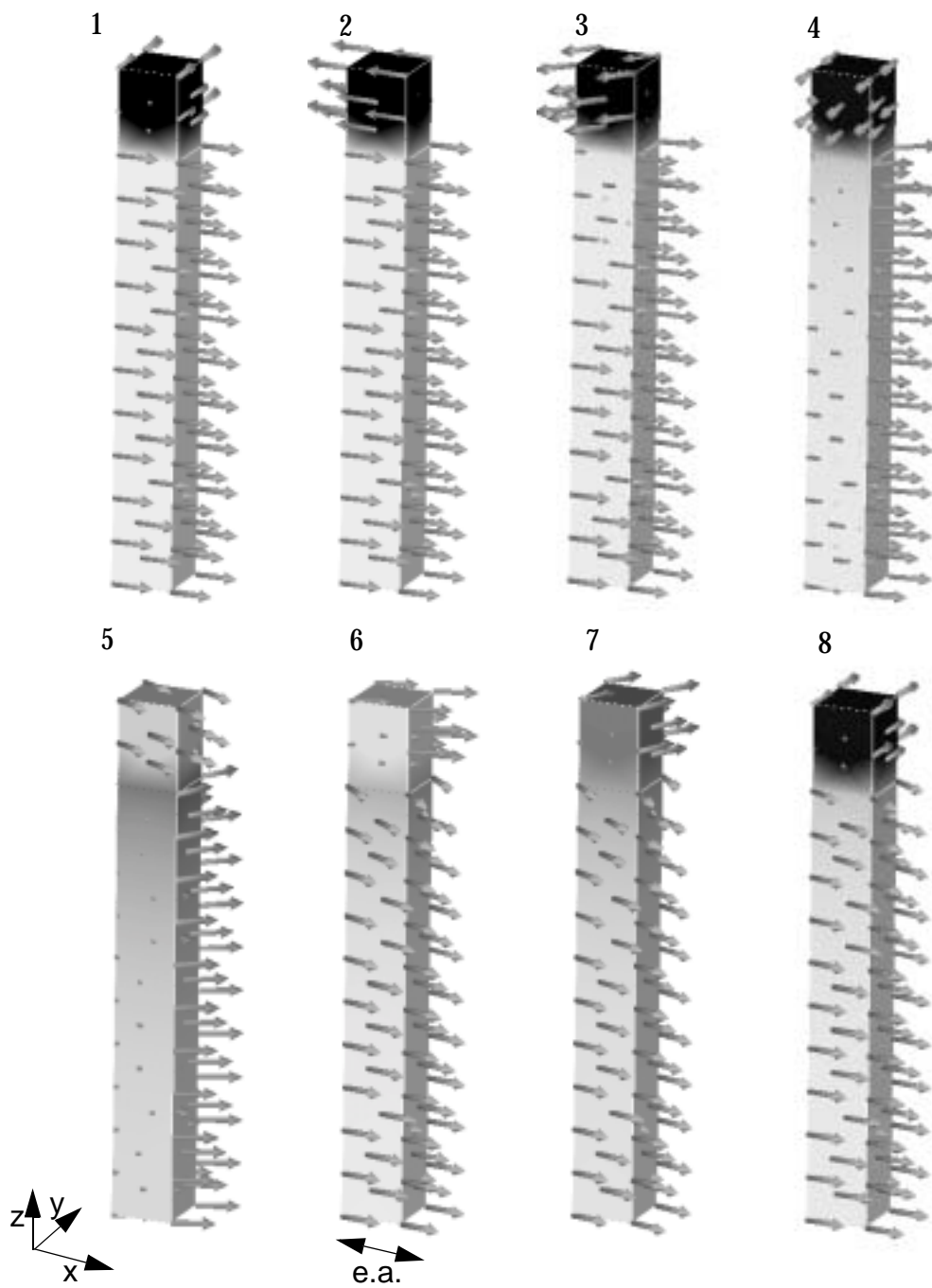


Figure 7.34: The spin configuration for a rotational external field is shown. 55% and 45% of the interface spins are coupled to sublattice A and sublattice B, respectively and $K_1 = 0.2 \text{ MJ/m}^3$.

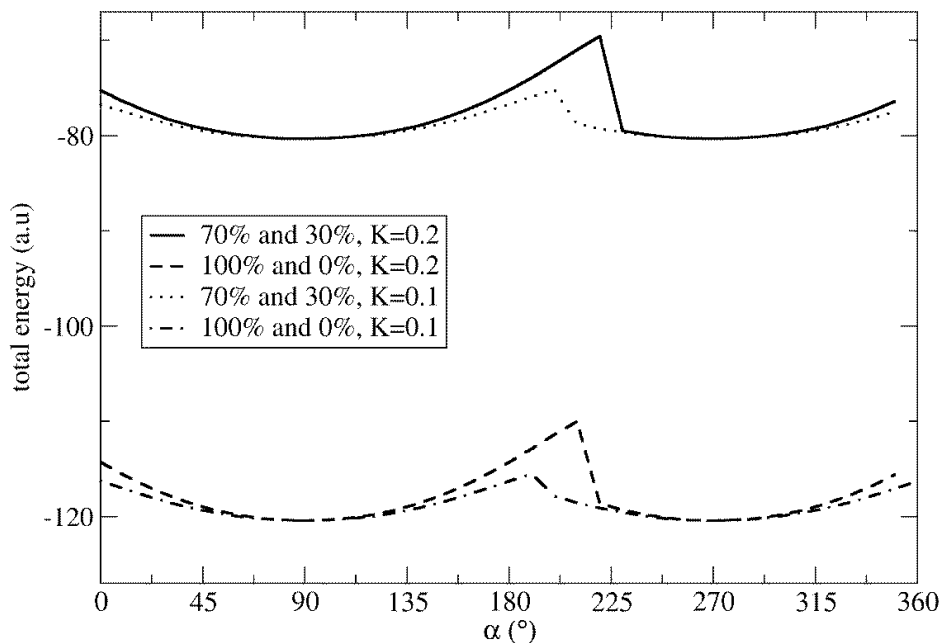


Figure 7.35: Total energy for different fractions of uncompensated spins at the interface and different values of the anisotropy constant. The anisotropy constant K is measured in MJ/m^3

A.2 Bias field for mixed interfaces

In the following the effect of spin flop coupling on the exchange bias field will be investigated. Let us distinguish two limits.

1. Domain wall energy in the antiferromagnet much larger than the interface energy:

The wall energy is large. Therefore the spins are parallel to the easy axis everywhere because a twist in the AF is unfavorable. In the upper image (A) of figure 7.37 the antiferromagnetic grain is assumed to have its easy axis parallel to the external field. The uncompensated interface in the antiferromagnet owing to defects creates a net moment. For a negative exchange integral across the interface the ferromagnet aligns antiparallel to the net moment. Exchange bias occurs. The spins at the interface are not canted because of the collinear orientation between the antiferromagnet and ferromagnet.

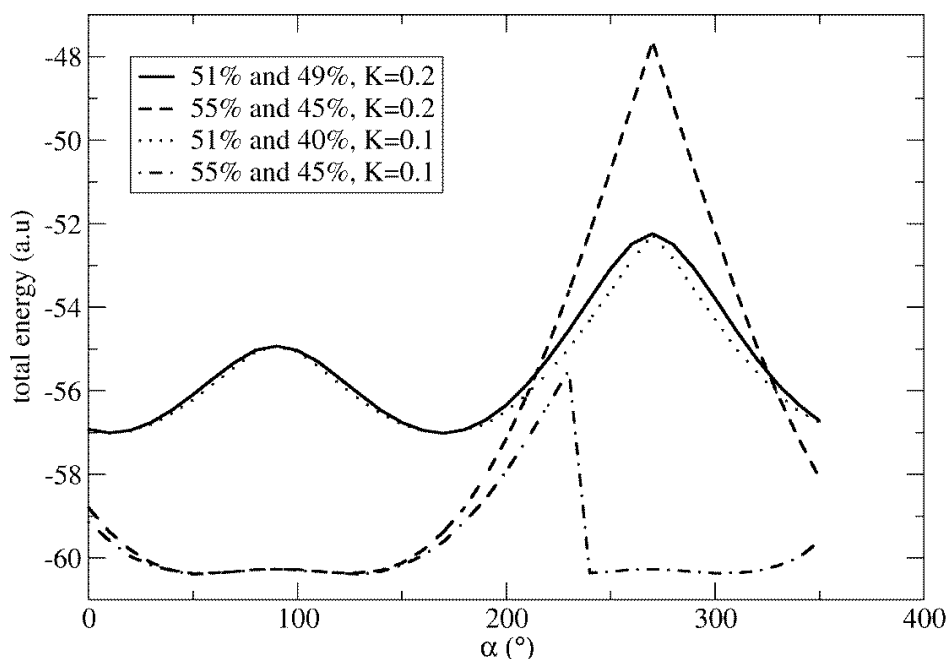


Figure 7.36: Energy for a small fraction of uncompensated spins at the interface. The anisotropy constant K is measured in MJ/m^3

If the easy axis of the antiferromagnetic grain is perpendicular to the external field the interfacial spins cant as shown in figure 7.37 (B). Spin flop coupling results. The net moment owing to uncompensated spins in the antiferromagnet is perpendicular to the ferromagnet for both the field cooled and the switched state. Thus both states are equal in energy. No bias but an enhanced coercivity occurs. The same arguments apply for an arbitrary direction of the easy axis in the antiferromagnetic grain. Thus, in that limit spin flop coupling has no influence on the exchange bias field for polycrystalline antiferromagnets.

To investigate the energy difference between the field cooled and switched state in more detail for different direction of the easy axis we performed a simulation of a ferromagnet/antiferromagnet bilayer with a fraction of uncompensated spins at the interface. The ferromagnet is saturated in different directions α . All directions are parallel to the interface. The dashed line in figure 7.38 shows the total energy of the bilayer. The interface exchange constant is $A = 1 \times 10^{-11} \text{ J}/\text{m}$. The anisotropy constant is $K_1 = 1 \text{ MJ}/\text{m}^3$. 51% and 49% of the ferromagnetic interface spins are coupled to sublattice A and B , respectively. All other param-

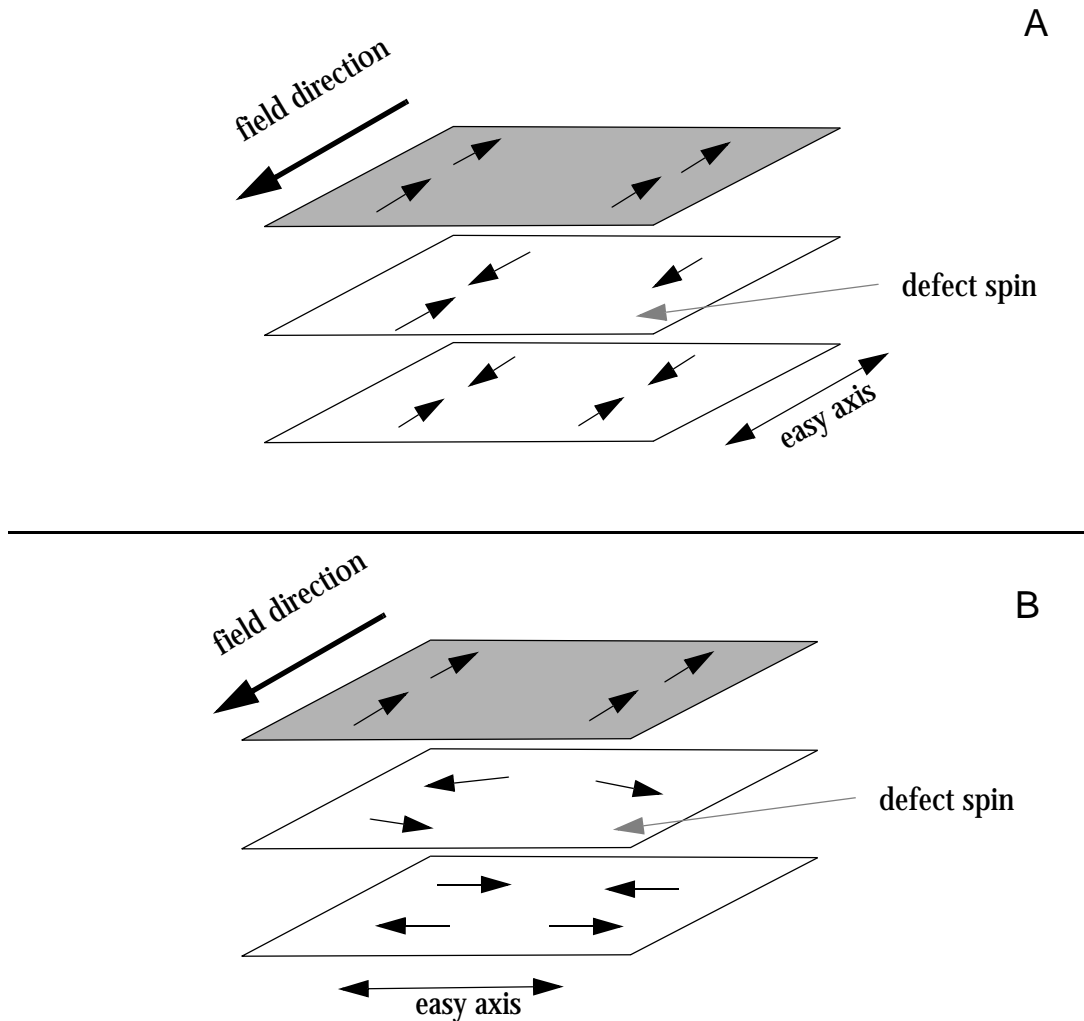


Figure 7.37: (A) The field direction is parallel to the easy axis in the antiferromagnet. A net magnetic moment acts on the ferromagnet. Bias occurs.

(B) The easy axis in the antiferromagnet is perpendicular to the field direction. The ferromagnetic spins and the antiferromagnetic spins are spin flop coupled. The net magnetic moment in the antiferromagnet is perpendicular to the ferromagnet. Thus the ferromagnet is not exchange biased.

eters are the same as in the sample of the previous section. If the ferromagnet is saturated in the direction α_1 the reversed state is determined by $\alpha_2 = \alpha_1 + 180^\circ$. The energy difference is $\Delta E = E(\alpha_2) - E(\alpha_1)$. Figure 7.38 shows that for all initial states ($0 < \alpha_1 < 180^\circ$) the reversed state has higher energy.

1. Interface energy is larger than the domain wall energy:

If the direct coupling is stronger than the spin flop coupling (large fraction of uncompensated

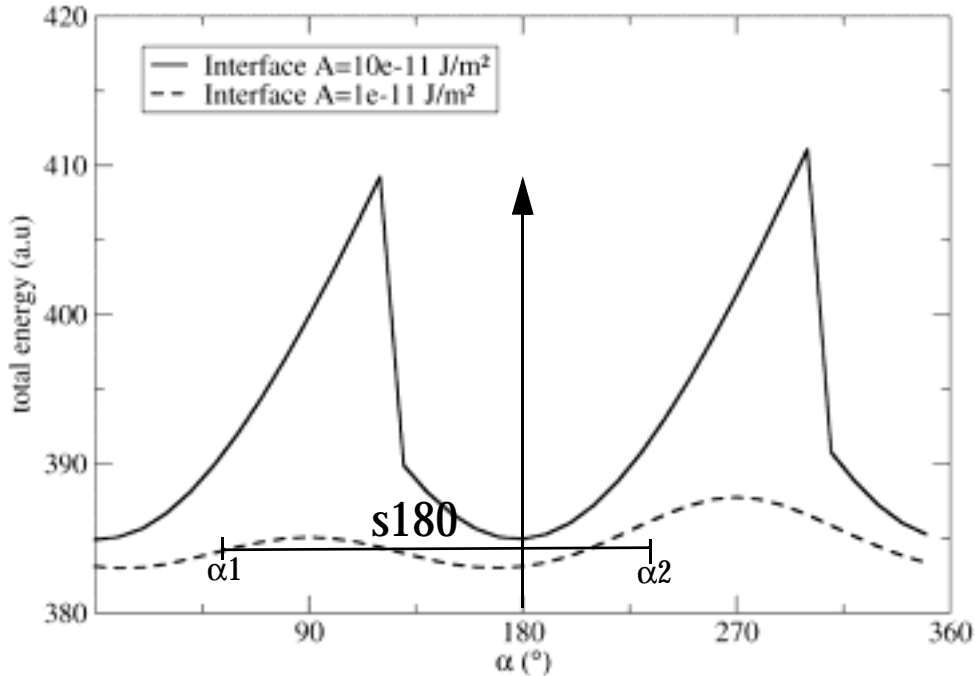


Figure 7.38: Energy as a function of the angle α for partial uncompensated interfaces and a thickness of the AF of, $l = 10$ nm. $K_1 = 1$ MJ/m³. 51% and 49% of the interfacial spins are coupled to sublattice A and B , respectively. The exchange constant between the ferromagnet and antiferromagnet is $A = 10^{-10}$ J/m (solid line) and $A = 10^{-11}$ J/m (dashed line).

spins) the ferromagnetic and antiferromagnetic spins are collinear. In that case the spins at the interface are not canted. Thus no spin flop coupling occurs. Exchange bias is solely determined by the direct coupling energy.

The situation becomes more complicated when the spin flop coupling is stronger than the direct coupling. Since the spins between antiferromagnet and ferromagnet are perpendicularly oriented it is not obvious that the net moment caused by uncompensated spins at the interface influences the hysteresis properties. If the spin flop coupling is much stronger than the direct coupling the net moment caused by uncompensated spins points perpendicular to the ferromagnet. This is true for the field cooled state and in the reversed state. Thus the net moment does not change the energy of the field cooled state and the reversed state. Hence it does not contribute to exchange bias.

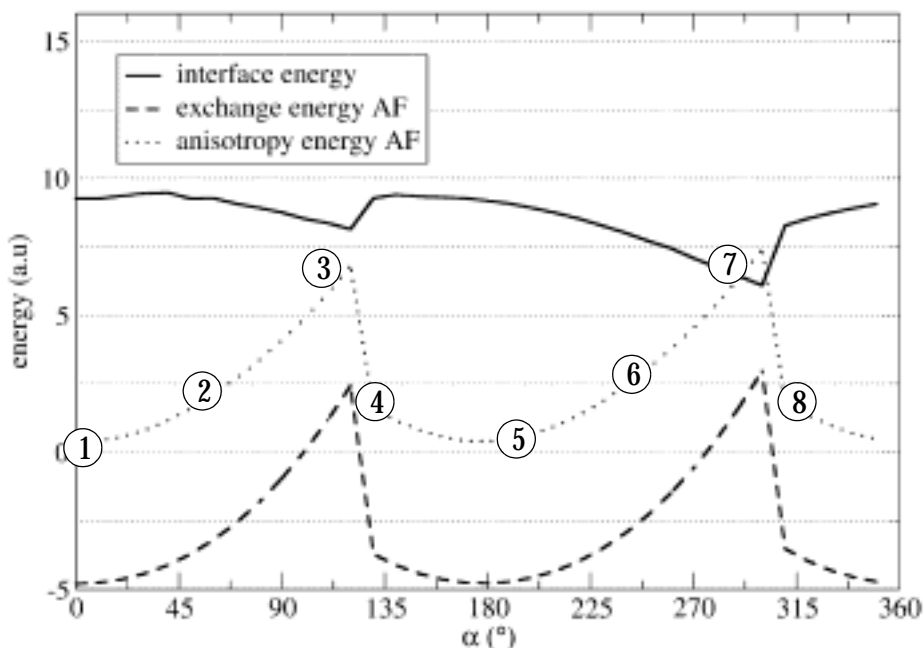


Figure 7.39: Different energy contributions for the sample with an interface exchange constant $A = 10$ J/m. The numbers refer to magnetization states shown in figure 7.40.

Stiles and McMichael[41] derived an expression for the total energy for a granular antiferromagnet, when both spin flop and direct coupling are considered. They assumed that spin flop coupling is so strong that the spins at the interface are locked in a configuration that minimizes the interfacial energy, forcing partial domain walls wound up in the antiferromagnet when the ferromagnet is rotated. Under that assumption they found that with increasing spin flop coupling the unidirectional anisotropy and hence the bias field decreases. The unidirectional energy decreases with $1/h$, where $h = 2J_{sf}/J_{net}$. J_{sf} is the prefactor of the biquadratic term of the interface energy. J_{net} is the effective direct coupling. For a completely uncompensated interface J_{net} is equal to the exchange integral. For a rough interfaces the effective direct coupling decreases J_{net} by approximately a factor $1/\sqrt{N}$, where N is the number of interfacial spins of the grain. J_{net} is the prefactor of the direct coupling energy (scalar product between AF and F interface spins) of the interface energy.

Micromagnetic simulations could not confirm the assumption that the interfacial spins are locked perpendicular to the ferromagnet for a strong interface coupling. In figure 7.39 the

interface energy is plotted as a function of the field angle α . 51% and 49% of ferromagnetic interface spins are coupled to sublattice A and B , respectively. Although the exchange constant across the interface of $A = 10^{-10}$ J/m is 10 times larger than the exchange constant in the antiferromagnet the interface energy does not remain constant during the rotation of the ferromagnet. The anisotropy constant is $K_1 = 1$ MJ/m³. If the interface exchange constant is increased further the antiferromagnetic spins at the interface align antiparallel to the ferromagnetic spins and parallel to each other. Effectively the interface is shifted by one monolayer into the antiferromagnet. Spin flop coupling occurs between the first and the second monolayer apart from the interface. It is obvious that the exchange constant between this artificial interface is that of the bulk antiferromagnet. Thus the spin flop coupling is weak and the antiferromagnetic spins at the artificial interface cannot be locked to minimize interface energy.

At a first glance one could assume that in the case where spin flop dominates direct coupling no exchange bias occurs because the net moment caused by the uncompensated spins are perpendicular to the magnetization of the ferromagnet. Hence the uncompensated spins do not contribute to the total energy and the field cooled state and the reversed state are equal in energy. However by comparing the energies $E_1 = E(\alpha_1)$ and $E_2 = E(\alpha_1 + 180^\circ)$ in figure 7.38 one can find that the energy E_2 is larger than E_1 . As a consequence exchange bias occurs. Figure 7.39 compares different energy contributions during the reversal of the ferromagnet. When the angle $\alpha = 0$ the ferromagnet points perpendicular to the antiferromagnet, as shown in (1) in figure 7.40. As the ferromagnet is rotated a twist is formed in the antiferromagnet (compare spin configurations (2) and (3) in figure 7.40) resulting in an increase of the anisotropy energy and exchange energy in the antiferromagnet, as shown by the dotted and dashed line in figure 7.39, respectively. When the external field angle α exceeds 110° the twist in the antiferromagnet becomes unstable and consequently unwinds. It is important to note that the twist that is formed at $\alpha = 290^\circ$ is not symmetric to the twist formed at $\alpha = 110^\circ$ as shown by the spin configurations (3) and (7) in figure 7.40. The uncompensated spins at the interface are responsible that a larger twist is formed at $\alpha = 290^\circ$ than at $\alpha = 110^\circ$. Thus the exchange energy and anisotropy energy is highest for $\alpha = 290^\circ$. So we expect the system to be exchange biased. To verify the hypothesis that the system is exchange biased, hysteresis loop calculations were performed. The hysteresis loop calculations will be discussed in the following.

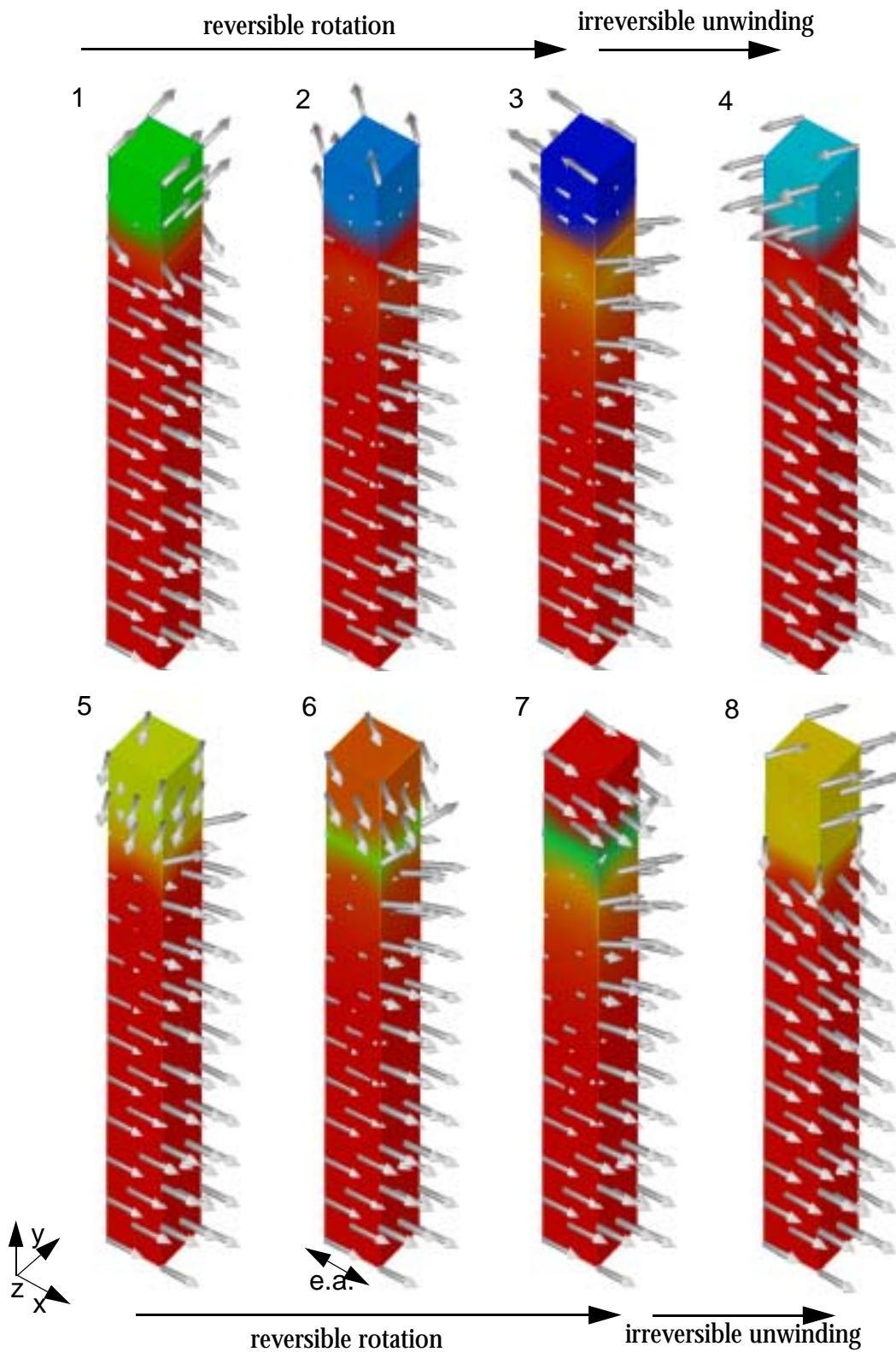


Figure 7.40: 51% and 49% of the interface spins are coupled to sublattice A and sublattice B , respectively and $K_1 = 1 \text{ MJ/m}^3$. The ferromagnet is rotated by a rotational external field. The interface exchange constant $A = 10^{-10} \text{ J/m}$.

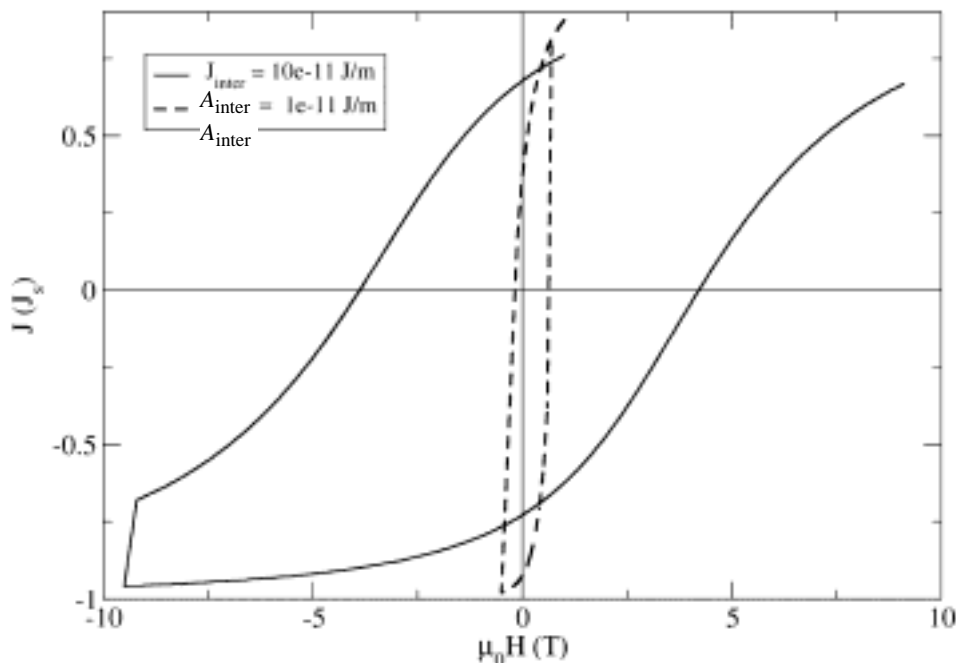


Figure 7.41: Hysteresis loop for two different values of the interface exchange constant. The AF thickness is, $l = 10$ nm. The anisotropy is $K_1 = 1$ MJ/m³. 51% and 49% of the interfacial spins are coupled to sublattice A and B , respectively. The exchange constant between the ferromagnet and antiferromagnet is $A = 10^{-10}$ J/m (solid line) (dashed line) $A = 10^{-11}$ J/m.

Figure 7.41 compares the hysteresis loop for two different interface exchange constants ($A = 10^{-10}$ J/m and $A = 10^{-11}$ J/m). The angle between the external field and the easy axis is 45° . The field direction is parallel to the interface between ferromagnet and antiferromagnet.

For $A = 10^{-10}$ J/m a large twist is formed in the antiferromagnet as shown in figure 7.40. Figure 7.41 confirms that exchange bias occurs although the ferromagnet and antiferromagnet are spin flop coupled as discussed in the previous paragraph. The bias field is $\mu_0 H_b = -0.16$ T and the coercivity is $\mu_0 H_c = 0.4$ T.

The bias field increases as the interface exchange constant is decreased to $A = 10^{-11}$ J/m. For $A = 10^{-11}$ J/m the antiferromagnetic spins remain during the reversal of the ferromagnet almost parallel to the easy axis. The frozen antiferromagnet leads to a decrease of the coercive field of $\mu_0 H_c = 0.23$ T. Since the interface spins are aligned parallel to the easy axis the angle between the uncompensated spins and the ferromagnet is approximately 45° for the field cooled state and the reversed state. Thus an energy difference between the field cooled state and the reversed state occurs because of different interface energies. The bias field is $\mu_0 H_b = -0.40$ T.

8

SELECTED PUBLICATIONS

- [1] D. Suess, T. Schrefl, W. Scholz, J. V. Kim, R. L. Stamps, J. Fidler, "Micromagnetic simulation of antiferromagnetic/ferromagnetic structures," IEEE Trans. Magn., in press.
- [2] D. Suess, R. L. Stamps, T. Schrefl, J. V. Kim, J. Fidler, "Exchange bias of polycrystalline antiferromagnets with perfectly compensated interface," Phys. Rev. Lett., submitted.
- [3] D.C. Crew, E. Girt, D. Suess, T. Schrefl, K.M. Krishnan, G. Thomas and M. Guilot, "The effect of magnetic interactions between grains on reversal behavior in diluted $\text{Nd}_2\text{Fe}_{14}\text{B}$," Phys. Rev. B., submitted.
- [4] D. Suess, V. Tsiantos, T. Schrefl, J. Fidler, W. Scholz, H. Forster and R. Dittrich, "Time resolved micromagnetics using a preconditioned finite element method," J. Magn. Magn. Mater., in press.
- [5] D. Suess, T. Schrefl, J. Fidler, R. C. Woodward, T. G. St. Pierre, R. Street, S. Sun, C. Murray, L. Folds and B. Terris, "Reversal Processes in FePt Nanoparticle Arrays," J. Magn. Magn. Mater., submitted.
- [6] D. Suess, V. Tsiantos, T. Schrefl, W. Scholz, J. Fidler, "Nucleation in polycrystalline nano elements using a preconditioned finite element method," J. Appl. Phys., vol. 91, pp. 7977, 2002.
- [7] T. Schrefl, J. Fidler, R. Dittrich, D. Suess, W. Scholz, V. Tsiantos, and H. Forster, "Fast switching of mesoscopic magnets", Spin dynamics in confined magnetic structures II, Eds: B. Hillebrands, K. Ounadjela, Springer, in press.
- [8] T. Schrefl, J. Fidler, D. Suess, W. Scholz and V. Tsiantos, "Micromagnetic simulation of dynamic and thermal effects," Advanced magnetic materials, Eds: Y. Liu, D.J. Sellmyer and D. Shindo, 2002, in press
- [9] D. Suess, W. Scholz, T. Schrefl, and J. Fidler, "Fast switching of small magnetic particles", J. Magn. Magn. Mater., vol. 242-245, pp. 426, 2002.
- [10] D. Payer, D. Suess, T. Schrefl and Josef Fidler, "Reversal processes in circular nanomagnets," J. Magn. Magn. Mater., submitted.
- [11] W. Scholz, D. Suess, T. Schrefl, and J. Fidler, "Domain structures and domain wall pinning in arrays of elliptical NiFe nanoelements," J. Appl. Phys., vol. 91, pp. 7047, 2002.
- [12] D. Suess, T. Schrefl and J. Fidler, "Reversal modes, thermal stability, and exchange length in perpendicular recording media," IEEE Trans Magn., vol. 27 pp. 1664, 2001.

- [13] T. Schrefl , H. Forster, D. Suess, W. Scholz, V. D. Tsiantos and J. Fidler, "Micromagnetic simulation of switching events", *Advances in Solid State Physics* 41, Ed: Bernhard Kramer, Springer Verlag, 2001, pp. 623-635.
- [14] V. D. Tsiantos, D. Suess, T. Schrefl and J. Fidler, "Stiffness analysis for the micromagnetic standard problem No. 4," *J. Appl. Phys.*, vol 89, pp. 7600, 2001.
- [15] D. Suess, T. Schrefl, J. Fidler and V. Tsiantos, "Reversal dynamics of interacting circular nanomagnets," *IEEE Trans. Magn.*, vol. 37, pp. 1960, 2001.
- [16] D. Suess, M. Dahlgren, T. Schrefl, R. Grössinger and J. Fidler, "Micromagnetic analysis of remanence and coercivity of nanocrystalline Pr-Fe-B magnets," *J. Appl. Phys.*, vol. 87, pp. 6573, 2000.
- [17] D. Suess, T. Schrefl and J. Fidler, "Micromagnetic simulation of high energy density permanent magnets," *IEEE Trans. Mag.*, vol. 36, pp. 3282, 2000.
- [18] D. Süß, T. Schrefl, Fidler and J. N. Chapman, "Micromagnetic simulation of the long range interaction between NiFe nano-elements using the BE-method," *J. Magn. Magn. Mater.*, vol. 196, pp. 617, 1999.
- [19] J. Fidler, T. Schrefl and D. Suess, "Grain boundaries in high performance magnets, reasons for poor or excellent properties" *Proc. of Workshop on Grain Boundaries: Their Characterisation and influence on properties*, Birmingham, UK, Sept. 1999, edited by I.R. Harris and I.P. Jones, The University Press, Cambridge, 2001, pp. 147-163.
- [20] D. Suess, "Mikromagnetische Simulation der Keimbildung in SE-Magneten," *Diplomarbeit*, Institut für Angewandte und Technische Physik, TU Wien, 1999

If I could live my life over again,
in the next one I would try to make more mistakes.

I wouldn't try to be so perfect, I would relax more.
I would be sillier than I've been,
In fact, I would take very few things seriously.
I would be less fastidious.
I would take more risks,
I would go on more trips,
I would contemplate more sunsets,
I would climb more mountains,
I would swim more rivers.
I would go to more places where I have never been,
I would eat more ice cream and fewer beans,
I would have more real problems and fewer imaginary ones.

I was one of those people who lived every minute
of his life sensibly and productively;
of course I had moments of happiness.
But if I could go back I would try
to have only good moments.
Because if you don't already know it,
this is what life is made of, only of moments,
Don't let the present moment slip away.
I was one of those who never
went anywhere without a thermometer,
a hot water bottle,
an umbrella and a parachute;

If I could live my life over again, I would travel lighter.
If I could live again I would start going barefoot
at the beginning of spring
and I would stay barefoot until the end of fall.
I would go on more merry-go-round rides,
I would contemplate more sunrises,
and I would play with more children,
if my life were ahead of me once again.

But, now you see, I am 85 years old and I know that I am dying.

(Jorge Luis Borges)

Dieter Süß

Rathausplatz 18
 A - 3130 Herzogenburg
 Tel.: 0676 6385926
 email: suess@magnet.atp.tuwien.ac.at
 http: magnet.atp.tuwien.ac.at/suess

Personal

Date of birth 15/12/1975
Parents Dipl. Ing. Rudolf Süß and Elisabeth Süß
Nationality Austria

Education

Ph.D. in Technical Physics at the Vienna University of Technology
 2000-2002
Graduation with excellence. The topic of the diploma thesis was
 01/12/1999 "Micromagnetic Simulations of Nucleation in Rare Earth Magnets"
Study of Technical Physics at the Vienna University of Technology
 1994-1999
BRG Krems-Ringstraße High school in Krems
 1986-1994
Primary school Herzogenburg
 1981-1986

Experience

University of Western Australia work at the Theory group of Prof. Dr. Bob Stamps
 10/2001-12/2001 supported by the Australian Research Council
IMA - Madrid short visit to the research group of Prof. J. M. Gonzales
 10/2000
University of Western Australia visit to Theory group of Prof. Dr. Bob Stamps
 08/2000-09/2000
Working group of Prof. Dr. J. Fidler researcher in the field of micromagnetic simulation
 12/1999-2002
Austrian Academy of Science design of the virtual exhibition for its 150th anniversary.
 06/1997 Collaboration on the section on magnetism
Union Herzogenurg implementation of a database for the Sport club of Herzogenburg
 06/1996
Institute for efficient teaching and learning giving lectures in mathematics, mechanics, geometry, physics
 10/1995 and 10/1996
Fa. Heigl working for an engineering company
 10/1994